

Novel Hybrid Materials And Their Applications

by

Aaron Charles Small



A thesis submitted to Victoria University of Wellington

In fulfilment of the requirements for the degree of

Doctor of Philosophy in Chemistry

Victoria University of Wellington

2008

Abstract

The development of novel hybrid materials of cellulose fibres and substrates with nanoparticles, conducting polymers and quantum dots, opens up novel application for new packaging materials and paper based products for the 'smart packaging' and 'functional products' areas that are emerging in the paper and packaging industries. Examples of these materials which have been developed here include cellulose fibres and substrates functionalised with magnetic nanoparticles, electrically conducting polypyrrole, and photoluminescent zinc sulfide quantum dots.

Such materials were synthesised and then characterised using Alternating Gradient Magnetometry (AGM), Atomic Absorption Spectroscopy (AA), Cotec Profilometer Measurements, DC Conductivity Measurements, Photoluminescence Spectroscopy (PL), Scanning Electron Microscopy (SEM), SQUID Magnetometry, Transmission Electron Microscopy (TEM), Vibrational Sample Magnetometry (VSM), X-ray Diffraction (XRD), X-ray Fluorescence (XRF) and X-ray Photoelectron Spectroscopy (XPS).

Ferrimagnetic magnetite nanoparticles (particle size 12-26 nm) were synthesised by a simple aqueous precipitation method and had a magnetic saturation of approximately 60 emu g⁻¹, a coercive field of approximately 12-120 Oe, and a remnant magnetisation of approximately 11 emu g⁻¹.

Magnetite coated Kraft fibres (1.2 – 3.15 wt. % Fe) were synthesised by adding a colloidal suspension of magnetite nanoparticles to a suspension of Kraft fibres. The fibres retained their inherent properties, such as tensile strength and flexibility, but inherited the magnetic properties of the magnetic nanoparticles. The nanoparticles remained unchanged on bonding - presumably through

hydrogen bonding between the surface hydroxyl groups of the cellulose and the oxygen present in the magnetite.

Newsprint, Kraft Board and Cotton fabric were coated with polypyrrole using a chemical polymerisation method. SEM shows a complete coating, whereby the fibres are completely encapsulated by the polymer, including individual fibrils. Again, bonding is facilitated through hydrogen bonding between the surface hydroxyl groups of the cellulose and the lone pairs of the nitrogen in the polypyrrole backbone. Samples were doped with *p*-toluenesulfonic acid to increase conductivity, of which up to 4 S cm^{-1} was achieved.

The samples were coated with magnetite nanoparticles using a starch binder, and tested for their application in EMI shielding. A maximum shielding effectiveness of 43 % in the 1-18 GHz range and 47 % in the 16-40 GHz range was obtained using cotton fabrics coated with both polypyrrole and magnetite. A synergistic effect is observed on using a polypyrrole and magnetite coating.

Photoluminescent ZnS quantum dots, synthesised using an aqueous precipitation method, were doped with Mn^{2+} and Cu^{2+} to achieve emissions at approximately 600 nm (Mn^{2+}) and 530 nm (Cu^{2+}) on irradiation with UV light. The quantum dots had a particle size of approximately 2 nm, and were present in the zinc blende phase.

Doped ZnS-coated Kraft fibres (5 – 30 wt. % Zn) were synthesised by a number of methods, the most successful being the ‘in-situ’ method, in which a uniform and complete coating was afforded. The fibres retained their inherent properties, such as tensile strength and flexibility, but inherited the photoluminescent properties of the ZnS quantum dots. The quantum dots remained unchanged on bonding - presumably through hydrogen bonding between the surface hydroxyl groups of the cellulose and the sulfur present in the ZnS quantum dots.

ABSTRACT

ZnS quantum dots doped with Mn^{2+} and Cu^{2+} were successfully formulated for inkjet printing by capping with mercaptosuccinic acid. Upon irradiation with UV light, emissions at approximately 600 nm (Mn^{2+} -doped) and 530 nm (Cu^{2+} -doped) were observed. These were successfully inkjet printed in intricate patterns onto a number of substrates, including photographic quality inkjet paper, cotton, and wool.

Acknowledgements

I am indebted to my supervisors **Prof. Jim Johnston** and **Dr. Thomas Borrmann**, for their direction, encouragement and knowledge throughout the course of this PhD project.

Thank you to the **members of Laby 107** past and present. In particular, **Michael Richardson, Andy McFarlane, Matthew Cairns, James Grindrod, Fern Kelly and Kerstin Burridge**.

To **Wendy Popplewell, Jonathan Singh, Ray Vagana** and **John Watt** and the many other **postgraduate students in the SCPS**, thank you for making VUW such a special place to be a post graduate student.

Thank you to the **SCPS General Staff** for answering all my questions about equipment, lending or ordering me chemicals and equipment, and for always being so cheerful and friendly. A special mention must go to **David Flynn** for all the help he has given me in the performing and interpretation of electron microscopy.

Thank you to **Prof. Jeffery Tallon** and **Dr. Grant Williams** at IRL for help with Magnetometry measurements.

Thank you to **Dr. Andrew Amiet** of the Australian Defence Science and Technology Organisation in Melbourne, Australia, for his help with EMI Shielding measurements.

Thank you to **Dr. Noel Clark** and **Dr. Nafty van der Hoek** of CSIRO Forest Biosciences for their help with inkjet printing.

ACKNOWLEDGEMENTS

For hosting me in the ITC-WGT at the Forschungszentrum Karlsruhe, Germany, I would like to thank **Prof. Dr. Wolfgang Höll** and **Prof. Dr. Matthias Franzreb**. Thank you to **Dr. Hartmut Gliemann** and **Andre Petershans** for help with Atomic Force Microscopy, **Jens Bolle** for help with Alternating Gradient Magnetometry, and to my lab mates, **Dr. Asma Saeed**, **Carla Calderon**, **Marcelo Gonzalez**, and **Dirk Patzig** for making my time in Karlsruhe so enjoyable.

I acknowledge the funding provided for this project by the **MacDiarmid Institute of Advanced Materials and Nanotechnology**, and the assistance given to me by the **Curtis-Gordon Research Scholarship in Chemistry**, the **New Zealand Postgraduate Study Abroad Awards**, and the **VUW Science Faculty Small Grants Committee**.

As my time at VUW draws to a close, I feel it is appropriate to thank the **friends I have made while here at VUW**, firstly in Weir House in 2001, and subsequently. There are too many of you to name here, but you know who you are. Thank you for making Wellington an outstanding place to go to university.

To **Mum, Dad, Jonathan** and my **Grandparents**. Words cannot express how grateful I am for everything you have done for me. Thank you for always being so supportive, and encouraging me to follow a career in science.

Finally I would like to thank **Lizzie**, for all her love and support over the course of this PhD. Thank you for being the most welcome of distractions, for keeping me sane, for sharing the good times with me and for helping ease me through the tough times (as you do so well).

ACS.

Contents

Abstract	i
Acknowledgements	iv
List of Figures	ix
List of Tables	xvi
Glossary of Terms	xviii
1 Introduction	1
1.1 Hybrid Materials.....	1
1.2 Cellulose	1
1.3 Magnetic Nanoparticles	11
1.4 Photoluminescent Nanoparticles	22
1.5 Stabilisation of Nanoparticles and Quantum Dots.....	32
1.6 Conducting Polymers	41
1.7 Electromagnetic Interference Shielding.....	48
1.8 Inkjet Printing.....	50
1.9 Scope of the Project	51
2 Methods	54
2.1 Instrumental Methods.....	54
2.2 Experimental Methods	70
3 Magnetic Kraft Fibres	86
3.1 X-Ray Diffraction (XRD).....	86

3.2	X-Ray Fluorescence Measurements (XRF)	91
3.3	Magnetic Properties	91
3.4	Scanning Electron Microscopy (SEM)	99
3.5	X-Ray Photoelectron Spectroscopy (XPS)	107
3.6	Chapter Summary	113
4	Photoluminescent Kraft Fibres	115
4.1	X-Ray Diffraction (XRD)	115
4.2	Atomic Absorption Spectroscopy (AA)	119
4.3	Photoluminescence Spectroscopy (PL)	121
4.4	Scanning Electron Microscopy (SEM)	129
4.5	X-Ray Photoelectron Spectroscopy (XPS)	139
4.6	Synthesis of SiO ₂ -coated ZnS:Mn ²⁺ Quantum Dots	144
4.7	Synthesis of ZnS:Ag ⁺ Quantum Dots	145
4.8	Chapter Summary	147
5	Electromagnetic Interference (EMI) Shielding	148
5.1	Scanning Electron Microscopy (SEM)	149
5.2	DC Conductivity Measurements	166
5.3	EMI Shielding Measurements	168
5.4	Chapter Summary	175
6	Inkjet Printing	176
6.1	Printer Properties	176
6.2	Surfactants	177
6.3	Fluid Properties	180
6.4	Inkjet Printing	180
6.5	Photoluminescence Spectroscopy (PL)	184
6.6	Scanning Electron Microscopy (SEM)	189
6.7	Cotec Profilometer Measurements	192
6.8	Transmission Electron Microscopy (TEM)	193
6.9	Chapter Summary	194

CONTENTS

7	Conclusions	197
8	Future Work	202
	Appendix A Publications	205
	Appendix B Conference Presentations	226
	Appendix C Quantum Dot Fibres Patent Application	230
	Bibliography	238

List of Figures

1.1.	Structure of cellulose ($C_6H_{10}O_5$) _n	2
1.2.	Microscopic and sub-microscopic structure of cellulose.....	3
1.3.	Approximate chemical composition of wood	4
1.4.	2D representation of the structure of lignin	5
1.5.	Average composition of softwoods and hardwoods.....	6
1.6.	A refiner used in mechanical pulping of wood	7
1.7.	SEM images showing microfibrils in fibres produced from the RMP method and 'clean' fibres produced from the Kraft method	8
1.8.	Yield of major wood components during Kraft pulping of pine at different stages of delignification	9
1.9.	Plot of M vs. H and χ vs. H for a diamagnetic material.....	13
1.10.	Plot of M vs. H and χ vs. H for a paramagnetic material.....	14
1.11.	Simple schematic diagram showing ferromagnetic ordering	14
1.12.	Plot of M vs. T for a ferromagnetic material.....	15
1.13.	Simple schematic diagram showing antiferromagnetic ordering.....	16
1.14.	Simple schematic diagram showing ferromagnetic ordering	16
1.15.	Quarter unit cell of inverse spinel structure. A site (tetrahedral position) B site (octahedral position).....	17
1.16.	Domains are formed in ferromagnetic and ferrimagnetic materials in order to reduce surface charge	18
1.17.	Magnetic hysteresis curve for a ferrimagnetic sample of $CoFe_2O_4$	19
1.18.	Jablonski Diagram showing the various pathways of excitation, relaxation, and emission in a photoluminescent material	23
1.19.	A copper-doped ZnS phosphorescent powder under visible light, ultraviolet light, and total darkness.....	26
1.20.	Different sized quantum dots of CdS give rise to a number of possible colours	28
1.21.	Two dyes from the Rhodamine family, Rhodamine B and Rhodamine 6G	31
1.22.	Schematic diagram showing the electrical double layer	35
1.23.	Electrostatic stabilization of colloidal particles	35
1.24.	Schematic diagram showing polymeric stabilization using anchored polymers.....	38
1.25.	Schematic showing polymeric stabilization by adsorbed polymers	39
1.26.	Schematic showing 'bridging'	39

LIST OF FIGURES

1.27.	Schematic showing ‘depletion stabilisation’	40
1.28.	Unsubstituted monomers and substituted monomers	42
1.29.	Effect of doping on conducting polymers	44
1.30.	Effect of photodoping on polyacetylene	45
1.31.	Oxidative polymerisation of pyrrole	46
2.1	Schematic diagram showing AFM sample mounting of Kraft fibres	55
2.2	Schematic of the linear 4-point probe technique for DC conductivity measurements... ..	57
2.3	Schematic set-up of free space measurements.....	58
2.4	Photographs of the experimental set-up for free space measurements.....	59
2.5	Image of 2811 Dimatix Materials Printer and printhead.....	63
2.6	Image of Dimatix Materials Printer Cartridge	63
2.7	Quantum Design MPMS SQUID Magnetometer, housed at Industrial Research Ltd.....	66
3.1	XRD pattern of synthesised Fe_3O_4 nanoparticles.....	87
3.2	Reference pattern of crystalline Fe_3O_4	87
3.3	Reference pattern of crystalline $\gamma\text{-Fe}_2\text{O}_3$	87
3.4	Comparison between the XRD patterns of Fe_3O_4 nanoparticles synthesised with different $\text{FeCl}_2 \cdot 4\text{H}_2\text{O}$ concentrations.....	89
3.5	The effect of precursor concentration on particle size in the formation of Fe_3O_4 nanoparticles	90
3.6	Comparison between the XRD pattern of cellulose and Fe_3O_4 -coated cellulose fibres. .	90
3.7	Hysteresis loops for Fe_3O_4 nanoparticles synthesised with different precursor concentrations.....	91
3.8	Enlarged section of hysteresis loops for Fe_3O_4 nanoparticles synthesised with different precursor concentrations	92
3.9	Hysteresis loops for Fe_3O_4 nanoparticles synthesised via different methods	93
3.10	Hysteresis loops at 10 K and 300 K for Fe_3O_4 nanoparticles.....	94
3.11	Enlarged section of hysteresis loops at 10 K and 300 K for Fe_3O_4 nanoparticles.....	94
3.12	Hysteresis loops at 300 K for Fe_3O_4 -coated Kraft fibres (cellulose).....	95
3.13	Hysteresis loop for CoFe_2O_4 nanoparticles.....	96
3.14	Enlarged section of hysteresis loop for CoFe_2O_4 nanoparticles showing ferrimagnetic character.....	97
3.15	Hysteresis loop for CoFe_2O_4 -coated Kraft fibres (cellulose).....	97
3.16	Hysteresis loop for Polypyrrole and Fe_3O_4 -coated Kraft fibres(magnetite over polypyrrole)	98
3.17	Optical microscope images (90x magnification) of uncoated cellulose fibres and Fe_3O_4 coated Kraft fibres	100
3.18	Low magnification image of Fe_3O_4 -coated Kraft fibres.....	100
3.19	Magnetic Kraft fibres being picked up by a ‘hand held’ NdFeB permanent magnet.....	100

LIST OF FIGURES

3.20	High magnification SEM image of Fe ₃ O ₄ -coated cellulose fibres showing coating of individual fibrils.....	101
3.21	High magnification SEM image of Fe ₃ O ₄ -coated cellulose fibres showing coating of individual fibrils.....	102
3.22	High magnification SEM image of Fe ₃ O ₄ -coated cellulose fibres.....	102
3.23	High magnification SEM image of Fe ₃ O ₄ -coated cellulose fibres.....	103
3.24	High magnification SEM image of Fe ₃ O ₄ -coated cellulose fibres.....	103
3.25	EDS maps of Fe ₃ O ₄ coated cellulose fibres, complementary SEI images and elemental Fe maps	105
3.26	EDS elemental maps showing a cross-sectional view of a Fe ₃ O ₄ -coated Kraft fibre.....	105
3.27	EDS spectrum for Fe ₃ O ₄ -coated Kraft fibres.....	106
3.28	Enlarged view of EDS spectrum for Fe ₃ O ₄ -coated Kraft fibres	106
3.29	C 1s XPS spectrum of Kraft fibres (cellulose).....	107
3.30	Structure of cellulose (C ₆ H ₁₀ O ₅) _n	107
3.31	C 1s XPS spectrum for Fe ₃ O ₄ -coated Kraft fibres (cellulose)	108
3.32	Fe 2p XPS spectrum of Fe ₃ O ₄ nanoparticles	109
3.33	Fe 2p XPS spectrum of Fe ₃ O ₄ -coated Kraft fibres (cellulose)	109
3.34	Offset Fe 2p XPS spectra of Fe ₃ O ₄ nanoparticles and Fe ₃ O ₄ -coated Kraft fibres (cellulose), showing their peak positions and FWHM values.....	110
3.35	Overlaid Fe 2p XPS spectra of Fe ₃ O ₄ nanoparticles and Fe ₃ O ₄ -coated Kraft fibres (cellulose)	111
3.36	O 1s XPS spectra for cellulose fibres, Fe ₃ O ₄ nanoparticles, and Fe ₃ O ₄ -coated cellulose fibres.....	112
4.1	Reference XRD pattern of ZnS (zinc blende)	116
4.2	XRD pattern of undoped ZnS	116
4.3	Comparison between the XRD patterns of ZnS:Mn Nanoparticles with varying dopant levels (wt. %)	117
4.4	XRD pattern of ZnS:Cu ²⁺ quantum dots.....	118
4.5	XRD pattern of ZnS:Mn ²⁺ - and ZnS:Cu ²⁺ -coated Kraft fibres.....	119
4.6	Graphical representation of amount of Mn ²⁺ dopant included in ZnS lattice vs. amount of Mn ²⁺ dopant in the reaction mixture	120
4.7	Graphical representation of amount of Cu ²⁺ dopant included in ZnS lattice vs. amount of Cu ²⁺ dopant in the reaction mixture	121
4.8	PL excitation spectrum of ZnS:Mn ²⁺ (10 mol. % Mn ²⁺) quantum dots	122
4.9	PL excitation spectrum of ZnS:Cu ²⁺ (0.2 mol. % Cu ²⁺) quantum dots.....	122
4.10	PL emission spectrum of ZnS:Mn ²⁺ (10 mol. % Mn ²⁺) quantum dots	123
4.11	Recombination mechanism for ZnS:Mn ²⁺ quantum dots.....	123
4.12	Comparison between PL emission spectra of ZnS:Mn ²⁺ quantum dots with different dopant levels (mol. % in the reaction mixture)	124

LIST OF FIGURES

4.13	Photograph of ZnS:Mn ²⁺ quantum dots with different dopant levels under ambient light conditions and under UV light	125
4.14	PL emission spectrum of ZnS:Cu ²⁺ quantum dots	126
4.15	Recombination mechanism for ZnS:Cu ²⁺ quantum dots	126
4.16	Comparison between PL emission spectra of ZnS:Cu ²⁺ quantum dots with different dopant levels (mol. % in the reaction mixture)	127
4.17	Photograph of ZnS:Cu ²⁺ quantum dots with different dopant levels under UV light	128
4.18	PL emission spectrum of ZnS:Cu ²⁺ -coated Kraft fibres (cellulose)	128
4.19	PL emission spectrum of ZnS:Cu ²⁺ -coated Kraft fibres (cellulose)	129
4.20	Photograph showing PL emission under UV light from doped ZnS quantum dots and doped ZnS-coated fibres	129
4.21	SEM image of ZnS:Mn ²⁺ quantum dots	130
4.22	SEM image of ZnS:Mn ²⁺ quantum dots	130
4.23	SEM image of ZnS:Cu ²⁺ quantum dots	131
4.24	SEM image of ZnS:Cu ²⁺ quantum dots	131
4.25	EDS elemental maps of ZnS:Mn ²⁺ quantum dots	132
4.26	EDS elemental maps of ZnS:Mn ²⁺ quantum dots	133
4.27	SEM image showing ZnS:Mn ²⁺ -coated Kraft fibres synthesised using the 'colloid method'	134
4.28	SEM image showing ZnS:Mn ²⁺ -coated Kraft fibres synthesised using the 'double dip method'	135
4.29	SEM image showing ZnS:Mn ²⁺ -coated Kraft fibres synthesised using the 'PDADMAC method', using 1 cm ³ PDADMAC	135
4.30	SEM image showing ZnS:Mn ²⁺ -coated Kraft fibres synthesised using the 'PDADMAC method', using 6 cm ³ PDADMAC	136
4.31	SEM image of ZnS:Mn ²⁺ -coated Kraft fibres synthesised using the 'in-situ method'	137
4.32	SEM image of ZnS:Mn ²⁺ -coated Kraft fibres synthesised using the 'in-situ method'	137
4.33	SEM image of ZnS:Mn ²⁺ -coated Kraft fibres synthesised using the 'in-situ method'	138
4.34	EDS maps of doped ZnS-coated Kraft fibres	139
4.35	Zn 2p XPS spectrum for ZnS quantum dots	140
4.36	Zn 2p XPS spectrum for ZnS-coated Kraft Fibres (cellulose)	141
4.37	Overlaid Zn 2p XPS spectrum showing bonding energy shift between doped ZnS quantum dots and doped ZnS-coated Kraft fibres (cellulose)	142
4.38	2p XPS spectra for doped ZnS-coated cellulose fibres and doped ZnS quantum dots	143
4.39	Photoluminescence emission spectrum of SiO ₂ -coated ZnS:Mn ²⁺ quantum dots	145
4.40	Photograph depicting the colours doped ZnS quantum dots	146
4.41	Photoluminescence emission spectrum of ZnS:Ag ⁺ quantum dots	146
5.1	Low magnification SEM image of uncoated newsprint	149
5.2	SEM image of fibre surface of uncoated newsprint showing starch binder particles	149

LIST OF FIGURES

5.3	Low magnification SEM image of magnetite-coated newsprint	150
5.4	SEM image of magnetite-coated newsprint showing magnetite agglomerations present in the starch coating.....	150
5.5	SEM image of polypyrrole-coated newsprint	151
5.6	High magnification SEM image of polypyrrole-coated newsprint.....	151
5.7	Low magnification SEM image of magnetite and polypyrrole-coated newsprint	152
5.8	SEM image of magnetite and polypyrrole-coated newsprint	153
5.9	SEM image of uncoated Kraft board.....	153
5.10	SEM image of magnetite-coated Kraft board	154
5.11	SEM image of magnetite-coated Kraft board	154
5.12	SEM image of polypyrrole-coated Kraft fibres	155
5.13	SEM image of polypyrrole-coated Kraft board, showing individually coated fibrils.....	156
5.14	SEM image of polypyrrole-coated Kraft board, showing individually coated fibrils.....	156
5.15	EDS maps of polypyrrole-coated Kraft fibres	157
5.16	Low magnification SEM image of magnetite and polypyrrole-coated Kraft board.....	158
5.17	SEM image of magnetite and polypyrrole-coated Kraft board.....	158
5.18	EDS maps of polypyrrole and magnetite-coated Kraft fibres	159
5.19	High magnification EDS map of Fe, showing the magnetite agglomerations present within the starch binder.....	160
5.20	Low magnification SEM image of uncoated cotton fabric.....	160
5.21	SEM image of uncoated cotton fabric	161
5.22	Low magnification SEM image of magnetite-coated cotton fabric	161
5.23	Low magnification SEM image of polypyrrole-coated cotton fabric.....	162
5.24	SEM image showing polypyrrole-coated cotton fibres.....	162
5.25	SEM image showing polypyrrole coating on cotton fibre surface.....	163
5.26	EDS maps of polypyrrole-coated cotton fabric.....	164
5.27	Low magnification SEM image of magnetite and polypyrrole-coated cotton fabric.....	164
5.28	SEM image of magnetite and polypyrrole-coated cotton fabric	165
5.29	EDS maps of polypyrrole and magnetite-coated cotton fabric	165
5.30	Photograph showing polypyrrole-coated cotton fabrics synthesised using different pyrrole monomer concentrations.....	167
5.31	EMI shielding effectiveness of a metal plate	168
5.32	EMI shielding effectiveness of coated newsprint samples in the 1-18 GHz range	169
5.33	EMI shielding effectiveness of coated newsprint samples in the 16-40 GHz range.....	170
5.34	EMI shielding effectiveness of coated Kraft board samples in the 1-18 GHz range.....	170
5.35	EMI shielding effectiveness of coated Kraft board samples in the 16-40 GHz range	171
5.36	EMI shielding effectiveness of coated cotton fabrics in the 1-18 GHz range.....	172
5.37	EMI shielding effectiveness of coated cotton fabrics in the 16-40 GHz range.....	172

LIST OF FIGURES

5.38	Plot showing the comparison between shielding effectiveness in the 1-18 GHz range of a number of substrates with different thicknesses.....	174
5.39	Plot showing the comparison between shielding effectiveness in the 16-40 GHz range of a number of substrates with different thicknesses.....	174
5.40	Effect of conductivity on EMI shielding effectiveness of polypyrrole-coated cotton samples in the 1-18 GHz range	175
6.1	Photograph of ZnS:Mn ²⁺ quantum dots capped with MSA, showing different MSA:Zn ²⁺ ratios.	178
6.2	Schematic showing the binding of MSA to the ZnS quantum dot surface	178
6.3	IR spectrum of MSA	179
6.4	IR spectrum of MSA-capped ZnS:Mn ²⁺	179
6.5	Photo quality inkjet paper with a strip of ZnS:Mn ²⁺ quantum dots printed on the surface. Under normal light conditions and under UV light conditions	181
6.6	A detailed inkjet printed image of a printed circuit board template on photo quality inkjet paper using ZnS:Mn ²⁺ quantum dots. Viewed under UV light.....	181
6.7	A detailed inkjet printed image of the Victoria University of Wellington logo on photo quality inkjet paper using ZnS:Mn ²⁺ quantum dots. Viewed under UV light	181
6.8	Comparison between images printed using 1 layer and 2 layers of ZnS:Mn ²⁺ quantum dots. Viewed under UV light.....	182
6.9	A detailed inkjet printed image of the Victoria University of Wellington logo on photo quality inkjet paper using ZnS:Cu ²⁺ quantum dots. Viewed under UV light.....	183
6.10	A detailed inkjet printed image of the Victoria University of Wellington logo on cotton fabric using ZnS:Mn ²⁺ quantum dots. Viewed under UV light	183
6.11	PL emission spectrum of MSA-capped ZnS:Mn ²⁺ Quantum Dots	185
6.12	PL emission spectrum for one layer of ZnS:Mn ²⁺ quantum dots printed onto photographic quality inkjet paper	186
6.13	PL emission spectrum for two layers of ZnS:Mn ²⁺ quantum dots printed onto photographic quality inkjet paper	186
6.14	PL emission spectrum for two layers of ZnS:Mn ²⁺ quantum dots printed onto cotton fabric	187
6.15	PL emission spectrum for two layers of ZnS:Mn ²⁺ quantum dots printed onto merino wool fabric.....	187
6.16	PL emission spectrum of MSA-capped ZnS:Cu ²⁺ Quantum Dots.....	188
6.17	PL emission spectrum for two layers of ZnS:Cu ²⁺ quantum dots printed on photographic quality inkjet paper	189
6.18	Cross sectional SEM image of photographic quality inkjet paper printed with two layers of ZnS:Mn ²⁺ quantum dots	190
6.19	Cross sectional SEM image of photographic quality inkjet paper printed with two layers of ZnS:Mn ²⁺ quantum dots	191

LIST OF FIGURES

6.20	Cross sectional SEM image of photographic quality inkjet paper printed with two layers of ZnS:Mn ²⁺ quantum dots.....	191
6.21	Cross sectional SEM image of photographic quality inkjet paper printed with two layers of ZnS:Mn ²⁺ quantum dots.....	192
6.22	TEM images of MSA-capped ZnS:Mn ²⁺ quantum dots.....	192
6.23	2D Cotec Profilometer measurements of the letter 'r' in the Victoria University of Wellington logo, printed by with ZnS:Mn ²⁺ quantum dots.....	193
6.24	3D Cotec Profilometer measurements of the letter 'r' in the Victoria University of Wellington logo, printed by with ZnS:Mn ²⁺ quantum dots.....	194

List of Tables

1.1	Comparison between the average dimensions of hardwood and softwood fibres.....	6
1.2	Properties of Cellulose Fibres	11
1.3	Definition of some magnetic terms	12
1.4	Magnetic properties of some common magnetic materials	20
1.5	Conductivities of various conducting polymers. Conductivity of oriented polymer	43
2.1	Summary of experimental conditions for AA measurements of doped ZnS nanoparticles.....	55
2.2	Typical experimental conditions for an AFM measurement.....	56
2.3	Summary of fluid properties for inkjet printing	63
2.4	Summary of reagent quantities used for the formation of Fe ₃ O ₄ nanoparticles	71
2.5	Summary of amounts of Fe ₃ O ₄ used for coating Kraft fibres	72
2.6	Summary of dopant levels in the synthesis of ZnS:Mn ²⁺ quantum dots.....	76
2.7	Summary of dopant levels in the synthesis of ZnS:Cu ²⁺ quantum dots.....	77
2.8	Summary of attempts made to dope ZnS with Cu ²⁺	77
2.9	Summary of attempts made to dope ZnS with Ag ⁺	78
2.10	Summary of amounts of ZnS:Mn ²⁺ used in the coating of Kraft fibres.....	80
2.11	Summary of the amounts of PDADMAC used in the synthesis of ZnS:Mn ²⁺ -coated Kraft fibres.....	81
2.12	Summary of amounts of ZnS:Cu ²⁺ used in the coating of Kraft fibres.....	82
2.13	Summary of the amounts of PDADMAC used in the synthesis of ZnS:Cu ²⁺ -coated Kraft fibres.....	83
2.14	Table showing optimal molar ratios of MSA to Zn ²⁺ for the synthesis of soluble ZnS:Mn ²⁺ quantum dots.....	83
2.15	Table showing optimal molar ratios of MSA to Zn ²⁺ for the synthesis of soluble ZnS:Cu ²⁺ quantum dots.....	84
2.16	Surfactants used in the synthesis of soluble ZnS:Mn ²⁺ quantum dots.....	85
3.1	XRD peak data for synthesised Fe ₃ O ₄ nanoparticles	88
3.2	XRD peak data for crystalline Fe ₃ O ₄	88
3.3	XRD peak data for crystalline γ-Fe ₂ O ₃	88
3.4	Effect of precursor solution concentration on particle size of Fe ₃ O ₄ nanoparticles.....	89
3.5	Summary of magnetic properties of Fe ₃ O ₄ nanoparticles	93
3.6	Summary of magnetic properties of synthesised materials.....	99

LIST OF TABLES

3.7	Summary of Fe 2 <i>p</i> XPS binding energies and shifts for Fe ₃ O ₄ nanoparticles and Fe ₃ O ₄ -coated cellulose fibres.....	113
4.1	XRD peak data for reference ZnS (zinc blende).....	116
4.2	XRD peak data for undoped ZnS (zinc blende).....	117
4.3	Summary of AA analysis of doped ZnS quantum dots.....	119
4.4	Summary of Zn 2 <i>p</i> XPS binding energies and shifts for doped ZnS quantum dots and doped ZnS-coated Kraft fibres (cellulose).....	142
5.1	Table summarising the conductivities of a variety of polypyrrole-coated cotton fabrics, based on the concentration of pyrrole monomer used in the synthesis	166
5.2	Table summarising the conductivities of a variety of polypyrrole-coated cotton fabrics, based on the concentration of <i>p</i> -toluenesulfonic acid used in the synthesis.....	167
5.3	Effect of temperature on the conductivity of polypyrrole-coated cotton fabrics.....	168
5.4	Table showing the thicknesses of a number of substrates and their shielding effectiveness.....	173

Glossary of Terms

AA	Atomic Absorption Spectroscopy
a_B	Exciton Bohr radius
abu	Absorbance units
AFM	Atomic Force Microscopy
AGM	Alternating Gradient Magnetometry
B	Magnetic flux density
χ	Magnetic susceptibility
cps	Counts per second
CS	Continuous jet
DBSA	Dodecylbenzenesulfonic acid
DC	Direct current
DLVO	Derjaguin, Landau, Verwey and Overbeek
DOD	Drop On Demand
E_g	Bandgap energy
EDS	Energy Dispersive X-ray Spectroscopy
EMI	Electromagnetic Interference
ϵ_r^*	Relative complex permittivity
ϕ	Fluorescence quantum yield
FWHM	Full Width at Half Maximum
Γ	Reflection coefficient
H	Magnetic field
h^+	Hole
H_c	Coercivity
$h\nu$	Light
i	Current

I	Intensity
ICP	Intrinsically Conducting Polymer
IR	Infrared
ITO	Indium tin oxide
k_f	Rate of spontaneous photon emission
k_i	Excited state decay
m	Magnetic moment
M	Magnetisation
μ_0	Vacuum permeability
M_r	Magnetic remanence
M_s	Magnetic saturation
MSA	Mercaptosuccinic acid
PDADMAC	Poly(diallyldimethylammonium chloride)
PEDOT	Poly(3,4-ethylenedioxythiophene)
PET	Poly(ethylene terephthalate)
PL	Photoluminescence
PPy	Polypyrrole
p-TSA	<i>para</i> -Toluenesulfonic acid
r	Radius
R	Resistivity
r_D	Double layer thickness
R_y	Rydberg energy
σ	Magnetic moment per mass
S_0	Ground state
S_1	Excited state
S_{11}	Scattering parameter (reflected signal)
S_{21}	Scattering parameter (transmitted signal)
SE	Shielding Effectiveness
SEI	Secondary Electron Image
SEM	Scanning Electron Microscopy
SQUID	Superconducting Quantum Interference Device
t	Fluorescence lifetime

GLOSSARY OF TERMS

T	Transmission coefficient
T_1	Triplet state
T_c	Curie temperature
TEM	Transmission Electron Microscopy
TEOS	Tetraethylorthosilicate
V_A	Attractive force
V_{rep}	Repulsive force
VSM	Vibrating Sample Magnetometry
XPS	X-ray Photoelectron Spectroscopy
XRD	X-ray Diffraction
XRF	X-ray Fluorescence
ψ	Electric potential

Chapter 1

INTRODUCTION

1.1. Hybrid Materials

The combination of organic and inorganic materials provides the opportunity to develop new materials that not only retain the inherent properties of their component precursors but may also exhibit new properties due to synergistic interaction of the precursors.

Of particular interest is the development of new hybrid materials comprising cellulose fibre substrates that have been functionalised by transition metal oxide nanoparticles, conducting polymers or quantum dots, and the exploration of potential applications. Examples of such nanoparticles and nanomaterials are the magnetic iron oxides, photoluminescent zinc sulfide quantum dots, and the conducting polymer, polypyrrole. The chemistry of these materials, along with their preparation and application will be discussed below.

1.2. Cellulose

More than 100 million tonnes of organic material are produced each year by photosynthetic organisms such as plants, algae and some bacteria. Half of this material is made up of cellulose, which as a result, makes it one of the most abundant molecules on earth¹. This carbohydrate macromolecule is the principal structural element in the cell walls of the majority of plants and is also a major component of wood and cotton fibres.

As a result, cellulose has always played an important role in the life of man. Methods for the fabrication of cellulose based substrates for writing date back to the early Chinese dynasties. Today, cellulose and its derivatives (paper, nitrocellulose, cellulose acetate, etc.) are principal materials generated by industry for diverse markets and see a considerable economic investment².

Cellulose, $(C_6H_{10}O_5)_n$, is a long-chain polymeric carbohydrate of β -glucose. It is the fundamental structural component of green plants, in which the primary cell wall of the plant is predominantly cellulose, and the secondary wall contains cellulose with variable amounts of lignin. Lignin and cellulose, considered together, are termed lignocellulose, which (as wood) is the most common biopolymer on earth². Cellulose monomers (β -glucose) are linked together through 1,4 glycosidic bonds by condensation. Each monomer is oriented 180° to the next, as seen in Figure 1.1, and the chain is built up two units at a time³.

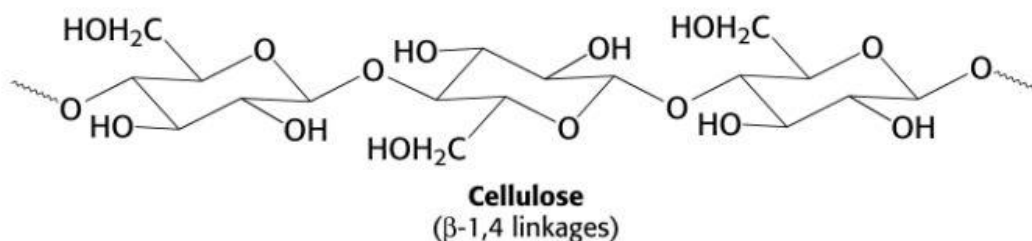


Figure 1.1. Structure of cellulose $(C_6H_{10}O_5)_n$.

The cellulose chains are formed into micro fibrils that constitute the basic framework of the plants cell. In micro fibrils, the multiple hydroxyl groups on the glucose units hydrogen bond with each other, holding the chains firmly together and contributing to their high tensile strength. This strength is important in cell walls, where they are meshed into a carbohydrate matrix that helps keep the plant cells rigid¹⁻⁴. The microscopic and sub-microscopic structures of cellulose are shown in Figure 1.2.

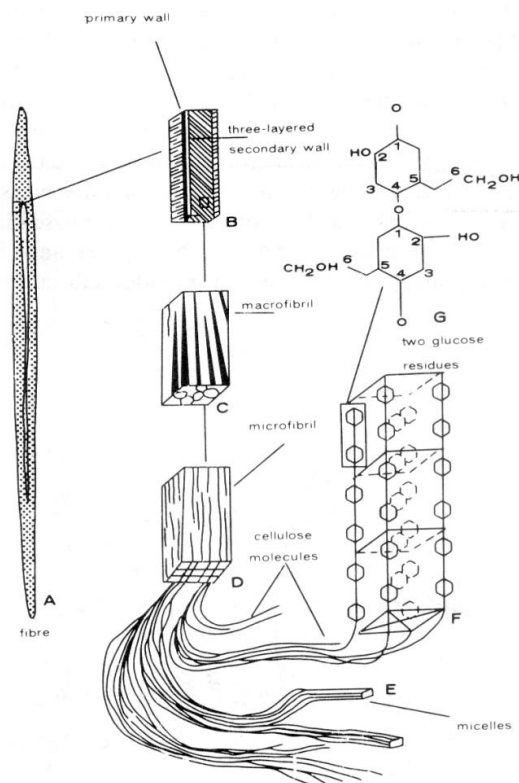


Figure 1.2. Microscopic and sub-microscopic structure of cellulose⁵.

1.2.1. Cellulose Derivatives

The hydroxyl groups of cellulose can be partially or fully reacted with various chemicals to provide derivatives with useful properties. Cellulose esters and cellulose ethers are some of the most important commercial materials. In principle, though not always in current industrial practice, cellulosic polymers are renewable resources¹.

Among the ester derivatives are cellulose acetate and triacetate, which are film- and fibre-forming materials that find a variety of uses. The inorganic ester nitrocellulose was initially used as an explosive and was an early film forming material. Ether derivatives include ethylcellulose, a water-insoluble commercial thermoplastic used in coatings, inks, and binders; hydroxypropyl methyl cellulose (E464), used as a viscosity modifier, gelling agent, foaming agent and binding agent; and hydroxyethyl methyl cellulose, used in production of cellulose films¹.

1.2.2. Paper

Paper is one of the most commonly used materials in today's world. It is cheap and easy to produce. Because paper is so widely used, papers made for different end-uses can be vastly different. In order to understand these differences it is important to look at the differences in the papermaking process and in the original fibre feedstock.

1.2.3. Wood

Paper is essentially made of wood. Once the high value lumber has been removed from the logs of wood, the remnants, called wood residuals, are turned into paper.

1.2.4. Composition of Wood

Wood consists of four separate components; cellulose, hemicellulose, lignin and extractives, as shown in Figure 1.3. Cellulose and hemicellulose are the most important of these components in the papermaking process⁶.

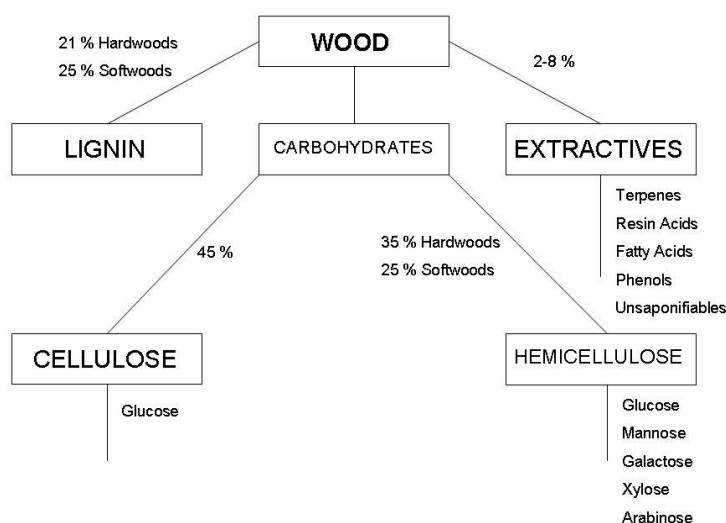


Figure 1.3. Approximate chemical composition of wood⁵.

While cellulose is made up of exclusively glucose units, hemicellulose contains a mixture of five different sugars; glucose, mannose, galactose, xylose and arabinose. The hemicelluloses are more easily degraded than cellulose and therefore are present in smaller quantities in wood⁶.

Lignin is a complex and highly polymerised material consisting of phenyl propane units linked together three dimensionally. A simplified two-dimensional representation of the structure is shown below in Figure 1.4.

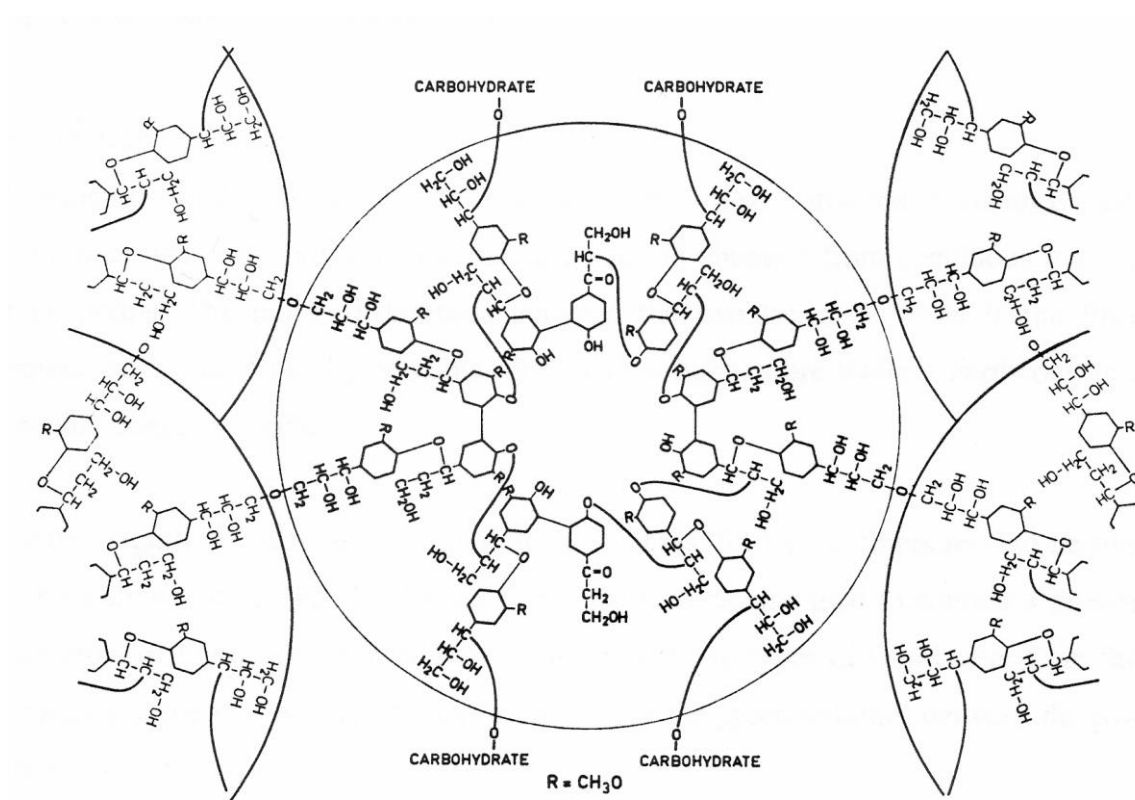


Figure 1.4. 2D representation of the structure of lignin⁵.

The main role of lignin is to act as the “glue” which holds the fibres together in the wood matrix. The amounts of lignin, along with cellulose and hemicelluloses, vary between different wood types⁶ (Figure 1.5).

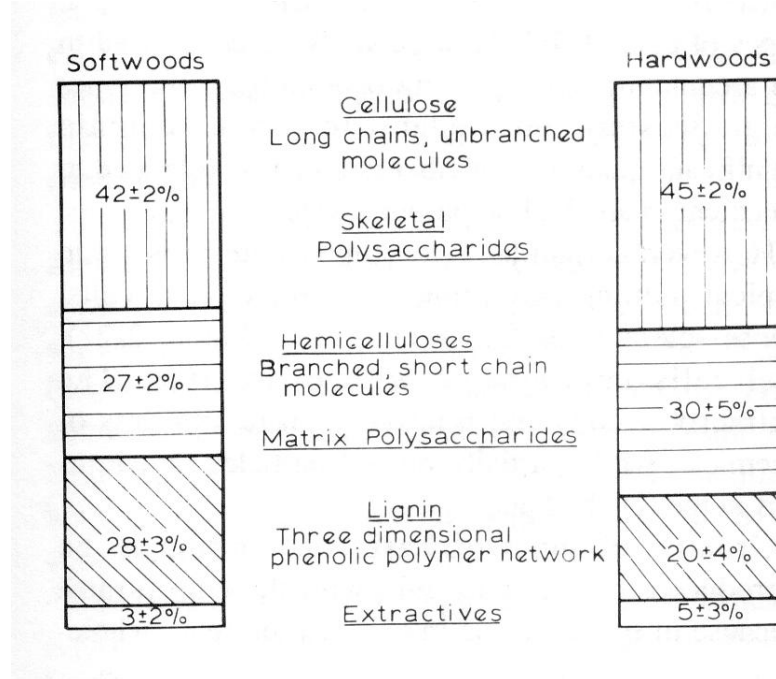


Figure 1.5. Average composition of softwoods and hardwoods⁵.

1.2.5. Types of Wood

Wood is classified into two main categories: soft wood (gymnosperms) and hard wood (angiosperms). Soft woods are obtained mostly from coniferous trees, while hardwoods are obtained mostly from deciduous trees. The major differences between the two types are the fibre content and the fibre dimensions, Table 1.1.

Woods	Length (mm)	Diameter (μm)
Coniferous (softwood)	4.0	40
Deciduous (hardwood)	2.0	22

Table 1.1. Comparison between the average dimensions of hardwood and softwood fibres

Hardwood typically contains ~65 % (by volume) fibre while softwood typically contains ~95 %, and as a result more lignin. Softwood fibres also tend to be two to three times longer than hardwood fibres⁶, and roughly twice as thick.

1.2.6. Pulping

Pulping is the process whereby wood residuals are reduced to a fibrous mass by the breaking of the bonds between the fibres. There are two main types of pulping; mechanical and chemical.

1.2.6.1. Mechanical Pulping

Mechanical pulping is the older of the two forms of pulping. The process works by grinding or shredding intact fibres from the wood and washing them away with jets of water. Older methods involve pressing blocks of wood against a rotating, roughened grinder. This method is not commonly used today⁶.

The current method of mechanical pulping involves shredding wood chips between the rotating discs of a machine known as a refiner, Figure 1.6. The pulp produced by this process is called refined mechanical pulp (RMP) and typically contains longer fibres than pulp produced from older mechanical methods⁶.

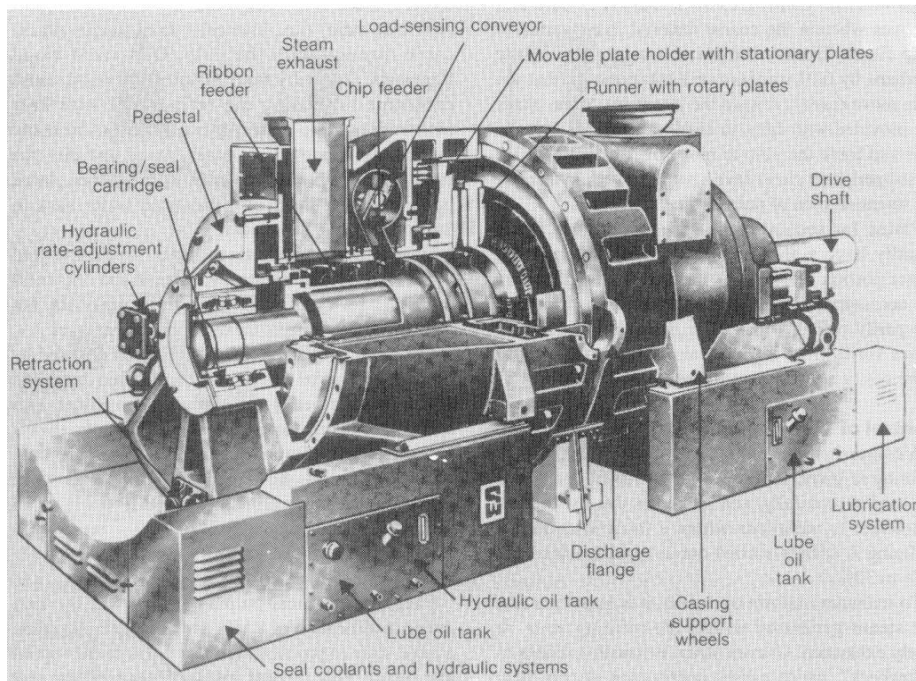


Figure 1.6. A refiner used in mechanical pulping of wood⁵.

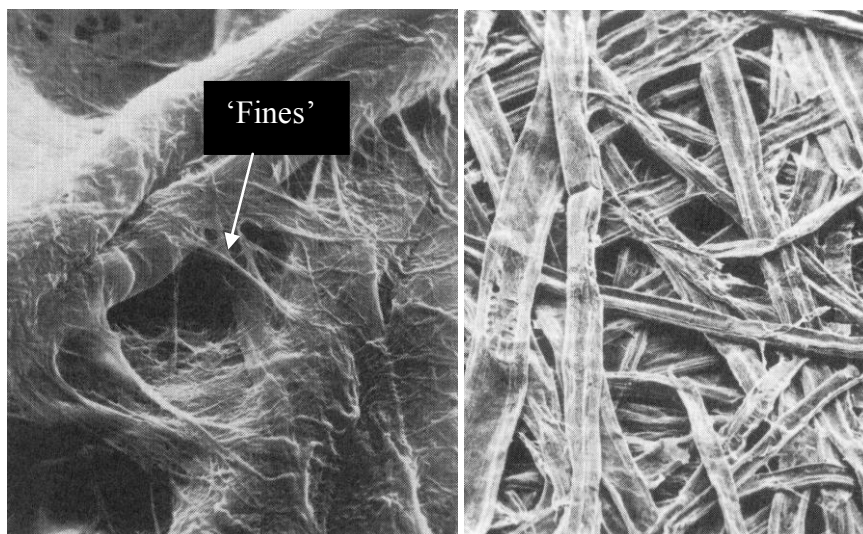


Figure 1.7. SEM images showing 'fines' in fibres produced from the RMP method (left), and 'clean' fibres produced from the Kraft method (right)⁵.

During mechanical pulping, cellulose fibres tend to unwind to a certain extent, producing fibrils and micro-fibrils. These fibrils and micro-fibrils (or fines), seen in Figure 1.7, help to fill the network voids of paper and as a result enhance optical and print properties.

There are a number of disadvantages associated with mechanical pulping. These include the high energy consumption involved in the pulping process, the weakening of fibres due to fibre damage during the pulping process, and that papers made from mechanical pulp darken on exposure to light (as the lignin is not removed in the mechanical pulping process).

1.2.6.2. Chemical Pulping

The objective of chemical pulping is to dissolve away the lignin and leave only the cellulose fibres. This is achieved by cooking the wood at elevated temperatures along with the appropriate chemicals. Chemical pulping produces undamaged fibres that are stronger than those produced by mechanical pulping methods. This is of benefit as stronger fibres produce a stronger paper. The pulps also have low lignin content and do not darken on exposure to light.

However, some of the fibres are dissolved with the lignin during the process and the overall yield of fibres is low, typically between 40 % and 50 % of the original wood residuals, Figure 1.8.

In addition, there are less fibre fines in chemical pulp than in mechanical pulp, so papers produced from chemical pulping methods are 'cleaner' (Figure 1.7), and because of this often have poor opacity⁷. The low fines content does, however, allow for faster water drainage and allows papermaking machines to run at higher speeds.

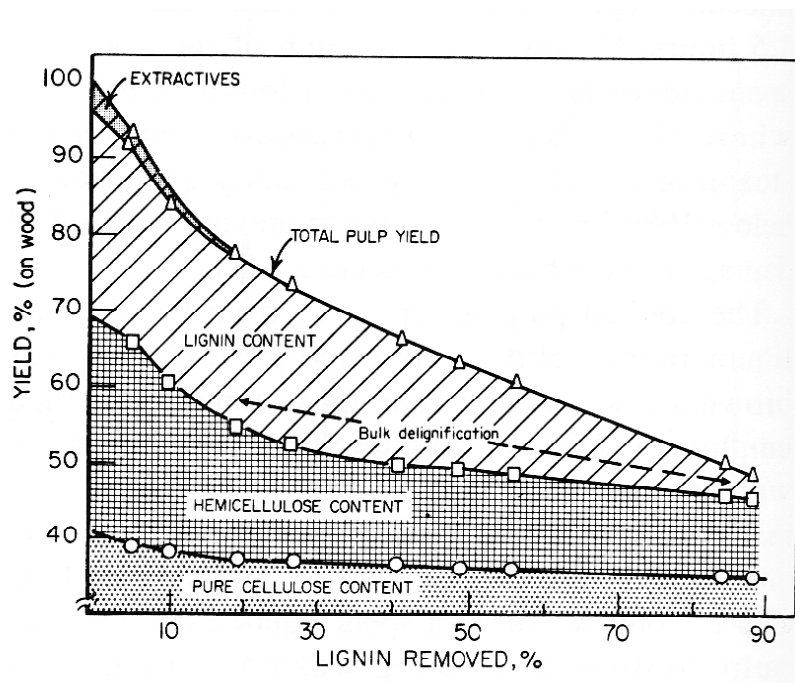


Figure 1.8. Yield of major wood components during Kraft pulping of pine at different stages of delignification⁵.

There are various methods of chemical pulping, but the most common is the Kraft process. Here the wood is cooked in a solution of sodium hydroxide (NaOH) and sodium sulfide (Na₂S). The alkaline NaOH causes the lignin to break down into smaller molecules whose sodium salts are soluble in the solution. Kraft pulp tends to yield very strong papers with a characteristic brown colour, as used in cardboard boxes and packaging materials⁶.

1.2.7. Bleaching

Since a large proportion of paper is produced for printing or writing on, it must have a certain level of whiteness. Pulp from both mechanical and chemical processes has a brown colour largely due to the chromophores associated with the residual lignin, and must be bleached⁷. It is thought that oxidative mechanisms convert part of the lignin's phenolic groups to quinone-like substances that can absorb light. Heavy metal ions can also form coloured complexes with the phenolic groups, contributing to the discolouring of the pulp⁶.

Chemical pulps are generally bleached by the removal of any residual lignin, while mechanical pulps are bleached by the chemically altering the chromophores associated with the lignin – little of which is removed during the mechanical pulping process.

1.2.8. Use of Cellulose as a Substrate

A number of properties, summarised in Table 1.2, make cellulose an excellent choice as a substrate material. In particular the presence of surface hydroxyl groups which allow the binding of various materials (in the case of this study, magnetic nanoparticles, the conducting polymers, and doped ZnS quantum dots) through hydrogen bonding.

The combination of cellulose fibres and nanoparticles, conducting polymers and quantum dots, allows for the development of a number of materials with not only the inherent properties of the fibre, but also a range of interesting new properties. Examples are magnetic, photoluminescent and electrically conductive properties, which will be discussed below.

Properties of Cellulose Fibres
• High tensile strength
• Suppleness (flexibility, conformability)
• Resistance to plastic deformation
• Water dispersible
• Hydrophilic
• Wide range of dimensions
• Inherent bonding ability (H-bonding)
• Ability to absorb modifying additives
• Chemically stable
• Relatively colourless

Table 1.2. Properties of Cellulose Fibres.

1.3. Magnetic Nanoparticles

In order to accommodate magnetic centres into or on a cellulose fibre without compromising its morphology, the particles must be considerably smaller than the fibre itself. This necessitates the use of nanoparticles, which by definition have at least one dimension less than 100 nm. As shown in Table 1.1, softwood fibres have a diameter of approximately 40 μm . Therefore, a nanoparticle of diameter 100 nm, is 400 times smaller than the width of the fibre.

1.3.1. Magnetism

Consider a loop of radius r with a current (i) flowing through it. A magnetic field (H) will be generated at its centre. Associated with this magnetic field are a magnetic moment (μ), magnetisation (M), magnetic susceptibility (χ), magnetic moment per unit mass (σ), and magnetic flux density (B). These terms and their dimensions are summarised in Table 1.3 below.

Magnetic Term	Symbol	SI Unit	CGS* Unit	Conversion Factor
Magnetic flux density	B	Tesla (T)	Gauss (G)	$1 \text{ T} = 10^4 \text{ G}$
Magnetic field	H	A m^{-1}	Oersted (Oe)	$1 \text{ A m}^{-1} = 4\pi \times 10^{-3} \text{ Oe}$
Magnetisation	M	A m^{-1}	emu cm^{-3}	$1 \text{ A m}^{-1} = 10^{-3} \text{ emu cm}^{-3}$
Mass magnetisation	σ	$\text{A m}^2 \text{ kg}^{-1}$	emu g^{-1}	$1 \text{ A m}^2 \text{ kg}^{-1} = 1 \text{ emu g}^{-1}$
Magnetic moment	μ	A m^2	emu	$1 \text{ A m}^2 = 10^3 \text{ emu}$
Magnetic Susceptibility	χ	Dimensionless	Dimensionless	$\chi_{\text{SI}} \equiv 4\pi\chi_{\text{CGS}}$

Table 1.3. Definition of some magnetic terms⁸.

The spin of an electron combined with its orbital angular momentum, results in a magnetic dipole moment that is proportional to its spin angular momentum and creates a magnetic field. The origin of magnetism lies in how these dipole moments interact with each other. The main distinction is that in some materials there is no collective interaction between the moments, while in others there are very strong interactions.

The magnetisation (M) of a material is the average molecular magnetic dipole moment multiplied by the number density of molecules in the material. The magnetisation induced by a magnetic field (H) is proportional to H , where χ is the dimensionless volume magnetic susceptibility:

$$M = \chi H \quad (1.1)$$

The magnetic flux density (B) is related to the applied field by the equation:

$$B = \mu_0(H + M) = \mu_0(1 + \chi)H \quad (1.2)$$

where μ_0 is the vacuum permeability, $\mu_0 = 4\pi \times 10^{-7} \text{ J C}^{-2} \text{ m}^{-1} \text{ s}^2$. The magnetic flux density can be thought of as the density of magnetic lines of force permeating the medium.

* centimetre, gram, second system of units.

Magnetic behaviour can be classified into the following five groups; diamagnetism, paramagnetism, ferromagnetism, ferrimagnetism, and superparamagnetism⁹.

1.3.2. Diamagnetism

Diamagnetism is a fundamental property of all materials, although it is usually very weak. Diamagnetic substances are composed of atoms that have no net magnetic moments because all their orbital shells are full and contain no unpaired electrons. When exposed to a magnetic field, a negative magnetisation results and thus the susceptibility is less than zero⁹ (Figure 1.9).

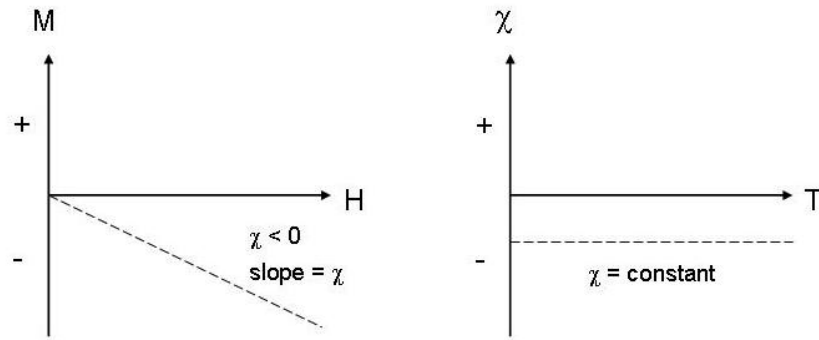


Figure 1.9. Plot of M vs. H and χ vs. T for a diamagnetic material.

1.3.3. Paramagnetism

In this class of magnetic material some of the atoms have unpaired electrons in partially filled orbitals and as a result have magnetic moments. In the presence of a magnetic field there is a partial alignment of these moments in the direction of the field resulting in a net positive magnetisation and susceptibility (Figure 10).

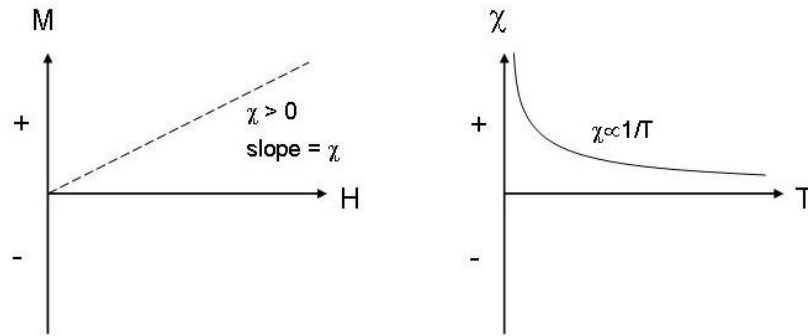


Figure 1.10. Plot of M vs. H and χ vs. T for a paramagnetic material.

However, the individual magnetic moments do not interact with each other, and like diamagnetism, there is no net magnetisation when the field is removed⁹.

1.3.4. Ferromagnetism and Antiferromagnetism

Unlike paramagnetic materials, the individual magnetic moments in ferromagnetic materials exhibit very strong interactions. In ferromagnetic materials magnetic moments of neighbouring atoms tend to align parallel to each other (Figure 1.11), because of the Pauli Exclusion Principle: two electrons with the same spin state cannot lie at the same position, and thus feel an effective additional repulsion that lowers their electrostatic energy. This difference in energy is called the exchange energy and induces nearby electrons to align, resulting in very large internal magnetic fields⁹.

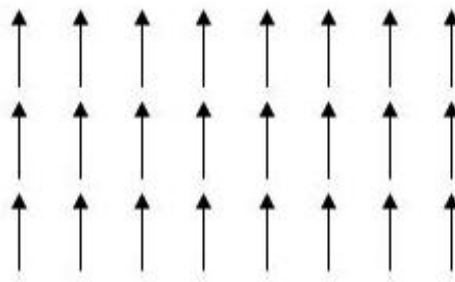


Figure 1.11. Simple schematic diagram showing ferromagnetic ordering.

However, over long range the exchange energy is overtaken by the classical tendency of the individual magnetic moments to anti-align. Rather, they organise into magnetic domains (or *Weiss domains*) that are aligned (magnetised) at short range, but at long range adjacent domains are anti-aligned⁹.

Thus, an ordinary piece of iron generally has little or no net magnetic moment. However, if it is placed in a strong enough external magnetic field, the domains will re-orient in parallel with the applied field, and will remain re-oriented when the field is turned off, creating a "permanent" magnet. This magnetisation as a function of the external field is described by a hysteresis curve, which along with domains, are discussed in section 1.3.7.

Even though the individual magnetic moments interact strongly with each other in a ferromagnet, thermal energy eventually overcomes these interactions and causes a randomizing effect. This occurs at a particular temperature for the material known as its Curie temperature (T_c) (Figure 1.12). Below the Curie temperature, the ferromagnet is ordered, and above it, disordered. At the Curie temperature, the saturation of the material will go to zero⁹.

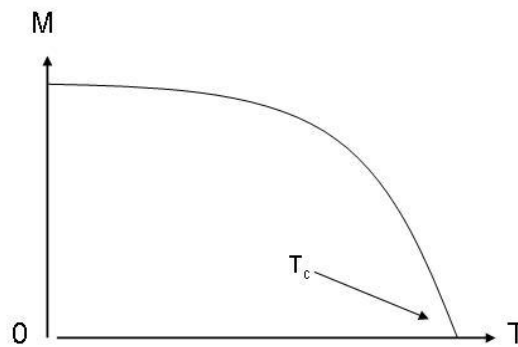


Figure 1.12. Plot of M vs. T for a ferromagnetic material.

Antiferromagnetism occurs when all spins are aligned antiparallel (Figure 1.13).

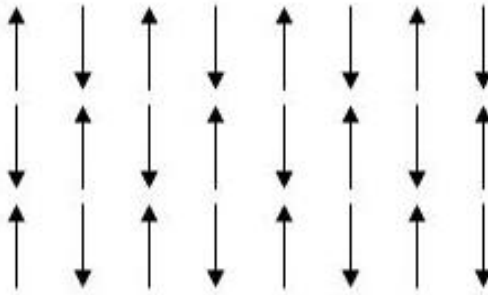


Figure 1.13. Simple schematic diagram showing antiferromagnetic ordering.

1.3.5. Ferrimagnetism and Antiferrimagnetism

In ionic compounds, such as oxides, a more complex form of magnetic ordering can occur due to the crystal structure of the material. One type of magnetic ordering is called ferrimagnetism, first postulated by Neel in 1948^{10, 11}. In a ferrimagnetic crystal, two sub-lattices exist. The magnetic moments of each paramagnetic entity are aligned within the sub-lattice, but their net moments are aligned anti-parallel. If the magnetic moments of each lattice are of unequal magnitude the crystal has a net magnetic moment, and is therefore ferrimagnetic in character⁹.

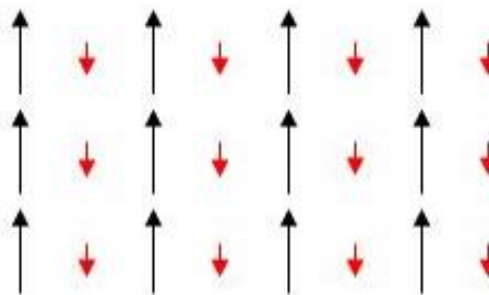


Figure 1.14. Simple schematic diagram showing ferromagnetic ordering.

Magnetite (Fe_3O_4) and maghemite ($\gamma\text{-Fe}_2\text{O}_3$) are examples of ferrimagnetic materials⁹. Magnetite crystallizes in the inverse spinel structure¹² and has the formula $[\text{Fe}^{\text{III}}]_{\text{A}}[\text{Fe}^{\text{II}}\text{Fe}^{\text{III}}]_{\text{B}}\text{O}_4$, where A represents tetrahedral sites within the cubic lattice and B represents octahedral sites. This is shown in Figure 1.15.

Antiferrimagnetism is a special case of ferrimagnetism where the net magnetic moments of two sub-lattices equal zero. An example of an antiferrimagnetic material is hematite ($\alpha\text{-Fe}_2\text{O}_3$)¹².

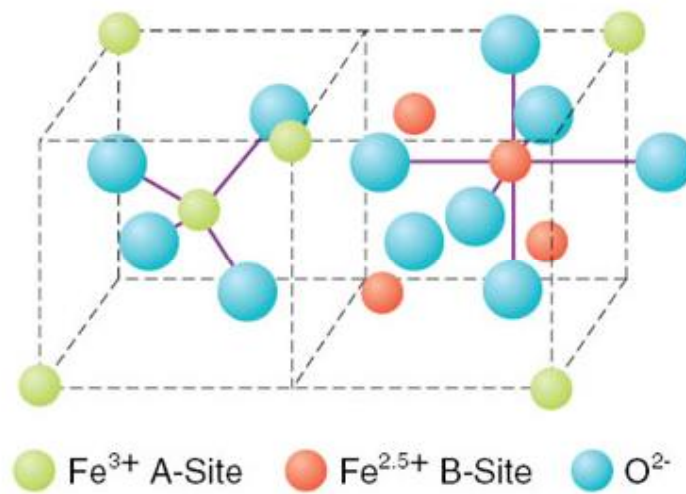


Figure 1.15. Quarter unit cell of inverse spinel structure. A site (tetrahedral position) B site (octahedral position).

1.3.6. Superparamagnetism

Superparamagnetism is a phenomenon whereby magnetic materials may exhibit behaviour similar to paramagnetism at temperatures below the Curie temperature. Superparamagnetism occurs when the material is composed of very small crystallites, 1-20 nm in size. Even though the material is below its Curie temperature and the thermal energy is not sufficient to overcome the coupling forces between neighbouring atoms, the thermal energy is however large enough to cause fluctuations in the direction of magnetisation of the entire crystallite⁹.

These resulting fluctuations cause the magnetic field to average to zero. The material behaves in a manner similar to paramagnetism, the only difference being that instead of each individual atom being independently influenced by an external magnetic field, the magnetic moment of the entire crystallite tends to align with the magnetic field⁹.

The energy required to change the direction of magnetisation of a crystallite is called the crystalline anisotropy energy and depends on both the material's properties and the crystallite size. As the crystallite size decreases, so does the crystalline anisotropy energy, resulting in a decrease in the temperature at which the material becomes superparamagnetic.

For magnetite, superparamagnetism is usually observed when the particles are less than 30 nm in diameter⁹.

1.3.7. Macroscopic Characteristics

Ferromagnetic and ferrimagnetic materials, unlike paramagnetic ones, exhibit hysteresis when subjected to a cyclic magnetic field. This is due to the presence of domains within the material. Because a large magnetic field is present, charge separation will occur on the surface of the material. The dipole caused by this charge separation can be reduced if the magnetic moment separates in two or more domains. This is shown in Figure 1.16 below.

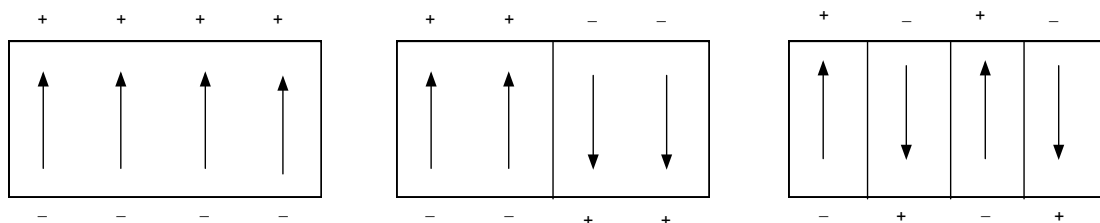


Figure 1.16 Domains are formed in ferromagnetic and ferrimagnetic materials in order to reduce surface charge.

Domains have a finite size, and in the case of magnetite, are usually less than 80 nm in size¹³. The presence of magnetic domains in a sample leads to hysteresis

characteristics shown in Figure 1.17 below. The curve exhibiting hysteresis was measured with a sample of CoFe_2O_4 coated Kraft fibres. Saturation magnetisation (σ_s or M_s), magnetic remanence (σ_r or M_r), and coercivity (H_c) are shown.

Remanence is the magnetic moment or magnetisation present at zero field while coercivity is the reverse field that must be applied to reduce the magnetic moment to zero. Saturation magnetisation is reached when the applied magnetic field is strong enough to align the moments of all the domains present within the sample. Even in the absence of a magnetic field, individual domains have reached their saturation magnetisation, but they are so poorly aligned with each other that the observed moment is heavily reduced.

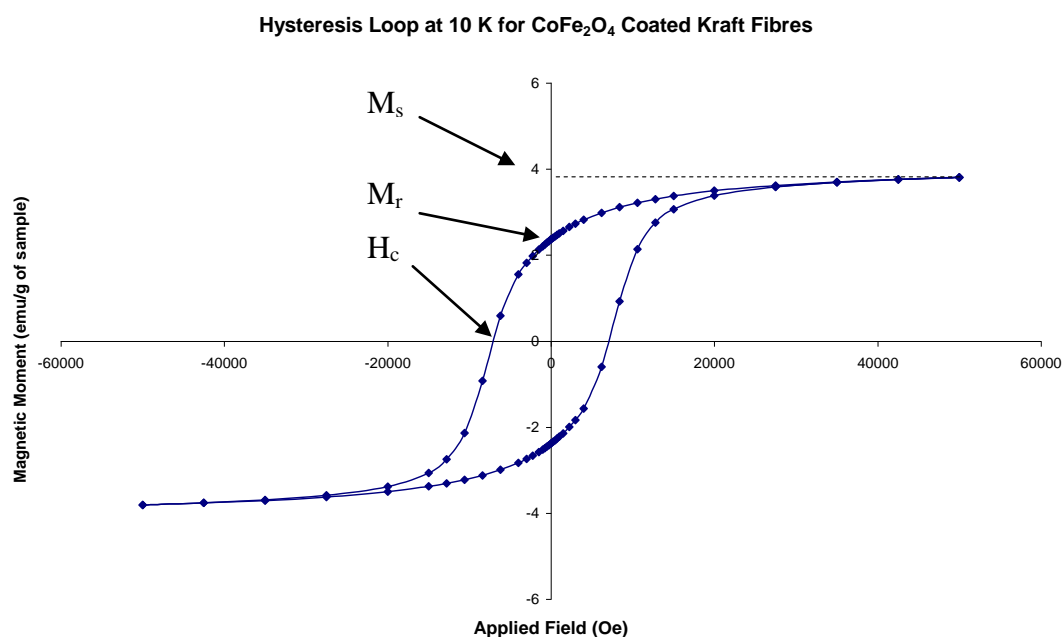


Figure 1.17. Magnetic hysteresis curve for a ferrimagnetic sample of CoFe_2O_4 .

1.3.8. Synthesis of Magnetic Nanoparticles

As shown in Table 1.4 below, iron exhibits a high room temperature saturation magnetisation. Iron nanoparticles, however, have a high specific surface area and are more readily oxidized. Consequently, their applications are limited to

non-oxidising and non-aqueous environments. As a result, the oxides of iron, magnetite (Fe_3O_4), maghemite ($\gamma\text{-Fe}_2\text{O}_3$) and analogues of magnetite, (*e.g.* CoFe_2O_4 , MnFe_2O_4 etc.) are more commonly used as magnetic centres in oxidising and aqueous environments¹⁴.

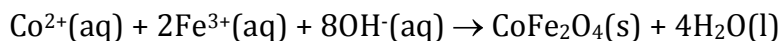
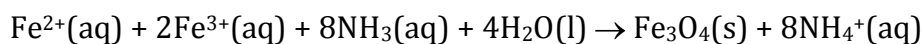
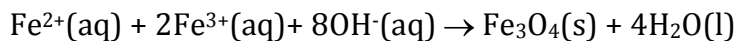
Compound	Composition	Magnetic Order	T _c (°C)	σ_s (A m ² kg ⁻¹)
Iron	Fe	Ferromagnetic	1316	218
Cobalt	Co	Ferromagnetic	1660	161
Nickel	Ni	Ferromagnetic	900	54
Magnetite	Fe_3O_4	Ferrimagnetic	575	90
Maghemite	$\gamma\text{-Fe}_2\text{O}_3$	Ferrimagnetic	600	80
Jacobsite	MnFe_2O_4	Ferrimagnetic	300	77

Table 1.4. Magnetic properties of some common magnetic materials⁹.

There are a number of ways to prepare such nanoparticles. The most basic is the grinding of naturally occurring magnetite. This method was employed by Papell¹⁵ to create a stable colloidal suspension of magnetite nanoparticles called a ferrofluid. In this method, ionic surfactants such as tetraethylammonium hydroxide are used to stabilize the suspensions in polar solutions such as water^{16, 17}. In non-polar solutions, oleic acid is used as the surfactant¹⁸.

There are several disadvantages of this method however, namely the lack of morphological control, and the substantial energy costs involved in grinding. Consequently, chemical methods of preparation are used when control of both stoichiometry and particle size are required.

A simpler and less energy intensive route to the formation of iron oxides is the co-precipitation method. Here, a room temperature synthesis for magnetite was developed by Massart¹⁹ in which ammonia is added to a solution of iron (II) and iron (III) chlorides. The method does not require an inert atmosphere and has been adapted for the synthesis of maghemite via the oxidation of magnetite particles by iron (III) nitrate^{17, 20, 21}.



Although the saturation magnetisation of maghemite is lower than magnetite, maghemite particles are more chemically inert. The method has also been adapted for the synthesis of magnetite analogues, $\text{M}^{\text{II}}\text{Fe}^{\text{III}}_2\text{O}_4$, whereby M^{II} is substituted for Co^{2+} , Mn^{2+} , or Ni^{2+} in the co-precipitation reaction²². In another co-precipitation method used by Welo and Baudisch²³, magnetite was prepared by precipitation of iron (II) and iron (III) sulfates with boiling sodium hydroxide.

A number of other synthetic routes also exist. David and Welch²⁴ synthesised magnetite via the formation of iron (II) hydroxide gel and its subsequent oxidation to magnetite by potassium nitrate.

Other methods include hydrothermal²⁵ and mechanochemical²⁶ syntheses, the reduction of iron (III) salts²¹, and the decomposition of iron alkoxides²⁷ and organo-iron species²⁸. Water-in-oil micro-emulsion techniques have also been used^{29, 30}. Many of these methods have been used to prepare Co and Mn magnetic compounds as well^{14, 31-44}.

Magnetic particles such as magnetite and CoFe_2O_4 have successfully been incorporated into paper fibres. The two methods used are the 'in situ' approach⁴⁵⁻⁴⁷ and the 'lumen loading' method⁴⁶⁻⁴⁸. The former is an adaptation of the co-precipitation method where the paper fibres are present in the solution of iron (II) and iron (III) chlorides, for example.

In the lumen loading method, the magnetic particles (as a filler) are synthesised separately and then added to the paper fibres. The particles are taken up into the inner cavity (or lumen) of the fibre through 'pit-holes' in the fibre surface.

Lumen loading was first applied as a means of incorporating inorganic fillers into softwood fibres while leaving the external surface free of filler. The filler is protected by the cell wall and hence the particles do not interfere with inter-fibre bonding, and dusting problems in paper usage are greatly reduced. Due to the type of fibres used and the pulping process used to obtain them, the magnetic particles do not adhere to the outer surface of the fibre and excess particles are washed away in the filtering step.

1.4. Photoluminescent Nanoparticles

Molecules that emit light from excited electronic states created by either a physical (absorption of light, heat), mechanical (friction), or chemical mechanism are termed luminescent. Generation of luminescence through excitation of a molecule by ultraviolet or visible light is a phenomenon known as photoluminescence. This category is formally divided into two sub-categories, fluorescence and phosphorescence. A related type of luminescence is called electroluminescence, an electrical and optical phenomenon whereby a material emits light in response to an electric current being passed through it⁴⁹.

1.4.1. Fluorescence

A singlet excited state (S_1) results when an electron is promoted from its ground state (S_0), while conserving its spin (an "allowed" transition). Relaxation back to the ground state is very fast because the multiplicity doesn't change⁵⁰ (Figure 1.18).

The phenomenon of fluorescence occurs when a molecule (or quantum dot) relaxes from its excited state to its ground state after absorbing visible or ultraviolet light. Upon this relaxation, a photon is released that has a wavelength longer than that of the light used to excite it⁵⁰ (Figure 1.18).

$$\text{Excitation: } S_0 + h\nu \rightarrow S_1 \quad (1.3)$$

$$\text{Fluorescence (Emission): } S_1 \rightarrow S_0 + h\nu \quad (1.4)$$

The fluorescence process is governed by three important events, all of which occur on timescales that differ by several orders of magnitude (see Figure 1.18). Excitation of a susceptible molecule by an incoming photon occurs in femtoseconds (10^{-15} s), while vibrational relaxation of excited state electrons to the lowest energy level is slower and happens in picoseconds (10^{-12} s). The final process, emission of a longer wavelength photon and return of the molecule to the ground state, occurs over a relatively longer time-period of nanoseconds (10^{-9} s)⁵⁰.

A molecule in its excited state can return to its ground state by a number of competing pathways. A 'non-radiative relaxation' can take place, in which the excitation energy is dissipated as molecular vibrations (heat). Excited molecules can also relax via conversion to a triplet state that may subsequently relax via phosphorescence or by a secondary non-radiative relaxation step⁵⁰.

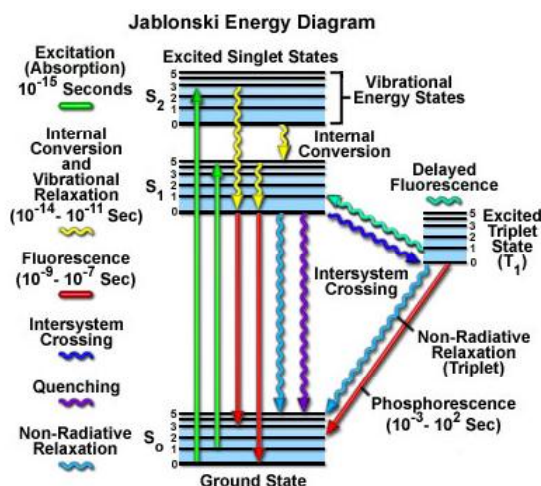


Figure 1.18. Jablonski Diagram showing the various pathways of excitation, relaxation, and emission in a photoluminescent material⁵¹.

Relaxation of a molecule in its excited state can also occur through interaction with a second molecule. This is termed 'fluorescence quenching'. Due to its triplet ground state, molecular oxygen (O_2) is an extremely efficient quencher of fluorescence. Excited molecules can also transfer energy to a second 'sensitiser'

molecule by a process called ‘intersystem crossing.’ The sensitiser molecule is then converted to its excited state and can subsequently fluoresce⁵⁰. This process is used in light sticks. These transitions are summarised in Figure 1.18.

The efficiency of the fluorescence process is given by the fluorescence quantum yield, ϕ . This is defined as the ratio of the number of photons emitted to the number absorbed. The maximum fluorescence quantum yield is 1.0, occurring when every photon absorbed results in a photon emitted. However, materials with fluorescence quantum yields of 0.1 are still considered rather fluorescent⁵⁰.

$$\phi = \frac{\text{number of photons emitted}}{\text{number of photons absorbed}} \quad (1.5)$$

Another way to define fluorescence quantum yield, is by the rates of excited state decay:

$$\frac{k_f}{\sum_i k_i} \quad (1.6)$$

where k_f is the rate of spontaneous photon emission and $\sum_i k_i$ is the sum of all rates of excited state decay. Other states of excited decay are caused by the mechanisms shown in Figure 1.18 above, for example, non-radiative relaxation, quenching, and intersystem crossing⁵⁰. Fluorescence quantum yields are measured in comparison to a known standard. Quinine sulfate in sulfuric acid is a common fluorescent standard⁵².

The fluorescence lifetime of a material refers to the time it stays in its excited state before emitting a photon. Fluorescence typically follows first order kinetics:

$$[S_1] = [S_1]_0 e^{\frac{-t}{\tau}} \quad (1.7)$$

$[S_1]$ is the remaining concentration of excited state molecules at time = t , $[S_1]_0$ is the initial concentration of excited state molecules after excitation. The lifetime is related to the rates of excited state decay by the equation:

$$\tau = \frac{1}{\sum_i k_i} \quad (1.8)$$

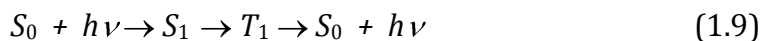
Thus, fluorescence is similar to a first-order chemical reaction in that the first order rate constant is the sum of all the rates. Therefore, the fluorescent lifetime is related to the relaxation pathway (the reaction pathway in a chemical reaction). If the rate of spontaneous emission, or any of the other rates are fast, the fluorescent lifetime is short⁵⁰.

The fluorescent lifetimes of commonly used fluorescent compounds that emit photons with energies ranging from the ultraviolet to the near infrared are within the range 0.5 to 20 nanoseconds⁵⁰.

1.4.2. Phosphorescence

The second type of photoluminescence is phosphorescence. It is similar to fluorescence, but is distinguished from it by much slower time scales for transitions between excited and ground states.

The first steps in the sequence of events leading to phosphorescence are the same as in fluorescence. However, the presence of a triplet state (T_1) plays an important role. The molecule may undergo ‘intersystem crossing’⁵³ (a non-radiative transition) and become a triplet state. Transition to the triplet state involves a ‘forbidden’ spin flip (electrons cannot exist in between the two states in a molecule). This process is kinetically slow, but thermodynamically favourable because the triplet is lower in energy⁵⁰ (Figure 1.18).



If an excited molecule converts to a triplet state, it will dissipate energy into its surroundings. As this is taking place, it is moving down the triplet's vibrational energy ladder and becomes trapped (because the triplet state is lower in energy than the singlet state it crossed from). To return to the singlet state only 'forbidden' transitions are available. These transitions, although 'forbidden', will still occur but are kinetically unfavoured and progress over significantly slower time-periods. It is the slow release of energy from this reverse transition that gives rise to phosphorescence⁵⁰.

In some cases this energy is dissipated by the emission of a photon corresponding to the energy difference between the triplet state and ground state, but often it is dissipated vibrationally. The ratio between these two phenomena for a single molecule is known as the phosphorescence quantum yield. If the phosphorescence quantum yield is high, these substances will release significant amounts of light over long time scales, up to several hours⁵⁰.

Most phosphorescent compounds are still relatively fast emitters, with triplet lifetimes of the order of milliseconds. Some materials however, have triplet lifetimes of minutes or even hours, creating the so-called "glow in the dark" materials such as copper doped zinc sulfide, strontium aluminate and bismuth doped calcium and strontium sulfide (Figure 1.19).

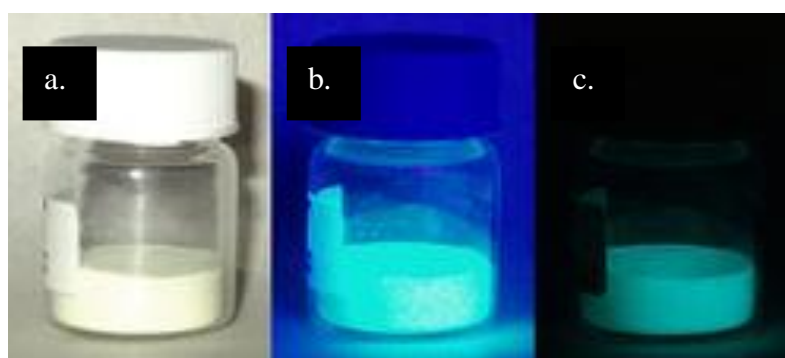


Figure 1.19. A copper-doped ZnS phosphorescent powder under visible light (a), ultraviolet light (b), and total darkness (c).

There are other types of emission from triplet-excited states. For example, a process known as delayed fluorescence (Figure 1.18) occurs when two triplets

encounter each other by delocalisation in the solid state or in solution or the gas phase and additively annihilate to produce one singlet-excited state of higher energy. If this state then emits light it will be of the shorter wavelength associated with fluorescence emission, but on a similar time scale to phosphorescence⁵⁰.

1.4.3. Synthesis of Photoluminescent Nanoparticles

Recently, semiconductor and metal nanoparticles have been extensively studied by the scientific community. Many new optical and electronic properties such as quantum confinement and finite size effects have been discovered and prospective applications have been developed⁵⁴.

In a semiconductor, electrons can jump from the valence band to the conduction band of the material. In doing so, they create two quasi particles, a hole h^+ with a mass m_h^* and an electron e^- with a mass m_e^* . This jump is known as the band gap (E_g) and its physical distance is measured by the Exciton Bohr Radius, a_B :

$$a_B = \frac{4\pi\epsilon_0\hbar^2}{m_e e^2} \quad (1.10)$$

where \hbar is the reduced Planck constant, e is the charge on an electron, and ϵ_0 is the dielectric constant. The size of this radius controls how large a crystal must be before its energy bands can be treated as continuous⁵⁵. Therefore, the Exciton Bohr Radius can rightly be said to define whether a crystal can be called a semiconductor quantum dot, or simply a bulk semiconductor⁵⁰.

A quantum dot is a crystal of a semiconductor compound with a diameter of the order of the compound's Exciton Bohr Radius. Quantum dots are usually between 2 and 10 nanometers wide (10 and 50 atoms)⁵⁰, and for ZnS, the Bohr radius is 2.5 nm⁵⁶.

In a regular semiconductor crystal, the bandgap (E_g) is fixed owing to continuous energy states. With quantum dots, the size of the bandgap is controlled simply by adjusting the size of the dot. Because the emission frequency of a quantum dot is dependent on the bandgap:

$$h\nu = E_g - Ry^*, \text{ where } Ry^* = \frac{e^2}{2\epsilon a_B} \quad (1.11)$$

with ν the frequency and Ry^* the Rydberg energy, it is therefore possible to control the output wavelength of a dot with extreme precision⁵⁵. In effect, it is possible to tune the bandgap of a dot, and therefore specify its 'colour output'.

One such material is cadmium sulfide, CdS. This material, with its band gap of $E_g \sim 2.4$ eV, is easily synthesised. By tuning the particle size of CdS quantum dots, a number of different colours are obtainable (Figure 1.20).



Figure 1.20. Different sized quantum dots of CdS give rise to a number of possible colours.

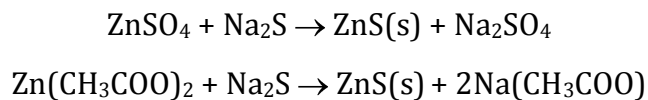
However, CdS is extremely toxic to both the liver and the kidneys and for this reason, its application in many commercially available products is severely restricted⁵⁷⁻⁵⁹.

A much more environmentally acceptable material is zinc sulfide (ZnS), which has received much attention due to its excellent properties such as its large

band gap energy ($E_g \sim 3.6$ eV), direct recombination, and its resistance to high electric field. Doped ZnS is also a well-known phosphor with photoluminescent and electroluminescent properties and thus has been used in both laser and display technologies⁶⁰.

Pure zinc oxide (ZnO) is a high temperature oxidation product of ZnS, and another potential material for low voltage luminescence and optoelectronic devices such as light emitting diodes. It is a piezoelectric and can be used as a pressure sensor, for example, in surface acoustic wave devices. Recently, Wang and Gao have synthesised ZnO nanowires with diameters of 50-80 nm and lengths of up to 6 μm ⁶¹. Nanowires of ZnO could see a number of exciting applications in nanoscale electronics and photonics.

A simple and common method of preparing ZnS nanoparticles is by precipitation in aqueous solutions⁶².



ZnS and ZnO powders have been synthesised by a number of other methods including sol-gel methods^{63, 64}, solid-state methods^{65, 66}, gas-phase condensation⁶⁷, and ion complex transformation methods⁶⁸.

The sol-gel method used by Toyoda *et al.*⁶⁴ uses the decomposition of the metal alkoxide $\text{Zn}(\text{NO}_3)(\text{OCH}_2\text{CH}_2\text{OCH}_3)$ at temperatures between 250-500 °C to form ZnO nanoparticles.

Bhattacharjee *et al.*⁶³ use the hydrolysis of tetraethylorthosilicate (TEOS) and subsequent heating to decompose thiourea (sulfide source) and form SiO_2 coated ZnS from zinc salts.

Solid state syntheses^{65, 66} of ZnS and ZnO involve heating the precursor zinc salts and dopants to high temperatures (800-1200 °C) in N₂ or oxidizing atmospheres.

The gas-phase condensation method⁶⁷ uses a commercial ZnS sample heated to 1373 K in a vacuum (5 x 10⁻⁷ Torr). The nanosized ZnS was collected on a cold Cu plate.

The ion complex transformation method used by Sang *et al.*⁶⁸ uses polyvinyl alcohol to complex Zn²⁺ and dopant ions which are then spin coated to various substrates and subsequently exposed to Na₂S or H₂S to form ZnS.

Because ZnS emits in the ultraviolet region, a considerable amount of work has been focused on doping ZnS nanoparticles in order to shift the emission back into the visible region. The dopants act as recombination centres for the excited electron-hole pairs, resulting in strong and characteristic luminescence.

Hence, the photoluminescence emission of doped ZnS quantum dots is not associated with the bandgap of the material, as is the case with CdS. The source of the emission instead arises from the inclusion of dopants in the host lattice, hence changing the particle size, and consequently the Bohr radius of the material, has no effect on the photoluminescence emission of doped ZnS.

The size of the quantum dots does have an affect on the fluorescence quantum yield of the quantum dots, and was described by Bhargava, *et al.*⁶⁹ as:

$$\phi = \frac{1}{1 + \beta D^2} \quad (1.12)$$

where D is the diameter, and β is the ratio of the non-radiative and radiative decay lifetimes. From the equation it can be seen that the smaller the particle size, the larger the fluorescence quantum yield.

Bhargava, *et al.* cite the reason for this as being that with decreasing particle size a strong hybridisation of the s-p states of the ZnS host and the d states of the Mn^{2+} dopant could occur. This hybridisation results in a faster energy transfer between the host and dopant, and gives rise to an increase in fluorescence quantum yield.

Since Bhargava *et al.*⁶⁹ reported the novel properties of ZnS doped with Mn^{2+} ions, many studies have been conducted on Mn, Ni, Cu and rare-earth activated nanometer scale semiconductor materials^{60, 63, 70, 71}. Doping with such ions gives rise to red-orange (Mn^{2+}), and green (Cu^{2+} , Ni^{2+}) emissions.

More recently attention has turned to co-doped ZnS nanocrystals such as Cu^{+} - Cu^{2+} , Co^{2+} - Cu^{2+} , Cu^{2+} - Al^{3+} , and Cu^{2+} -RE (where RE = Ce^{3+} , Er^{3+} , Tb^{3+} , Nd^{3+} , Y^{3+}) in order to give a combination of different emissions⁷²⁻⁷⁵.

Other fluorescent compounds exist, namely the Rhodamine group of dye molecules. Examples of these are Rhodamine 6G and Rhodamine B, shown below in Figure 1.21. Rhodamine dyes fluoresce, and can thus be measured easily and inexpensively.

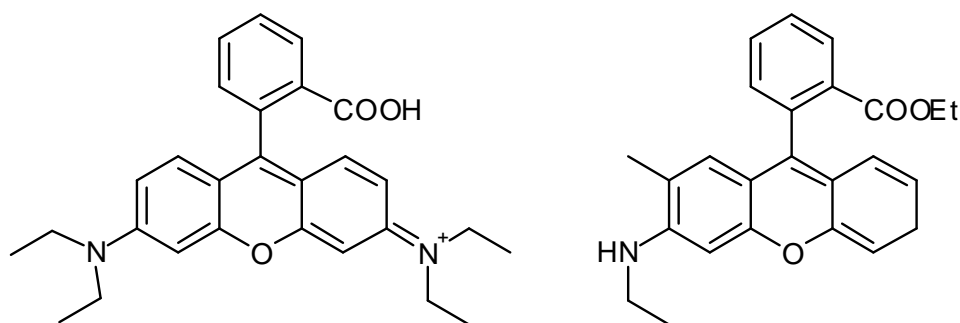


Figure 1.21. Two dyes from the Rhodamine family, Rhodamine B (left), and Rhodamine 6G (right).

Rhodamine B, $\text{C}_{29}\text{H}_{31}\text{N}_2\text{O}_3\text{Cl}$, is used in biology as a staining fluorescent dye. It is also often used as a tracer within water to determine the rate and direction of flow and transport⁵².

Rhodamine 6G, $C_{28}H_{31}N_2O_3Cl$, is often used as a laser dye because of its remarkably high photo-stability, high fluorescence quantum yield, low cost, and close proximity to the absorption maximum (approximately 530 nm).

Gavilan and co-workers⁷⁶ have synthesised fluorescent mesoporous aluminosilicate nanoparticles in a one-pot procedure from precursors aluminium isopropoxide, tetraethyl orthosilicate and tetraethyl ammonium hydroxide in the presence of Rhodamine B. They report interesting mesoporous properties with narrow pore size distribution as well as excellent chemical and thermal stability.

Sahoo *et al.*⁷⁷ have synthesised magnetite nanoparticles functionalized by Rhodamine 110. Biocompatible ferrofluids with fluorescent properties enable optical tracking of basic biological processes at the cellular level along with magnetic manipulation. Such particles can be taken up by cells in vitro and optically tracked using confocal fluorescence microscopy. Their magnetic properties allow them to be controlled more easily by the use of magnetic fields.

Nanorods of ZnO have been grown on cotton fabrics (cellulose, the same substrate used in this work) at 200 °C by Wang *et al.*⁷⁸ They have achieved nanorod arrays on the fibre substrate where typical nanorods are 10-50 nm in diameter and 300-500 nm in length. A material of this type has potential in acoustic wave sensing applications due to its high surface area and piezoelectric character, and also in photocatalysis.

1.5. Stabilisation of Nanoparticles and Quantum Dots

Nanoparticles and quantum dots, due to their small size, and consequently large surface area, have a propensity to aggregate. This can be avoided by the use of surfactants or stabilising the particles electrostatically. To understand the

rationale behind this, it is worthwhile to consider the forces acting on such particles.

1.5.1. Forces between atoms and molecules

Since the work of van der Waals in 1873, it is known that attractive forces exist between non polar molecules. London showed in 1934 that these attractive forces are a result of fluctuating dipoles arising from the movement of electrons with the electron clouds of atoms. These interactions are commonly called dispersion interactions or London interactions. The overall calculation of these forces is complicated, however, a good approximation for the interaction is given by the London formula:

$$V_A = -\frac{C}{r^6}, \text{ where } C = \frac{3}{2} \alpha_1' \alpha_2' \frac{I_1 I_2}{I_1 + I_2} \quad (1.13)$$

Where r is the distance between molecules, α_1' and α_2' are the polarisability volumes of molecule 1 and 2, and I_1 and I_2 are their ionisation energies⁴⁹.

1.5.2. Forces between particles

In 1937, Hamaker extended London's work on the dispersion forces between atoms and molecules, to calculate those acting on colloidal particles. The result for the attraction (V_A) between two spheres, each of radius a , is calculated by:

$$V_A = -\frac{A_H}{6} G \quad (1.14)$$

Where the geometrical term $G = 2/(s^2-4) + (2/s^2) + \ln([s^2-4]/s^2)$, and A_H is the Hamaker constant. The parameter $s = (H_0 + 2a)/a$, where H_0 = the minimum distance separating the spheres. If H_0 is small compared to the particle radius, then the first term in the expression for G is dominant and the equation reduces to:

$$V_A \sim -\frac{A_H a}{12H_0} \quad (a \gg H_0) \quad (1.15)$$

It can be seen that as the size of the particle increases, the attractive forces decrease considerably slower than for molecules or atoms. This has a significant effect on the stability of colloidal dispersions⁷⁹.

1.5.3. Electrostatic stabilisation

Particles in an aqueous dispersion normally show a surface charge due to either ionisation, adsorption of charged species, or simply the presence of ions. From Coulomb's law, every charge creates an electric potential that will be compensated for by opposite charges in its proximity. Every positive ion, for example, will be surrounded by a layer of negatively charged ions.

This is known as the electric double layer, first introduced by Helmholtz in 1879. It was first imagined that potential decreased linearly, however, Gouy and Chapman postulated in 1913, that thermal motion would cause a distribution of counter ions, forming a diffuse double layer (Figure 1.22).

This type of double layer gives rise to an electric potential that decreases exponentially with interparticle distance (z) in the formula:

$$\psi = \psi_0 e^{-\frac{\kappa z}{z}} \quad (1.16)$$

where ψ_0 is the electric potential at the particle surface, and κ is the Debye parameter.

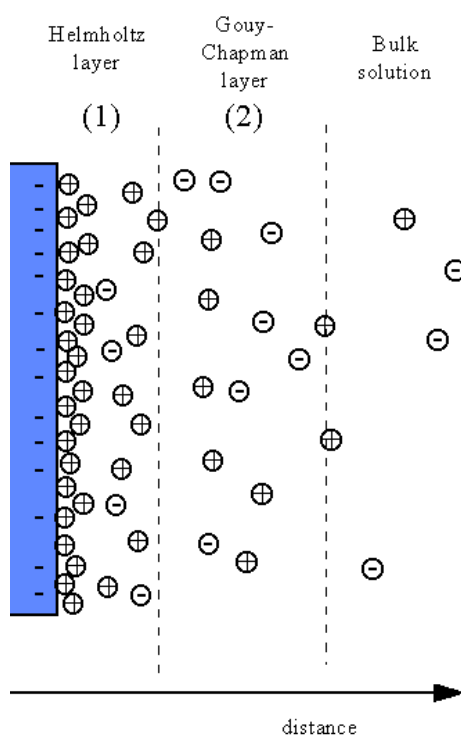


Figure 1.22. Schematic diagram showing the electrical double layer.

The overall result is illustrated in Figure 1.23, where the minimum in potential energy shows a stable arrangement that is easily disrupted by medium effects and thermal motion. Hence if the electrostatic potential of the double layer is sufficiently high, electrostatic repulsion prevents agglomeration.

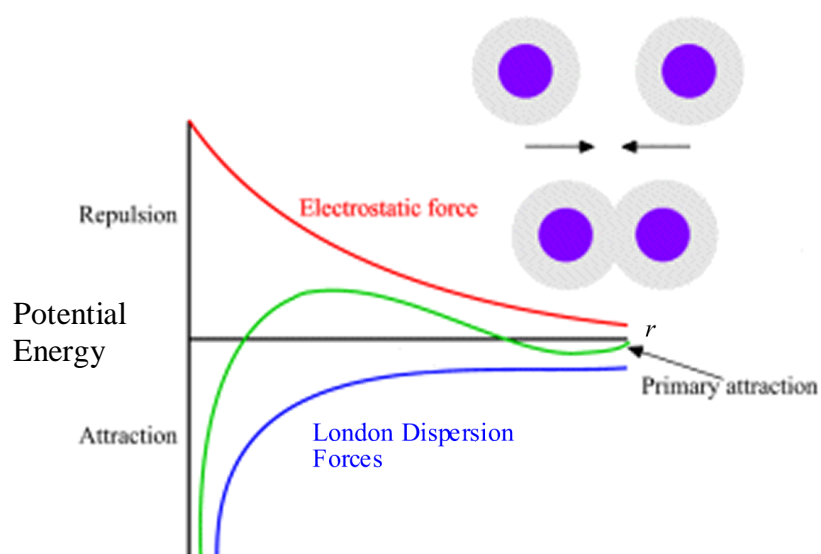


Figure 1.23. Electrostatic stabilisation of colloidal particles.

At long range two particles will not interact. However, at closer distances their double layers will overlap like an electron cloud. If they are charged in the same way, they will repel each other – the basis of DLVO theory. DLVO theory takes two interactions into account: van der Waals attractive forces and the repulsion forces arising from the overlapping of the double layers. The potential energy arising from the repulsion of double layers on particles of radius a is given by:

$$V_{rep} = + \frac{Aa^2\zeta^2}{R} e^{-s/r_D} \quad (1.17)$$

where A is a constant, ζ is the zeta potential, R is the separation of the two centres, s is the separation of the two surfaces of the two particles ($s = R - 2a$ for spherical particles of radius a), and r_D is the thickness of the double layer. The double layer thickness can be estimated from the expression:

$$r_D = \left(\frac{\epsilon RT}{2\rho F^2 I b^\circ} \right) \quad (1.18)$$

where I is the ionic strength, F is the Faraday constant (96484 C mol^{-1}), ρ is the mass density, and $b^\circ = 1 \text{ mol kg}^{-1}$.

Hence, the stabilising effect of surface ions is not only dependant on the concentration of the ions in solution, but on the concentration of any adsorbed ions at the particle surface. If any of the adsorbed ions are displaced, resulting in a reduction in surface charge, the particles can collide and agglomerate under the influence of van der Waals forces⁸⁰.

1.5.4. Steric stabilisation

Colloidal particles can be sterically stabilised by the addition of a surfactant (in most cases a polymer). The surfactant provides a protecting layer around the particle, preventing flocculation. Steric stabilisation, although widely studied in

the literature^{79, 80}, is not as well understood as electrostatic stabilisation. However, it does have some advantages:

1. It is a thermodynamic method, so that the particles are always re-dispersible
2. A very high concentration can be accommodated
3. It is not electrolyte sensitive
4. It is suitable to multiple phase systems.

Compared to electrostatic stabilisation, steric stabilisation offers an additional advantage in the synthesis of nanoparticles, particularly when narrow size distribution is required.

Polymer layers adsorbed on the surface of nanoparticles serve as a diffusion barrier to the growth species, resulting in a diffusion-limited growth in the subsequent growth of nuclei. Diffusion-limited growth reduces the size distribution of the initial nuclei, leading to monosized nanoparticles. The dual functionalities of polymeric layers on the surface of nanoparticles explain the fact that steric stabilisation is widely used in the synthesis of nanoparticles.

Depending on the interaction between the polymer and the solid surface, the polymer can be grouped into three groups⁷⁹:

1. Anchored polymers, which irreversibly bind to the solid surface by one end only
2. Adsorbing polymers, which are weakly adsorbed onto the solid surface at random points along the polymer backbone
3. Non-adsorbing polymers, which do not attach to the solid surface and hence do not contribute to steric stabilisation

1.5.4.1. Anchored polymers

Anchored polymers bind irreversibly to the particle surface, either by chemical bonding or strong specific binding (Figure 1.24).

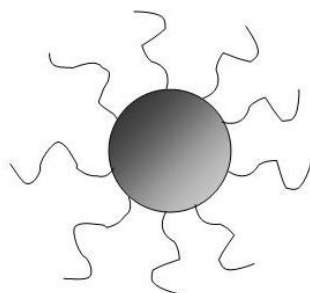


Figure 1.24. Schematic diagram showing polymeric stabilisation using anchored polymers.

The more the polymer resembles the solvent, the more its chains will be directed outward into the solvent. In this case the solvent is termed a ‘good solvent’.

When two particles collide the surfactant or polymer layers will penetrate each other. This has two consequences. Firstly, the local density of the polymer will be increased and the resulting osmotic pressures acting on the surfaces of the particles will cause a diffusion of solvent molecules between the two surfaces to diminish the polymer concentration. This pushes the particles apart.

Secondly, the higher polymer concentration resulting from two polymer layers penetrating each other, leads to an increase in the number of possible arrangements of the chains. Consequently, this decreases the entropy by a value ΔS , and increases the free repulsive energy by $T\Delta S$. This is called entropic repulsion.

The longer the polymer chain length the better the stabilisation, as the repulsion strength depends strongly upon the thickness of the surfactant layer around the molecule.

1.5.4.2. Adsorbing polymers

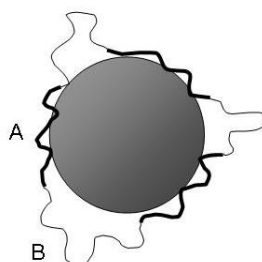


Figure 1.25. Schematic showing polymeric stabilisation by adsorbed polymers, in this case a diblock polymer consisting of an adsorbing block, A, and a non-adsorbing block, B.

The situation regarding adsorbed polymers (Figure 1.25) is somewhat more complicated for two main reasons.

Firstly, if two particles approach each other to a sufficiently close distance, a polymer originally attached to the solid surface of one particle may interact with and adsorb onto another particle surface forming bridges between the two particles as a result (Figure 1.26).

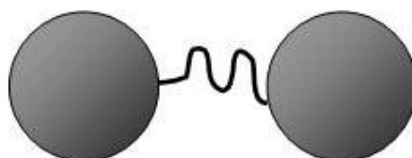


Figure 1.26. Schematic showing 'bridging'.

Secondly, given sufficient time, the attached polymer can desorb from the surface and migrate out of the polymer layer.

When a polymer has a strong adsorption and forms a full coverage, interaction between two polymer layers produces a purely repulsive force. This results in an increased free energy when the distance between two particles reduces below twice the thickness of the polymer layer.

When only a partial coverage is achieved, the nature of the solvent can have a significant influence on the interaction between two particles. In a good solvent, if the polymer layers of two partially covered particles interpenetrate into each other, this results in a reduced occupancy space and a more ordered polymer arrangement. As a result, the entropy reduces and the Gibbs free energy increases.

However, in a poor solvent (one unlike the polymer chains), interpenetration promotes further coiling up of the polymers, leading to an increase in entropy which results in a reduced free energy. The interaction force of adsorbing polymer layers in a poor solvent is similar to that of anchored polymer layers with partial coverage in poor solvent; however, the process involved is somewhat different due to multiple adsorption sites at both surfaces.

It is always the case that a repulsive force develops and repels two particles away from each other, when the distance is less than the thickness of the polymer layer.

1.5.4.3. Non-adsorbing polymers (Depletion stabilisation)

Dissolved non-adsorbing polymers must change their configuration if their centre of mass is to approach a particle surface. This creates a depletion layer around the particle surface (Figure 1.27).

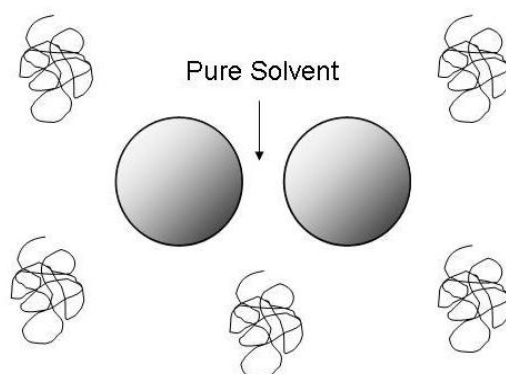


Figure 1.27. Schematic showing ‘depletion stabilisation’.

A particle immersed in a polymeric solution experiences an osmotic pressure at its surface. When the depletion layers of two particles overlap, there forms an area where the polymer is excluded, resulting in an imbalance in pressure. Consequently, the concentration of the polymer is higher in the volume outside the two particles and as a result the polymer will diffuse out into the volume causing the particles to flocculate⁷⁹.

1.6. Conducting Polymers

Since their initial discovery in 1977⁸¹, conducting polymers have generated a large amount of interest within the scientific community. They possess a range of properties that are ideally suited for use in actuator, anti-static, electrochromic, electroluminescent, free radical scavenging, light harvesting, metal recovery, photochromic, sensor and thermochromic applications.

In 1977, Chiang *et al.*⁸² discovered that films of polyacetylene were electrically conductive due to the conjugation of the π -system, allowing electrons to travel along the polymer chain. Other materials such as polypyrrole, polyaniline and polythiophene were later discovered to have similar properties to polyacetylene. These materials are classed as Intrinsically Conducting Polymers (ICP's) in which their conductivity is intrinsic to a 'doped' form of the polymer, however, they are commonly referred to as conducting polymers.

Further investigations resulted in the discovery of several monomers suitable for the formation of ICP's. The addition of alkyl, allyl or other substituents further increases the range of monomers available for polymerisation⁸³ (Figure 1.28).

While conductivity is an important property of ICP's, there are many other properties, which make them commercially important. Polypyrrole films have potential for use as gas sensors⁸⁴ or soft actuators⁸⁵, while polypyrrole woven

into textiles can be used for electromagnetic interference shielding (EMI shielding)⁸⁶, heat generation^{87, 88} and the recovery of gold from solution⁸⁹.

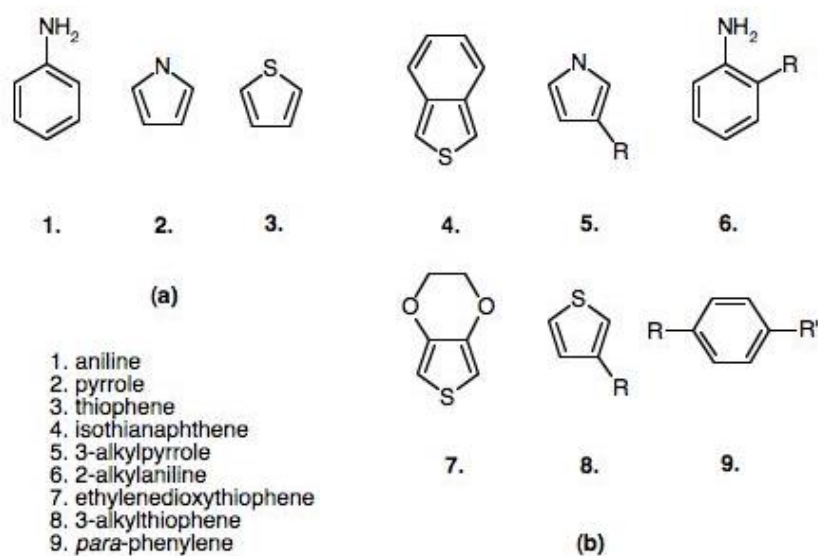


Figure 1.28. (a) Unsubstituted monomers and (b) substituted monomers⁸³.

The addition of functional groups to the polymer chains leads to further uses. For example, functionalised polythiophenes (Table 1.5) can be used in photovoltaic cells^{90, 91}, and ferrocene-functionalised polypyrrole can be using for electrochemical biosensing⁹².

Poly(3-alkylthiophene) (Table 1.5) is an exciting prospect for display technology as it exhibits such properties as thermochromism and electroluminescence⁹³⁻⁹⁵.

Poly-3,4-ethylenedioxythiophene (PEDOT) (Table 1.5), in particular, has been investigated extensively due to its potential use in transparent, flexible and disposable electronic applications⁹⁶.

Depending on the particular monomer used, the resulting ICP's can have a wide range of conductivities (Table 1.5). The method of polymerisation, level of doping, crystallinity, and alignment of the polymer backbone are all important

in determining the overall electrical conductivity of the synthesised conducting polymer

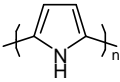
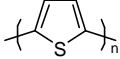
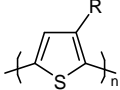
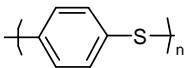
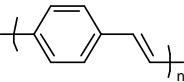
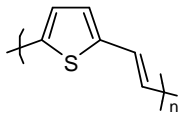
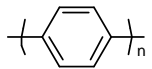
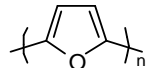
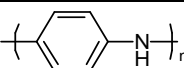
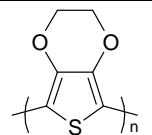
Polymer	Structure	Doping Materials	Approximate Conductivity (S cm ⁻¹)
Polyacetylene	(CH) _n	I ₂ , Br ₂ , Li, Na, AsF ₃	10000 ^a
Polypyrrole		BF ₄ ⁻ , ClO ₄ ⁻ , tosylate ^b	100
Polythiophene		BF ₄ ⁻ , ClO ₄ ⁻ , tosylate ^b , FeCl ₃	1000
Poly(3-alkylthiophene)		BF ₄ ⁻ , ClO ₄ ⁻ , FeCl ₃	1000-10000 ^a
Polyphenylene sulfide		AsF ₅	500
Polyphenylenevinylene		AsF ₅	10000 ^a
Polythienylenevinylene		AsF ₅	2700 ^a
Polyphenylene		AsF ₅ , Li, K	1000
Polyfuran		BF ₄ ⁻ , ClO ₄ ⁻	100
Polyaniline		HCl	1000 ^a
Poly(3,4-ethylenedioxythiophene)		Polystyrene sulfonate	50

Table 1.5. Conductivities of various conducting polymers. ^aConductivity of oriented polymer, ^b*p*-Methylphenylsulfonate⁹⁷.

1.6.1. Doping

Doping involves controlled addition of non-stoichiometric quantities of chemical species to the polymer in small amounts. This can result in significant changes in the electrical, magnetic and optical properties of the polymer. During the doping process, an organic polymer (either an insulator or semiconductor) with a conductivity in the range of 10⁻¹⁰ to 10⁻⁵ S cm⁻¹, is converted to a conducting polymer with a conductivity in the metallic range, typically 1-10⁴ S

cm⁻¹. Figure 1.29 shows the effect of doping on the electrical conductivity of polyacetylene and polyaniline.

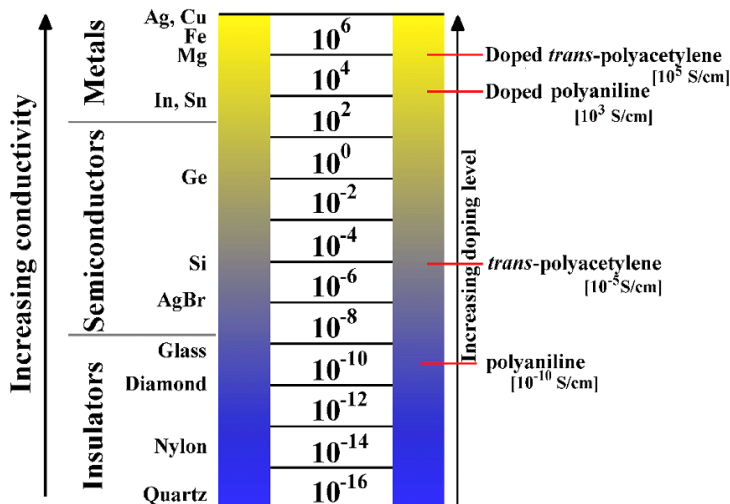


Figure 1.29. Effect of doping on conducting polymers⁹⁸.

The polymer backbone remains largely unchanged after the doping process, and the doped state is charge-stabilised by the dopant counterions. The doping process is reversible and can be achieved either chemically or electrochemically. There are two major types of doping: redox doping and non-redox doping⁹⁸.

1.6.2. Redox Doping

Conducting polymers can undergo p- or n-type doping, resulting in a change of the number of electrons associated with the polymer backbone. A partial oxidation of the π -system of the polymer backbone results in p-doping, while a partial reduction of the polymer backbone results in n-type doping. p-Type doping was first discovered by treating *trans*-(CH)_x with an oxidizing agent such as iodine, while n-type doping was discovered by treating *trans*-(CH)_x with a reducing agent such as sodium amalgam or sodium naphthalide⁹⁸. Both p- and n-type doping involve the addition of dopant counterions to stabilize the charge on the polymer backbone, however, there are other forms of redox doping which do not involve the addition of counterions.

Photo-doping occurs when the polymer adsorbs a photon of energy greater in energy than its band gap. The polymer backbone then carries both positive and negative charge until the radiation is discontinued and the charges recombine⁹⁸. Figure 1.30 shows the effect of photodoping on polyacetylene.

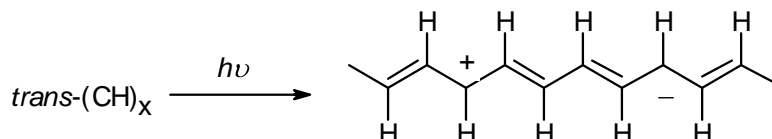


Figure 1.30. Effect of photodoping on polyacetylene⁹⁸.

1.6.3 Non-Redox Doping

Non-redox doping differs from redox doping in that the number of electrons associated with the polymer backbone remains unchanged. Instead a rearrangement of the energy levels takes place during the doping process. This was first discovered when polyaniline was treated with strong protonic acids, resulting in a 9-10 order of magnitude increase in conductivity⁹⁸.

1.6.4. Chemical Polymerisation

Chemical polymerisation uses a well-known chemical oxidant such as ferric chloride (FeCl_3) or ammonium persulfate ($(\text{NH}_4)_2(\text{S}_2\text{O}_8)$) to bring about the oxidation of the monomer to an intermediate species.

For example, in the synthesis of polypyrrole (shown in Figure 1.31), the pyrrole monomer (a) is oxidized to a cationic radical (b). This radical then undergoes a dimerisation to form the charged species (c), which, after deprotonation, yields the neutral bipyrrrole molecule (d). Subsequent oxidation, recombination and deprotonation steps result in the formation of polypyrrole⁹⁹.

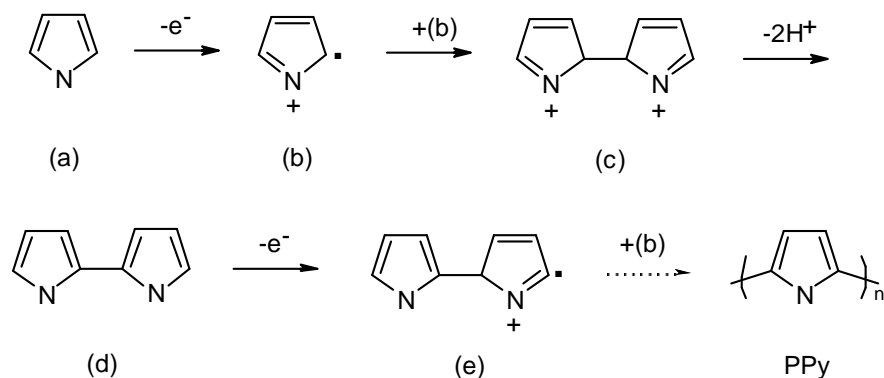


Figure 1.31. Oxidative polymerisation of pyrrole⁹⁹.

1.6.5. Electrochemical Polymerisation

Electrochemical polymerisation typically yields a very ordered polymer, which as a result, has a high conductivity. The electrodes used are typically Pt or SnO₂ and are placed in an acidic solution containing the monomer for polymerisation, an electrolyte and the dopant if required. Once the polymerisation has taken place the film is stripped from the electrodes and dried. The resultant films are usually insoluble and extremely difficult to process¹⁰⁰.

1.6.6. Polypyrrole

Polypyrrole is one of the most widely used conducting polymers due to its ease of use. The polymer consists of pyrrole rings, linked in the α, α' positions, although NMR and IR spectroscopy suggest there are other types of bonding present. As a result of the predominantly α, α' bonding, the polymer chains have a planar geometry¹⁰¹.

Polypyrrole has excellent conductivity in the doped state, with up to 108 S cm⁻¹ reported in the literature for thin films spin-coated onto glass slides¹⁰². Pyrrole can be polymerised by either the chemical or electrochemical method, and the choice of method affects the conductivity of the resultant polymer. Electrochemical polymerisation usually yields a polymer of higher conductivity,

but this choice of method is also problematic for its lack of processability. A mechanism for the polymerisation of pyrrole is depicted in Figure 1.31.

The monomer itself has a relatively low oxidation potential and hence can be polymerised easily with a number of readily available chemical oxidants such as FeCl_3 , $(\text{NH}_4)_2\text{S}_2\text{O}_8$ and I_2 . The choice of oxidant plays an important role in the determining the structure and therefore the conductivity of the resultant polymer.

Like many polymers, polypyrrole is almost impossible to obtain in soluble form, severely affecting its processability. A number of attempts have been made at creating soluble forms of polypyrrole, in particular, one method involving the polymerisation of a pyrrole monomer substituted with a long alkyl chain¹⁰³. While this affords an increase in solubility in organic solvents, it does result in a decrease of conductivity of the obtained polymer as ionic dopants cannot be used.

More recent attempts have therefore used unsubstituted monomers and instead concentrated on doping the polymer with long chain sulfonic acids such as dodecylbenzenesulfonic acid (DBSA) or bis-(2-ethylhexyl) sulfosuccinic acid (DEHS, or otherwise known as AOT). These acids act as a surfactant and increase the solubility of the polymer in weakly polar solvents such as chloroform, DMF and DMSO.

Using this method, Jang *et al.* synthesised polypyrroles doped with AOT. These polymers had solubilities ranging from ~0.5-4 wt. % in alcohols¹⁰⁴. Using a similar method, Oh *et al.*¹⁰⁵ reported the formation of polymers with solubilities ranging from 2-5 wt. % in acetic acid, benzene and chloroform, while solubility was increased to 7-9 wt. % when using relatively more polar solvents such as DMF or NMP¹⁰⁵.

There is very little mention of water-soluble polypyrrole in the literature, although Jang *et al.* have managed to synthesize water-soluble pyrroles with solubilities up to 4 wt. %¹⁰⁶. The solubility of polypyrrole is still a major issue and a rather substantial disadvantage when compared to other conducting polymers such as polyaniline.

Johnston *et al.*¹⁰⁷ have already demonstrated that polypyrrole will bind readily to cellulose fibres through hydrogen bonding between the surface hydroxyl groups of the cellulose fibres and the lone pairs on the nitrogen present in the polypyrrole backbone¹⁰⁸.

1.7. Electromagnetic Interference Shielding

The increased use of electrical equipment and wireless systems over the past few decades has led to an increase in the vulnerability to electromagnetic interference (EMI). Electromagnetic (EM) energy consists of a magnetic component (*H*-field) and an electric (*E*-field) component perpendicular to each other, and propagates at right angles to the plane containing both components¹⁰⁹.

The ratio of the *E* to *H* fields is defined as the wave impedance (Z_w , in ohms) and depends upon the type of source and the distance from the source. Large impedances characterise *E* fields, while small impedances characterise *H* fields. Far from the source the impedance remains constant at $377\ \Omega$ (the impedance of free space). In EMI shielding two regions are present: the near field and far field shielding regions. When the distance between the radiation source and the shield is larger than $\lambda/2\pi$ (where λ is the wavelength of the EM radiation), it is in the far field shielding region. In this scenario the EM plane wave theory is applicable. If the distance between source and shield is less than $\lambda/2\pi$, it is in the near field shielding region and the theory is based upon the contribution of both electric and magnetic dipoles¹⁰⁹.

Attenuation of an EM wave by a shield generally occurs by three mechanisms: reflection, absorption and multiple internal reflections. The reflection loss is a function of the ratio of $\frac{\sigma_r}{\mu_r}$ whereas the absorption loss is a function of the product of $\sigma_r \times \mu_r$, where σ_r is the electrical conductivity of the shield with respect to copper metal, and μ_r is the magnetic permeability of the shield relative to free space¹⁰⁹. Hence the electrical conductivity and magnetic properties of the shield are important in determining its overall shielding effectiveness (SE). SE in decibels (dB) is a measure of the reduction of EM radiation at a specific frequency by a shield, and is defined as:

$$SE = 10 \log \frac{P_o}{P_t} = 20 \log \frac{E_o}{E_t} = 20 \log \frac{H_o}{H_t} \quad (1.19)$$

where P_o , E_o and H_o are the power and the electric and magnetic field intensities incident on the shield, and P_t , E_t and H_t are the counterparts transmitted through the shield¹⁰⁹. Useful transmission values for commercial applications in electronic housings are in excess of 40 % at frequencies of 1 GHz. For military applications and for near-field shielding requirements even better performance in the region of 80 - 100 % is required¹¹⁰.

The traditional approach to EMI shielding uses metallic materials, which supply excellent SE. However, these materials in the form of bulk sheets, meshes, plated coatings, powders and fibres impose severe weight penalties and can become costly on a large scale. Furthermore, the ever-present threat of corrosion is another major drawback of these materials¹⁰⁹.

Carbon fillers in the form of fibres and powders are also used in EMI shielding applications due to their electrical conductivity, chemical resistance and low density. Unfortunately with the exclusive use of carbon in EMI shielding applications, the conductivity and resulting SE is inadequate. A large amount of work has gone into increasing the conductive and EM performances of carbon,

namely in the form of nano-carbons. However, at this time the cost of such materials make them an expensive alternative¹⁰⁹.

Conducting polymers have been extensively studied as potential candidates for use as EMI shielding materials due to their high conductivities (compared to carbons) and low densities (compared to metals). One major drawback in the use of ICP's is their lack of processability. This has been overcome by coating substrates such as cotton, lycra and polyester with various conducting polymers. Several groups have synthesised such materials and evaluated their EMI shielding properties^{86, 111-113}.

1.8. Inkjet Printing

The basic imaging element in inkjet printing is a droplet of ink. Two main sub-categories exist: continuous jet (CS) and drop on demand jet (DOD). CS inkjet printing is utilised in commercial printing for the marking and coding of products, while DOD inkjet technology is widely used in consumer inkjet printers¹¹⁴.

In CS inkjet technology, a high-pressure pump directs ink through a gun body and microscopic nozzle. A piezoelectric crystal generates acoustic waves as it vibrates in the gun body, generating a continuous stream of ink droplets. Droplet formation and size are strongly influenced by the nozzle size and pressure, and the perturbation of the ink stream by the piezoelectric crystal. Droplets "chosen" for printing are selected from the stream by electrostatic charging and deflected towards the substrate, while non-printing drops are collected in a chamber away from the substrate¹¹⁴.

There are two types of DOD inkjet printing, piezoelectric inkjet and thermal inkjet. Piezoelectric inkjet printing uses a piezoelectric crystal to induce a pulse and force a droplet from the nozzle, while thermal inkjet printing uses steam explosions in electrically heated chambers to achieve the same end result¹¹⁴.

The inkjet printing of CdSe quantum dots and has been achieved by de Gans *et al.*¹¹⁵, while Althues *et al.*^{116, 117} have successfully printed ZnS:Mn²⁺ solubilised by acrylic acid and methacrylic acid onto plastic substrates. After the addition of azobisisobutyronitrile (AIBN) and subsequent UV hardening, a transparent polymer containing ZnS:Mn²⁺ was obtained.

1.9. Scope of the Project

NZ paper exports total over \$600 million per annum as commodity newsprint and packaging grades¹¹⁸. Papers and packaging materials functionalised by nanoparticles, conducting polymers and quantum dots will add value post paper manufacturing by low cost coating methods and inkjet printing by small enterprise industries. New markets in higher value printing and packaging papers of \$50 million per annum are expected in 10 years.

To capitalise on the development of this upcoming higher value printing and packaging market, this PhD research program seeks to develop, characterise and carry out initial applications tests for a suite of novel hybrid materials based on cellulose fibres (paper) and magnetic nanoparticles (iron oxide), conducting polymers (polypyrrole), and quantum dots (doped zinc sulfide).

For simplicity, magnetic nanoparticles of magnetite and cobalt ferrite will be synthesised by the aqueous chemical methods listed in 1.3.8. They will then be characterised using Alternating Gradient Magnetometry (AGM), Energy Dispersive X-ray Spectroscopy (EDS), Scanning Electron Microscopy (SEM), SQUID Magnetometry, Transmission Electron Microscopy (TEM), Vibrating Sample Magnetometry (VSM), X-ray Diffraction (XRD), X-ray Fluorescence (XRF) and X-ray Photoelectron Spectroscopy (XPS).

The surface hydroxyl groups present on the cellulose substrate and the oxygen atoms present in the iron oxide nanoparticles will allow for the surface binding

of nanoparticles to the substrate through the formation of hydrogen bonds between both components.

The coating of cellulose fibres with magnetic nanoparticles synthesised by the methods listed in chapter 1.3.8, will be done either *in situ* or by synthesizing the magnetic nanoparticles and subsequently mixing them with suspensions of the fibres.

These hybrid materials will then be characterised by the use of Atomic Force Microscopy (AFM), AGM, EDS, SEM, SQUID Magnetometry, VSM, XRD, XRF and XPS.

The resultant materials will allow the investigation of new concepts in papermaking, packaging and security paper.

Polypyrrole-coated paper and cotton sheets will be synthesised by a chemical polymerisation method (1.6.4) and characterised using DC conductivity measurements, EDS, infrared spectroscopy (IR) and SEM.

Hybrid materials of cellulose and polypyrrole will then be combined with magnetic nanoparticles synthesised in 1.3.8 and tested for application in Electromagnetic Interference Shielding (EMI) at the Defence Science Technology Organisation in Melbourne, Australia.

Their properties will be characterised by a number of methods including DC conductivity measurements, EDS, and SEM.

Photoluminescent doped ZnS quantum dots will be prepared by a simple chemical precipitation method outlined in section 1.4.3. Characterisation of these materials will include the use of Atomic Absorption Spectroscopy (AA), EDS, Photoluminescence Spectroscopy (PL), SEM, Transmission Electron Microscopy (TEM), XRD and XPS.

As with magnetic nanoparticles, the goal of this part of the project is to capture photoluminescent doped ZnS quantum dots on the cellulose fibre surface. This will be attempted by precipitating the quantum dots (as in 1.4.3) either *in situ*, or by first synthesizing the quantum dots and subsequently mixing them with a suspension of the fibres.

The materials will then be characterised by EDS, PL Spectroscopy, SEM, XRD, XRF, and XPS.

Doped ZnS quantum dots will also be solubilised for inkjet printing at CSIRO Forest & Biosciences and printed onto various substrates, including photocopy paper, photo quality inkjet paper, PET plastic, ITO-coated PET plastic, ITO, glass and silicon.

The combination of the two precursor materials will give rise to cellulose fibres that have retained their inherent properties of flexibility and tensile strength, but also the newly imparted property of photoluminescence. Such materials may have interesting applications in the paper, packaging and fashion industries.

Chapter 2

METHODS

2.1 Instrumental Methods

The following section briefly describes equipment and instrumental procedures used in this PhD research program.

2.1.1. Alternating Gradient Magnetometry (AGM)

An alternating gradient magnetometer was used to measure magnetisation versus applied field curves (*M vs. H curves, or hysteresis loops*) of synthesised iron oxides. From these data the saturation magnetisation (M_s) and the magnetic susceptibility of the material (χ) can be obtained by the equation:

$$M = \chi H \quad (2.1)$$

Measurements were conducted on powder samples sealed in gelatin capsules, and taken at 300 K on an Alternating-Gradient Magnetometer 2900 from Princeton Measurements Corporation with an X-Axis AGM probe. Applied fields ranged from -1 to 1 T. The AGM method was proposed by Flanders in 1988¹¹⁹.

2.1.2. Atomic Absorption Spectroscopy (AA)

Atomic absorption spectroscopy was carried out on a GBC-206AA instrument in order to ascertain what percentage of dopant in the reaction mixture was actually incorporated in the crystal lattice of ZnS.

A summary of conditions for individual elements is shown below in Table 2.1. Gas flows were optimised for each experiment using the most concentrated standard solution. Fresh standards were prepared for each new day of measurements and were acidified with 6 M nitric acid in order to prevent any precipitation. Colloidal samples were dissolved in 6 M nitric acid also.

Element	Lamp Current (mA)	Flame type	AA wavelength (nm)	Slit width (nm)	Sensitivity (ppm)
Zn	5.0	Air-acetylene (oxidizing)	213.9	0.5	0.008
Mn	5.0	Air-acetylene (stoichiometric)	403.1	0.2	0.15
Cu	3.0	Air-acetylene (oxidizing)	217.9	0.2	0.16

Table 2.1. Summary of experimental conditions for AA measurements of doped ZnS quantum dots.

2.1.3. Atomic Force Microscopy (AFM)

AFM measurements were carried out at the Helmholtz-Gemeinschaft Institute for Technical Chemistry at the Forschungszentrum Karlsruhe in Germany in order to assess the morphology of coated Kraft fibres at the nano-scale. Individual fibres were clamped down across the stub of a custom made sample holder using a small rubber band or plastic ring in order to attempt to keep the fibre still during imaging (Figure 2.1).

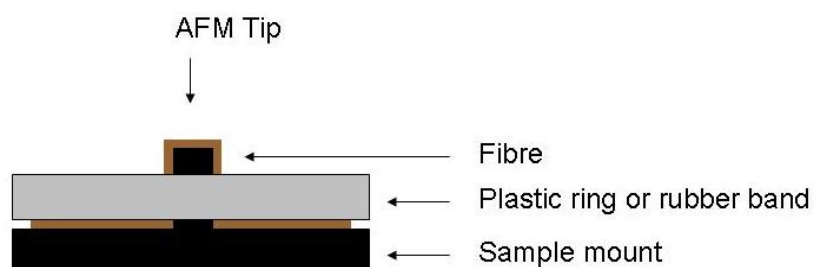


Figure 2.1. Schematic diagram showing AFM sample mounting of Kraft fibres.

Images were taken with a Multimode AFM connected to a Nanoscope IIIa controller (Digital Instruments, USA). The AFM was operated in air at room temperature in contact mode. Silicon cantilevers (NSC 36 MicroMasch, USA) were used with typical force constants between 0.6 and 1.8 N m⁻¹. A typical set of conditions is shown in Table 2.2.

The technique proved unsuccessful due to the difficulty of clamping down a single fibre and keeping it still enough for measurement as the AFM tip was dragged across the surface. This was problematic in both contact and tapping modes. The technique was abandoned.

Setting	Value
Set point	1.8 V
Scan speed	1 $\mu\text{m s}^{-1}$
Resolution	256
Rotation	0°
Proportional Gain	1.0
Integral Gain	0.2
Frequency	1.0 Hz
Drive Amplitude	69.67 mV

Table 2.2. Typical experimental conditions for an AFM measurement

2.1.4. Cotec Profilometer Measurements

A profilometer was used to measure the distribution and morphology of inkjet printed quantum dots applied to a silicon wafer (100mm diameter, 7-13 $\Omega\text{ cm}^{-1}$ resistance, 450 \pm 25 μm thickness, from University Wafer, USA). The wafer was examined using a Cotec Altisurf 500 non-contact surface profiler (Cotec, France), readily available at CSIRO Forest and Biosciences in Melbourne, Australia. Measurements were made of the thickness of the dry quantum dot film across an area corresponding to printed text.

2.1.5. DC Conductivity Measurements

Samples were measured for their electrical conductivity using the linear four-point probe technique. The method uses a power source to deliver a constant current in the milliamp range to a sample placed between four gold electrodes (A,B,C,D). The voltage across the sample is measured across electrodes B and C, while the current is measured through electrodes A and D. A schematic of the set-up is shown in Figure 2.2.

Samples were taken from random areas of the polypyrrole-cellulose composites and their thickness measured using a digital micrometer. Resistivity is calculated using the equation:

$$R = 2 \times \pi \times t \times \frac{P}{I} \quad (2.2)$$

where P is the potential across points B and C, I the current across points A and D, and t the thickness in cm. The conductivity of the sample in $S\ cm^{-1}$ is calculated by taking the inverse of the resistivity ($1/R$).

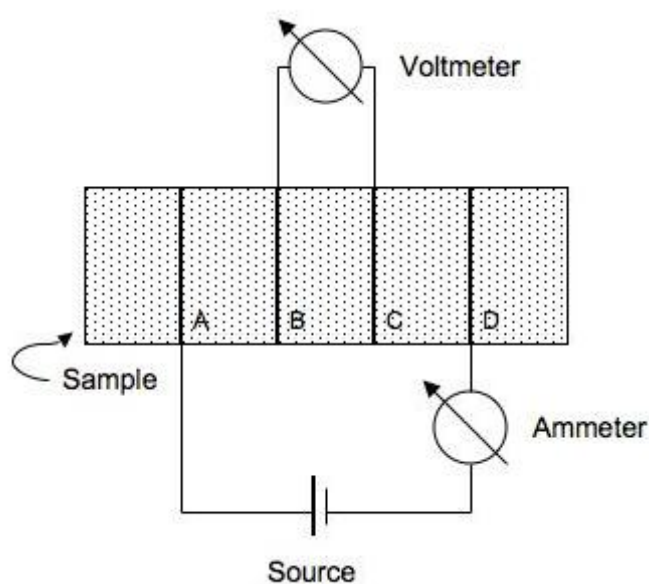


Figure 2.2. Schematic of the linear 4-point probe technique for DC conductivity measurements.

2.1.6. Electromagnetic Interference (EMI) Shielding Measurements

The EMI shielding effect of polypyrrole and magnetite coated substrates was measured at the Australian Defence Science and Technology Organisation (DSTO) in Melbourne, Australia.

2.1.6.1. Free Space Measurements

Free space measurement is used to determine broadband dielectric properties of large sheet materials. The method involved placing 500 x 500 mm samples between two microwave horns and measuring the reflection and transmission from the sample. Figure 2.3 shows the schematic set-up of signal detection.

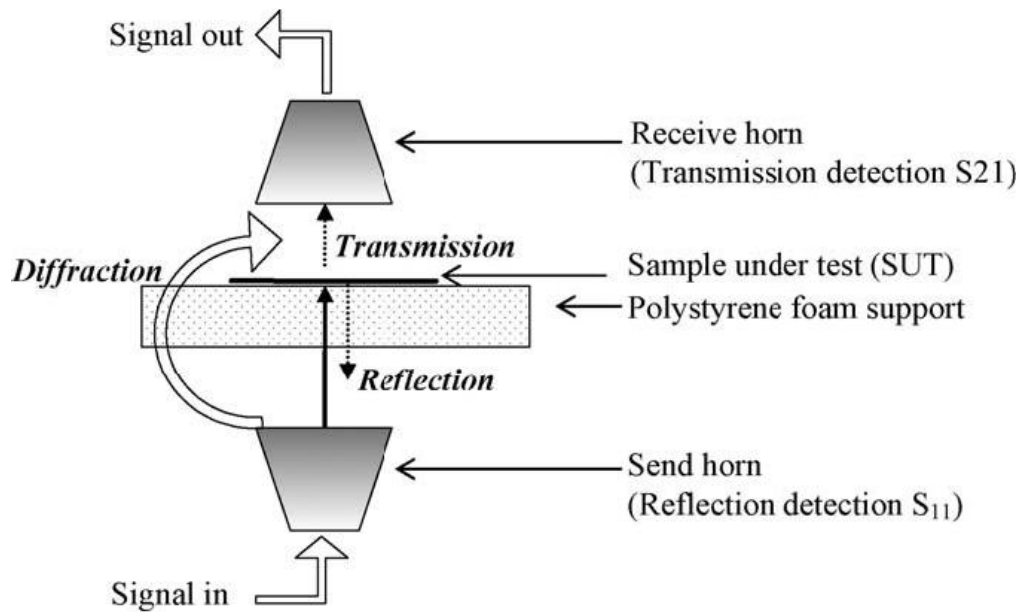


Figure 2.3. Schematic set-up of free space measurements¹²⁰.

An Agilent Technology 8510C vector network analyzer is used to perform all the measurements at microwave frequencies. The 8510C analyzer is connected to an 8517A S-Parameter Test Set with an 83651B Synthesised Frequency Source. The frequency range of this system covers 45MHz to 50 GHz. The network analyzer has a dynamic range of greater than 100 dB, and a resolution of 0.01

dB in magnitude and 0.01° in phase. The system is computer controlled and uses software written by Dr. Andrew Amiet of the DSTO. A photograph of the instrument is shown below in Figure 2.4.

Output from the system is in the form of S -parameters, where S_{11} is the reflected signal (measured at port 1) and S_{21} is the transmitted signal (measured at port 2) when an input signal is present at port 1. These complex quantities are transformed into absolute magnitude and phase of the reflection and transmission, and the permittivity and permeability of a material can be extracted by calculation. The scattering parameters S_{11} and/or S_{21} are recorded at 401 frequency points across the band, with 500 readings averaged at each frequency point. The magnitudes of reflection and absorption were later calculated using the permittivity values derived from the measured S_{21} (transmission) data.



Figure 2.4. Photographs of the experimental set-up for free space measurements.

The frequency range of the horns was 1–40 GHz and the gain of the horn antenna was between 6 and 16 dB. The distance between the transmission horn and the calibration plane was set to 310 mm, and the distance between the receive horn and the calibration plane was set to 165 mm.

One of the main sources of error in free space dielectric measurements is the diffraction around the sample being tested. The errors caused by diffraction are reduced when the sample size is sufficiently large. However, the diffracted signal can be determined by measuring the signal reached from port 1 to port 2 when a metal sheet that is exactly the same size as the test specimens is placed in the sample plane. Since none of the signal travels through the metal sheet, only the diffracted signal reaches port 2. This is then removed mathematically from the sample transmission values, thus increasing the accuracy of the permittivity calculation. Another source of error in all dielectric measurements, particularly in the case of conducting polymer-coated fabrics, is accurate thickness measurements. For these experiments, the sample thicknesses were averaged over the sample area to improve accuracy.

2.1.6.2. Calculations

The behaviour of a material under the influence of an electromagnetic field can be determined using complex permittivity and complex permeability. The complex permittivity (ϵ^*) is related to the electrical component of the field, while the complex permeability (μ^*) is due to the magnetic component of the field (1.7).

The complex permittivity of any material consists of a real part associated with the energy storage of the material, and an imaginary part, associated with the energy dissipation. Permittivity is often expressed in relative units to that of free space. Relative complex permittivity is equal to:

$$\epsilon_r^* = \frac{\epsilon^*}{\epsilon_0} = \epsilon_r' + i\epsilon_r'' \quad (2.3)$$

where ε^* is the permittivity of the material and ε_0 is the permittivity of free space ($\varepsilon_0 = 8.854 \times 10^{-12} \text{ F m}^{-1}$). All permittivities used in this study are relative permittivities, although the subscript r will not be used in notation.

The fraction of incident radiation reflected from the surface of the material is known as the reflection coefficient (Γ) and the fraction of incident radiation transmitted through the material is referred to as the transmission coefficient (T). At a material/air interface the reflection and transmission coefficients can be expressed in terms of relative permittivity and permeability:

$$\Gamma = \frac{\sqrt{\frac{\mu}{\varepsilon}} - 1}{\sqrt{\frac{\mu}{\varepsilon}} + 1} \quad (2.4)$$

$$T = e^{-i\left(\frac{\omega}{c}\right)d\sqrt{\varepsilon\mu}} \quad (2.5)$$

where ω is the angular frequency and d is the thickness of the material.

The output from the Agilent Technology 8510C vector network analyzer is in terms of scattering parameters, S_{11} and S_{21} . The first number refers to the port the signal is measured at, and the second number refers to the port where the signal originated from. Hence, S_{11} is the reflected signal and S_{21} is the transmitted signal.

For electrically thin materials, Nicholson and Ross¹²¹ showed that the scattering parameters can be expressed as:

$$S_{11}(\omega) = \frac{(1 - T^2)\Gamma}{1 - T^2\Gamma^2} \quad (2.6)$$

$$S_{21}(\omega) = \frac{(1 - \Gamma^2)T}{1 - T^2\Gamma^2} \quad (2.7)$$

Using the free space measurement technique it is possible to calculate the complex permittivity and permeability by measuring both the S_{11} and S_{21} parameters.

If the material is non-magnetic in nature, such as polypyrrole, it is sufficient to calculate the complex permittivity only, using either the reflection or transmission signals. The transmission signal is easiest to measure with greatest accuracy, and is chosen for this type of approximation. By rearranging equation 2.7, and using equations 2.4 and 2.5, the transmission (S_{21}) can be expressed as in terms of μ and ϵ . This can then be solved using the Newton method¹²².

2.1.7. Freeze Drying

Samples were dried on a Labconco Freezone 4.5 Freeze Dryer at a collector temperature of -41 °C and a pressure of 0.036 Torr for 24 h. Colloidal suspensions of doped ZnS quantum dots were filtered down to a filter cake and subsequently frozen by liquid N₂ before placing on the freeze drier.

2.1.8. Infrared Spectroscopy (IR)

Infrared spectroscopy was used to ascertain the type of bonding between the capping agent and ZnS in water soluble quantum dot samples. Measurements were taken on a Bruker Tensor 27 FT-IR spectrometer. A drop of a colloidal suspension (in water) was placed on a pressed NaBr disc for measurement, and 16 scans were taken for each sample.

2.1.9. Inkjet Printing

The quantum dot solutions were inkjet printed using a 2811 Dimatix Materials Printer (FUJIFILM Dimatix, USA), shown in Figure 2.5, housed at CSIRO Forest and Biosciences, Melbourne, Australia.

The quantum dot solution had been previously formulated and optimised to be within reasonable range of a number of properties suitable for inkjet printing by the 2811 Dimatix Materials Printer. These are summarised in Table 2.3.



Figure 2.5. Image of 2811 Dimatix Materials Printer (FUJIFILM Dimatix, USA) and printhead.

Property	Value
Viscosity	10-12 centipoise at 60 °C
Surface Tension	28-33 dynes at 60 °C
Low volatility	Boiling points < 100 °C
Density	Specific gravity > 1 g cm ⁻¹
Filtration	Filtered to 0.2 µm

Table 2.3. Summary of fluid properties for inkjet printing.

A 1.5 cm³ DMC-11610 (10 picolitre nominal drop volume) cartridge (Figure 2.6) was used and the solution printed with a 15 micron drop spacing and 30°C reservoir temperature.



Figure 2.6. Image of Dimatix Materials Printer Cartridge.

These settings gave an acceptable balance between print uniformity and edge resolution on most substrates. Substrates were taped down onto the platen using masking tape. The number of ‘passes’ of the printhead over the substrate was set at 1, 2 or 3.

2.1.10. Photoluminescence Spectroscopy (PL)

Photoluminescence measurements were carried out in order to characterise the excitation and emission wavelengths of doped ZnS quantum dots. A Perkin-Elmer LS-55 Photoluminescence Spectrometer was used for all PL measurements.

In the case of colloidal and liquid samples, quartz cuvettes (clear on all sides) were used, while solid samples (fibres and powders) were double-sided taped onto the sample mount provided.

For photoluminescence emission measurements, samples were excited with 320 nm light and scanned for their emission between 300 and 800 nm at a scan rate of 100 nm min⁻¹. A 320 nm cut-off filter was used to prevent any resonance peaks from the light source appearing in the output spectrum.

For photoluminescence excitation measurements, the emission wavelength was held constant (590 nm for ZnS:Mn²⁺ and 530 nm for ZnS:Cu²⁺) and the sample scanned for its maximum excitation wavelength between 200 and 400 nm at a scan rate of 100 nm min⁻¹.

The slit width for both emission and excitation was set at 5.0 nm for all experiments.

2.1.11. Scanning Electron Microscopy (SEM)

SEM imaging was completed on a Field-Emission JEOL-6500F Scanning Electron Microscope equipped with an Energy Dispersive X-ray Analysis Spectroscopy (EDS) probe for elemental mapping of sample composition.

Samples were prepared by mounting either powders or fibres on aluminium stubs. Conductive samples were sputter coated with 8 nm of platinum, while non-conducting samples were coated with 8 nm of platinum, plus an additional 4 nm coating of carbon.

Images were taken with an accelerating voltage of 10 kV and a probe current of 12 mA, while EDS was run with a higher accelerating voltage of 15 kV and a probe current between 14 and 17 mA, in order to obtain high counts for EDS analysis. A magnification range of 100 and 30,000 times was used.

2.1.12. SQUID Magnetometry

A Superconducting Quantum Interference Device from Quantum Design Ltd. (Model MPMS), housed at Industrial Research Ltd., was used for magnetic measurements of iron oxide nanoparticles and composites (Figure 2.7).

Superconductivity is the critical enabling technology that allows both the production of large, very stable magnetic fields, and also the ability to measure changes in those fields up to 14 orders of magnitude smaller. The SQUID is capable of resolving changes in external magnetic fields approaching 10^{-15} T, yet can operate at fields of up to 7 T.

A measurement is performed by passing a sample through the superconducting detection coils of the instrument. As the sample moves through the detection coils, the magnetic moment of the sample induces an electric current in the coils. The detection coils, the connection wires and the SQUID input coils form a

closed superconducting loop and so any change in the magnetic flux in the detection coils results in a change in the persistent current in the closed loop, which is proportional to the change in magnetic flux. The SQUID functions as a highly linear current to voltage converter and the variations in current in the detection coils produce corresponding voltage changes in the SQUID which are proportional to the magnetic moment of the sample.



Figure 2.7. Quantum Design MPMS SQUID Magnetometer, housed at Industrial Research Ltd.

For paper samples, a small rectangle of sample (1 cm x 0.5 cm) is placed between two drinking straws, one inside the other, and mounted on the end of a rigid sample rod. Powders samples were sealed in gelatin capsules and inserted into the middle of a straw and mounted on the end of the sample rod in the same fashion. This rod is then inserted into the sample chamber where it is kept at low pressure under helium. All samples are weighed accurately before measurement using an analytical balance.

Magnetisation versus applied field curves (M vs. H curves, or *hysteresis loops*) were measured at 10 K and 300 K and between -5 and 5 T. From these data the saturation magnetisation (M_s) and the magnetic susceptibility of the material (χ) can be obtained by the equation:

$$M = \chi H \quad (2.1)$$

2.1.13. Transmission Electron Microscopy (TEM)

Transmission Electron Microscopy was carried out using a JEOL-2011 Transmission Electron Microscope. Samples were prepared by diluting solutions and suspensions to sufficient concentrations for clear imaging, and then placing one drop on a copper TEM grid and evaporating by placing the grids under a halogen lamp. An accelerating voltage of 200 kV was used for imaging. Images were taken at magnifications ranging from 50,000-250,000 times.

2.1.14. Ultra Violet Lamp

Samples were visually assessed for their photoluminescence under a Camag Universal UV lamp, using a TL-900 tube emitting short wave ultra violet light at 254 nm, and long wave ultra violet light at 350 nm.

2.1.15 Vibrating Sample Magnetometer (VSM)

Magnetic hysteresis loops were measured in order to gain information on the magnetic saturation (M_s) and magnetic susceptibility (χ) of iron oxide nanoparticles and iron oxide-coated Kraft fibres. This was done using a Vibrating Sample Magnetometer from Lakeshore Instruments Ltd., housed at Industrial Research Ltd. As the VSM is not as sensitive as the SQUID (2.1.12) for the measurement of magnetic properties, it was only used for quick measurements (< 30 min scans).

Paper samples were cut to a size of 1 cm x 0.5 cm and teflon taped to the sample probe. Powder samples were sealed in gelatin capsules and mounted on the sample probe.

Magnetic hysteresis loops were measured at 300 K and up to 1 T, the limit of the instrument. As all samples were approaching magnetic saturation near 1 T, the instrument sensitivity was sufficient enough to provide the required information about the sample in a fast manner, albeit at lower fields and less sensitivity than the magnetic data obtained from using the SQUID.

2.1.16. Viscosity Measurements

Viscosity measurements were completed using a Brookfield Digital Viscometer, Model DV-II. A variety of manufacturer-supplied spindles were used and measurements taken at different rotation speeds (rpm). All measurements used 150 cm³ of solution and were conducted at room temperature and at 60 °C (the jetting temperature of the 2811 Dimatix Materials Printer).

2.1.17. X-ray Diffraction (XRD)

Powder X-ray diffraction measurements were carried out on a Philips X-ray generator (monochromatic Cu K α) with PW-3710 mpd controller with a voltage of 40 kV and a current of 20 mA. Samples were prepared by depositing powder on an aluminium, glass or perspex slide. Scans were typically run from 20-75° (2 θ) at a scan rate of 1° (2 θ) min⁻¹.

Particle sizes (t) were calculated using the Debye-Scherrer approximation for X-ray line broadening:

$$t = \frac{0.9\lambda}{B \cos \theta_B} \quad (2.8)$$

where λ is the radiation wavelength in nm, B is the peak broadening (determined by $B^2 = B_{colloid}^2 - B_{reference\ sample}^2$, where $B_{colloid}$ = FWHM of the main peak in the XRD pattern), and θ_B is the Bragg angle of the main peak.

2.1.18. X-ray Fluorescence (XRF)

X-ray Fluorescence measurements were completed by Mr. John Hunt at Spectrachem Analytical Ltd., Lower Hutt, Wellington, NZ. The analysis was conducted for trace elements, and included all elements from C to Bi (excluding N, O, Tc, Ru, Po, At, and the Noble gases).

2.1.19. X-ray Photoelectron Spectroscopy (XPS)

X-ray Photoelectron Spectroscopy measurements were taken at the Auckland University School of Engineering on a Kratos Axis Ultra DLD. The monochromatic Al K α X-ray source was run with a filament current of 10 mA and a voltage of 15kV. A pass energy of 160 eV was used for survey scans, while narrow scans were run with a pass energy of 20 eV. The scanned area was 300 x 700 μ m. A typical scan time for a narrow scan is 2 hours, and is completed with a system vacuum below 10⁻⁷ Torr. Binding energies were calibrated using the C-1s photoelectron peak at 285.0 eV. The effects of differential charging were circumvented by the use of a charge neutralisation gun.

Sample preparation involved mounting either powder or fibre samples on the aluminium sample holder provided. Powder samples were fixed to the sample mount using carbon tape, while fibre samples were mounted by clamping down rectangles (0.5 cm x 1 cm) cut from fibre mats using the copper plates and screws on the sample mount.

Peaks were fitted using the CasaXPS program. Most peaks were fitted with a Gaussian-Lorentzian peak shape with a ratio of 0.3:0.7, however in the case of

transition metals, a Doniac-Sunjic peak shape was used to give an asymmetrical fit, characteristic of some transition metals line shapes.

2.2. Experimental Methods

This following section outlines all chemical methods used in the research undertaken in this PhD program.

2.2.1. Kraft Fibre Suspensions

Bleached and unbleached Kraft Pulp Boards (*pinus radiata*) were obtained from Tasman Pulp and Paper Ltd. 0.5 g of this board was added to 25 cm³ of distilled water and blended in a commercial blender resulting in a 2 wt. % suspension of Kraft fibres. This suspension was filtered down to a damp filter cake and sealed in a plastic sample jar to keep humidity high.

2.2.2. Synthesis of Magnetite (Fe₃O₄) Nanoparticles

Magnetite nanoparticles were synthesised by two methods in this research.

In the method proposed by Berger *et al.*¹²³, magnetite nanoparticles are formed by adding aqueous ammonia (1 M, 50 cm³), dropwise from a burette, to a vigorously stirred solution containing dissolved FeCl₂·4H₂O (2 M, 1 cm³) and FeCl₃·6H₂O (1 M, 4 cm³). A black precipitate was formed immediately. The solution was left to stir for 30 mins, centrifuged for 15 mins at 1000 rpm, and then washed with distilled water. This washing step was repeated several times in order to eliminate any excess ammonia.

Unfortunately, the authors did not give much information about control over particle size. Because particle size has a strong influence on the overall magnetic properties of the material (1.3), another method proposed by Thapa *et al.*¹²⁴ was used in an effort to exert more control over particle size.

Here, 25 cm³ of a 7 M solution of NH₃ was added to a vigorously stirred solution containing 50 cm³ of distilled water and various amounts of dissolved FeCl₂·4H₂O. Again, a black precipitate was formed immediately. After stirring for 30 mins, the solution was centrifuged at 1000 rpm, washed with distilled water a number of times in order to eliminate any excess reagents and dispersed in 50 cm³ of distilled water. Quantities of reagents are shown in Table 2.4.

Sample	FeCl ₂ ·4H ₂ O concentration (wt. %)	Amount of H ₂ O (cm ³)	Weight of FeCl ₂ ·4H ₂ O (g)	FeCl ₂ ·4H ₂ O concentration (mol dm ⁻³)
53D	3	50	1.5	0.1509
53E	0.6	50	0.3	0.0302
53F	0.05	50	0.025	0.0025
53G	0.025	50	0.0125	0.0013

Table 2.4. Summary of reagent quantities used for the formation of Fe₃O₄ nanoparticles (2.2.2).

2.2.3. Synthesis of Cobalt Ferrite (CoFe₂O₄) Nanoparticles

Cobalt ferrite nanoparticles were formed by adding a solution containing dissolved CoCl₂·6H₂O (0.632 M, 7.90 cm³) and FeCl₃·6H₂O (0.697 M, 14.35 cm³) drop wise into NaOH (1.5 M, 200 cm³). The solution was adjusted to pH 12 by the addition of concentrated HCl. The precipitation occurred immediately and a brown-black solid was formed. Throughout the precipitation, the solution was vigorously stirred at a constant speed and the pH was kept at 11-12 by the addition of 1.5 M NaOH. The solution was centrifuged at 1000 rpm, washed with distilled water to remove any excess reagents and redispersed in 50 cm³ of distilled water.

This synthesis was also carried out at 80 °C with the aim of forming larger, ferrimagnetic nanoparticles¹²⁵.

2.2.4. Synthesis of Magnetite-coated Kraft Fibres

A colloidal suspension of the magnetite nanoparticles (53G was chosen as it had the lowest coercive field – required for shielding applications) formed in 2.2.2 was added to an approximately 2 wt. % suspension of bleached *pinus radiata* Kraft paper fibres (0.5 g in 25 cm³ water) and stirred vigorously for approximately 2 hours, after which they were filtered and washed with H₂O. The resulting coated fibres were then sonicated for 20 minutes in order to remove any loosely bound nanoparticles. Various volumes were added to obtain different loadings of magnetite nanoparticles on the fibre. These are summarised in Table 2.5.

Amount of 53G (cm ³)	Amount of Fe ₃ O ₄ in 53G (g)	Amount of Kraft Fibres (g)	Estimated Amount of Fe ₃ O ₄ on fibre (%)	Final fibre appearance
10	0.0029	0.5	0.6	Light brown
20	0.0058	0.5	1.2	Light brown
30	0.0087	0.5	1.7	Light brown
40	0.0116	0.5	2.3	Brown
50	0.0145	0.5	2.9	Dark brown
60	0.0174	0.5	3.5	Dark brown
70	0.0203	0.5	4.0	Excess particles

Table 2.5. Summary of amounts of Fe₃O₄ used for coating Kraft fibres.

2.2.5. Synthesis of Cobalt Ferrite-coated Kraft Fibres

1 cm³ of the colloidal suspension of cobalt ferrite nanoparticles (formed in 2.2.3) was added to an approximately 2 wt. % suspension of bleached *pinus radiata* Kraft paper fibres (0.5 g in 25 cm³ water) and stirred vigorously for approximately 2 hours, after which they were filtered and washed with H₂O. The resulting coated fibres were then sonicated for 20 minutes in order to remove any loosely bound nanoparticles.

2.2.6. Synthesis of Polypyrrole-coated Kraft Fibres

Polypyrrole-coated Kraft fibres were prepared via a chemical polymerisation method (1.6.4). Pyrrole monomer (0.5 M) and sodium dodecylbenzenesulfonic acid (DBSA) (0.05 M) as the surfactant, were dissolved in 200 cm³ distilled water. To this solution, 0.5 g of dispersed Kraft fibres were added and stirred vigorously for 1 h, after which they were filtered and blotted in order to remove any excess pyrrole monomer.

The blotted fibres were then added to a solution of FeCl₃·6H₂O (0.5 M, 100 cm³). The reaction proceeded quickly, as indicated by the colour change from white to dark green to black, over a time period of approximately 5 mins. The fibres were left in the oxidant solution for a further 3 h to ensure the polymerisation was complete, after which they were washed with a further 200 cm³ of distilled water in order to remove any excess reagents.

2.2.7. Synthesis of Magnetite and Polypyrrole-coated Fibres

Magnetite and polypyrrole-coated fibres were synthesised by two different pathways.

The first approach was to synthesise the magnetite-coated fibres by the method outlined in 2.2.2 and 2.2.4, followed by a drying step, subsequent soaking in a 0.5 M pyrrole solution, and the application of 1.115 M FeCl₃·6H₂O as the oxidant (as per 2.2.6). This approach is termed the ‘polypyrrole over magnetite approach.’

The second approach is simply a reversal of the first. Polypyrrole-coated fibres are prepared by the method outlined in 2.2.6, and then coated with magnetite nanoparticles using the method described in 2.2.2 and 2.2.4. This approach is termed the ‘magnetite over polypyrrole approach.’

2.2.8. Synthesis of Polypyrrole-coated Substrates

Unbleached cotton fabric, Kraft board, and newsprint were purchased from local fabric and stationery stores. Polypyrrole-coated cotton, -Kraft board and -newsprint, were prepared by a chemical polymerisation method outlined below.

Substrates were cut to 10 cm x 10 cm or 50 x 50 cm samples and placed in a polymerisation bath and soaked for 3 hours in a solution containing 0.2 M pyrrole, 0.02 M DBSA, and *p*-toluenesulfonic acid as a dopant. The dopant level was adjusted over the course of several experiments in order to monitor its effect on conductivity. Concentrations ranged from 10-100 mol. % (based on the concentration of pyrrole monomer).

After soaking, the substrate was blotted to remove any excess pyrrole monomer and then immersed in a solution of 0.443 M $\text{FeCl}_3 \cdot 6\text{H}_2\text{O}$. The monomer to oxidant ratio was kept at 1:2.23 for optimal polymerisation¹²⁶. To ensure complete polymerisation, a polymerisation time of 3 hours was allowed, carried out at either room temperature or 2 °C. The polymerisation bath was occasionally stirred to ensure an even coating on the substrates surface. The solution volume (monomer, dispersant, dopant, oxidant, solvent) was 1 L.

After the polymerisation was complete, the substrate was washed several times with distilled water and pegged on a rack to dry.

2.2.9. Synthesis of Magnetite-coated Substrates

Samples of cotton, Kraft board and newsprint (50 cm x 50 cm in size) were coated with magnetite nanoparticles synthesised by the method described in 2.2.2. A starch binder was used to bind the nanoparticles to the surface of the substrate.

In this procedure, 16 g of Ethylex™ starch was added to 50 cm³ of a magnetite nanoparticle suspension (53G, 0.03 wt. %) and heated to 60 °C with vigorous stirring. On thickening, the viscous liquid was painted onto one side of the substrate with a paintbrush, pegged, and left to dry. After drying, the process was repeated again. Each side of the substrate was given two coats.

2.2.10. Synthesis of Magnetite and Polypyrrole-coated Substrates

Polypyrrole-coated substrates were synthesised by the method outlined in 2.2.8, and coated with magnetite ('magnetite over polypyrrole') using the method described in 2.2.9. The process had to be completed in this order. If done the other way ('polypyrrole over magnetite'), Fe³⁺ ions leached from the magnetite coating and facilitated the oxidation of the pyrrole monomer during the soaking process, hindering the ability to form an even coating of polypyrrole on the surface of the substrate.

2.2.11. Synthesis of ZnS:Mn²⁺ Quantum Dots

Doped ZnS quantum dots were synthesised using a chemical precipitation method. All reagents used were AR grade. Double distilled water was used for all experiments.

In a typical synthesis of Mn²⁺ doped ZnS, 10 cm³ of 1 M ZnCl₂, 10 cm³ of 0.01 M MnCl₂ and 10 cm³ of 0.5 M sodium citrate solution were mixed and stirred at constant speed for 10 minutes. From a burette, 10 cm³ of 1 M Na₂S was added dropwise. A white precipitate was formed immediately. The resulting suspension was centrifuged, washed with distilled water and redispersed in 40 cm³ of distilled water. In some cases, the quantum dots were freeze-dried overnight.

Several experiments were conducted in which the dopant level was adjusted in order to observe its effect on the photoluminescence of the prepared sample.

For ZnS:Mn²⁺, dopant concentrations ranged from 1-10 mol. %. These are summarised in Table 2.6.

Sample	Zn ²⁺ concentration (mol dm ⁻³)	Mn ²⁺ concentration (mol dm ⁻³)	Dopant level (in reaction mixture) (mol. %)
12A	1	0.01	1
12B	1	0.02	2
12C	1	0.04	4
12D	1	0.06	6
12E	1	0.08	8
12F	1	0.1	10

Table 2.6. Summary of dopant levels in the synthesis of ZnS:Mn²⁺ quantum dots.

2.2.12. Synthesis of ZnS:Cu²⁺ Quantum Dots

ZnS:Cu²⁺ quantum dots were synthesised by a similar method to ZnS:Mn²⁺ quantum dots (2.2.11)¹²⁷.

In a typical synthesis of Cu²⁺ doped ZnS, 10 cm³ of 1 M ZnCl₂, 10 cm³ of 0.01 M Cu(CH₃COO)₂, 10 cm³ of 0.5 M sodium citrate and 10 cm³ of sodium thiosulfate were mixed and stirred for 10 minutes. From a burette, 10 cm³ of 1 M Na₂S was added dropwise. A white precipitate formed immediately. The resulting suspension was centrifuged, washed with distilled water and redispersed in 40 cm³ of distilled water. In some cases, the quantum dots were freeze dried overnight.

Again, dopant concentrations were adjusted to observe any changes in the photoluminescence of the prepared sample. For ZnS:Cu²⁺, dopant concentrations ranged from 0.2-1 mol. %. These are summarised in Table 2.7.

Sample	Zn ²⁺ concentration (mol dm ⁻³)	Cu ²⁺ concentration (mol dm ⁻³)	Dopant level (in reaction mixture) (mol. %)
25B	1	0.002	0.2
25C	1	0.004	0.4
25D	1	0.006	0.6
25E	1	0.008	0.8
25F	1	0.01	1

Table 2.7. Summary of dopant levels in the synthesis of ZnS:Cu²⁺ quantum dots.

The significantly large solubility difference between ZnS ($K_{sp} = \sim 2 \times 10^{-25}$) and CuS ($K_{sp} = \sim 8 \times 10^{-37}$), makes doping ZnS with Cu²⁺ more challenging than Mn²⁺ (K_{sp} of MnS = $\sim 3 \times 10^{-14}$)¹²⁸. Often unwanted CuS precipitates from solution before ZnS can properly form and trap Cu²⁺ ions in its lattice. A number of methods from the literature were attempted in order to form complexes with Cu²⁺ ions and thus inhibit the formation of CuS^{127, 129-137}. Many of these were unsuccessful. These are summarised in Table 2.8.

Method	Surfactant/ Complexing Agent	Reaction type	Result
Bol, <i>et. al.</i> ¹²⁹	Sodium hexametaphosphate	Chemical precipitation	Unsuccessful
Feldmann, <i>et. al.</i> ¹³⁰	Diethylene glycol	'Polyol' method, Chemical precipitation	Unsuccessful
Khosravi, <i>et. al.</i> ¹³¹	Sodium hexametaphosphate	Chemical precipitation	Unsuccessful
Lee, <i>et. al.</i> ¹³²	Thiourea	Chemical precipitation	Unsuccessful
Lynch, <i>et. al.</i> ¹³³	No surfactant or complexing agent	Chemical precipitation	Unsuccessful
Peng, <i>et. al.</i> ¹³⁴	Methacrylic acid	Chemical precipitation	Unsuccessful
Que, <i>et. al.</i> ¹³⁵	NP-5/NP-9	Microemulsion	Unsuccessful
Sun, <i>et al.</i>¹²⁷	Sodium thiosulfate	Chemical precipitation	Successful
Wang, <i>et. al.</i> ¹³⁶	Glycine	Chemical precipitation	Unsuccessful
Yang, <i>et. al.</i> ¹³⁷	Decomposition of thioacetamide	Chemical precipitation	Unsuccessful

Table 2.8. Summary of attempts made to dope ZnS with Cu²⁺.

2.2.13. Synthesis of ZnS:Ag⁺ Quantum Dots

The synthesis of ZnS:Ag⁺ quantum dots was attempted in order to obtain a 'blue-light emitting' quantum dot.

Due to the very large solubility difference between ZnS ($K_{sp} = \sim 2 \times 10^{-25}$) and Ag₂S ($K_{sp} = \sim 8 \times 10^{-51}$)¹²⁸ the synthesis of ZnS:Ag⁺ quantum dots presents an even greater challenge than that posed by their copper-doped counterparts, as unwanted Ag₂S often precipitates out before Ag⁺ ions can be incorporated into the ZnS lattice. A number of attempts were made following various literature sources, to dope ZnS with Ag⁺ by 'wet chemical', hydrothermal and microwave methods^{130, 133, 138-141}. All were unsuccessful (refer to 4.7). These are summarised in Table 2.9.

Method	Surfactant/ Complexing Agent/	Reaction type	Result
Feldmann, <i>et. al.</i> ¹³⁰	Diethylene glycol	'Polyol' method, chemical precipitation	Unsuccessful
Huang, <i>et. al.</i> ¹³⁸	Thiourea	Chemical precipitation	Unsuccessful
Jian, <i>et. al.</i> ¹³⁹	3-mercaptopropionic acid	Microwave	Unsuccessful
Luo, <i>et. al.</i> ¹⁴⁰	No surfactant/complexing agent	Hydrothermal	Unsuccessful
Lynch, <i>et. al.</i> ¹³³	No surfactant/complexing agent	Chemical precipitation	Unsuccessful
Sun, <i>et. al.</i> ¹⁴¹	Mercaptoacetic acid	Chemical precipitation	Unsuccessful

Table 2.9. Summary of attempts made to dope ZnS with Ag⁺.

2.2.14. Synthesis of SiO₂-capped ZnS:Mn²⁺ Quantum Dots

ZnS:Mn²⁺ quantum dots were capped with SiO₂ in order to decrease surface defects with the aim of increasing the strength of the photoluminescence

emission. SiO₂-capped ZnS:Mn²⁺ quantum dots were synthesised by two methods.

Steitz, *et al.*¹⁴² use tetraethoxyorthosilicate (TEOS) to cap the ZnS:Mn²⁺ quantum dots. Here 1 cm³ of ZnS:Mn²⁺ nanoparticles (as synthesised in 2.2.11) was added to 87 cm³ of water and 1.5 cm³ of TEOS added. The solution was sonicated for 2 minutes and then stirred for 24 h at room temperature. The ZnS:Mn²⁺ quantum dots were then separated by centrifugation at 1000 rpm, washed with a further 100 cm³ of water to remove any excess reagents, and then redispersed in 50 cm³ of distilled water.

Li, *et al.*¹⁴³ synthesised SiO₂-capped ZnS:Mn²⁺ in the presence of (3-mercaptopropyl) trimethoxysilane (MPS). They found the optimum ratio of MPS:Zn to be 1:2. In a beaker, 0.04 mmol of MPS was dissolved in 41 cm³ of water and stirred for 5 minutes. Zn(NO₃)₂ (0.04 M, 2 cm³) was added in a dropwise fashion with constant stirring for 10 minutes. The mixture was then titrated with tetraethylammonium hydroxide to pH 12 and stirred for 10 minutes, followed by the rapid addition of Na₂S (0.04 M, 2 cm³). The sample was stirred for a further 5 minutes before centrifuging.

2.2.15. Synthesis of ZnS:Mn²⁺-coated Kraft Fibres

The synthesis of ZnS:Mn²⁺-coated Kraft fibres was attempted by four different methods. In the first method ('colloid' method) a colloidal suspension of ZnS:Mn²⁺ quantum dots (formed in 2.2.11) was added to an approximate 2 wt. % suspension of bleached *pinus radiata* Kraft paper fibres (0.5 g in 25 cm³ of water) and stirred vigorously for approximately 2 hours, after which they were filtered and washed with H₂O. The resultant coated fibres were then sonicated for 20 minutes in order to remove any loosely bound quantum dots.

Various amounts of ZnS:Mn²⁺ quantum dots, ranging from ~ 5-50 wt. % were added to the suspension in order to obtain different loadings on the fibre surface. These are summarised in Table 2.10.

Amount of 12F (cm ³)	Amount of ZnS:Mn ²⁺ in 12F (g)	Amount of Kraft Fibres (g)	Estimated Amount of ZnS:Mn ²⁺ on fibre (wt. %)	Final fibre appearance
1	0.0243	0.5	4.9	White
2	0.0487	0.5	9.7	White
4	0.0975	0.5	19.5	White
6	0.1462	0.5	29.2	White
8	0.1950	0.5	39.0	Excess particles
10	0.2437	0.5	48.6	Excess particles

Table 2.10. Summary of amounts of ZnS:Mn²⁺ used in the coating of Kraft fibres.

The second method simply involves repeating the first, in a process termed the ‘double dip’ method.

Thirdly, the ZnS:Mn²⁺ quantum dots were synthesised as per 2.2.11, only this time 0.5 g of bleached *pinus radiata* Kraft fibres was added to the reaction mixture in order to coat the fibres using an ‘in situ’ approach. This approach was used in an attempt to form an even coating of ZnS:Mn²⁺. By forming the ZnS:Mn²⁺ quantum dots ‘in situ’, it was hoped that the particles would bind to the cellulose surface before they would have a chance to agglomerate.

In this method, ZnS:Mn²⁺ quantum dots were synthesised using the same method as in 2.2.11. The amount of Zn²⁺ used for the precipitation reaction was chosen to provide an optimum coating, based on the experimental work conducted using the ‘colloid’ method.

To 10 cm³ of 0.15 M Zn²⁺, 10 cm³ of 0.015 M MnCl₂, and 10 cm³ of 0.075 M sodium citrate, 10 cm³ of 0.15 M Na₂S was added dropwise from a burette. The resulting coated fibres were filtered, washed with 50 cm³ of water in order to

remove any excess reagents and quantum dots. The fibres were then sonicated for 20 mins to further remove any loosely bound quantum dots.

The fourth method involved using a linker molecule to adhere the particles to the surface. The amounts used in these experiments are summarised in Table 2.11.

Amount of 12F (cm ³)	Amount of ZnS:Mn ²⁺ in 12F (g)	Amount of Kraft Fibres (g)	Amount of PDADMAC		Estimated Amount of ZnS:Mn ²⁺ on fibre (%)	Final fibre appearance
			(g)	(wt. %)		
6	0.1462	0.5	0.025	1	29.2	White
6	0.1462	0.5	0.05	2	29.2	White
6	0.1462	0.5	0.1	4	29.2	White
6	0.1462	0.5	0.15	6	29.2	White
6	0.1462	0.5	0.2	8	29.2	White
6	0.1462	0.5	0.25	10	29.2	White

Table 2.11. Summary of the amounts of PDADMAC used in the synthesis of ZnS:Mn²⁺-coated Kraft fibres.

Varying amounts of polydiallyldimethylammonium chloride (poly-DADMAC), between 0.1-1 wt. % (relative to the solvent) were added to 25 cm³ of water and 0.5 g of bleached *pinus radiata* Kraft fibres. The mixture was stirred overnight after which the fibres were then filtered, blotted dry, and subsequently redispersed in 25 cm³ of water containing 6 cm³ of a colloidal suspension of ZnS:Mn²⁺ quantum dots (12F).

2.2.16. Synthesis of ZnS:Cu²⁺-coated Kraft Fibres

The synthesis of ZnS:Cu²⁺-coated Kraft fibres was attempted by similar methods used for ZnS:Mn²⁺-coated Kraft fibres (2.2.15).

A colloidal suspension of ZnS:Cu²⁺ (formed in 2.2.12) was added to an approximate 2 wt. % suspension of bleached *pinus radiata* Kraft paper fibres (1

g in 50 cm³ of water) and stirred vigorously for approximately 2 hours, after which they were filtered and washed with H₂O ('colloid' method). The resultant coated fibres were then sonicated for 20 minutes in order to remove any loosely bound quantum dots. Various amounts of ZnS:Cu²⁺ quantum dots, ranging from ~ 5-50 wt. % (based on the weight of Kraft fibres) were added to the suspension in order to obtain different loadings on the fibre surface. These are summarised in Table 2.12.

Amount of 12B (cm ³)	Amount of ZnS:Cu ²⁺ in 12B (g)	Amount of Kraft Fibres (g)	Estimated Amount of ZnS:Cu ²⁺ on fibre (%)	Final fibre appearance
1	0.0243	0.5	4.9	White
2	0.0487	0.5	9.7	White
4	0.0975	0.5	19.5	White
6	0.1462	0.5	29.2	White
8	0.1950	0.5	39.0	Excess particles
10	0.2437	0.5	48.6	Excess particles

Table 2.12. Summary of amounts of ZnS:Cu²⁺ used in the coating of Kraft fibres.

The 'double dip' and 'in situ' methods, and the use of poly-DADMAC were also used in the synthesis of ZnS:Cu²⁺-coated Kraft fibres.

For the 'in situ' method, 10 cm³ of 0.15 M Zn²⁺, 10 cm³ of 0.0003 M Cu(CH₃COO)₂ (to give a dopant level of 0.2 mol. %, as in 12B), 10 cm³ of Na₂S₂O₃ and 10 cm³ of 0.075 M sodium citrate were stirred vigorously for 10 min before 10 cm³ of 0.15 M Na₂S was added dropwise from a burette. The resulting coated fibres were filtered, washed with 50 cm³ of water in order to remove any excess reagents and quantum dots. The fibres were then sonicated for 20 mins to further remove any loosely bound quantum dots.

The amounts used for the synthesis of ZnS:Cu²⁺-coated Kraft fibres using PDADMAC as a linker molecule are summarised in Table 2.13.

Amount of 12B (cm ³)	Amount of ZnS:Cu ²⁺ in 12B (g)	Amount of Kraft Fibres (g)	Amount of PDADMAC		Estimated Amount of ZnS:Cu ²⁺ on fibre (%)	Final fibre appearance
			(g)	(wt. %)		
6	0.1462	0.5	0.025	1	29.2	White
6	0.1462	0.5	0.05	2	29.2	White
6	0.1462	0.5	0.1	4	29.2	White
6	0.1462	0.5	0.15	6	29.2	White
6	0.1462	0.5	0.2	8	29.2	White
6	0.1462	0.5	0.25	10	29.2	White

Table 2.13. Summary of the amounts of PDADMAC used in the synthesis of ZnS:Cu²⁺-coated Kraft fibres.

2.2.17. Synthesis of soluble ZnS:Mn²⁺ Quantum Dots

Soluble* ZnS:Mn²⁺ quantum dots were formulated for inkjet printing at CSIRO Forest and Biosciences by the following method. 1 cm³ of a suspension of ZnS:Mn²⁺ quantum dots synthesised in 2.2.11, was added to a solution of 1 M solution of mercaptosuccinic acid (MSA). To find the minimum amount of MSA necessary, an experiment was carried out using different MSA:Zn²⁺ ratios. This experiment is summarised in Table 2.14.

Amount of ZnS:Mn ²⁺ (cm ³)	Amount of MSA (cm ³)	MSA:Zn Molar ratio	Solution opacity
1	0.25	1	Cloudy
1	0.5	2	Cloudy
1	1	4	Cloudy
1	2	8	Clear
1	4	16	Clear
1	8	32	Clear
1	16	64	Clear

Table 2.14. Table showing optimal molar ratios of MSA to Zn²⁺ for the synthesis of soluble ZnS:Mn²⁺ quantum dots.

* If a clear solution is formed, a stable colloid has been obtained. While the particles themselves are not soluble, the term 'soluble quantum dots' is the term used in the literature for a stable colloid of very small nanoparticles with minimal agglomeration.

A cloudy solution equates to quantum dot agglomeration, which is undesirable for inkjet printing. A clear solution represents a stable colloidal suspension of quantum dots. The optimal molar ratio of MSA to Zn^{2+} was found to be 8:1.

2.2.18. Synthesis of soluble $\text{ZnS}:\text{Cu}^{2+}$ Quantum Dots

$\text{ZnS}:\text{Cu}^{2+}$ quantum dots were synthesised by the method outlined in 2.2.12. 1 cm^3 of this suspension was added to a 1 M solution of MSA. To find the minimum amount of MSA needed, an experiment similar to the one carried out in 2.2.18 was carried out using different MSA: Zn^{2+} ratios. Results are summarised in Table 2.15 below.

Amount of $\text{ZnS}:\text{Cu}^{2+}$ (cm^3)	Amount of MSA (cm^3)	MSA:Zn Molar ratio	Solution opacity
1	0.25	1	Cloudy
1	0.5	2	Cloudy
1	1	4	Clear
1	2	8	Clear
1	4	16	Clear
1	8	32	Clear
1	16	64	Clear

Table 2.15. Table showing optimal molar ratios of MSA to Zn^{2+} for the synthesis of soluble $\text{ZnS}:\text{Cu}^{2+}$ quantum dots.

A cloudy solution equates to quantum dot agglomeration, which is undesirable for inkjet printing. A clear solution represents a stable colloidal suspension of quantum dots. The optimal molar ratio of MSA to Zn^{2+} was found to be 4:1.

2.2.19. Surfactants

To develop doped ZnS quantum dots for inkjet printing, soluble quantum dots must be obtained. If any solids are present that can agglomerate, the printhead will become blocked during the jetting process.

For the development of soluble doped ZnS quantum dots, a screening of different surfactants was carried out in order to stabilise the colloid by steric or electrostatic stabilisation methods (described in 1.5). These surfactants are summarised in Table 2.16 below. Concentrations of surfactant were taken from the literature reports, and ranged from 0.01 – 1 wt. % of the total solution volume.

Surfactant	Comment
Chitosan ¹⁴⁴	Precipitation
Cetyltrimonium bromide ¹⁴⁵	Stable at low concentrations of ZnS:Mn ²⁺
Cysteine ¹⁴⁶⁻¹⁴⁹	Precipitation
Diethylene glycol ^{150, 151}	Stable for 2-3 days
Hexametaphosphate ¹⁵²	Precipitation
Hydroxyethyl cellulose ¹⁵³	Stable for 2-3 days, poor luminescence
Mercaptoacetic acid ¹⁴⁷	Stable for 2-3 days
Mercaptopropionic acid ¹⁵⁴	Stable for 2-3 days, corrosive
Mercaptosuccinic acid¹⁵⁵	Stable for months, excellent luminescence
Methacrylic acid ¹³⁴	Stable for 1-2 days, corrosive
NP-5/NP-9	Stable, poor luminescence
Polymethylmethacrylate ¹⁵⁶	Stable for 1-2 days
Polyvinyl alcohol	Stable for 1-2 days
Polyvinylpyrrolidone ¹⁵⁷⁻¹⁵⁹	Stable at low concentrations of ZnS:Mn ²⁺
Tetramethylammonium hydroxide	Destroys luminescence

Table 2.16. Surfactants used in the synthesis of soluble ZnS:Mn²⁺ quantum dots.

Chapter 3

MAGNETIC KRAFT FIBRES

Pinus radiata Kraft fibres coated with Fe_3O_4 and CoFe_2O_4 nanoparticles retain the inherent properties of the fibre; tensile strength, flexibility, and the ability to be made into a sheet (Table 1.2). The fibres also exhibit the magnetic properties of the surface bound nanoparticles. Sufficient hydroxyl groups exposed on the cellulose surface facilitate hydrogen bonding between the nanoparticles(1.2).

These fibres have been characterised using Alternating Gradient Magnetometry (AGM), SQUID Magnetometry, Scanning Electron Microscopy (SEM) with Energy Dispersive X-ray Spectroscopy (EDS), X-ray Fluorescence (XRF), X-ray Photoelectron Spectroscopy (XPS), X-ray Diffraction (XRD), and Vibrating Sample Magnetometry (VSM).

3.1. X-ray Diffraction (XRD)

A typical XRD pattern of Fe_3O_4 nanoparticles is shown in Figure 3.1, which reveals the formation of the Fe_3O_4 phase in all samples, characterised by the peaks at 30.30° , 35.67° , 43.29° , 53.51° , 57.29° and 62.67° (2θ , Cu $K\alpha$ radiation). Peak data from samples synthesised by the method (2.2.2) are shown in Table 3.1.

A reference pattern of crystalline Fe_3O_4 and the corresponding peak data are shown in Figure 3.2 and Table 3.2 respectively, while a reference pattern and the corresponding peak data for crystalline $\gamma\text{-Fe}_2\text{O}_3$ is shown in Figure 3.3 and Table 3.3 for comparison.

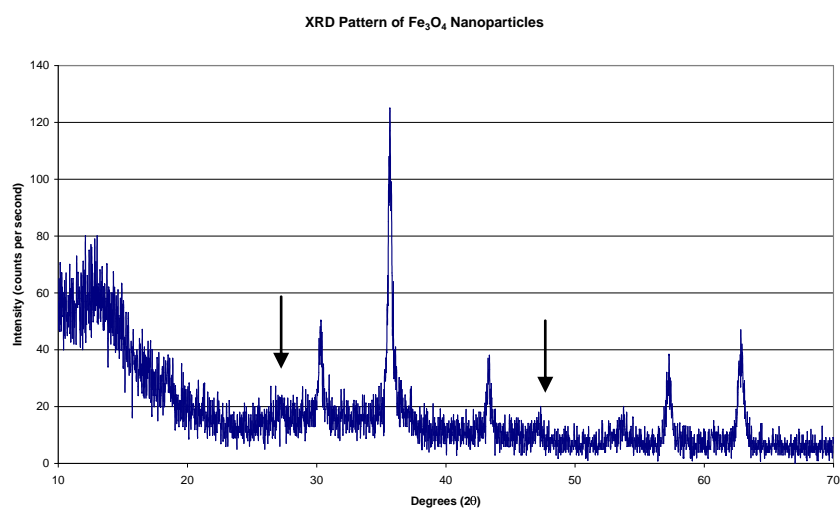


Figure 3.1. XRD pattern of synthesised Fe_3O_4 nanoparticles. $\downarrow = \alpha\text{-FeOOH}$ phase.

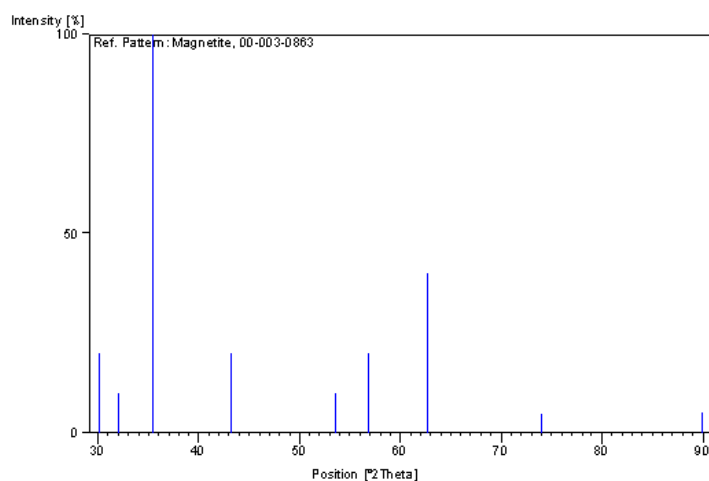


Figure 3.2. Reference pattern of crystalline Fe_3O_4 .

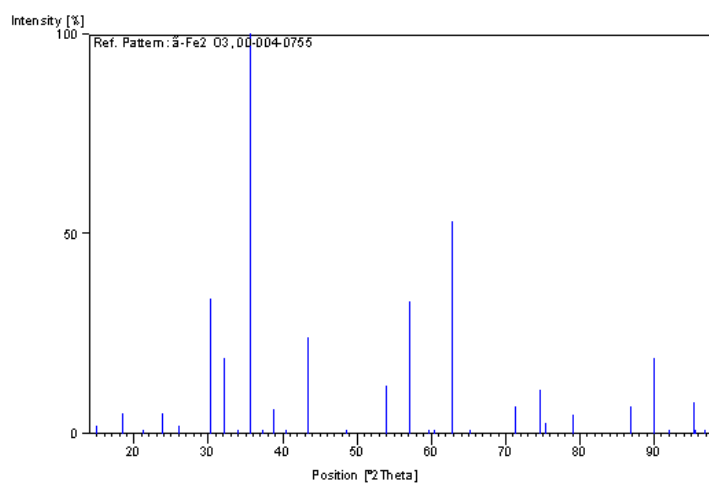


Figure 3.3. Reference pattern of crystalline $\gamma\text{-Fe}_2\text{O}_3$.

Peak	Degrees (2 θ)	I (%)
2	30.30	31
3	35.67	100
4	43.29	25
6	53.51	2
7	57.29	24
8	62.67	33

Table 3.1. XRD peak data for synthesised Fe₃O₄ nanoparticles.

Peak	Degrees (2 θ)	I (%)
1	30.17	20
2	32.05	10
3	35.45	100
4	43.25	20
5	53.55	10
6	56.78	20
7	62.73	40

Table 3.2. XRD peak data for crystalline Fe₃O₄.

Peak	Degrees (2 θ)	I (%)
1	30.27	34
2	32.17	19
3	35.60	100
4	43.47	24
5	53.89	12
6	57.17	33
7	62.73	53

Table 3.3. XRD peak data for crystalline γ -Fe₂O₃.

A good correlation exists between the XRD patterns of the Fe₃O₄ nanoparticles synthesised in this work and the reference pattern for crystalline Fe₃O₄.

There is the possibility that the Fe₃O₄ nanoparticles have oxidised to γ -Fe₂O₃. The γ -Fe₂O₃ phase has a very similar XRD pattern to Fe₃O₄, as both crystallize in the spinel structure. A reference pattern for γ -Fe₂O₃ is shown in Figure 3.3, and the corresponding peak data are summarised in Table 3.3. As the synthesised particles are on the nanoscale, the XRD line width can be very broad making it hard to distinguish between the two.

A comparison between Fe_3O_4 samples synthesised using varying precursor concentrations is shown in Figure 3.4. Consistent with the literature¹²⁴, particle size decreases as the concentration of $\text{FeCl}_2 \cdot 4\text{H}_2\text{O}$ decreases. X-ray line broadening analysis using Debye-Scherrer calculations indicates that samples have an average particle size of between 12 and 26 nm, depending on the concentration of $\text{FeCl}_2 \cdot 4\text{H}_2\text{O}$ in solution. These are summarised in Table 3.4.

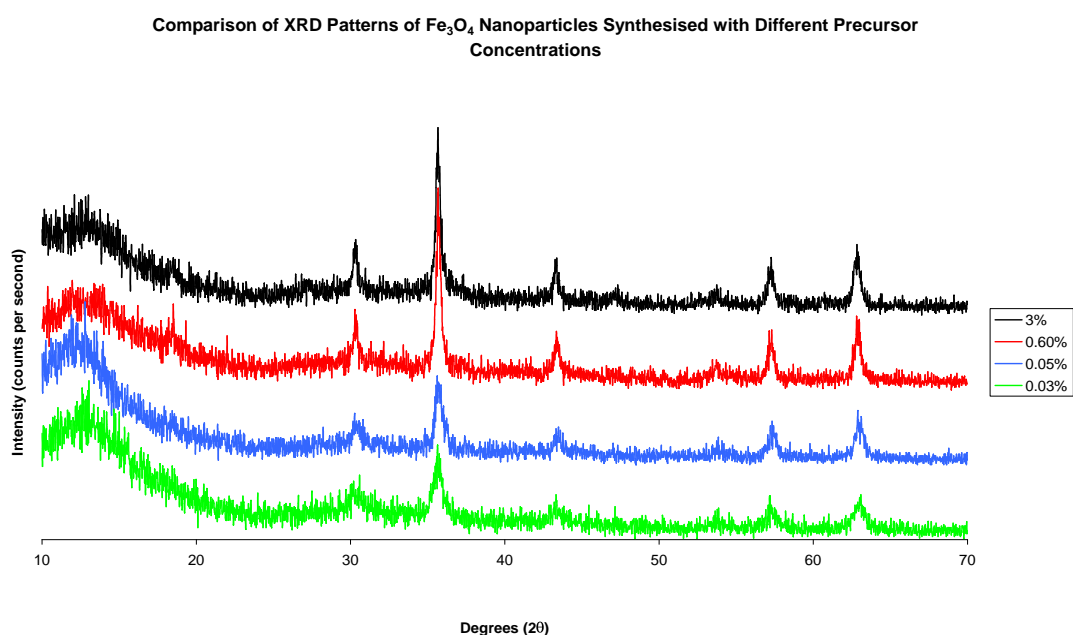


Figure 3.4. Comparison between the XRD patterns of Fe_3O_4 nanoparticles synthesised with different $\text{FeCl}_2 \cdot 4\text{H}_2\text{O}$ concentrations.

Sample	FeCl ₂ ·4H ₂ O conc.		Average particle size (nm)
	(%)	(mol dm ⁻³)	
53D	3.0	0.15	26
53E	0.60	0.03	24
53F	0.05	0.0025	15
53G	0.025	0.00125	12

Table 3.4. Effect of precursor solution concentration on particle size of Fe_3O_4 nanoparticles.

The plot in Figure 3.5 indicates that the particle size of Fe_3O_4 nanoparticles synthesised by the methods used in this thesis reaches a maximum at approximately 26 nm or at a $\text{FeCl}_2 \cdot 4\text{H}_2\text{O}$ concentration of approximately 3% or 0.15 mol dm⁻³.

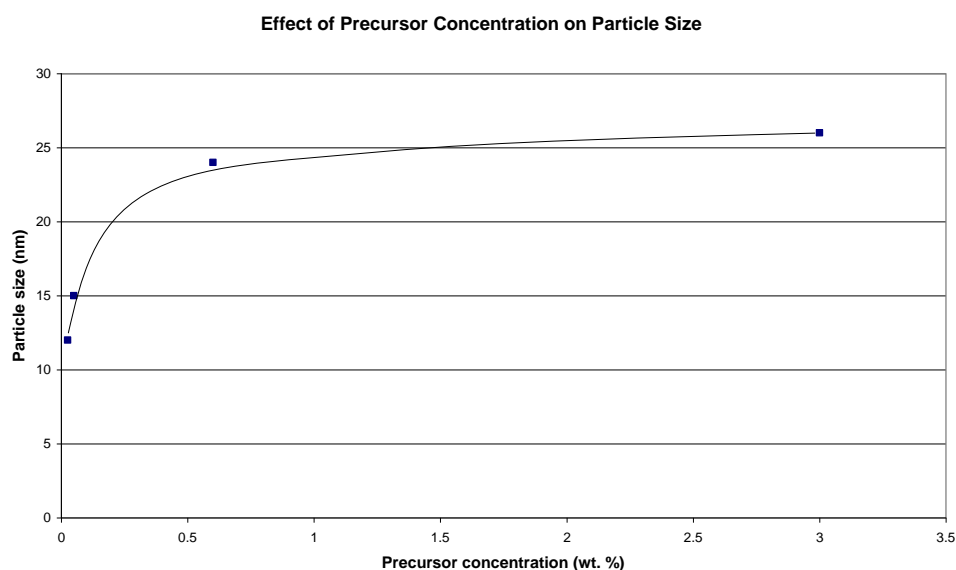


Figure 3.5. The effect of precursor concentration on particle size in the formation of Fe_3O_4 nanoparticles.

The peaks in the XRD pattern of Fe_3O_4 -coated cellulose fibres (Figure 3.6) are very broad and poorly resolved, presumably due to the thin layer, and hence relatively small amount of Fe_3O_4 present on the surface. Still, the characteristic peak at 35.67° (2θ) remains, indicating that Fe_3O_4 is present on the surface.

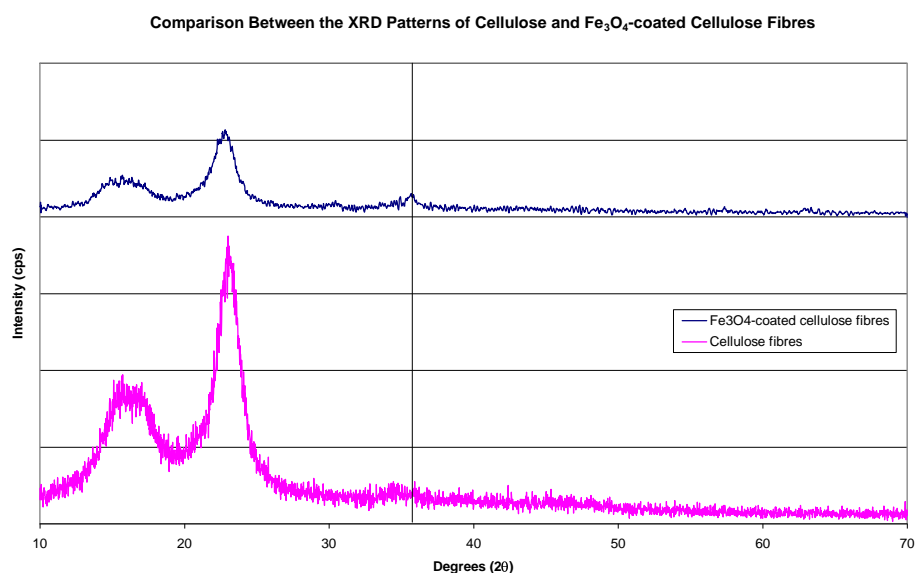


Figure 3.6. Comparison between the XRD pattern of cellulose and Fe_3O_4 -coated cellulose fibres.

3.2. X-ray Fluorescence Measurements (XRF)

XRF analysis shows that Kraft fibres are coated with Fe_3O_4 and CoFe_2O_4 nanoparticles between 1.2 and 3.15 wt. % Fe, depending on the amount of nanoparticles added during the coating process (section 2.2.4 and 2.2.5).

3.3. Magnetic Properties

The magnetic properties of Fe_3O_4 and CoFe_2O_4 nanoparticles were measured by AGM, SQUID and VSM, as outlined in the instrumental methods chapter of this thesis.

Fe_3O_4 nanoparticles were synthesised using differing precursor concentrations (2.2.2) to obtain different particle sizes, and their magnetic hysteresis loops (magnetisation (M) vs. applied field (H) curves) measured at 300 K using a VSM. These are shown in Figures 3.7 and 3.8.

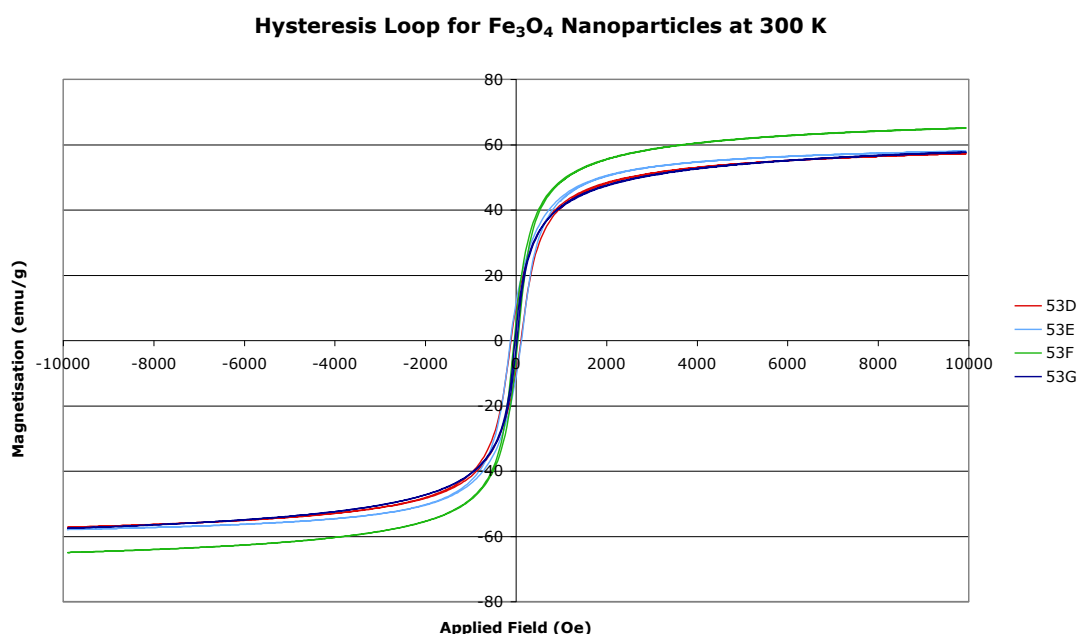


Figure 3.7. Hysteresis loops for Fe_3O_4 nanoparticles synthesised with different precursor concentrations.

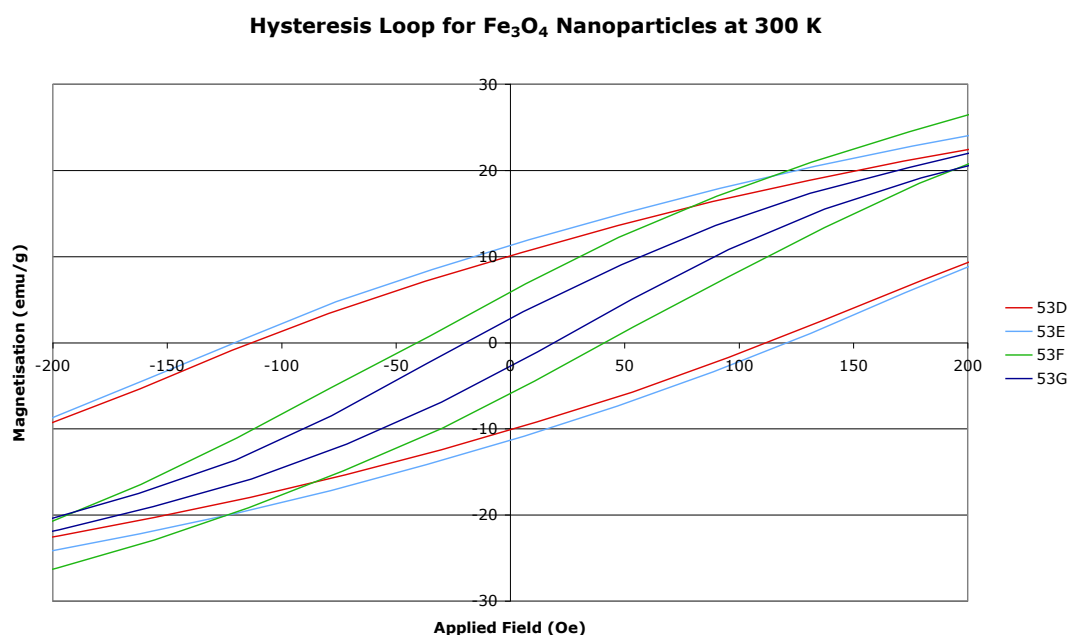


Figure 3.8. Enlarged section of hysteresis loops for Fe₃O₄ nanoparticles synthesised with different precursor concentrations.

Saturation magnetisation values for these materials are in the range of 62-70 emu g⁻¹ and such values are comparable to those in the literature¹⁶⁰⁻¹⁶² on nanoscale Fe₃O₄ of approximately 45 to 67 emu g⁻¹. The value is somewhat smaller than that of bulk magnetite (82 emu g⁻¹)⁹, however.

The specific saturation magnetisation of a material is independent of particle size, but dependent on temperature. Fluctuations in the temperature of the laboratory and of the instrument itself, coupled with the lack of sensitivity of the instrument compared to the SQUID magnetometer, account for the small variations in saturation magnetisation values recorded here.

Lowering the concentration of Fe²⁺ in the precursor solution results in the formation of smaller particles, and changes the coercive field accordingly. Particle sizes calculated using the Debye-Scherrer approximation for XRD are average particle sizes, hence a smaller average particle size means a larger number of particles will fall in the superparamagnetic range (for magnetite < 30 nm), and as a consequence, the coercive field is lowered (see Table 3.5).

Coercive fields at 300 K for these materials are very low ($H_c = \sim 20\text{-}120$ Oe). A coercive field as low as this is ideal for application in electromagnetic shielding. The materials also possess small remnant fields of $\sim 3\text{-}11$ emu g^{-1} at 300 K.

These magnetic properties are summarised in Table 3.5.

Sample	Solution conc. (%)	Average particle size (nm)	Saturation magnetisation (emu g^{-1})	Coercive field (Oe)	Remnant Magnetisation (emu g^{-1})
53D	3.00	26	62	122	11
53E	0.60	24	62	112	10
53F	0.05	15	70	42	6
53G	0.025	12	63	19	3

Table 3.5. Summary of magnetic properties of Fe_3O_4 nanoparticles.

Fe_3O_4 nanoparticles synthesised by the methods outlined in section 2.2.2 show similar saturation magnetisation values. A comparison can be seen in Figure 3.9. Both have saturation magnetisation values of approximately 62 emu g^{-1} .

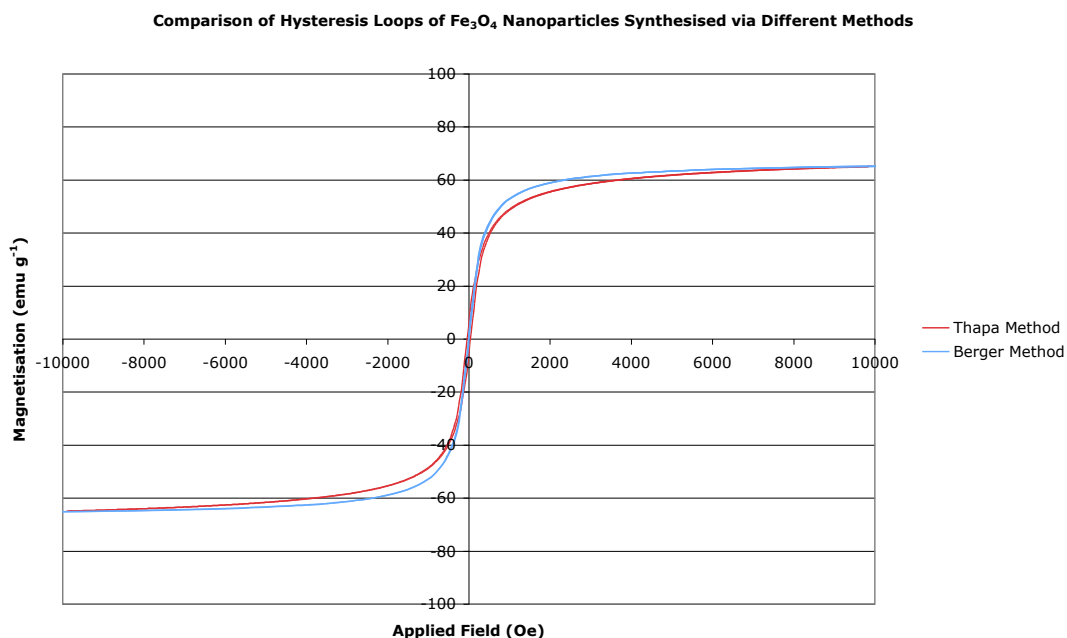


Figure 3.9. Hysteresis loops for Fe_3O_4 nanoparticles synthesised via different methods.

SQUID Magnetometry allowed the investigation of magnetic properties down to temperatures as low as 5 K. Examining magnetic properties of a material at such low temperatures gives information about its fundamental magnetic properties. Hysteresis loops of Fe_3O_4 at 10 K and 300 K are shown in Figure 3.10 and 3.11.

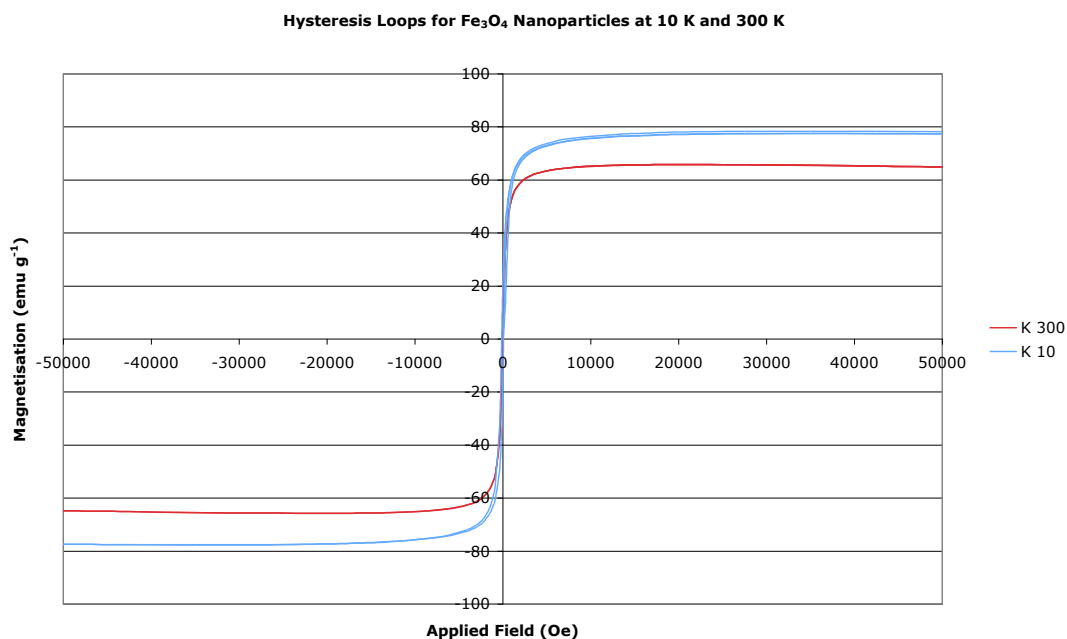


Figure 3.10. Hysteresis loops at 10 K and 300 K for Fe_3O_4 nanoparticles.

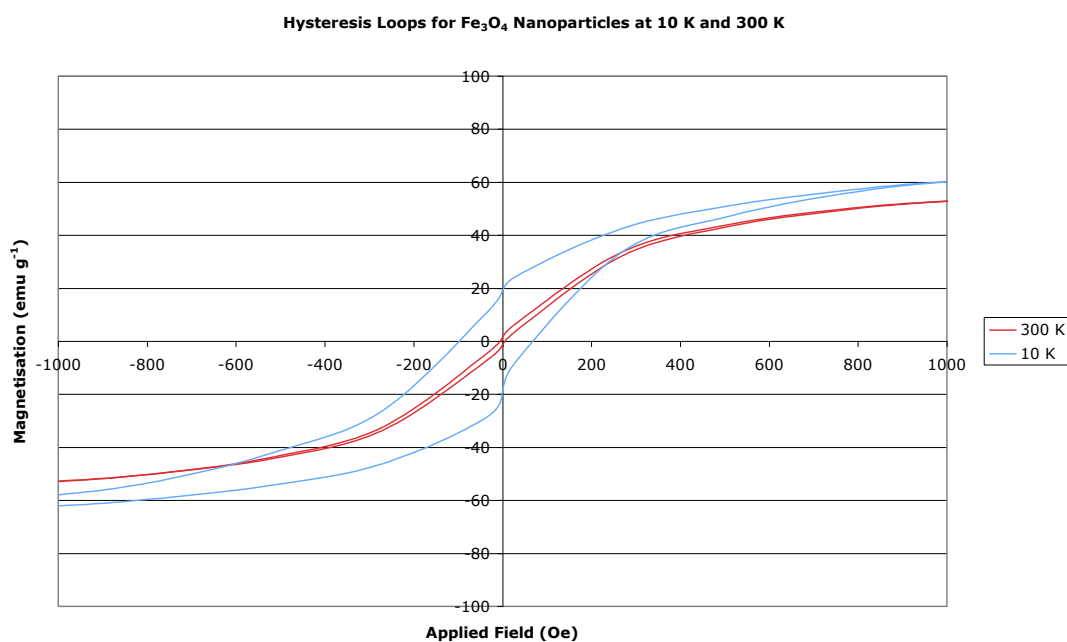


Figure 3.11. Enlarged section of hysteresis loops at 10 K and 300 K for Fe_3O_4 nanoparticles.

The hysteresis loops show that the material is fundamentally ferrimagnetic (1.3.5) in nature, although very weakly. At 10 K, the material has a larger saturation magnetisation value of approximately 80 emu g^{-1} . This is expected, as a larger magnetisation is needed to align the magnetic moments of the material due to reduced thermal motion.

The material also has a larger coercive field at 10 K than at 300 K as can be seen from Figure 3.11. This is because at lower temperatures a larger reverse field is needed to bring the magnetic moment of the material back to zero.

Pinus radiata Kraft fibres were coated with Fe_3O_4 and CoFe_2O_4 nanoparticles by the methods outlined in 2.2.4 and 2.2.5.

Hysteresis loops of Fe_3O_4 coated Kraft fibres were measured on an AGM at 300 K, and are shown in Figure 3.12.

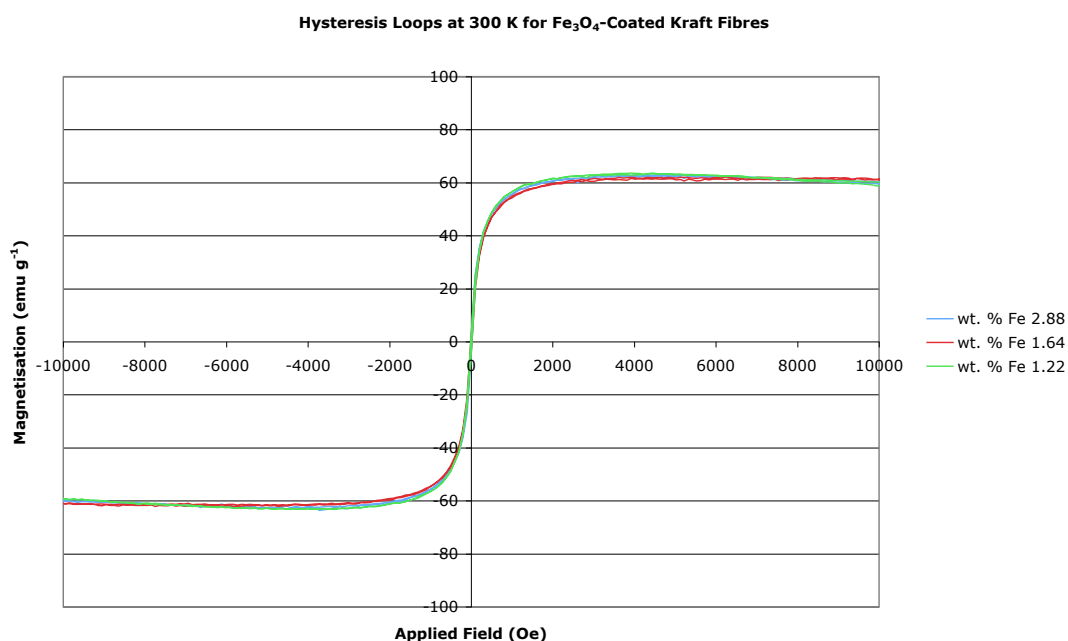


Figure 3.12. Hysteresis loops at 300 K for Fe_3O_4 -coated Kraft fibres (cellulose).

The materials all show a similar saturation magnetisation which is expected as the magnetite used in their synthesis is produced via the same method. Of note

is that on bonding to the cellulose fibres, the magnetic properties of the nanoparticles are not altered in any way.

This indicates that the particles are surface bound, through hydrogen bonding (1.2) between the surface hydroxyl groups of the cellulose and the oxygen present in the magnetite nanoparticles, and that the chemical bonding between the two components does not alter the chemistry or the inverse spinel bulk structure that gives rise to the ferrimagnetic character (1.3.5) of the magnetite nanoparticles.

CoFe_2O_4 nanoparticles were also used to coat Kraft fibres. The hysteresis loop of CoFe_2O_4 nanoparticles, taken at 300 K on a SQUID, is shown in Figure 3.13 and 3.14. As the Kim *et. al.*¹⁴ predicted, particles synthesised at 80 °C are ferrimagnetic in character. Synthesised particles have a remnant field of 7 emu g^{-1} , a coercivity of 78 Oe and a saturation magnetisation of 60 emu g^{-1} - values that are in concordance to those obtained by the authors. The saturation magnetisation is also close to that of bulk CoFe_2O_4 (70 emu g^{-1})¹⁴.

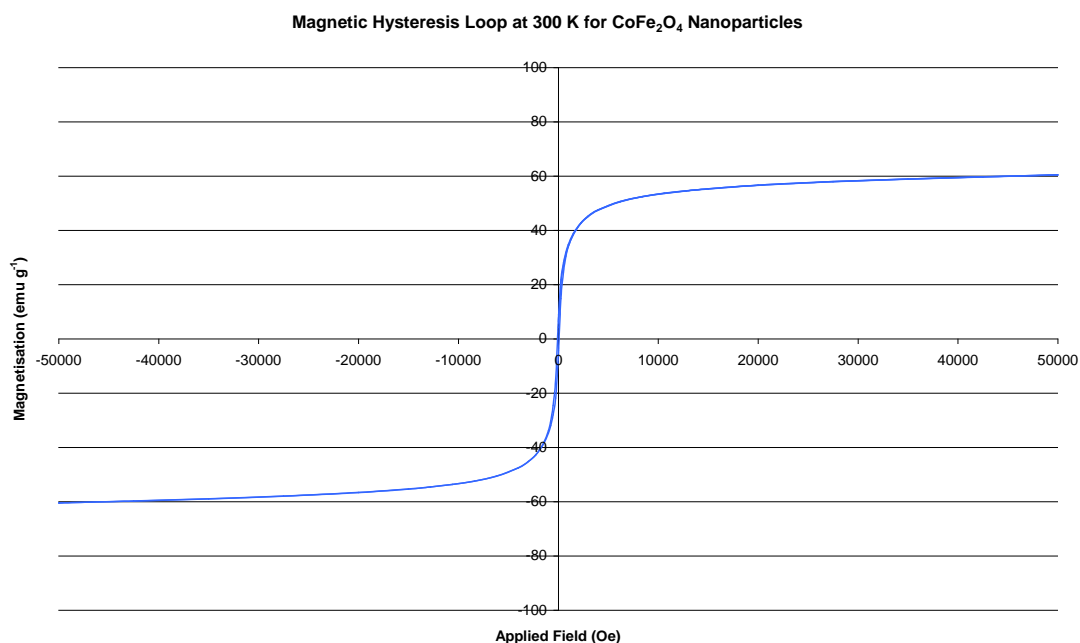


Figure 3.13. Hysteresis loop for CoFe_2O_4 nanoparticles.

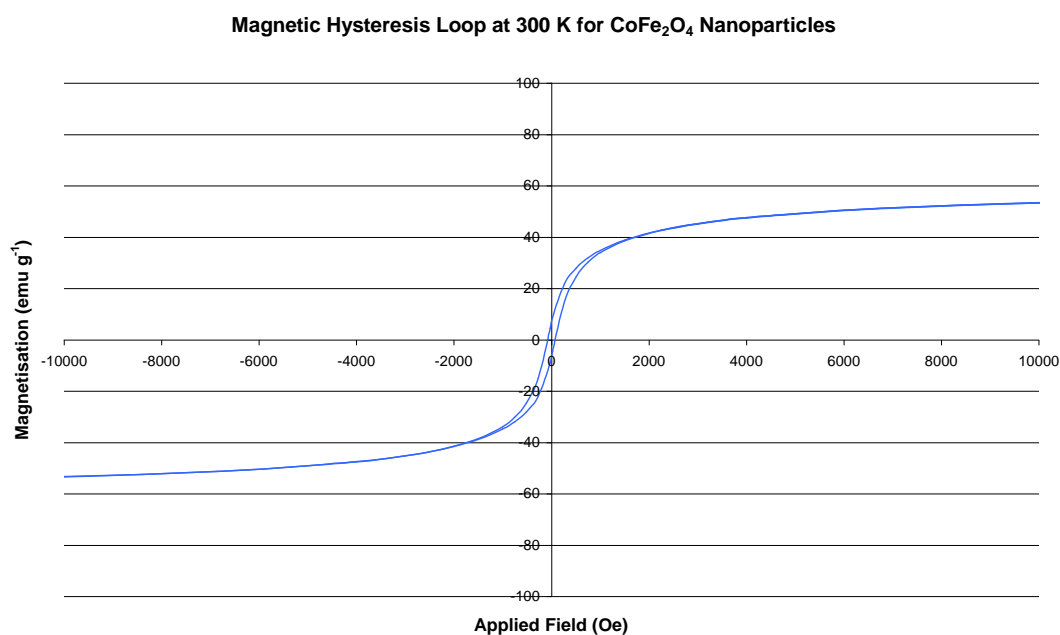


Figure 3.14. Enlarged section of hysteresis loop for CoFe₂O₄ nanoparticles showing ferromagnetic character.

The hysteresis loop of CoFe₂O₄-coated Kraft fibres was measured on a VSM, and is shown in Figure 3.15.

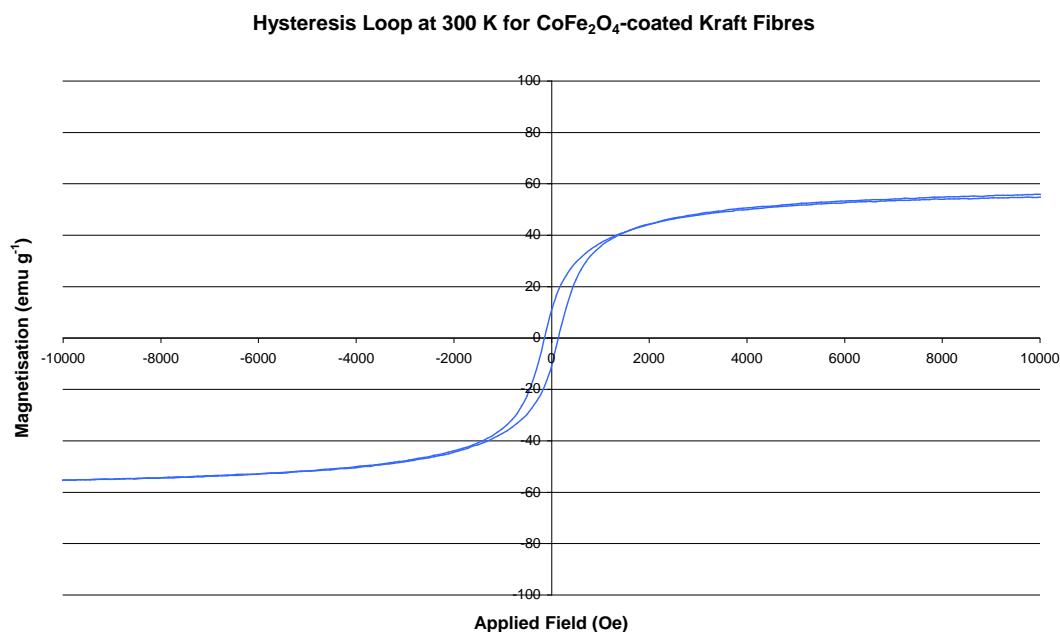


Figure 3.15. Hysteresis loop for CoFe₂O₄-coated Kraft fibres (cellulose).

On comparison of Figures 3.14 and 3.15 it is again evident that the magnetic properties of the nanoparticles are unaffected on bonding to the cellulose fibre, as they remain similar to those obtained for the nanoparticles themselves. This indicates that surface bonding of the nanoparticles to the cellulose fibres does not affect the bulk structure, and hence, the magnetic properties of the nanoparticles.

The magnetic properties of the cobalt ferrite nanoparticles, like their magnetite counterparts, arise from the bulk structure of the material, in this case an inverse spinel structure giving rise to a ferrimagnetic character (1.3.5). This bulk structure is unaffected on bonding to the cellulose fibre surface, and the bonding between the cobalt ferrite nanoparticles and the cellulose fibre surface occurs at the surface of the nanoparticles, presumably through hydrogen bonding (1.2) between the surface hydroxyl groups of the cellulose fibres and the oxygen in the cobalt ferrite nanoparticles.

Polypyrrole and magnetite-coated Kraft fibres (magnetite over polypyrrole) were synthesised by the method outlined in 2.2.6.

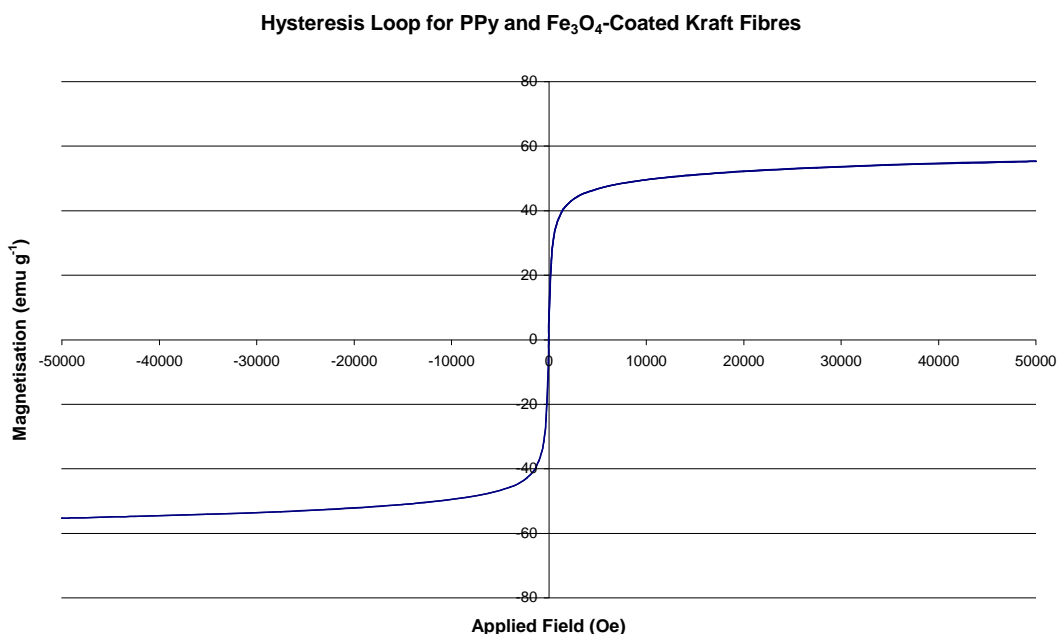


Table 3.16. Hysteresis loop for Polypyrrole and Fe_3O_4 -coated Kraft fibres(magnetite over polypyrrole).

The Fe_3O_4 nanoparticles are surface bound to the polypyrrole-coated fibres and the hysteresis loop (Figure 3.16) measured for such a material indicates that the presence of polypyrrole on the fibres does not affect the magnetic properties of Fe_3O_4 coating. The saturation magnetisation (61 emu g^{-1}), coercive field (6 Oe), and remnant magnetisation (2 emu g^{-1}) values are similar to those of their ‘magnetite only’ counterparts discussed previously.

A summary of the magnetic properties of the synthesised nanoparticles and hybrid materials can be seen in Table 3.6.

Material	Saturation magnetisation (emu g^{-1})	Coercive field (Oe)	Remnant Magnetisation (emu g^{-1})
Fe_3O_4 nanoparticles	62	19-112	3-11 (see Table 3.4)
Fe_3O_4 -coated Kraft Fibres	62	20	3
PPy+ Fe_3O_4 -coated Kraft Fibres	61	6	2
CoFe_2O_4 nanoparticles	61	80	7
CoFe_2O_4 -coated Kraft Fibres	56	140	10

Table 3.6. Summary of magnetic properties of synthesised materials.

3.4. Scanning Electron Microscopy (SEM)

Optical microscope images (Figure 3.17) at 90x magnification show that the coated fibres (right) retain the same morphology as the precursor Kraft fibres (left). The brown colour of the fibres (a change from the original white) indicates they are coated with the Fe_3O_4 nanoparticles. This is confirmed on examining the low magnification SEM image of coated Fe_3O_4 -coated Kraft fibres (Figure 3.18).

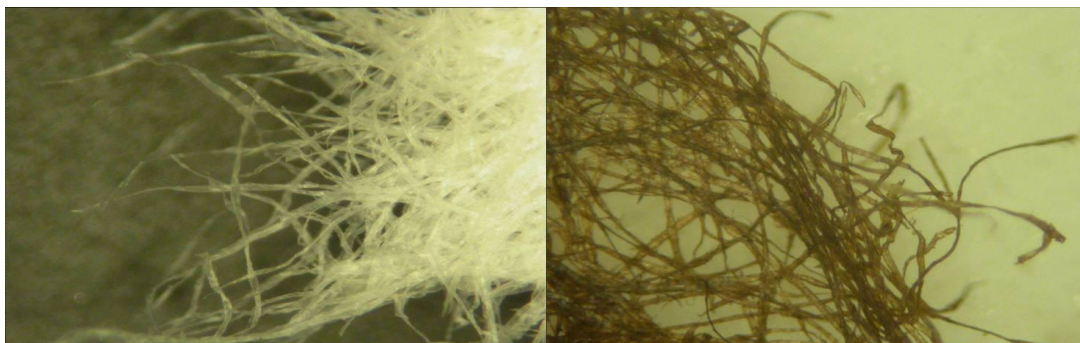


Figure 3.17. Optical microscope images (90x magnification) of uncoated cellulose fibres (left) and Fe₃O₄ coated Kraft fibres (right).

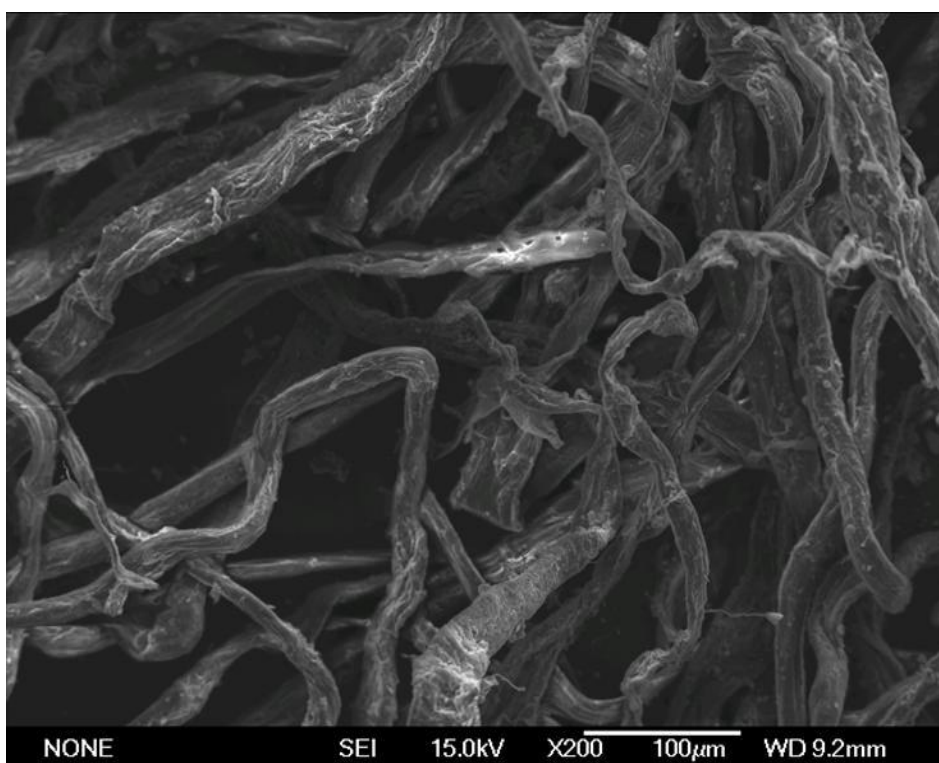


Figure 3.18. Low magnification image of Fe₃O₄-coated Kraft fibres.



Figure 3.19. Magnetic Kraft fibres being picked up by a 'hand held' NdFeB permanent magnet.

The photographs in Figure 3.19 show the magnetic nature of the coated fibres. Due to the magnetic coating, they are able to be picked up by a simple hand held magnet, in this case a NdFeB permanent magnet.

The SEM images in Figures 3.20-3.24 show the completeness of the coating. The Fe_3O_4 nanoparticles completely encapsulate the fibre and follow its morphology. Even individual fibrils are coated with Fe_3O_4 nanoparticles (Figures 3.20 and 3.21), similar to previous research involving cellulose fibres coated with conducting polymers¹⁰⁸.

The coating appears to be integral, and several nanoparticles thick. In places cracks appear in the coating and are due to the fibre swelling under the high energy of the electron beam during examination by SEM.

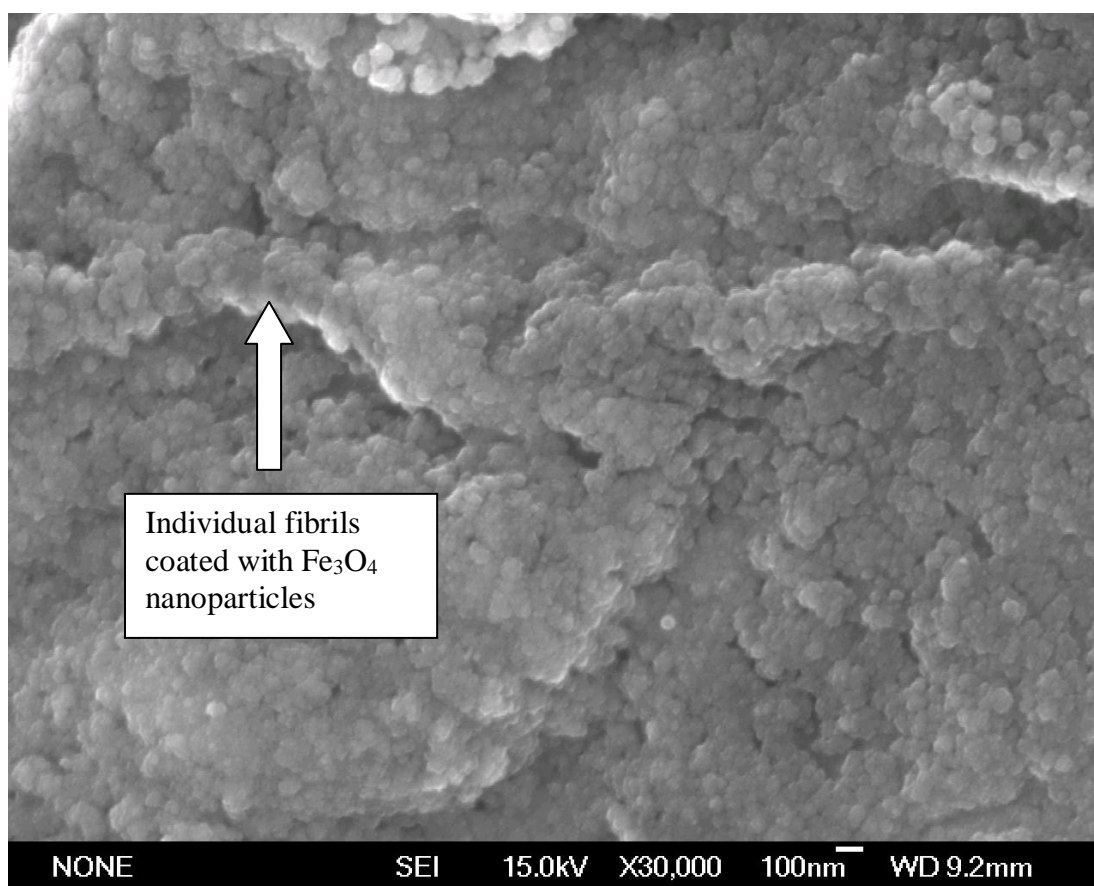


Figure 3.20. High magnification SEM image of Fe_3O_4 -coated cellulose fibres showing coating of individual fibrils.

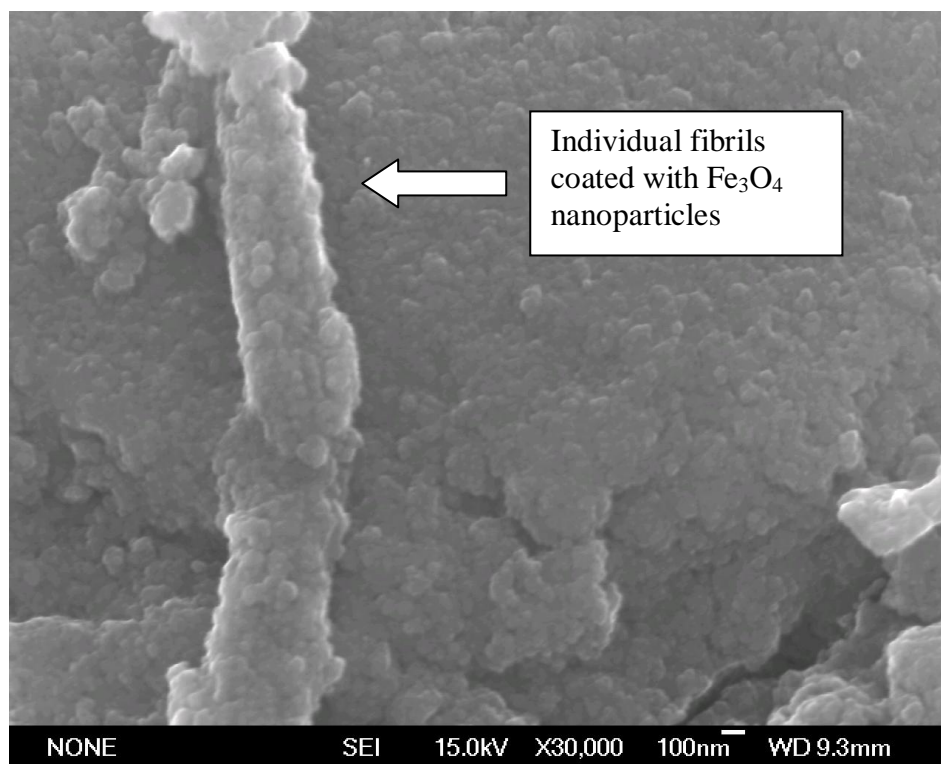


Figure 3.21. High magnification SEM image of Fe_3O_4 -coated cellulose fibres showing coating of individual fibrils.

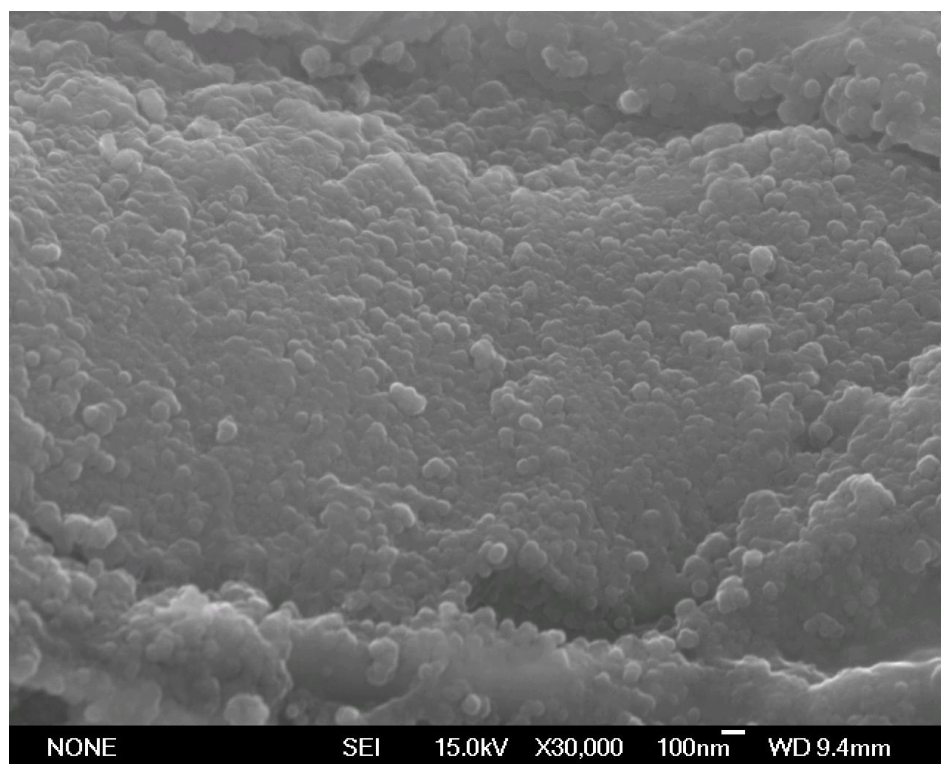


Figure 3.22. High magnification SEM image of Fe_3O_4 -coated cellulose fibres.

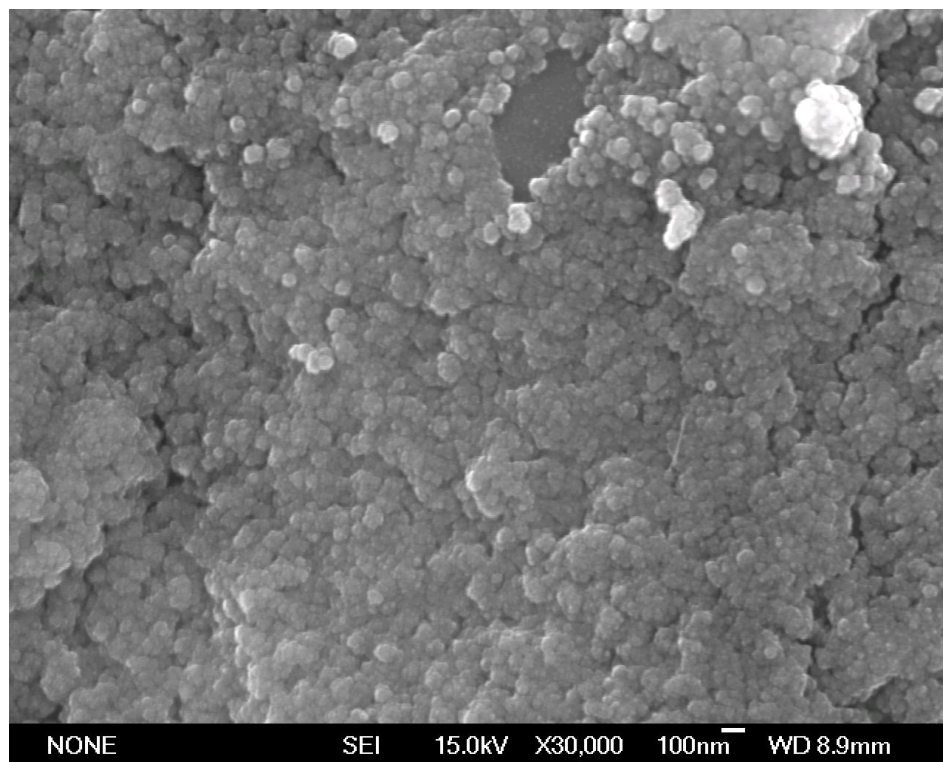


Figure 3.23. High magnification SEM image of Fe₃O₄-coated cellulose fibres.

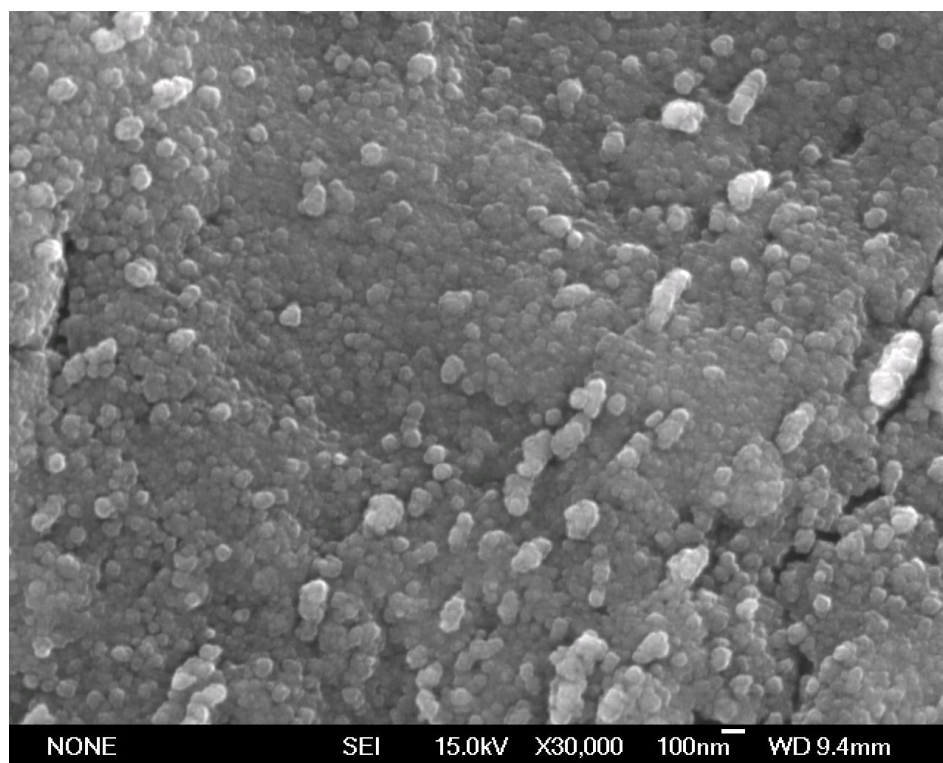


Figure 3.24. High magnification SEM image of Fe₃O₄-coated cellulose fibres.

Nanoparticles are present on the surface of the cellulose fibres in agglomerations of ~ 100 nm, as no surfactant was used in the synthesis procedure in order to simplify the synthesis. A particle size of this nature differs from the particle size calculated using the Debye-Scherrer approximation, where the individual crystallite size was calculated as being between 12-26 nm.

A surfactant would usually act to stabilize nanoparticles either by electrostatic or steric forces, as described in section 1.5. The lack of a surfactant leads to agglomeration, which is clear in this case.

The discrepancy between the viewed particle size and the calculated particle size arises from the lack of crystallographic alignment of the individual nanoparticles lattices, and whether or not a surfactant is used is irrelevant, however.

The completeness of the coating can also be seen from the EDS maps for Fe (Figure 3.25), which shows full coverage of the fibre surface.

An interesting point to note is that while Fe_3O_4 coverage is fairly uniform, as seen in the previously shown SEM images, EDS elemental maps for Fe show that areas exist where there is a higher concentration of Fe present. Such areas are typically 'valleys' or 'crevasses' on the fibre surface where there are thicker coatings of Fe_3O_4 present. One explanation for this is that such areas as a result of their larger surface area, will have associated with them a higher surface energy, which in turn attracts a larger number of nanoparticles.

EDS elemental maps showing a cross-sectional view of a Fe_3O_4 -coated Kraft fibre are shown in Figure 3.26. O is present right through the fibre due to the O in cellulose, however, Fe is absent from the centre (lumen) of the fibre. This shows that the coating is present only on the surface of the fibres and has not penetrated into the lumen of the fibre - contrary to the results reported by Zakaria, *et al.*^{163, 164}.

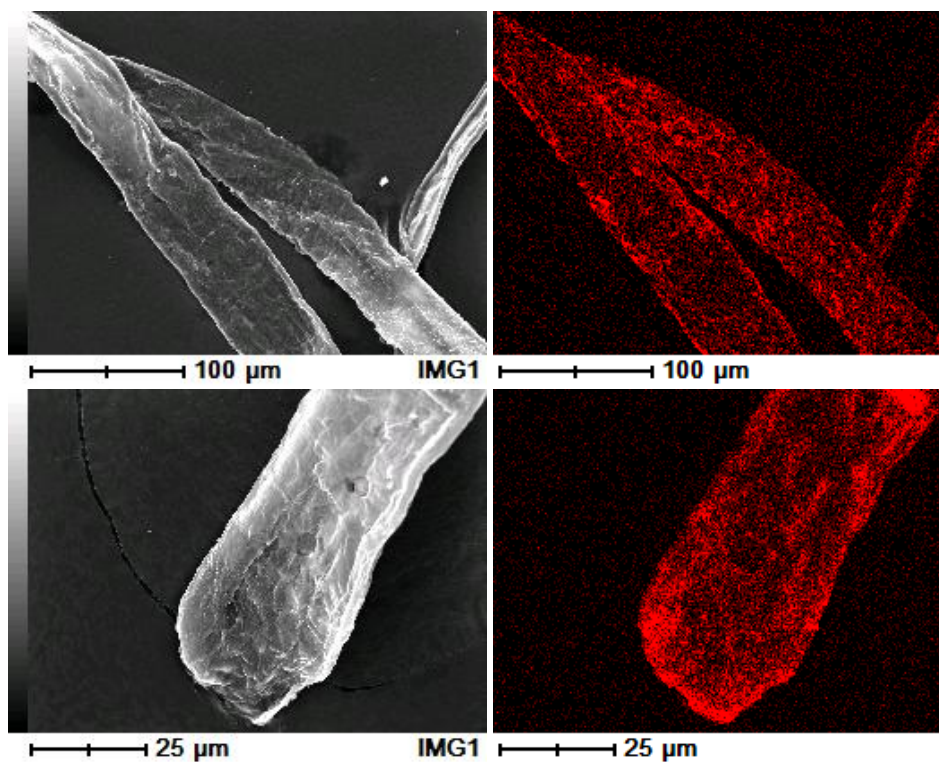


Figure 3.25. EDS maps of Fe_3O_4 coated cellulose fibres, complementary SEI images (left) and elemental Fe maps (right).

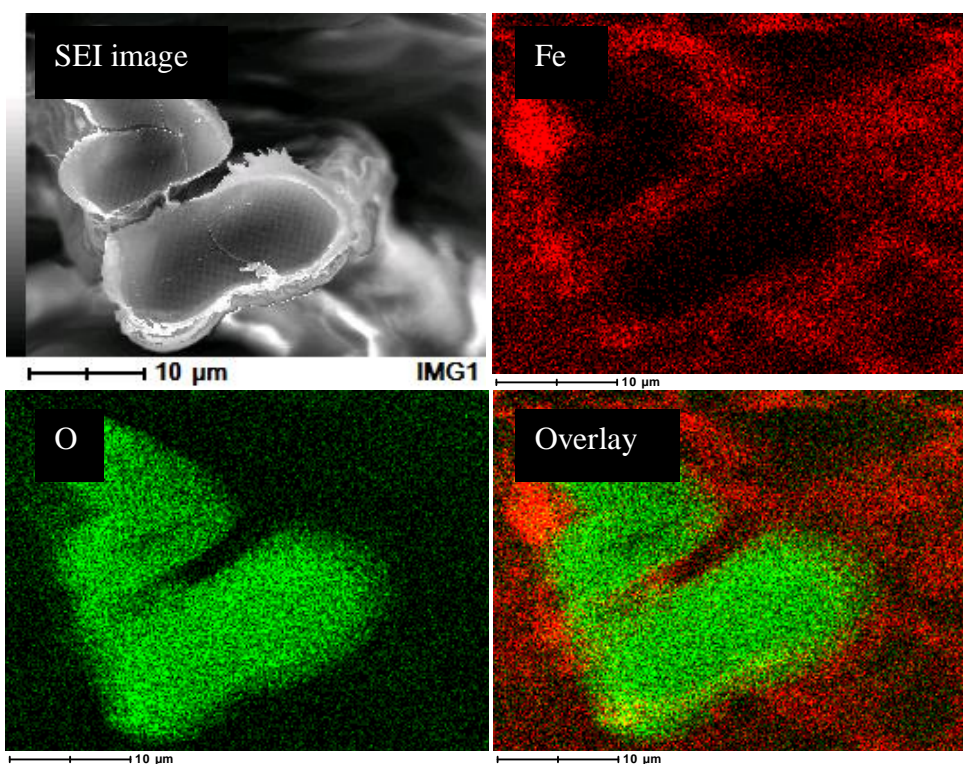


Figure 3.26. EDS elemental maps showing a cross-sectional view of a Fe_3O_4 -coated Kraft fibre. SEI image (top left), Fe (red), O (green), overlay (bottom right).

The EDS spectrum shown in Figure 3.27 and Figure 3.28 shows that Fe is present, as indicated by the presence of the Fe K α peak at 6.398 keV, the Fe K β peak at 7.057 keV and the Fe L α peak at 0.705 keV^{165, 166}. Oxygen K α peaks are also present and arise from oxygen in Fe₃O₄ and the cellulose fibre.

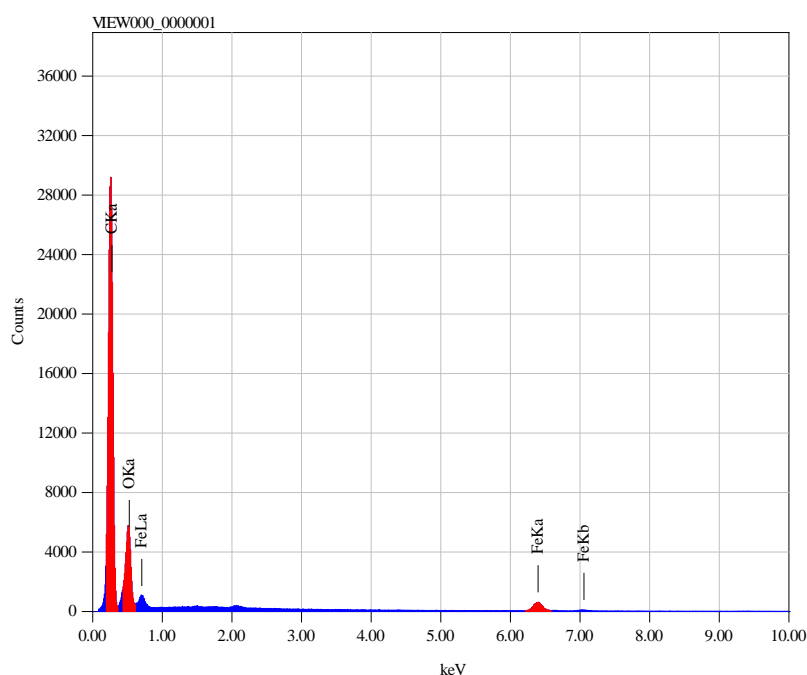


Figure 3.27. EDS spectrum for Fe₃O₄-coated Kraft fibres.

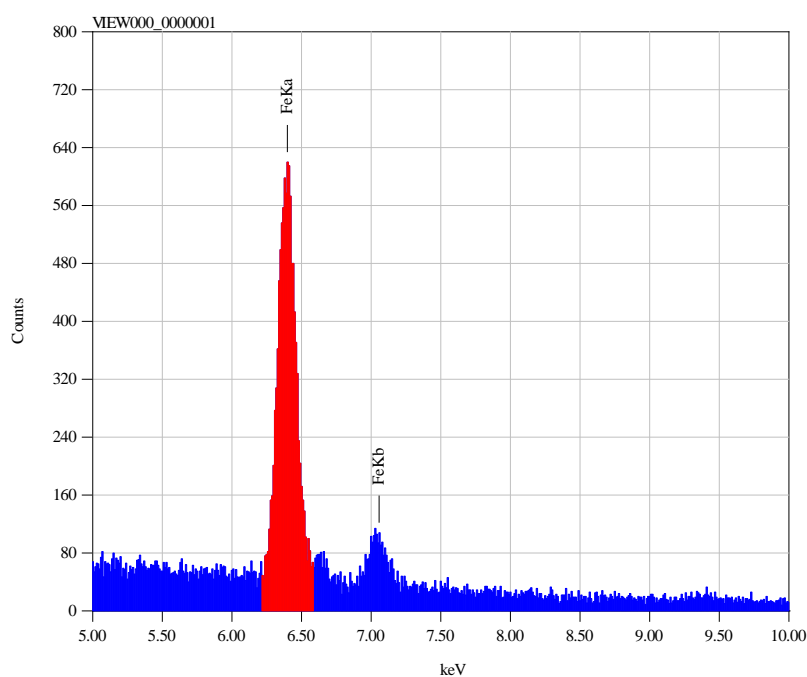


Figure 3.28. Enlarged view of EDS spectrum for Fe₃O₄-coated Kraft fibres.

3.5. X-ray Photoelectron Spectroscopy (XPS)

The C 1s XPS spectrum of Kraft fibres is similar to that of wood, published in the literature^{165, 166}. The peaks in the spectrum (Figure 3.29) can be assigned to the various carbon species present in the cellulose fibre (Figure 3.30), such as C-C, C-OH, O-C-O and also any carbonyl species present in extractives (Figure 1.3) from the pulping process.

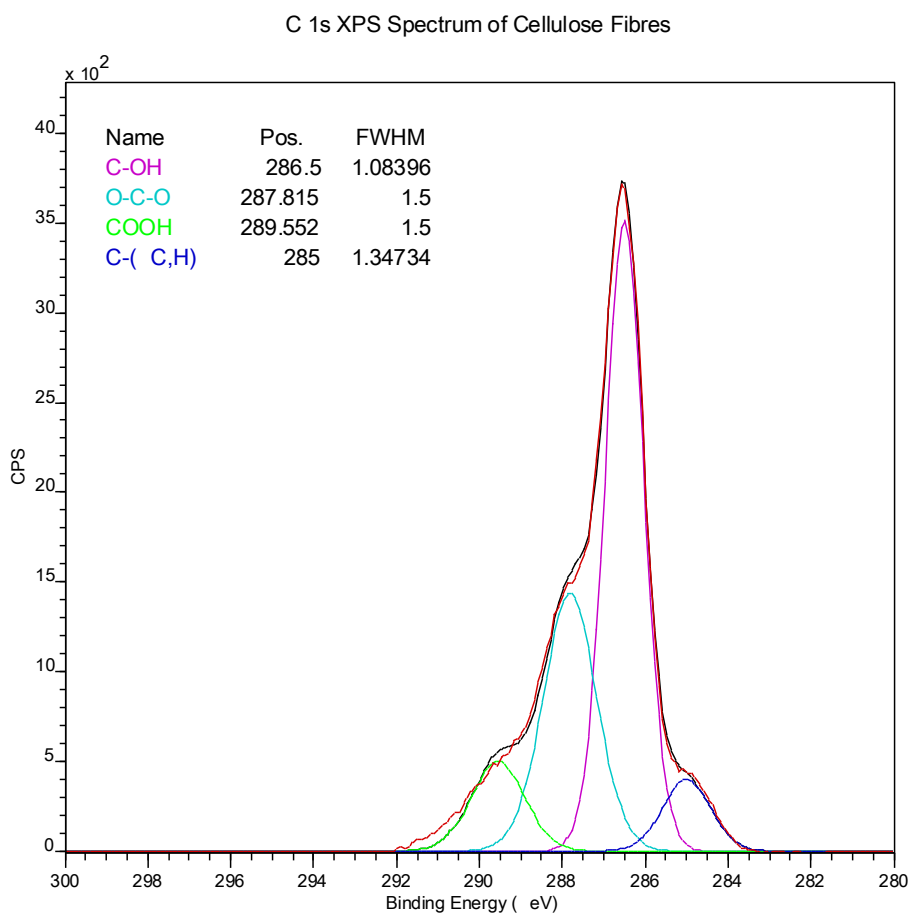


Figure 3.29. C 1s XPS spectrum of Kraft fibres (cellulose).

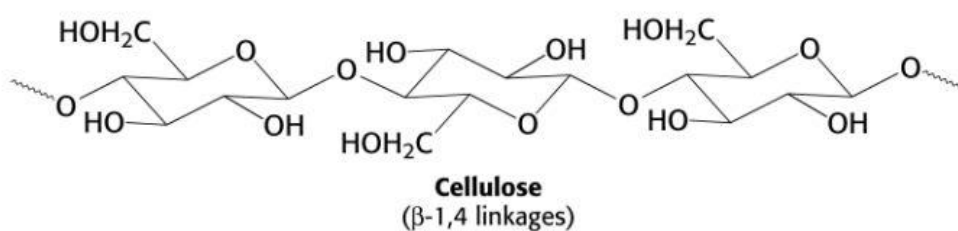


Figure 3.30. Structure of cellulose ($C_6H_{10}O_5$)_n.

The C 1s XPS spectrum of Fe₃O₄-coated Kraft fibres is shown in Figure 3.31. The line shape of this spectrum is similar to that of uncoated cellulose, as expected seeing as cellulose is the substrate, although the C-(C,H) 1s peak is larger. As no additional carbon was added in the synthesis, this increase is most likely due to the presence of grease from handling, or from oil vapour from the vacuum grease. The entire spectrum has shifted slightly also - up to 0.5 eV for the COOH assignment, 0.3 eV for the O-C-O assignment, and the C-OH assignment slightly less at approximately 0.2 eV.

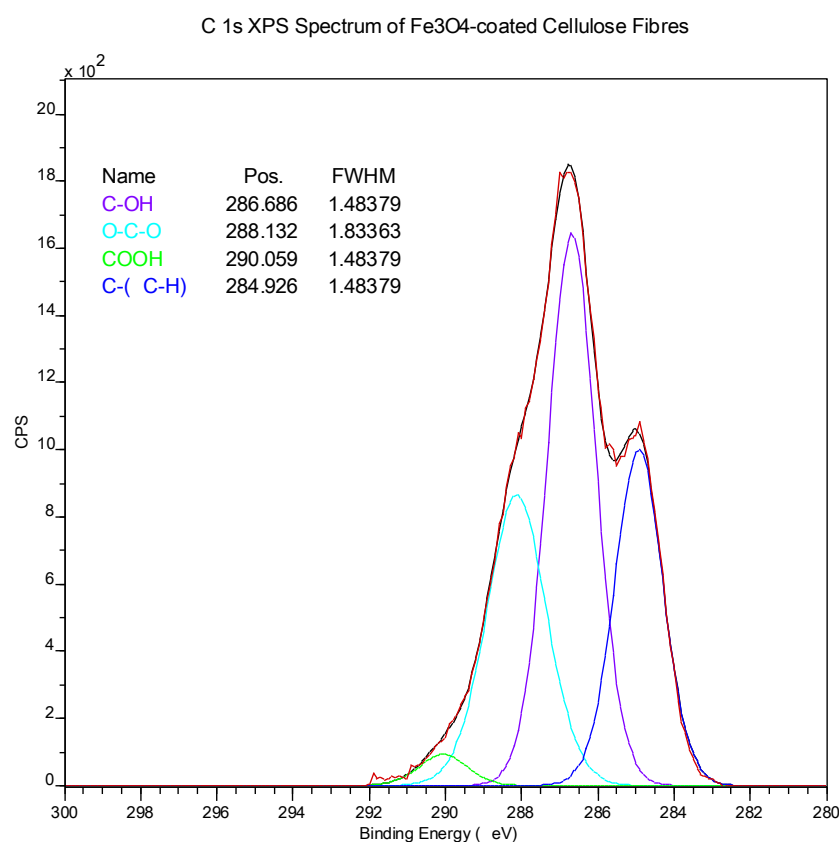


Figure 3.31. C 1s XPS spectrum for Fe₃O₄-coated Kraft fibres (cellulose).

The Fe 2p XPS spectrum of Fe₃O₄ nanoparticles (Figure 3.32) shows the Fe₃O₄ and α -FeOOH phases to be present¹⁶⁷⁻¹⁶⁹, consistent with XRD results and literature reports^{170, 171}. Here the two peaks (due to the 1/2 and 3/2 spin multiplicities) can be attributed to the presence of Fe₃O₄ (723.988 eV and 710.466 eV) and α -FeOOH (726.554 eV and 712.829 eV), confirming the presence of Fe₃O₄ nanoparticles on the surface of the fibre.

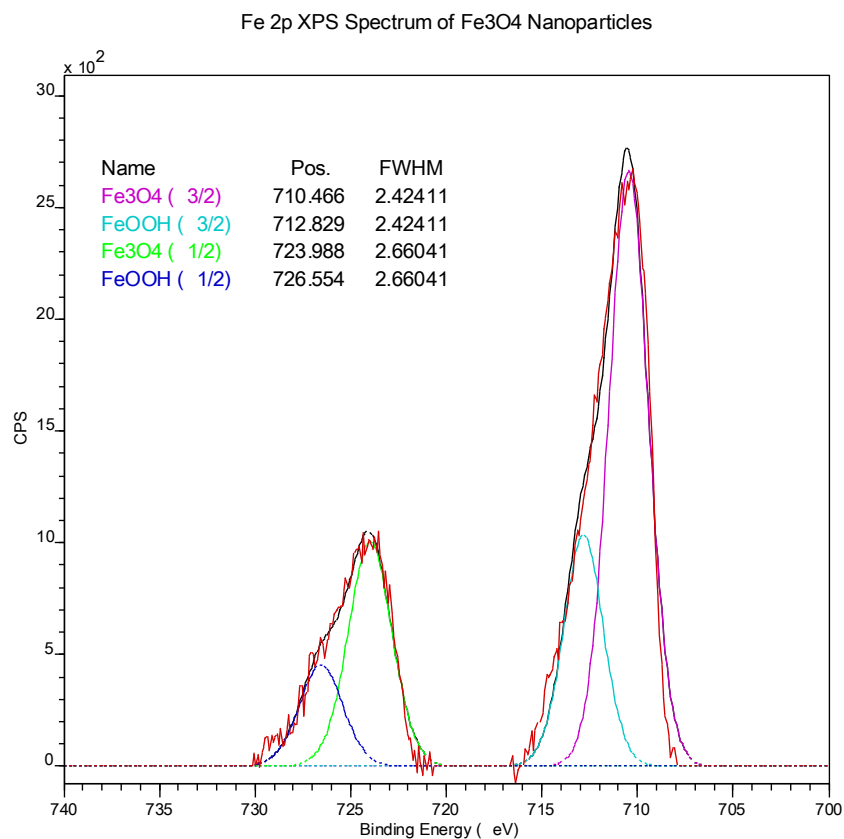


Figure 3.32. Fe 2p XPS spectrum of Fe₃O₄ nanoparticles.

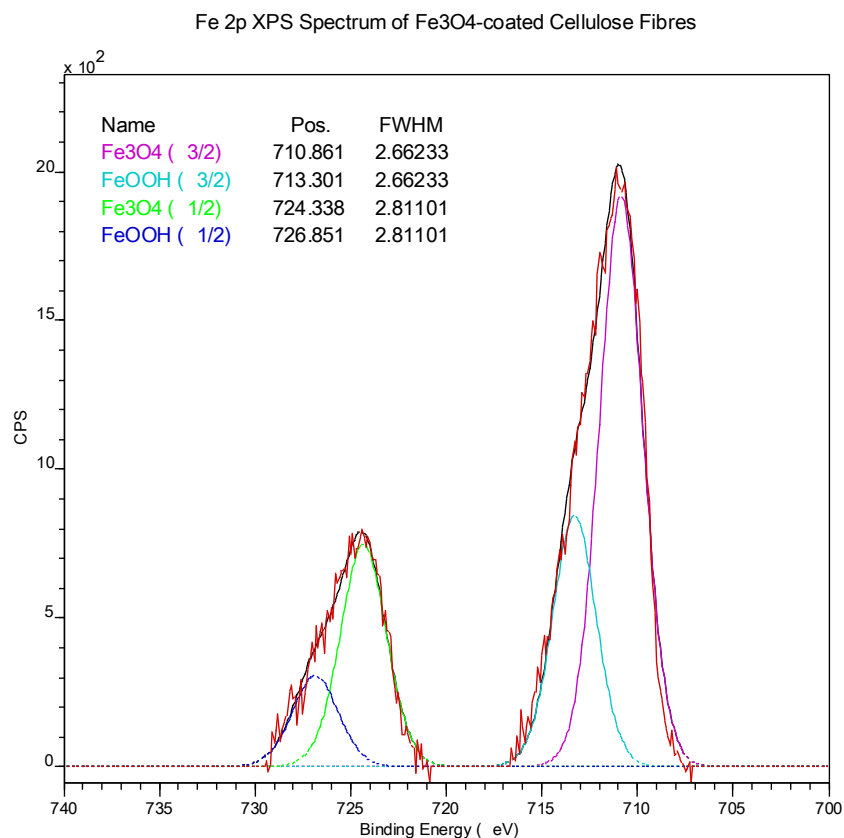


Figure 3.33. Fe 2p XPS spectrum of Fe₃O₄-coated Kraft fibres (cellulose).

The Fe 2p XPS spectrum of Fe₃O₄-coated Kraft fibres is shown in Figure 3.33. The spectrum retains the same line shape as its Fe₃O₄ nanoparticle precursor, only that in this case, there is a difference in the binding energies of the respective peaks.

A comparison between the Fe 2p XPS spectrum of Fe₃O₄ coated Kraft fibres (cellulose) and Fe₃O₄ nanoparticles (Figure 3.34 and 3.35) shows a shift towards lower binding energy of approximately 0.3 – 0.47 eV for both the 1/2 and 3/2 spin multiplicities of the coated samples. This is similar to the shifts in Ti 2p binding energies, of approximately 0.5 eV, for TiO₂-coated cellulose¹⁷².

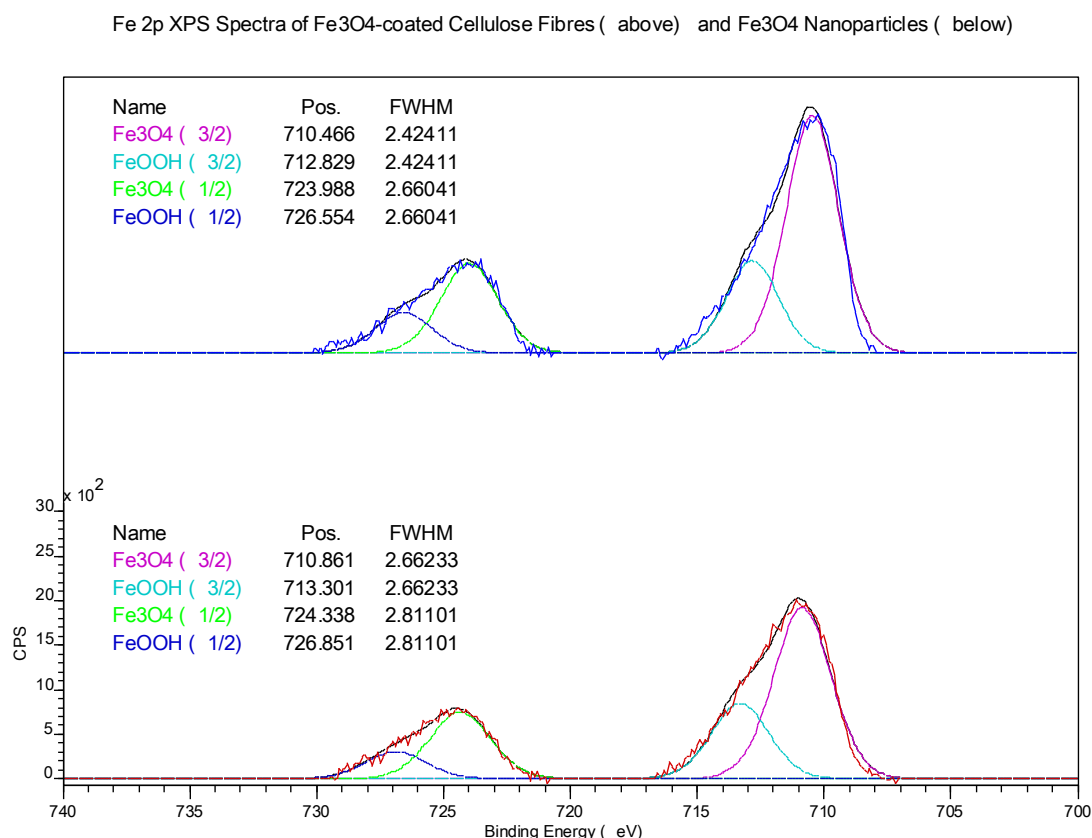


Figure 3.34. Offset Fe 2p XPS spectra of Fe₃O₄ nanoparticles and Fe₃O₄-coated Kraft fibres (cellulose), showing their peak positions and FWHM values.

This shift confirms that there is chemical bonding between the Fe₃O₄ nanoparticles and the cellulose fibre surface, presumably through hydrogen bonding (1.2) between the O in the Fe₃O₄ and α -FeOOH nanoparticles and the H of the OH groups present in cellulose.

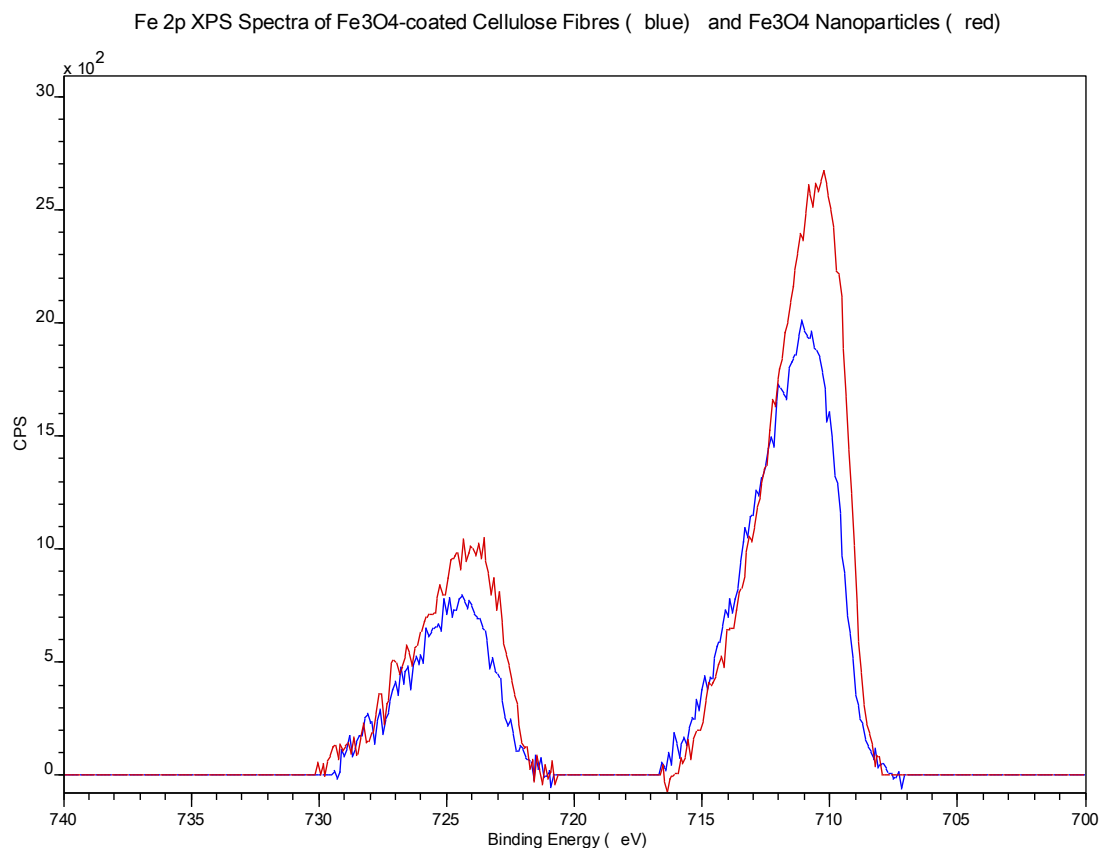


Figure 3.35. Overlaid Fe 2p XPS spectra of Fe₃O₄ nanoparticles and Fe₃O₄-coated Kraft fibres (cellulose).

The shape of the Fe 2p XPS spectrum of Fe₃O₄-coated cellulose fibres does not change compared to that of the Fe₃O₄ nanoparticles by themselves. This indicates that the chemical bonding between the Fe₃O₄ nanoparticles and the cellulose fibre does not alter the bulk structure and chemistry of the nanoparticles.

The O 1s XPS spectra of cellulose fibres, Fe₃O₄ nanoparticles, and Fe₃O₄-coated cellulose fibres is shown in Figure 3.36. The peaks can be assigned to the various oxygen containing species in cellulose (C-OH, C-O-C and COOH)¹⁷³, and Fe₃O₄ (Fe₃O₄, γ -Fe₂O₃ and α -FeOOH)¹⁶⁷. A shift in the entire spectra is seen – further indication that bonding is taking place between the magnetite nanoparticles and the fibre surface. The shift is similar to that of approximately 1.5 eV, seen in TiO₂-coated cellulose fibres¹⁷².

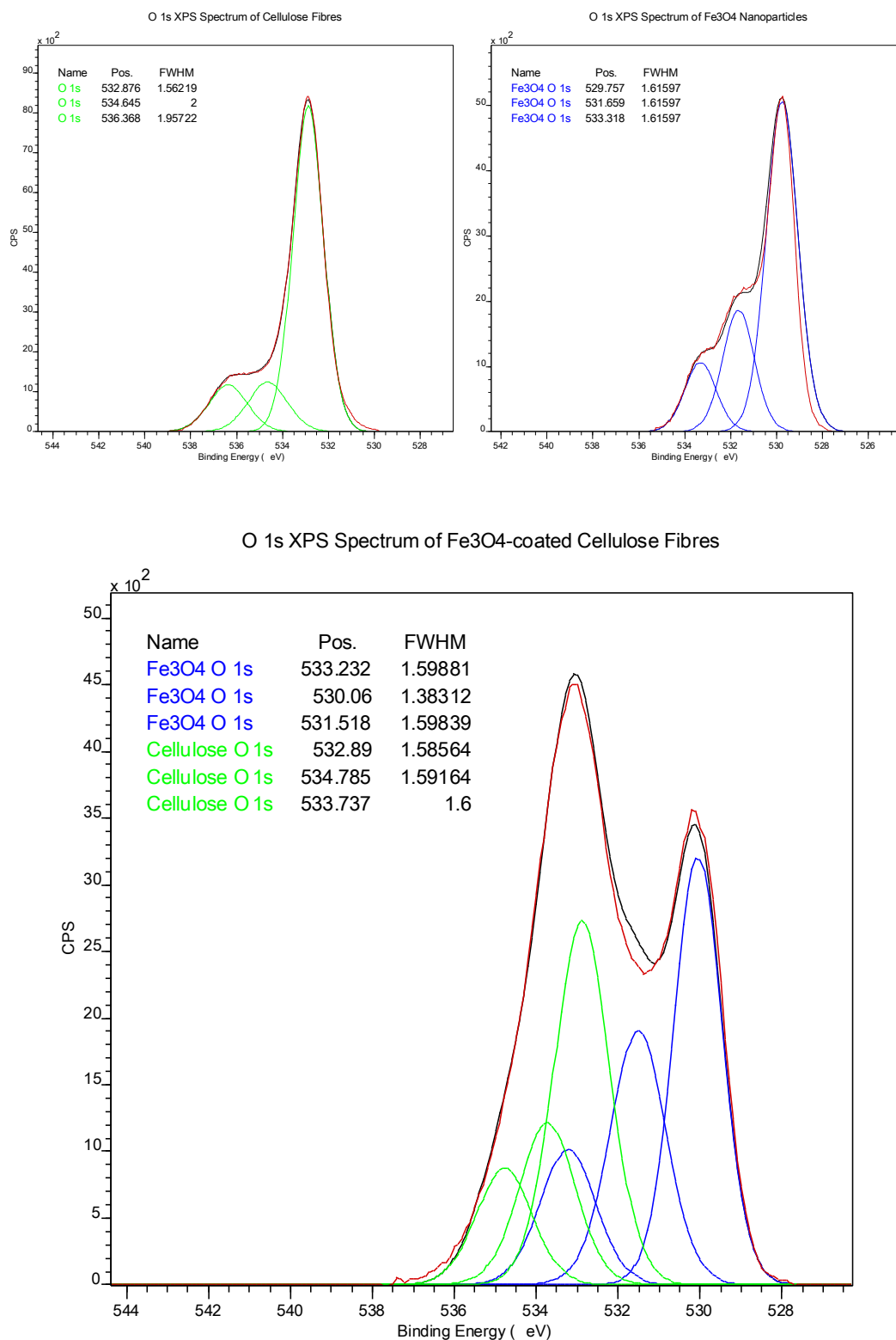


Figure 3.36. O 1s XPS spectra for cellulose fibres, Fe₃O₄ nanoparticles, and Fe₃O₄-coated cellulose fibres.

Table 3.7 summarizes the binding energies and shifts of these materials. The shifts are lower than those of other hybrid materials synthesised in this work, in

particular, doped ZnS-coated Kraft fibres, where a shift of up to 0.86 eV was observed (chapter 4.5).

	Fe₃O₄ nanoparticles	Fe₃O₄-coated cellulose fibres	
Species Present	Binding Energy (eV)	Binding Energy (eV)	Shift (eV)
Fe ₃ O ₄ (1/2)	723.988	724.338	0.35
Fe ₃ O ₄ (3/2)	710.466	710.861	0.395
α -FeOOH (1/2)	726.554	726.851	0.297
α -FeOOH (3/2)	712.829	713.301	0.472

Table 3.7. Summary of Fe 2p XPS binding energies and shifts for Fe₃O₄ nanoparticles and Fe₃O₄-coated cellulose fibres.

Even after repeated washing and sonication steps, the particles remain bound to the surface. This is contrary to other reports in the literature which state that particles on the fibre surface are removed in the washing step^{45, 46, 162, 174}.

3.6. Chapter Summary

Magnetic and cobalt ferrite nanoparticles were synthesised and characterised by a number of methods, including AGM, SQUID Magnetometry, VSM, XRD, XRF and XPS. The nanoparticles were present in the spinel structure and had a particle size of approximately 12-26 nm for magnetite and approximately 80 nm for cobalt ferrite.

The magnetic properties of the two materials were comparable to those in the literature. Magnetite nanoparticles were ferrimagnetic in character and had a saturation magnetisation of approximately 60 emu g⁻¹, a coercive field of 19-122 Oe, and a remnant magnetisation of 3-11 emu g⁻¹. Cobalt ferrite nanoparticles had a saturation magnetisation of approximately 61 emu g⁻¹, a coercive field of 80 Oe, and a remnant magnetisation of 7 emu g⁻¹.

Magnetite, with a particle size of 12 nm, was chosen to coat Kraft fibres due to its lower coercive field – ideal for EMI shielding applications. Kraft fibres coated

with magnetite nanoparticles are completely encapsulated by the magnetite nanoparticles, present on the surface in agglomerations approximately 100 nm in size.

The magnetite is bound to the surface of the cellulose fibre by hydrogen bonding. XPS analysis suggests bonding is taking place between the two components, indicated by shifts in the binding energy of Fe 2*p* electrons of up to 0.47 eV. The magnetic and structural properties of the magnetic nanoparticles remain unchanged on bonding to the fibre surface.

The nanoparticles are present on the surface of the fibre and not in the lumen of the fibre, as reported elsewhere in the literature. Presumably, this will interfere with inter-fibre bonding and hence it would be more appropriate from an industrial point of view to apply the coating post papermaking using, for example, a starch binder (Section 2.2.9).

XRF analysis suggests the amount of magnetite nanoparticles present on the surface of the cellulose fibre is between 1.2 and 3.15 wt. %, depending on the amount of nanoparticles added during the synthesis.

The methods used here are extremely simple and cost-effective, and may give rise to new cellulose based materials for the development of magnetic papers for the EMI shielding area of the upcoming 'smart paper' industry.

Chapter 4

PHOTOLUMINESCENT KRAFT FIBRES

Pinus radiata Kraft fibres coated with doped ZnS quantum dots retain the inherent properties of the fibre; tensile strength, flexibility, and the ability to be made into paper sheets and paper board. The fibres also possess the photoluminescent properties of the surface bound quantum dots.

These fibres have been characterised using Atomic Absorption Spectroscopy (AA), Photoluminescence Spectroscopy (PL), Scanning Electron Microscopy (SEM) with Energy Dispersive X-ray Spectroscopy (EDS), X-ray Photoelectron Spectroscopy (XPS), and X-ray Diffraction (XRD).

4.1. X-ray Diffraction (XRD)

A reference XRD pattern of bulk ZnS (zinc blende) is shown in Figure 4.1. The characteristic peaks are at 28.56° , 33.09° , 47.52° , and 56.29° (2θ , Cu $K\alpha$ radiation). Peak data for this reference sample are shown in Table 4.1.

The XRD pattern of an undoped ZnS is shown in Figure 4.2, and the peak data for this XRD pattern are shown in Table 4.2. It is clear that zinc sulfide has been formed in the zinc blende phase, as indicated by the peaks at approximately 28.8° , 47.1° and 57.0° (2θ , Cu $K\alpha$ radiation), similar to that of the reference XRD pattern in Figure 4.1 and Table 4.1. The sharp peaks present in this XRD pattern are due to the aluminium sample holder.

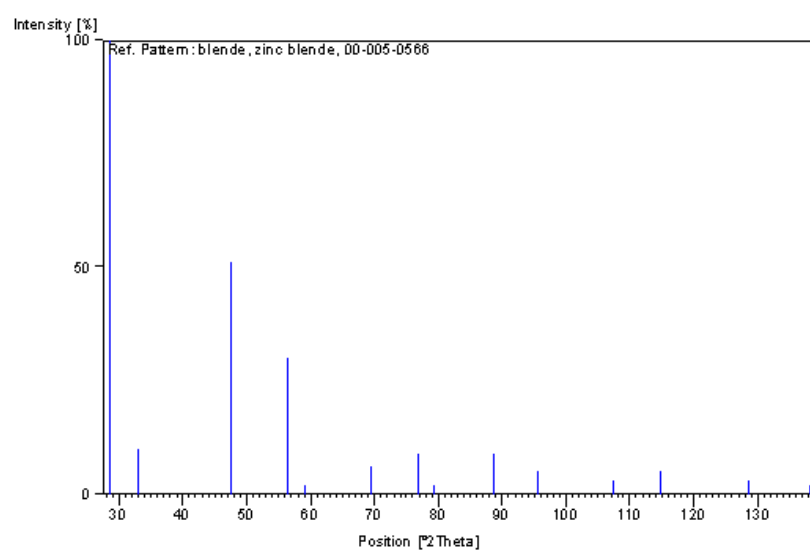


Figure 4.1. Reference XRD pattern of ZnS (zinc blende).

Peak	2 θ	Intensity (%)
1	28.56	100
2	33.09	10
3	47.52	51
4	56.29	30

Table 4.1. XRD peak data for reference ZnS (zinc blende).

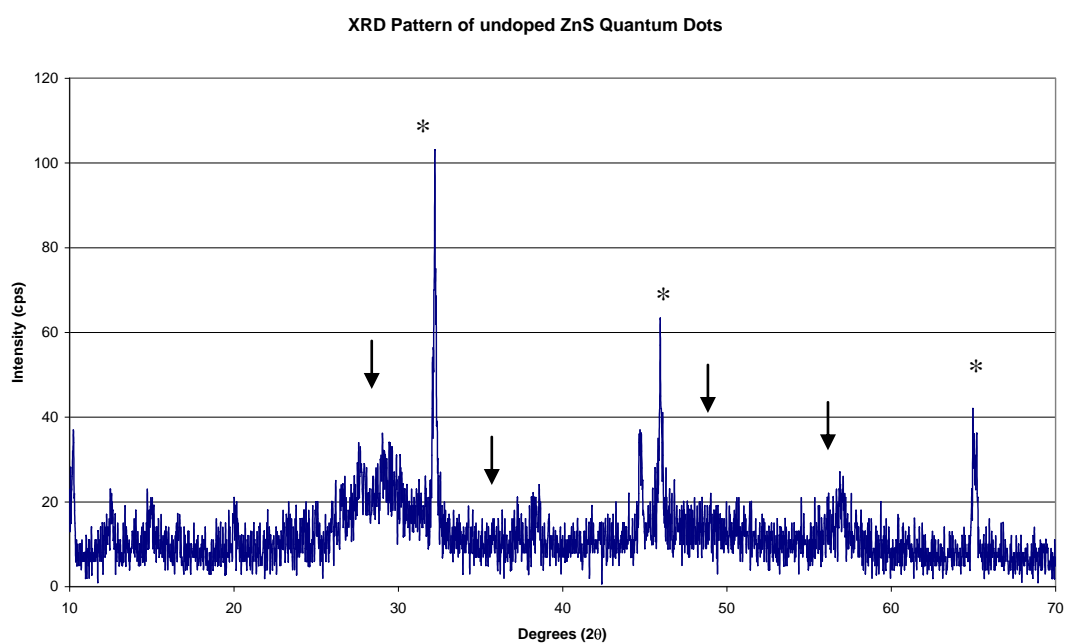


Figure 4.2. XRD pattern of undoped ZnS. ↓ = ZnS, * = aluminium sample holder.

Peak	2 θ	Intensity (%)
1	28.80	100
2	47.13	51
3	57.0	30

Table 4.2. XRD peak data for undoped ZnS (zinc blende).

The XRD patterns of Mn²⁺-doped ZnS are shown in Figure 4.3. On comparison with the XRD pattern of undoped ZnS, it is clear that ZnS has been formed in the zinc blende structure, indicating that doping with Mn²⁺ at the levels used here does not alter the structure of the material.

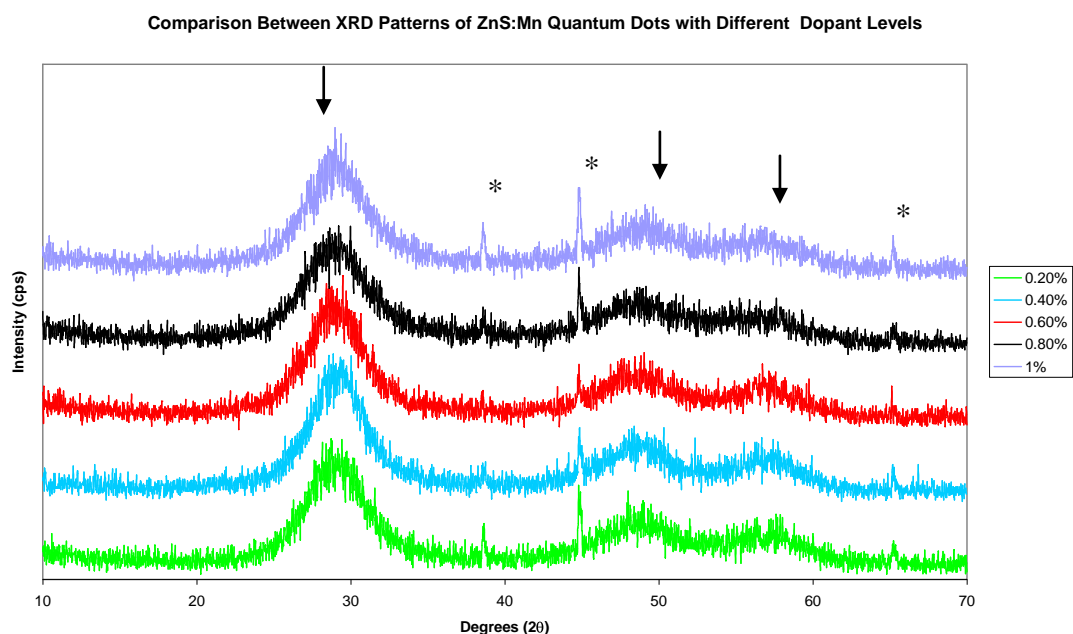


Figure 4.3. Comparison between the XRD patterns of ZnS:Mn quantum dots with varying dopant levels (wt. %). ↓ = ZnS, * = aluminium sample holder.

Three key factors are conducive to doping – all ions are transition metals, all are divalent, and all have similar ionic radii ($\text{Zn}^{2+} = 74 \text{ pm}$, $\text{Mn}^{2+} = 83 \text{ pm}$ and $\text{Cu}^{2+} = 73 \text{ pm}$)¹²⁸. Also, doping at the varying levels used here does not alter the crystal structure of the material, nor does it result in a real change in the crystallinity of the material. Due to the larger size of Mn²⁺ compared to Zn²⁺, doping at high levels could result in an alteration of the structure.

The characteristic peaks at approximately 28.8° , 47.1° and 57.0° (2θ , Cu $K\alpha$ radiation) are all present. The sharp peaks present in the XRD pattern are again due to the aluminium sample holder. On doping with Cu^{2+} , the zinc blende structure is also formed (Figure 4.4).

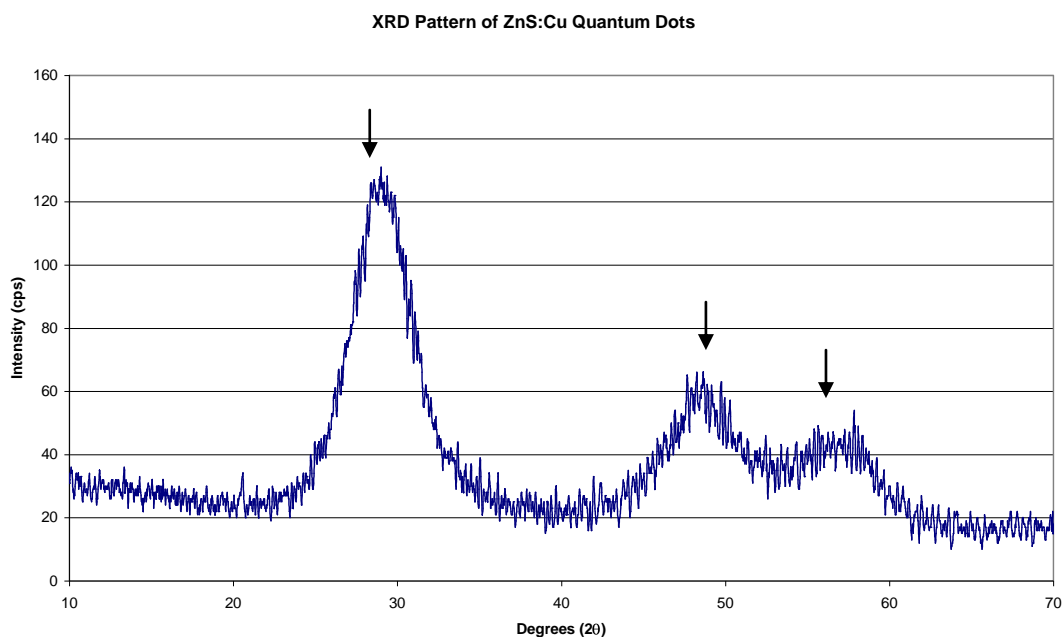


Figure 4.4. XRD pattern of ZnS:Cu^{2+} quantum dots. $\downarrow = \text{ZnS}$.

X-ray line broadening analysis for both varieties of doped ZnS indicates that the average particle size is approximately 2 nm. This means that the particle size is less than the Bohr radius of ZnS, and the synthesised particles can be called semiconductor quantum dots.

Apart from the main peak at approximately 23° (attributable to cellulose), the peaks in the XRD patterns of doped ZnS-coated Kraft fibres synthesised via the ‘in situ’ method are relatively broad and poorly resolved (Figure 4.5). This could either be due to the thin nature of the ZnS coating, the small particle size (2 nm), or both. If the ZnS peaks are visible, they are masked by peaks of a similar angle, present in the XRD pattern of cellulose.

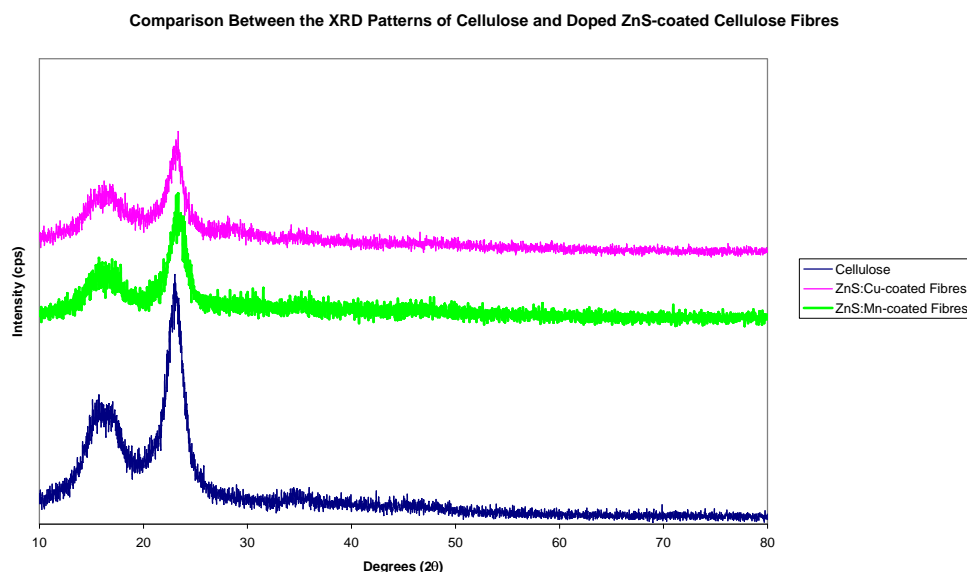


Figure 4.5. XRD pattern of ZnS:Mn²⁺- and ZnS:Cu²⁺-coated Kraft fibres.

4.2. Atomic Absorption Spectroscopy (AA)

It has been suggested that only a small amount of the dopant is actually incorporated into the ZnS host lattice during the synthesis of doped ZnS. Figures in the literature put the amount of dopant incorporated into the ZnS lattice at a level of 10 % of the initial dopant concentration in solution¹⁷⁵.

In order to determine how much of the dopant was incorporated into ZnS quantum dots synthesised in this study, the particles were analysed using atomic absorption spectroscopy. Table 4.3 summarises these results.

Amount of Mn ²⁺ in reaction mixture (mol. %)	Actual amount of Mn ²⁺ in ZnS QD's (mol. %)	Amount of Cu ²⁺ in reaction mixture (mol. %)	Actual amount of Cu ²⁺ in ZnS QD's (mol. %)
1	0.2	0.1	0.092
2	0.27	0.2	0.095
4	0.26	0.4	0.18
6	0.32	0.6	0.26
8	0.18	0.8	0.28
10	0.15	1.0	0.33

Table 4.3. Summary of AA analysis of doped ZnS quantum dots.

From Table 4.3 it can be seen that indeed only a small percentage of the dopant is actually incorporated into the ZnS lattice. Results suggest that the exact level incorporated in the ZnS lattice is not the 10 % suggested in the literature, but varies between 1.5 and 20 % of the reaction mixture for ZnS:Mn²⁺ quantum dots, and between 33 and 92 % of the reaction mixture for ZnS:Cu²⁺.

An interesting point to note is that the smaller the initial amount of dopant present, the greater the percentage included in the host lattice. This suggests that there may be a limit to what extent the lattice can be doped. This is shown graphically in Figures 4.6 and 4.7. The maximum level of doping with Mn²⁺ occurs at approximately 0.3 mol. % (or 6 mol. % in reaction mixture), however the maximum photoluminescence emission is observed at a dopant level of approximately 0.15 mol. % (10 mol. % in reaction mixture). This indicates that the photoluminescence emission and the level of dopant inclusion are not linearly related.

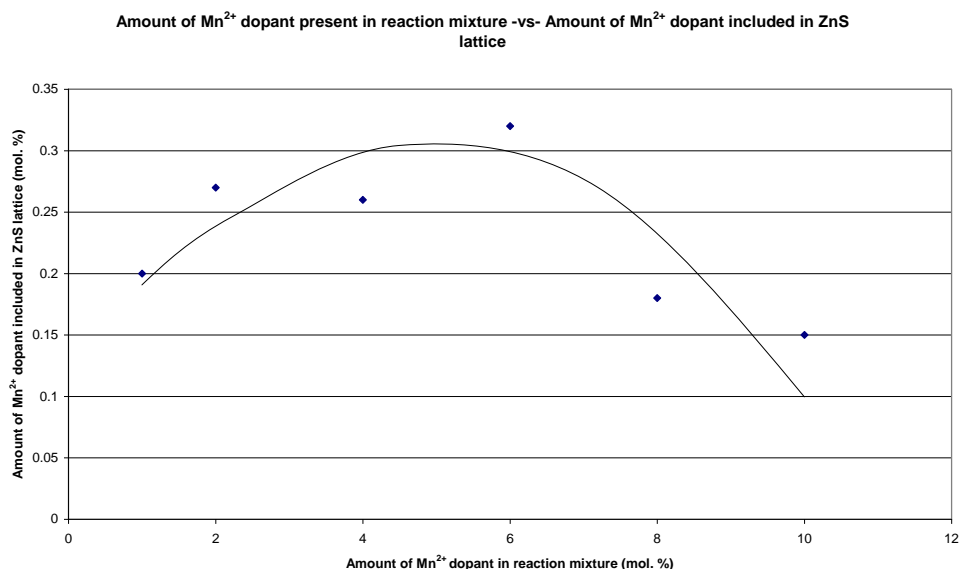


Figure 4.6. Graphical representation of amount of Mn²⁺ dopant included in ZnS lattice vs. amount of Mn²⁺ dopant in the reaction mixture.

For doping with Mn²⁺, if the dopant level in the reaction mixture exceeds 10 %, there is excess Mn²⁺ present which reacts to form MnS. This leads to a visible colour change in the precipitate, from white, to an undesirable brown.

The maximum level of doping with Cu^{2+} is not found here – the plot progresses in a linear fashion at this point as the amount of Cu^{2+} in the reaction mixture is lower than that of Mn^{2+} . As the maximum photoluminescence emission for $\text{ZnS}:\text{Cu}^{2+}$ quantum dots was obtained at a dopant level of 0.095 mol. % (0.2 mol. % in the reaction mixture), the doping level was not varied past 1 mol. % in the reaction mixture.

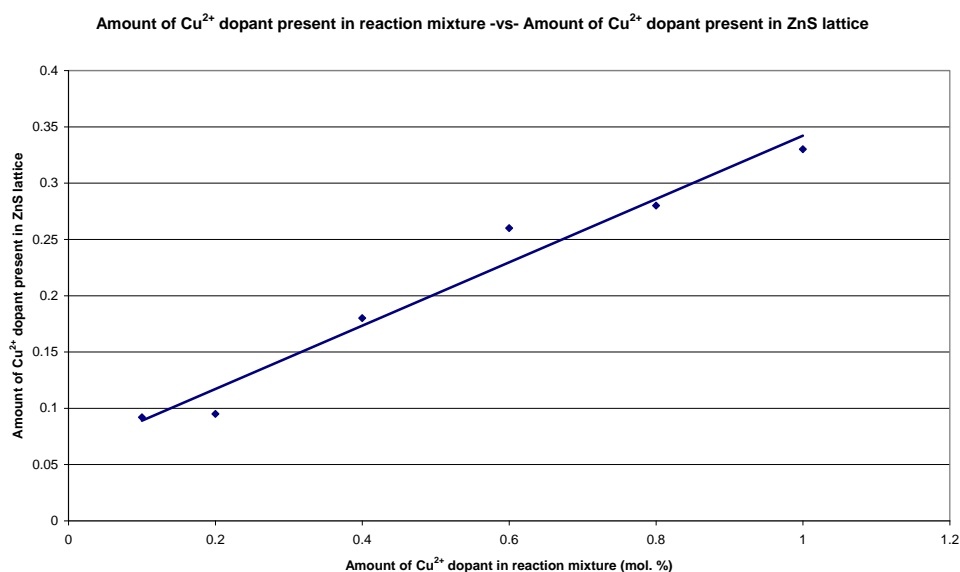


Figure 4.7. Graphical representation of amount of Cu^{2+} dopant included in ZnS lattice vs. amount of Cu^{2+} dopant in the reaction mixture.

4.3. Photoluminescence Spectroscopy (PL)

The photoluminescence (PL) excitation and emission spectra of doped ZnS quantum dots were measured as described in 2.1.10.

The PL excitation spectrum of $\text{ZnS}:\text{Mn}^{2+}$ (10 mol. % Mn^{2+}) is shown in Figure 4.8. From the spectrum it can be seen that the maximum excitation wavelength needed to produce an emission at 590 nm is approximately 335 nm. This wavelength was then used as the excitation wavelength for all subsequent PL emission spectra.

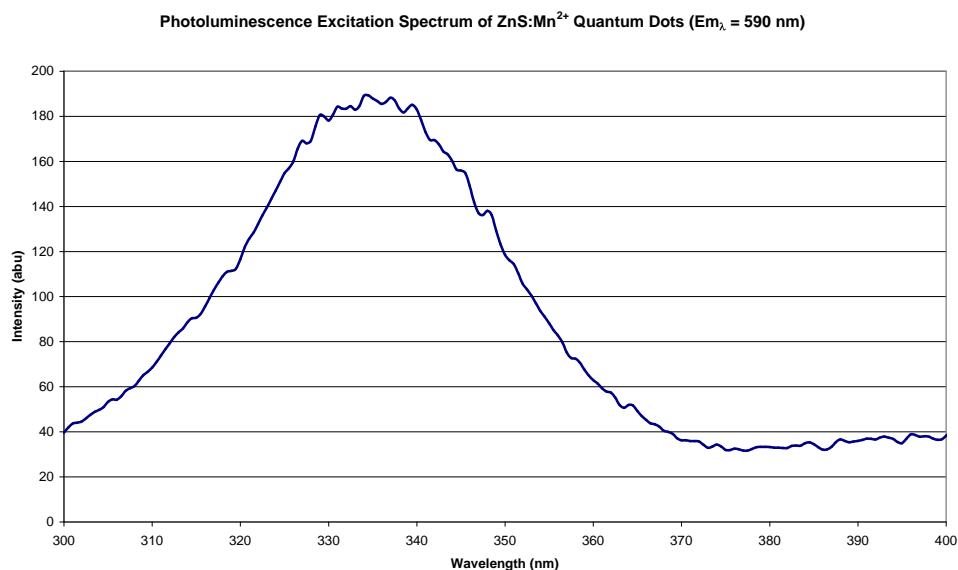


Figure 4.8. PL excitation spectrum of ZnS:Mn²⁺ (10 mol. % Mn²⁺) quantum dots.

The PL excitation spectra of ZnS:Cu²⁺ (0.2 mol. % Cu²⁺) is shown in Figure 4.9. From the spectrum it can be seen that the maximum UV excitation wavelength needed to produce an emission at 530 nm is approximately 330 nm. This wavelength was then used as the excitation wavelength for all subsequent PL emission spectra. A peak also exists at approximately 420 nm, which will give rise to the same emission at 530 nm.

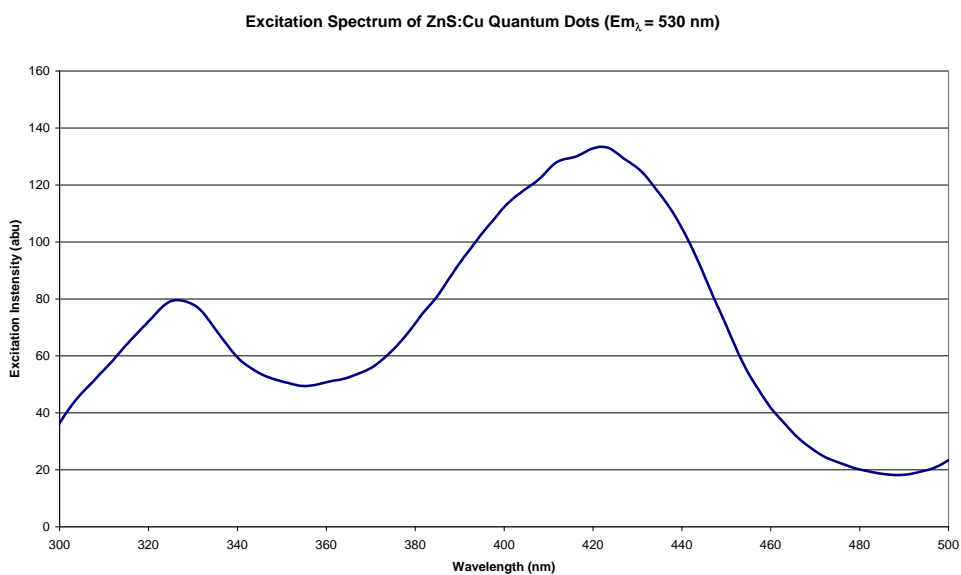


Figure 4.9. PL excitation spectrum of ZnS:Cu²⁺ (0.2 mol. % Cu²⁺) quantum dots.

The PL emission spectra of ZnS:Mn^{2+} quantum dots is shown in Figure 4.10.

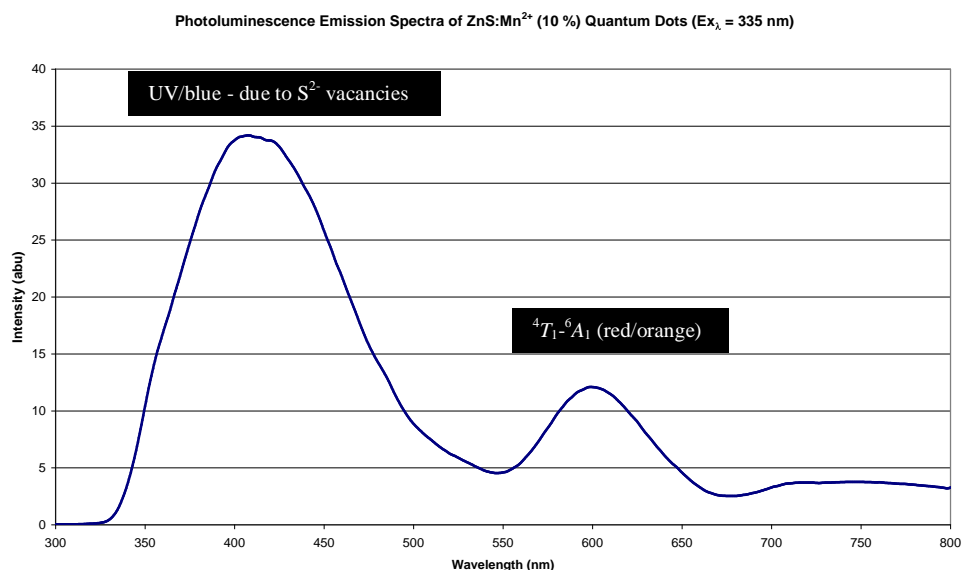


Figure 4.10. PL emission spectrum of ZnS:Mn^{2+} (10 mol. % Mn^{2+}) quantum dots.

A relatively strong luminescence at approximately 600 nm is observed in ZnS:Mn^{2+} quantum dots and is due to the presence of Mn^{2+} in the host ZnS lattice. This produces localised energy levels (4T_1 - 6A_1) in the band gap of the semiconductor ZnS quantum dots due to crystal field effects similar to those in bulk ZnS:Mn^{2+} . An electron can then undergo photo excitation in the ZnS lattice and undergo a non-radiative transition to the 4T_1 level from which it makes a radiative transition to the 6A_1 level, resulting in an emission at 600 nm⁶⁹. This recombination mechanism is shown in Figure 4.11.

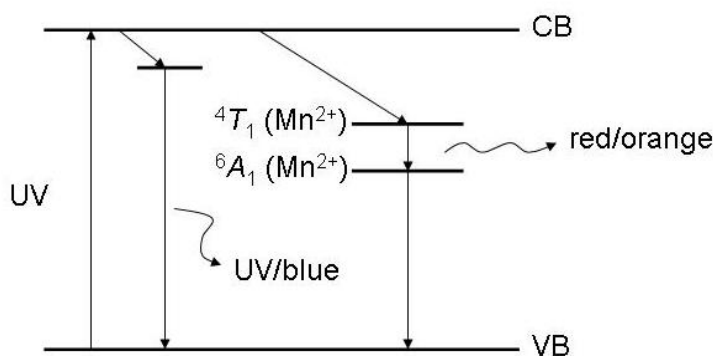


Figure 4.11. Recombination mechanism for ZnS:Mn^{2+} quantum dots.

Bhargava *et al.*⁶⁹ have reported that this emission is unaffected by particle size, and hence quantum size effects (1.4.3)

Fluorescence quantum yield is, however, affected by particle size (equation 1.12). Bhargava *et al.*⁶⁹ have suggested that with decreasing particle size a strong hybridisation of the s-p states of the ZnS host and the d states of the Mn^{2+} dopant could occur. This hybridisation results in a faster energy transfer between the host and dopant, and gives rise to an increase in fluorescence quantum yield. Although this is the case, fluorescence quantum yield was not measured in this study, as no facilities were available. Reports in the literature put the best fluorescence quantum yield of ZnS:Mn^{2+} quantum dots at 18 %⁶⁹.

The larger peak at 420 nm (Figure 4.10) can be attributed to an emission due to S^{2-} vacancies in the ZnS lattice that act as recombination centres for photogenerated electron-hole pairs¹⁷⁶.

A comparison between the PL emission spectra of ZnS:Mn^{2+} quantum dots with differing dopant levels is shown in Figure 4.12.

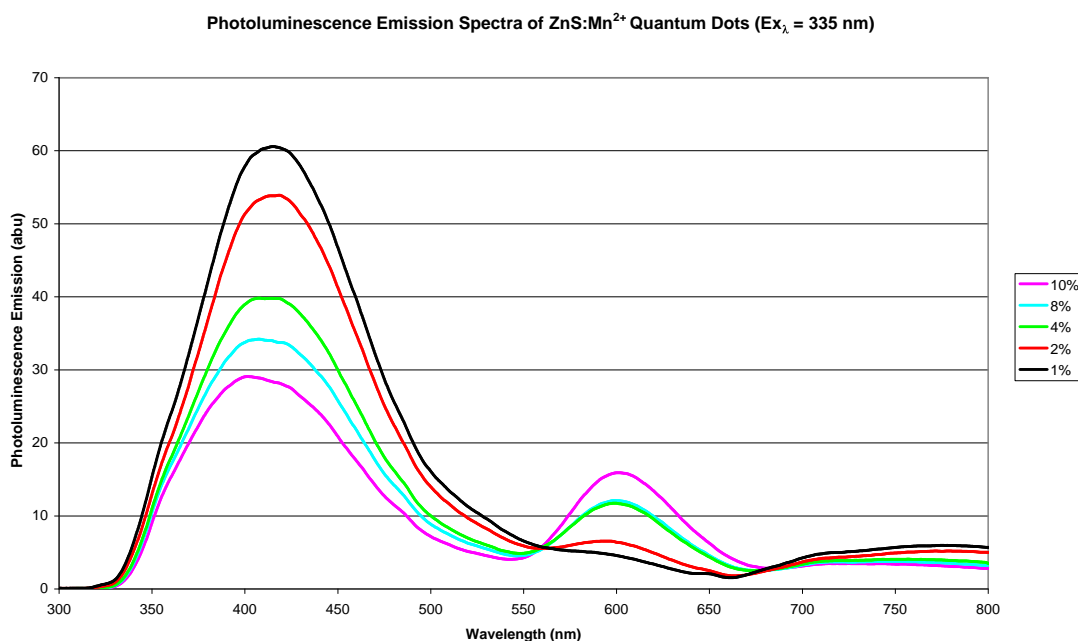


Figure 4.12. Comparison between PL emission spectra of ZnS:Mn^{2+} quantum dots with different dopant levels (mol. % in the reaction mixture).

The graph shows that for ZnS:Mn²⁺ quantum dots, the maximum PL emission at 600 nm is observed with a dopant level of 10 mol. % (in the reaction mixture). This equates to an approximate dopant level of 0.15 mol. % (as determined by AA spectroscopy in 2.1.2). At levels higher than 10 mol. %, the capacity of the ZnS to include Mn²⁺ ions is exceeded, and the precipitate becomes brown due to the presence of MnS.

The highest intensity for a 600 nm emission corresponds to the lowest intensity for a 420 nm emission. As the 420 nm emission is attributable to S²⁻ vacancies, presumably this indicates that on doping with a higher level of Mn²⁺, less S²⁻ vacancies are present. Consequently, if an electron-hole pair is generated by the absorption of UV light, there is a higher probability that it will recombine to produce an emission at 600 nm rather than at 420 nm, thus leading to a brighter luminescence at 600 nm.

A photograph of the photoluminescence emission of ZnS:Mn²⁺ quantum dots with different dopant levels is shown in Figure 4.13.



Figure 4.13. Photograph of ZnS:Mn²⁺ quantum dots with different dopant levels under ambient light conditions (top) and under UV light (below). (L-R): 1, 2, 4, 8, and 10 mol. % Mn²⁺ in the reaction mixture. photoluminescence emission of

The PL emission spectrum of $\text{ZnS}:\text{Cu}^{2+}$ is shown in Figure 4.14.

The emission peak at approximately 525 nm is attributable to a transition between the 2E and 2T_2 energy levels. An electron can undergo photo excitation in the ZnS lattice and undergo a non-radiative transition to the 2T_2 level from which it makes a radiative transition to the 2E level, resulting in an emission at 530 nm¹²⁷. This recombination mechanism is shown in Figure 4.15.

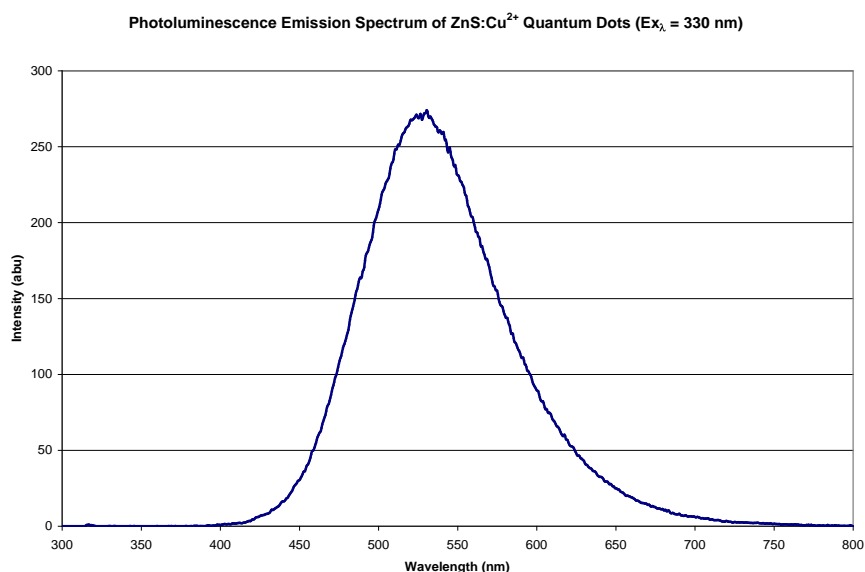


Figure 4.14. PL emission spectrum of $\text{ZnS}:\text{Cu}^{2+}$ quantum dots.

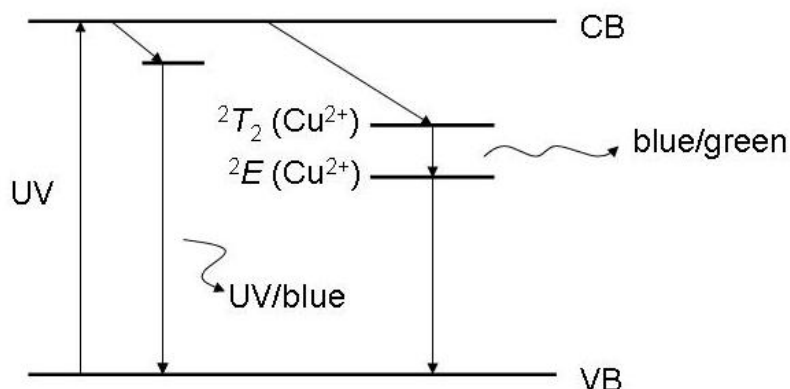


Figure 4.15. Recombination mechanism for $\text{ZnS}:\text{Cu}^{2+}$ quantum dots.

The peak at approximately 430 nm seen in the PL emission spectrum of ZnS:Mn²⁺ (Figure 4.10) is not seen in the PL emission spectra of ZnS:Cu²⁺. A possible explanation for this is that there are less S²⁻ vacancies due to the presence of S₂O₃²⁻ in the reaction mixture as a complexing agent for Cu²⁺ in the synthesis of the quantum dots. As S₂O₃²⁻ is too large to be incorporated into the lattice itself, it must be broken down. This gives rise to an excess of S²⁻ (4 moles of S²⁻ for every 1 mole of Cu²⁺ as per the square planar [Cu(S₂O₃)₂]²⁻ complex) and less sulfur vacancies.

A comparison between the PL emission spectra of ZnS:Cu²⁺ quantum dots doped with varying amounts of Cu²⁺ is shown in Figure 4.16.

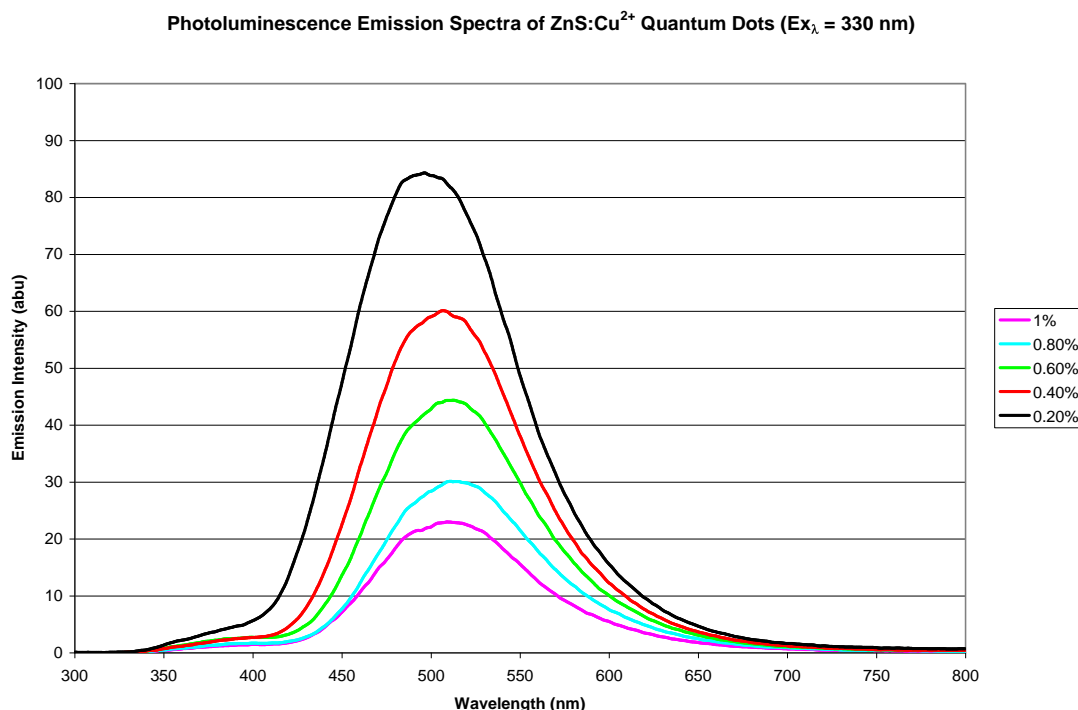


Figure 4.16. Comparison between PL emission spectra of ZnS:Cu²⁺ quantum dots with different dopant levels (mol. % in the reaction mixture).

It can be seen from the plot that the maximum PL emission is observed with a dopant level of 0.2 mol. %. This equates to an approximate dopant level of 0.095 mol. % (as determined by AA spectroscopy in 2.1.2).

On doping with 0.1 % Cu^{2+} , no distinguishable change is seen in the photoluminescence emission of $\text{ZnS}:\text{Cu}^{2+}$ quantum dots compared with that of 0.2 mol. % doped $\text{ZnS}:\text{Cu}^{2+}$ quantum dots. This is due to a relatively similar amount of Cu^{2+} being included in the lattice of the ZnS host, of approximately 0.092 and 0.095 mol. %, respectively (Table 4.3).

A photograph of the photoluminescence emission of $\text{ZnS}:\text{Cu}^{2+}$ quantum dots with different dopant levels is shown in Figure 4.17.

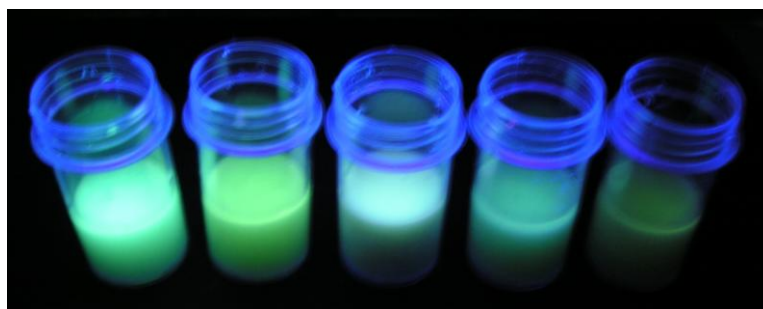


Figure 4.17. Photograph of $\text{ZnS}:\text{Cu}^{2+}$ quantum dots with different dopant levels under UV light. (L-R): 0.2, 0.4, 0.6, 0.8, and 1.0 mol. % Cu^{2+} (in the reaction mixture).

Coating Kraft fibres with both $\text{ZnS}:\text{Mn}^{2+}$ and $\text{ZnS}:\text{Cu}^{2+}$ quantum dots, leaves the PL emission spectra of the quantum dots essentially unchanged. These are shown in Figures 4.18 and 4.19.

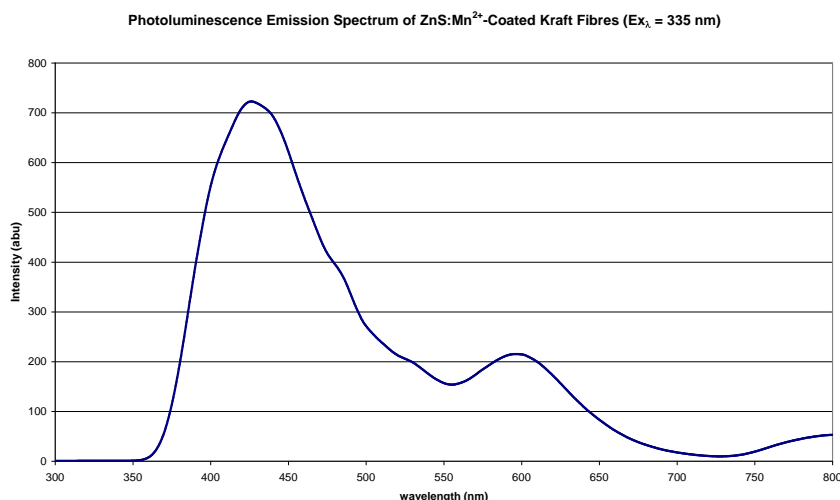


Figure 4.18. PL emission spectrum of $\text{ZnS}:\text{Mn}^{2+}$ -coated Kraft fibres (cellulose).

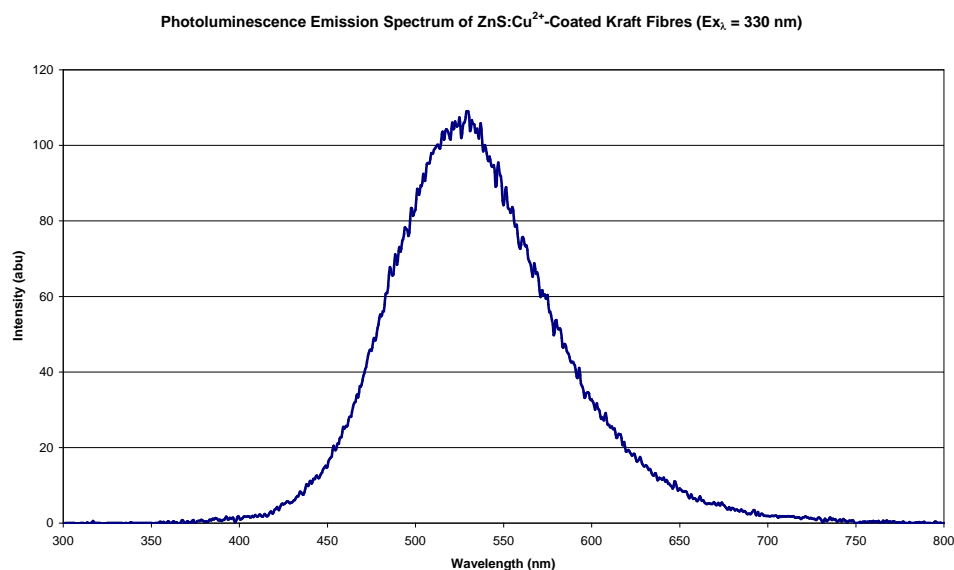


Figure 4.19. PL emission spectrum of ZnS:Cu²⁺-coated Kraft fibres (cellulose).

The photograph in Figure 4.20 shows a visual representation of the photoluminescence observed from ZnS:Mn²⁺ (10 mol. % Mn²⁺ in the reaction mixture) and ZnS:Cu²⁺ (0.1 mol. % Mn²⁺ in the reaction mixture) quantum dot powders, and ZnS:Mn²⁺ and ZnS:Cu²⁺-coated Kraft fibres (both synthesised using the respective powders present in the photograph). The powders are visually brighter than their coated fibre counterparts. This due to a greater density of quantum dots in the powder, and also in the doped ZnS-coated fibres, the colour is diluted by the white fibre background.

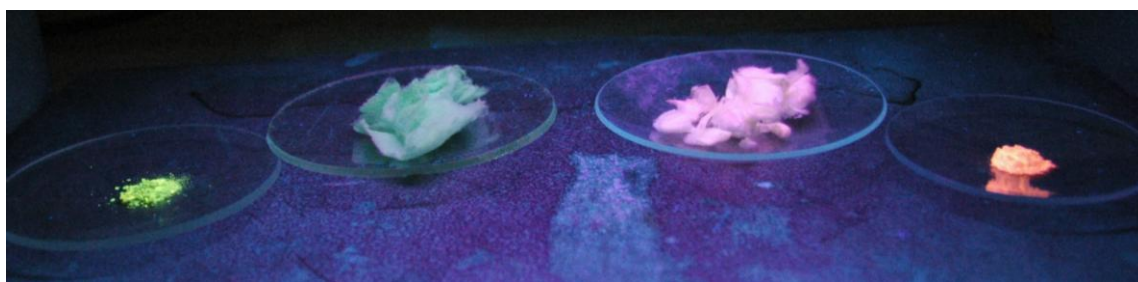


Fig 4.20. Photograph showing PL emission under UV light from doped ZnS quantum dots and doped ZnS-coated fibres. L-R: ZnS:Cu²⁺ quantum dot powder, ZnS:Cu²⁺-coated Kraft fibres, ZnS:Mn²⁺-coated Kraft fibres, ZnS:Mn²⁺ quantum dot powder.

4.4. Scanning Electron Microscopy (SEM)

Doped ZnS quantum dots and ZnS-coated Kraft fibres were examined under the Scanning Electron Microscope (SEM) in order to assess their morphological

character. Doped ZnS particles synthesised in 2.2.11 and 2.2.12 show a spherical morphology (Figures 4.21 - 4.24).

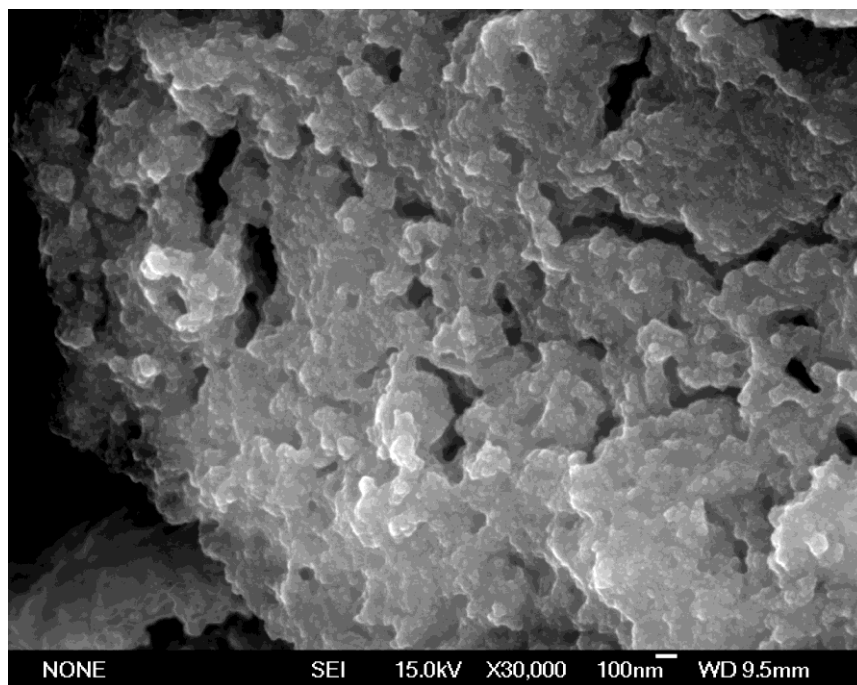


Figure 4.21. SEM image of ZnS:Mn²⁺ quantum dots.

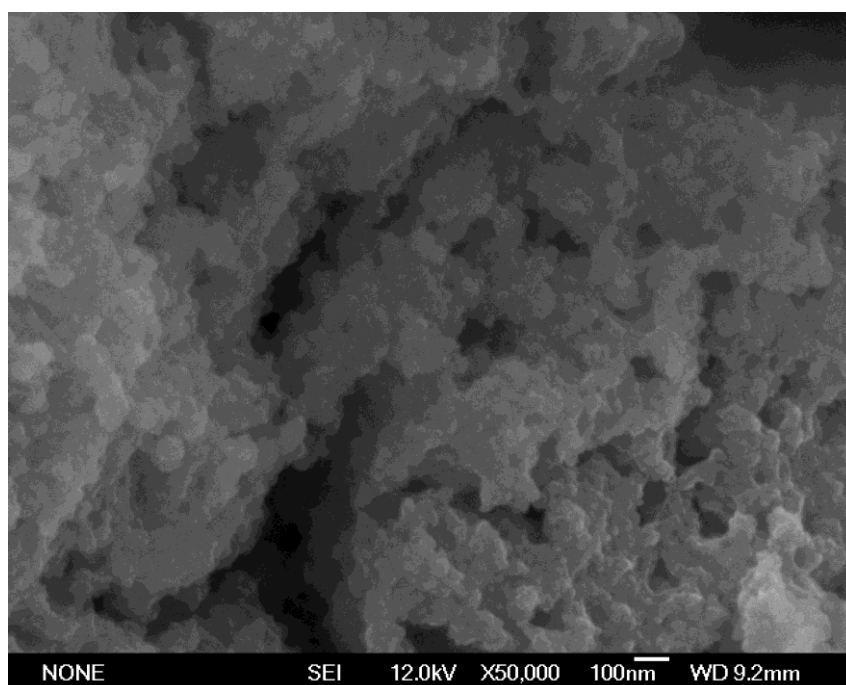


Figure 4.22. SEM image of ZnS:Mn²⁺ quantum dots.

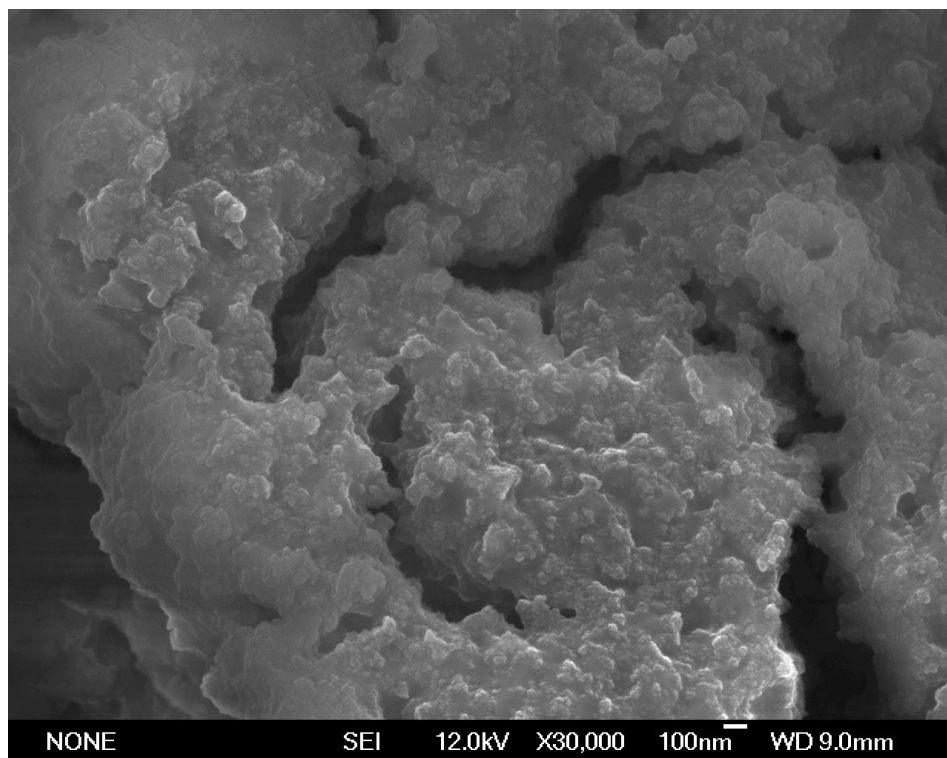


Figure 4.23. SEM image of ZnS:Cu²⁺ quantum dots.

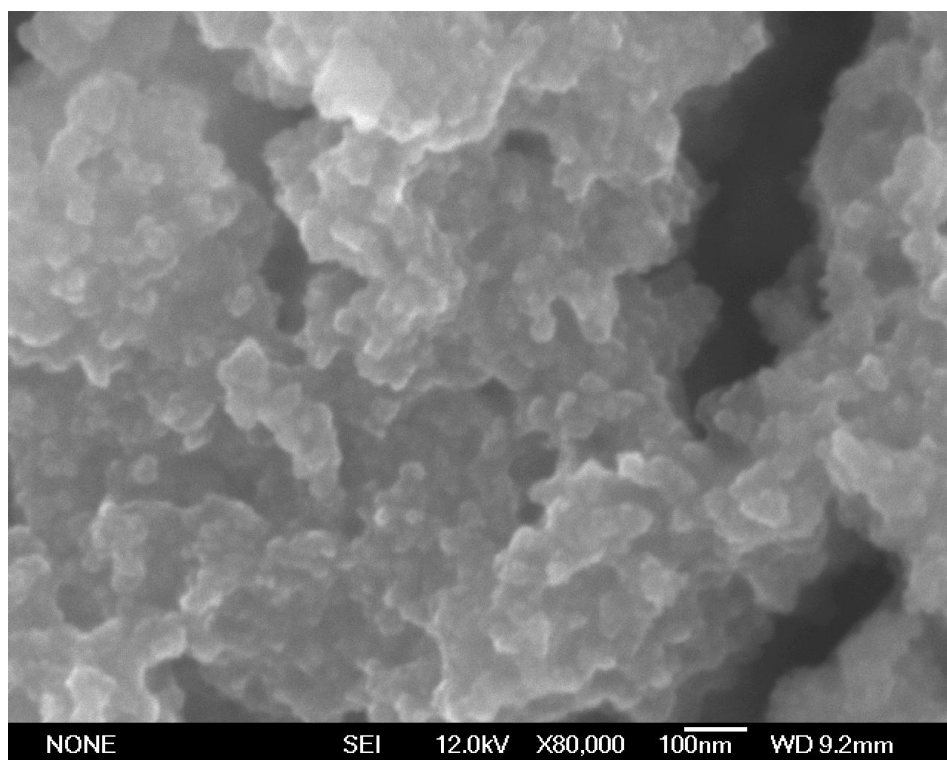


Figure 4.24. SEM image of ZnS:Cu²⁺ quantum dots.

Although XRD line broadening analysis shows that the doped ZnS quantum dots synthesised in this study are approximately 2 nm in diameter, SEM images show the particles to present in agglomerations of approximately 100 nm.

This is not surprising however, as no surfactant was used during their synthesis (as was the case with Fe₃O₄ nanoparticles synthesised in 2.2.2) in order to eliminate any unfavourable interactions between the surfactant and the cellulose fibre surface to which the quantum dots would be bonded to through hydrogen bonding (1.2).

EDS elemental maps of Zn, S, Mn and Cu show excellent correlation and hence confirm that the doped ZnS compounds have been formed. The EDS maps for Zn, Mn, Cu and S, and complementary SEI images are shown below in Figures 4.25 (ZnS:Mn²⁺ quantum dots) and 4.26 (ZnS:Cu²⁺ quantum dots).

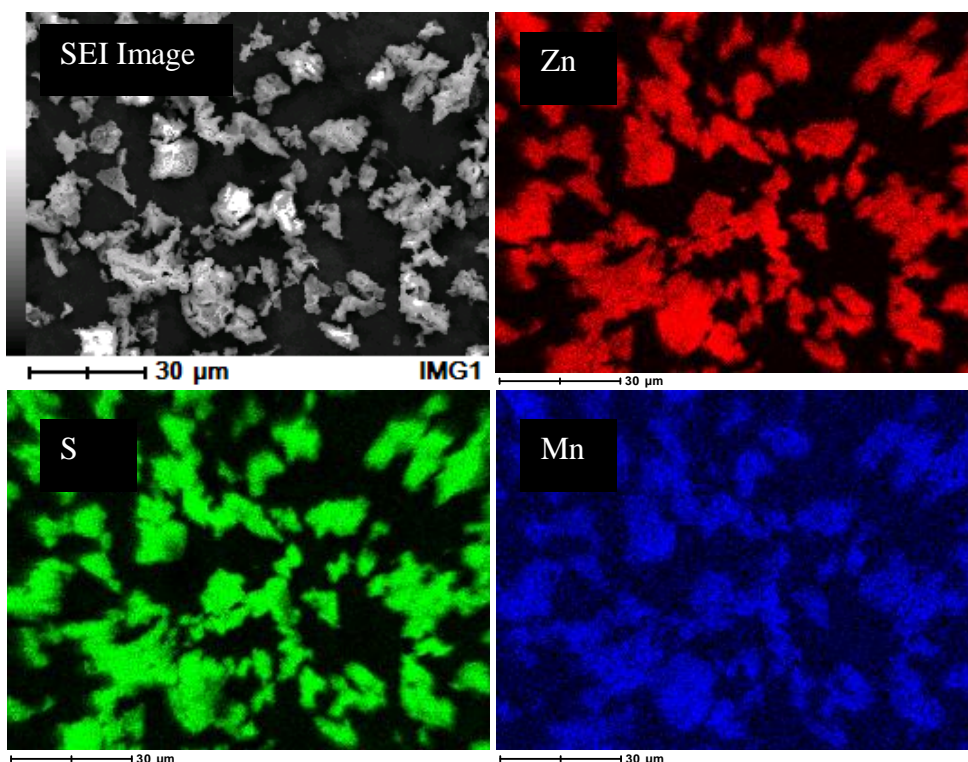


Figure 4.25. EDS elemental maps of ZnS:Mn²⁺ quantum dots. Zn (red), S (green), Mn (blue), and complementary SEI image (top left).

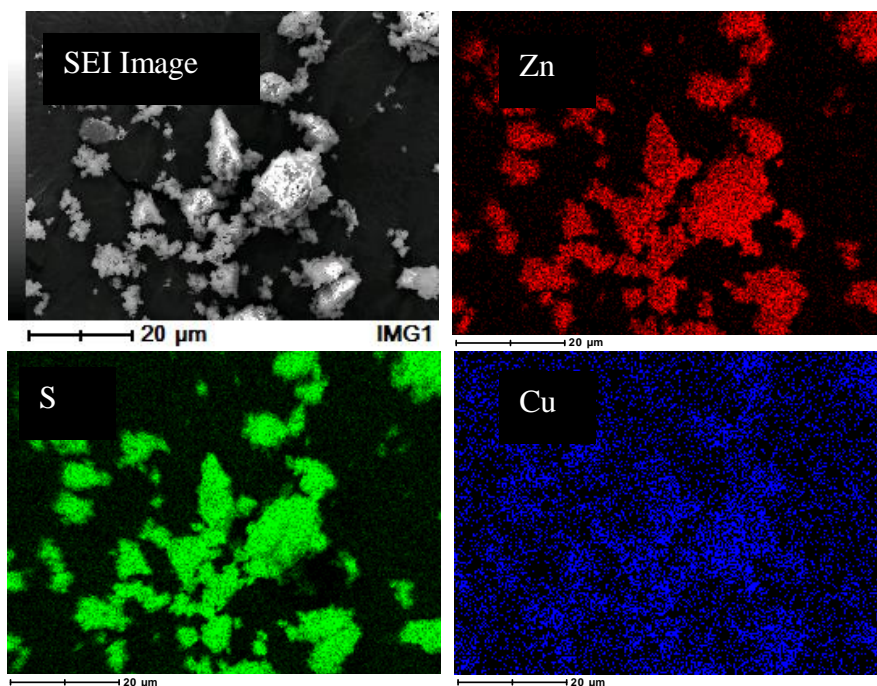


Figure 4.26. EDS elemental maps of ZnS:Mn²⁺ quantum dots. Zn (red), S (green), Cu (blue), and complementary SEI image (top left).

Kraft fibres coated with doped ZnS were synthesised by 4 different methods (2.2.15). The first ('colloid' method) involved the addition of an amount of a ZnS:Mn²⁺ or ZnS:Cu²⁺ colloid to a suspension of Kraft fibres, while the second method was simply a repeat of the first and was termed the 'double dip' method.

The third involved synthesising ZnS:Mn²⁺ or ZnS:Cu²⁺ quantum dots 'in situ' in order to obtain a more even coating before the quantum dots had a chance to agglomerate, and the final method involved the use of a linker molecule (PDADMAC) to bind the quantum dot to the surface of the cellulose fibre.

An SEM image of ZnS:Mn²⁺-coated Kraft fibres synthesised by the 'colloid' method is shown in Figure 4.27.

Of note is the uneven distribution of ZnS:Mn²⁺ quantum dots across the surface of the fibre. The quantum dots appear to be present on the surface of the cellulose fibre as agglomerations due to the lack of use of a surfactant.

Consequently, the quantum dots have a propensity to bind to themselves rather than forming a smooth coating by binding to the hydroxyl groups on the surface of the cellulose fibre. There are also areas on the fibre devoid of quantum dots. This was the case no matter what volume of the ZnS:Mn^{2+} colloid was added to the Kraft fibre suspension (see 2.2.15).

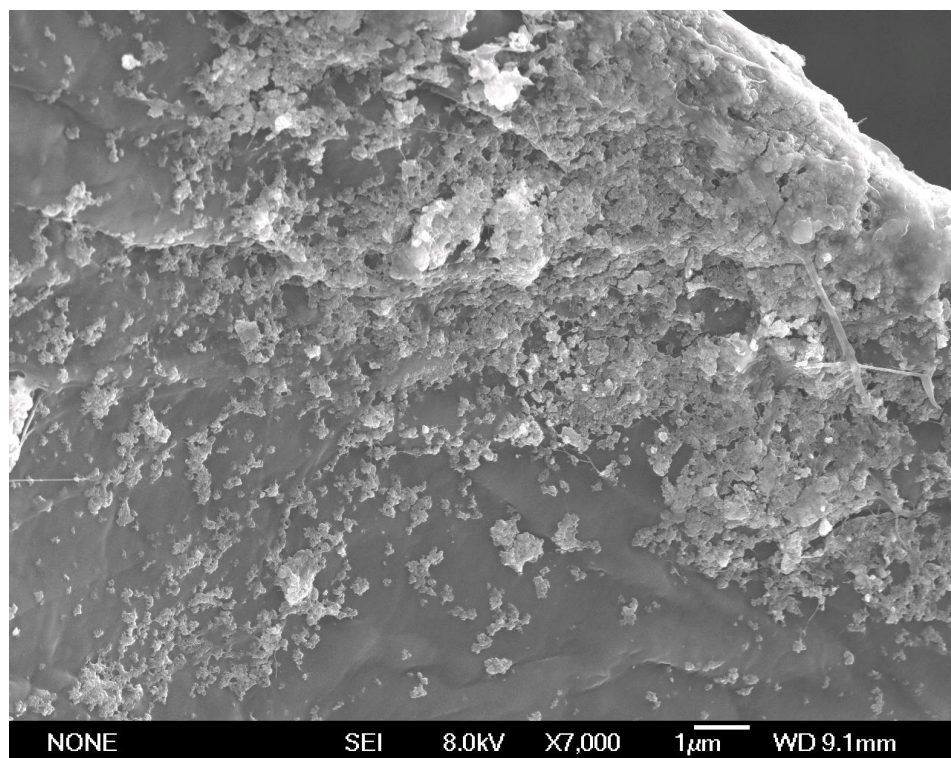


Figure 4.27. SEM image showing ZnS:Mn^{2+} -coated Kraft fibres synthesised using the ‘colloid method.’ Note the uneven coating of ZnS:Mn^{2+} over the surface of the fibre.

The ‘double dip’ method (2.2.15) was also unsuccessful in obtaining an even coating of ZnS:Mn^{2+} . SEM images of Kraft fibres coated using this method are shown in Figure 4.28.

Again, ZnS:Mn^{2+} quantum dots are present on the surface as agglomerations and there are large areas devoid of particles. As a result, the ‘colloid’ method and ‘double dip’ approaches were abandoned.

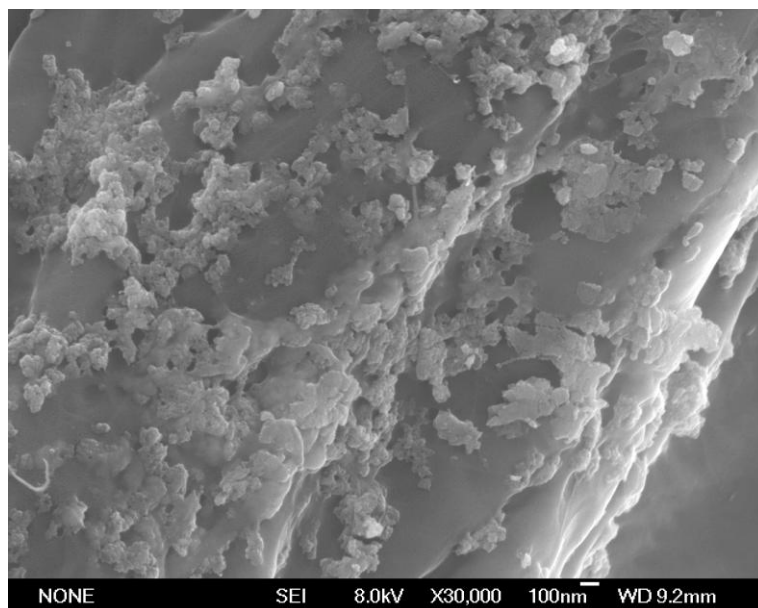


Figure 4.28. SEM image showing ZnS:Mn²⁺-coated Kraft fibres synthesised using the 'double dip method.' Note the uneven coating of ZnS:Mn²⁺ over the surface of the fibre.

The 'PDADMAC' method was also unsuccessful in obtaining an even coating of ZnS:Mn²⁺ quantum dots on the cellulose fibre surface. As was the case with both the 'colloid' and 'double dip' methods, the quantum dots are present on the cellulose fibre surface as agglomerations (Figures 4.29 and 4.30).

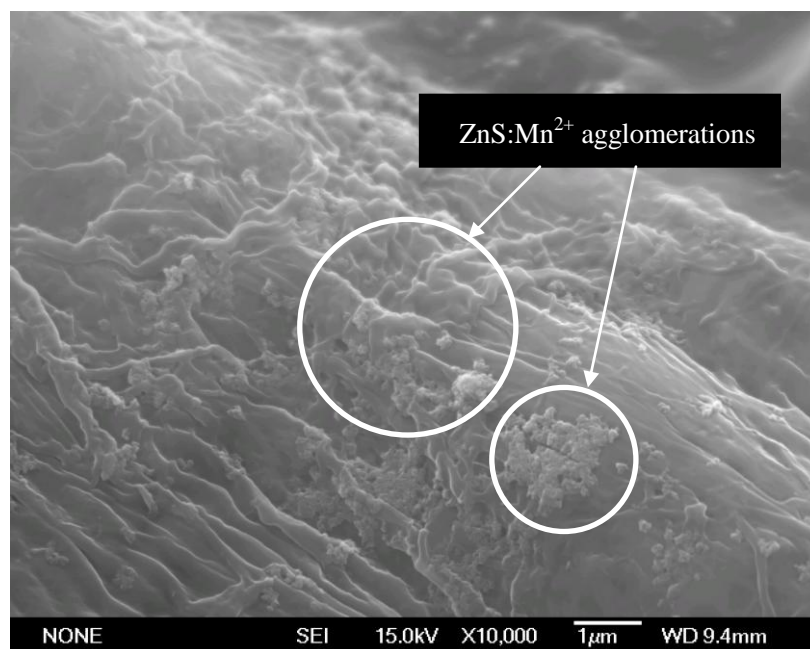


Figure 4.29. SEM image showing ZnS:Mn²⁺-coated Kraft fibres synthesised using the 'PDADMAC method', using 1 cm³ PDADMAC. Note the uneven coating of ZnS:Mn²⁺ over the surface of the fibre.

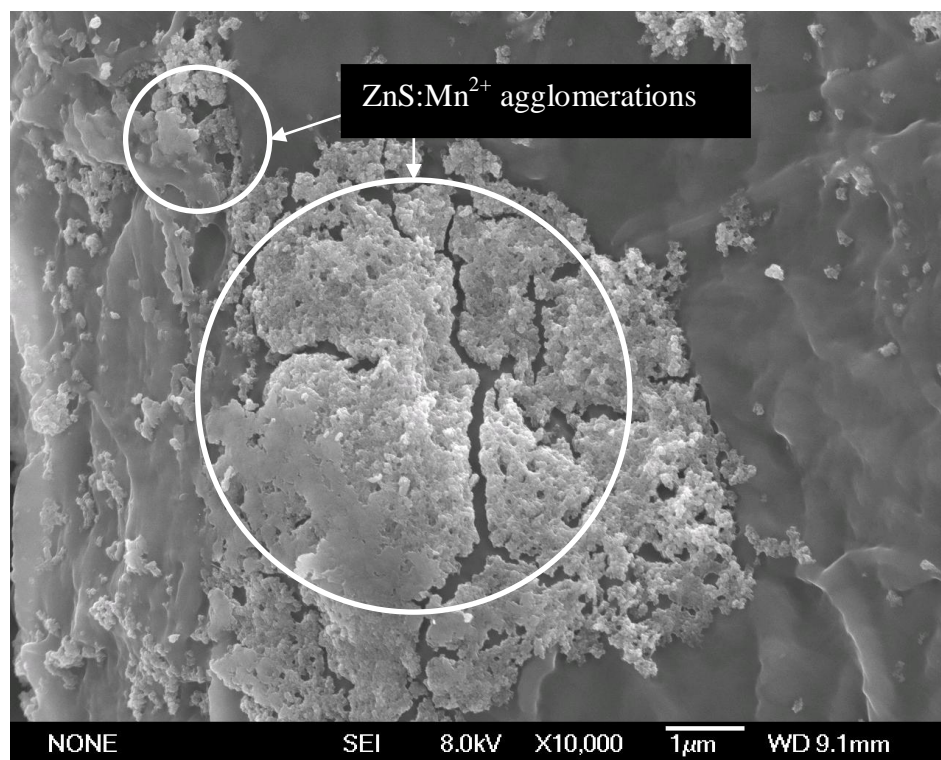


Figure 4.30. SEM image showing ZnS:Mn²⁺-coated Kraft fibres synthesised using the 'PDADMAC method', using 6 cm³ PDADMAC. Note the uneven coating of ZnS:Mn²⁺ over the surface of the fibre.

There are also areas which remain uncoated by the quantum dots, irrespective of how much PDADMAC was used in the synthesis. Due to the agglomeration of ZnS:Mn²⁺ and the uneven nature of the coating, the 'PDADMAC' method was abandoned.

The last method used was the 'in situ' method. This was chosen in order to bind the ZnS:Mn²⁺ quantum dots to the surface of the cellulose fibre as they formed, and thus before they had any chance to agglomerate. This method proved to be the most successful in coating Kraft fibres with doped ZnS quantum dots. The SEM images in Figures 4.31–4.33 show ZnS:Mn²⁺-coated Kraft fibres synthesised by the 'in situ' method.

Cracking of the coating and swelling of the fibre is caused by the high energy of the electron beam. This is most evident in Figure 4.31, where part of the fibre has ballooned and lead to cracks in the ZnS:Mn²⁺ coating.

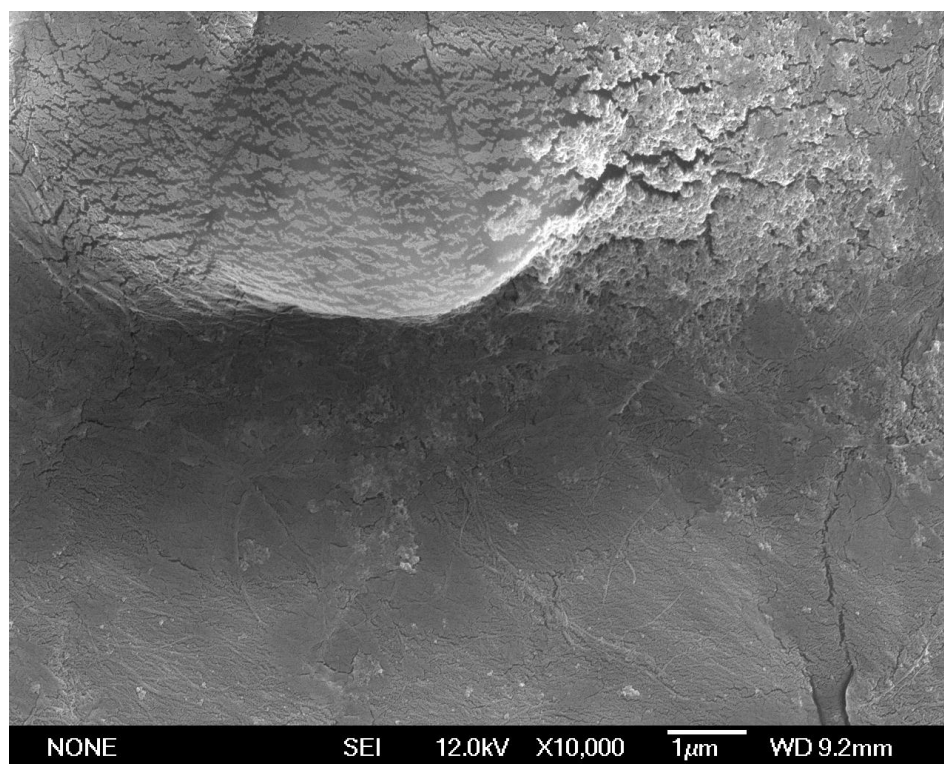


Figure 4.31. SEM image of ZnS:Mn²⁺-coated Kraft fibres synthesised using the 'in situ method.'

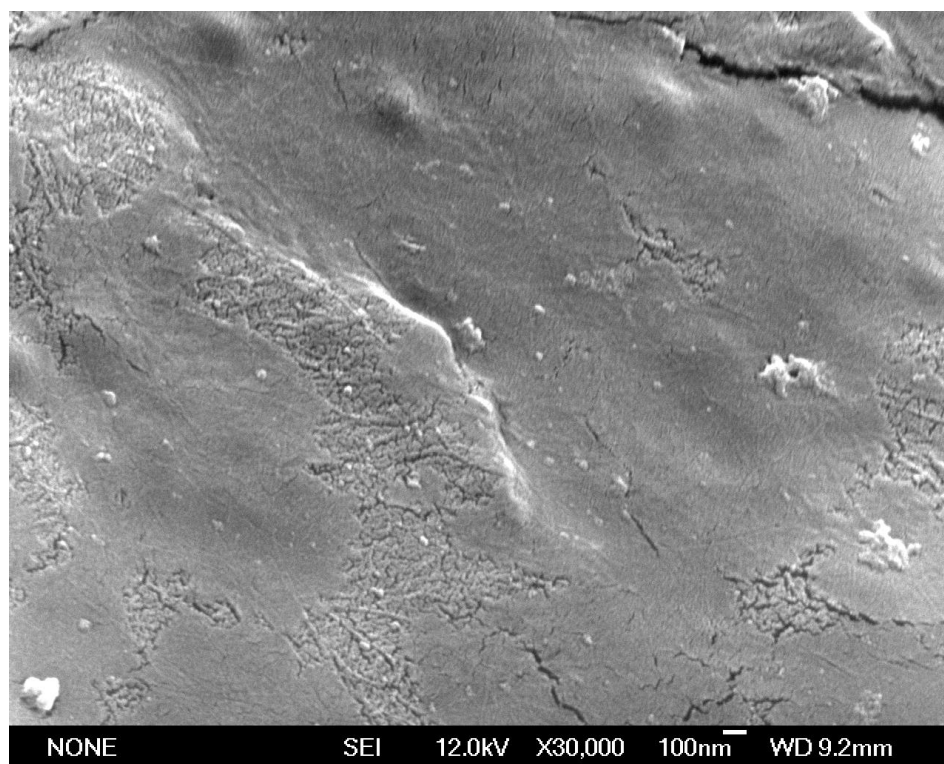


Figure 4.32. SEM image of ZnS:Mn²⁺-coated Kraft fibres synthesised using the 'in situ method.'

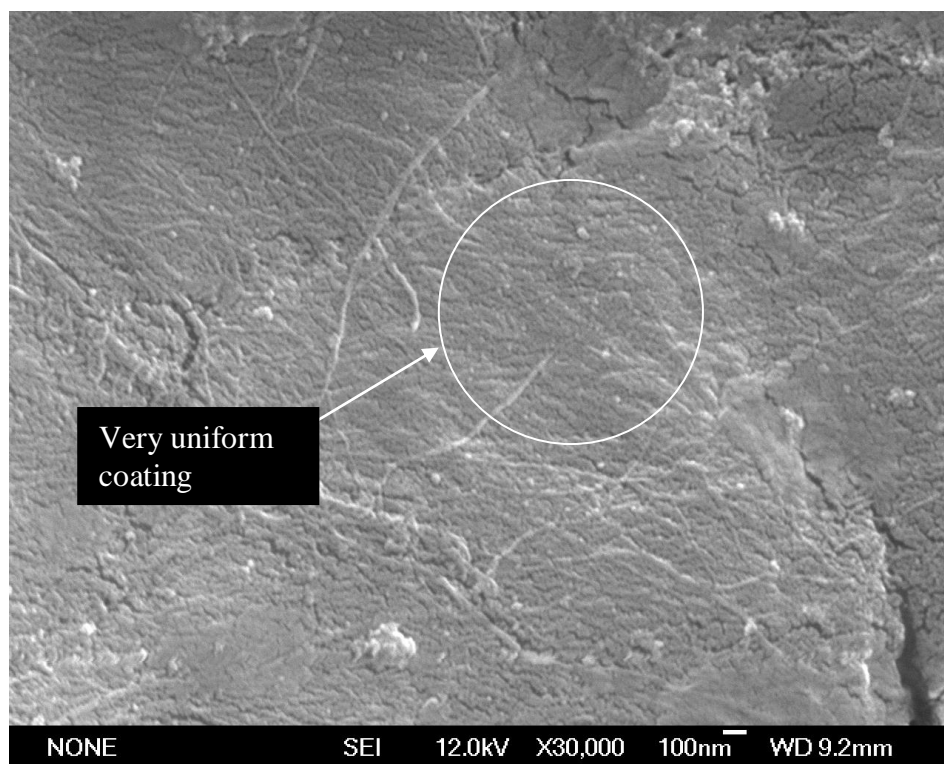


Figure 4.33. SEM image of ZnS:Mn²⁺-coated Kraft fibres synthesised using the ‘in situ method.’

As can be seen from the images, a uniform coating was achieved, with a particle size much smaller than that of ZnS:Mn²⁺ quantum dots synthesised as free-standing powders or present on ZnS:Mn²⁺-coated Kraft fibres synthesised by the ‘colloid’, ‘double dip’ or ‘PDADMAC’ methods. This indicates that the quantum dots are bound to the surface hydroxyl groups of the cellulose in preference to agglomeration with each other.

The particle size is closer to the particle size of 2 nm determined by XRD analysis, indicating that agglomeration has not taken place, or at least to not as large an extent, and that the particles are bonded to the fibre surface as they are formed.

EDS maps of doped ZnS-coated Kraft fibres are shown in Figure 4.34. The ZnS coating can be seen, with both Zn and S EDS maps correlating well. Some excess particles are also visible at this lower magnification.

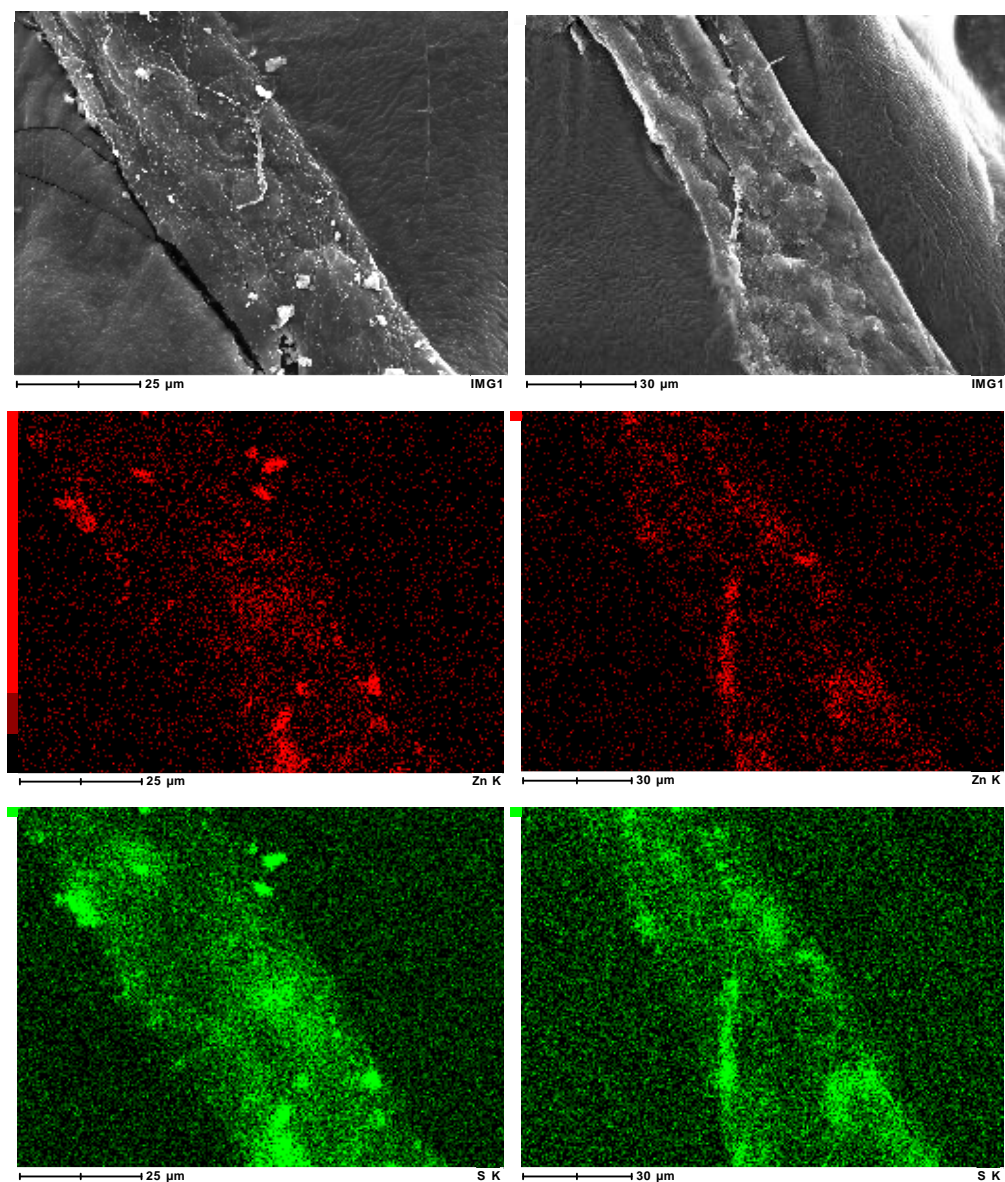


Figure 4.34. EDS maps of doped ZnS-coated Kraft fibres. SEI image (top left), Zn (red), S (green).

4.5. X-ray Photoelectron Spectroscopy (XPS)

The Zn 2*p* XPS spectrum of doped ZnS quantum dots (Figure 4.35) shows peaks consistent with ZnS^{169, 177}.

The two peaks arise from the 3/2 and 1/2 spin multiplicities of the Zn²⁺ in ZnS, and have a slightly asymmetric shape - common for some transition metals.

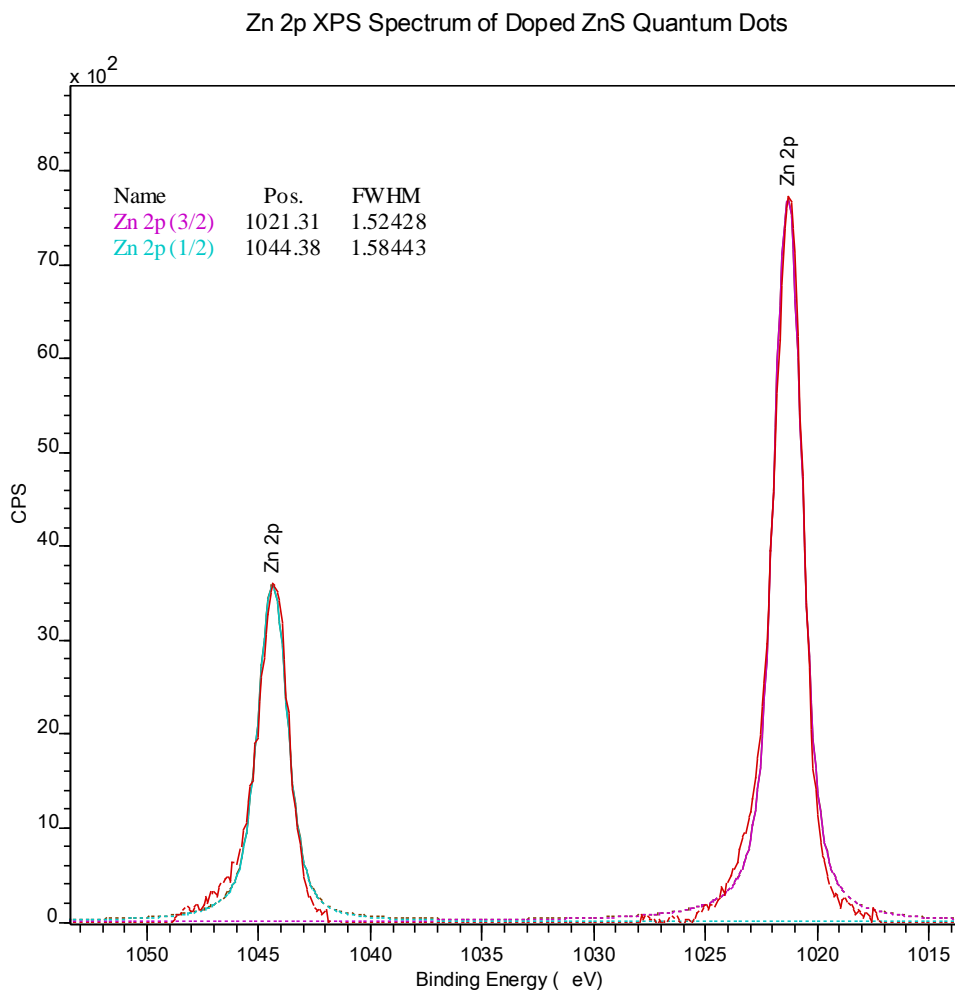


Figure 4.35. Zn 2p XPS spectrum for ZnS quantum dots.

On coating Kraft fibres with doped ZnS quantum dots, the XPS spectrum shifts slightly in energy indicating that bonding between the ZnS quantum dots and the cellulose surface is taking place (Figure 4.36).

Bonding is presumably through hydrogen bonding (1.2) between the surface hydroxyl groups of the cellulose fibre and the sulfur of the doped ZnS quantum dots. For the 3/2 spin multiplicity, this shift is approximately 0.86 eV, while for the 1/2 spin multiplicity, the shift is approximately 0.85 eV. These shifts are considered to be the same.

This result is comparable to the shift of the Fe 2p XPS spectrum for Fe₃O₄-coated Kraft fibres, where a shift of approximately 0.4 eV was observed.

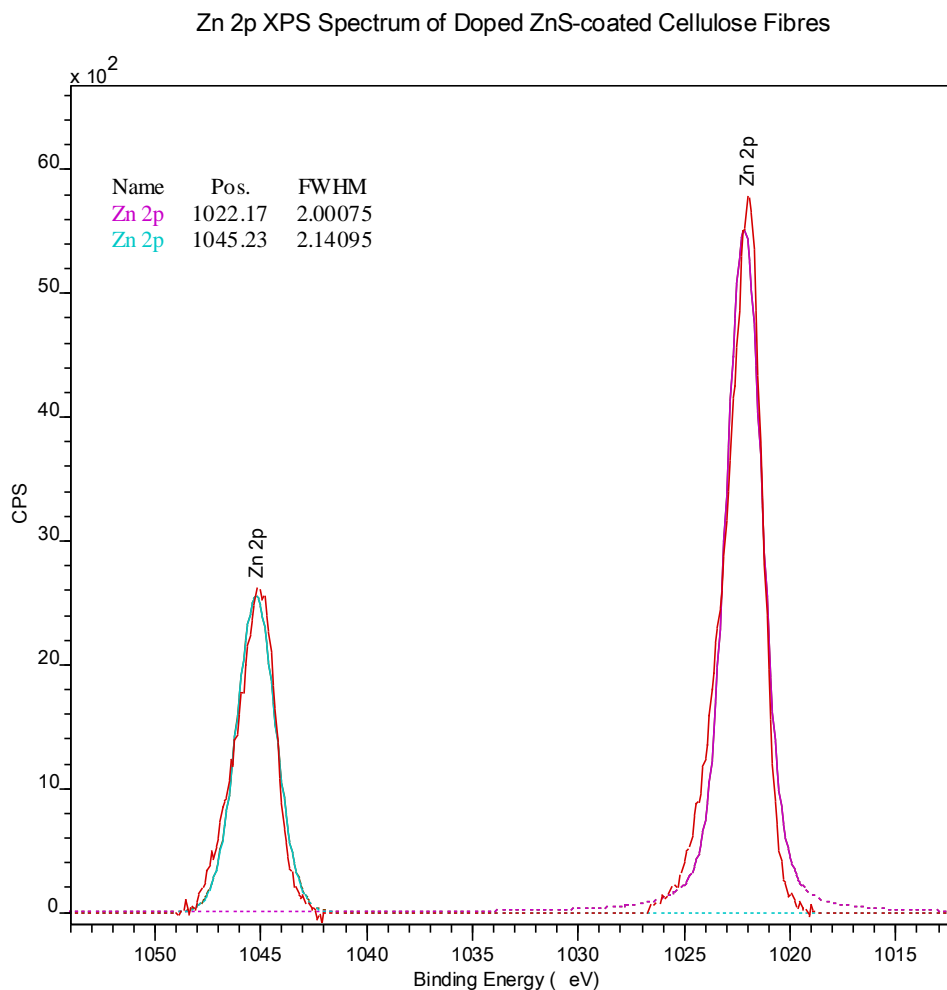


Figure 4.36. Zn 2p XPS spectrum for ZnS-coated Kraft Fibres (cellulose).

A comparison between the Zn 2p XPS spectra of doped ZnS quantum dots and doped ZnS-coated Kraft fibres is shown in Figure 4.37. From the plot, the shift in binding energy discussed above is clearly seen.

The respective peak heights are similar, although, the height of the doped ZnS-coated Kraft fibres is slightly smaller and is due to the smaller quantity of doped ZnS present on the cellulose fibre surface compared with doped ZnS quantum dot powder. Peak areas and full widths at half maximum (FWHM) are similar in all cases.

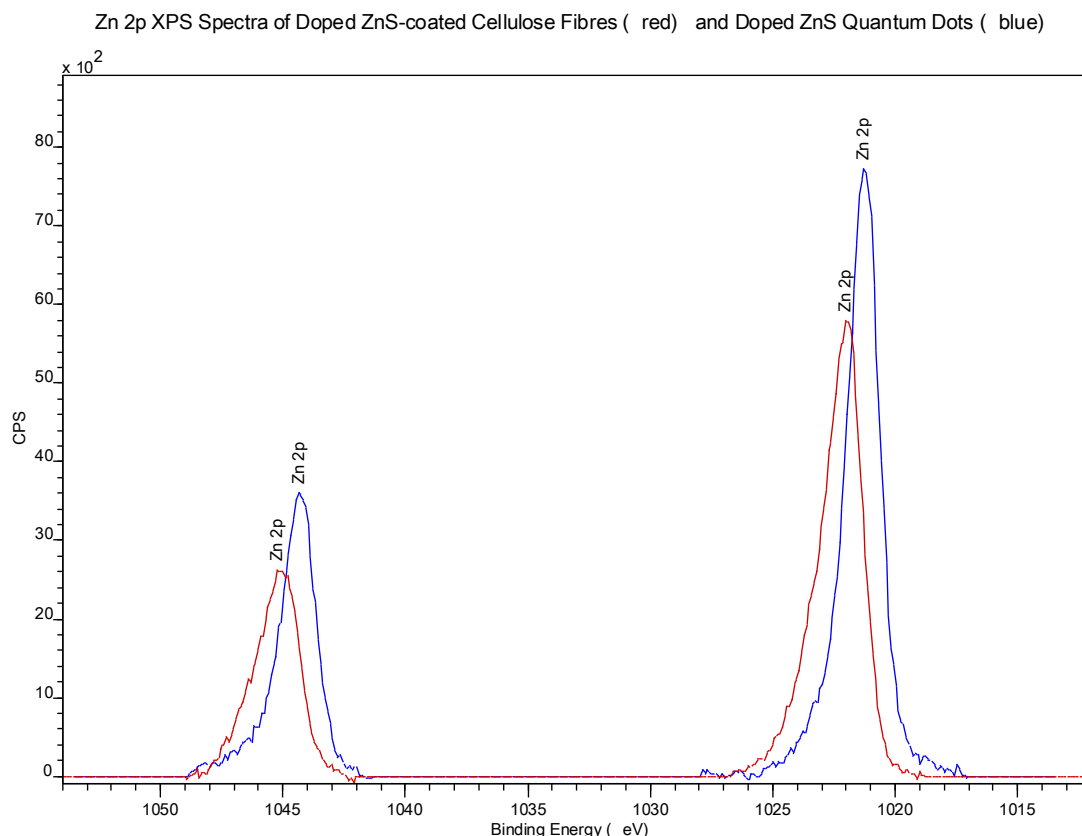
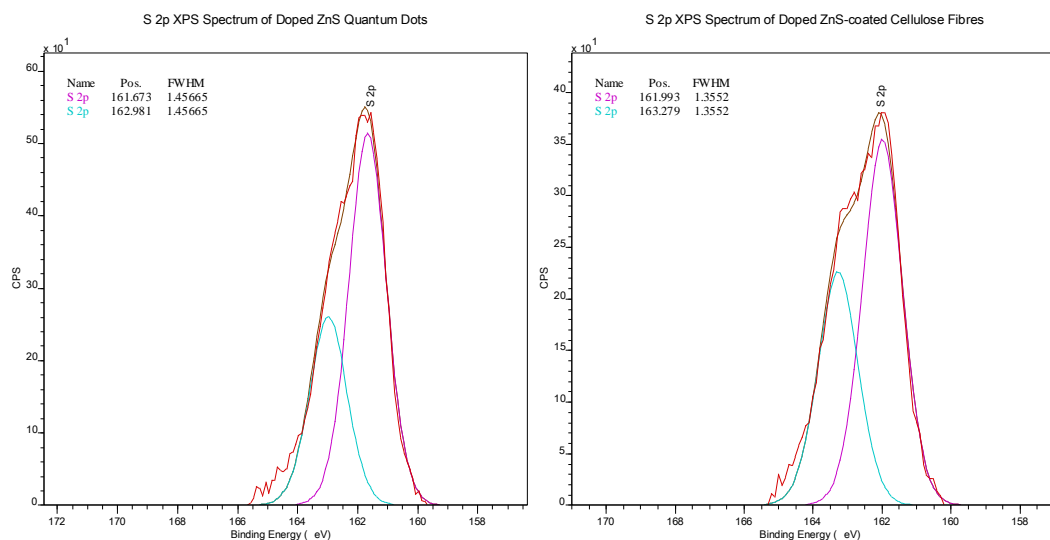


Figure 4.37. Overlaid Zn 2p XPS spectrum showing bonding energy shift between doped ZnS quantum dots and doped ZnS-coated Kraft fibres (cellulose).

The Zn 2p XPS data for doped ZnS quantum dots and doped ZnS-coated Kraft fibres are summarised in Table 4.4.

	Doped ZnS Quantum Dots	Doped ZnS- coated Kraft Fibres	
Species Present	Binding Energy (eV)	Binding Energy (eV)	Shift (eV)
ZnS (3/2)	1021.31	1022.17	0.86
ZnS (1/2)	1044.38	1045.23	0.85

Table 4.4. Summary of Zn 2p XPS binding energies and shifts for doped ZnS quantum dots and doped ZnS-coated Kraft fibres (cellulose).



S 2p XPS Spectrum of Doped ZnS-coated Cellulose Fibres (red) and Doped ZnS Quantum Dots (blue)

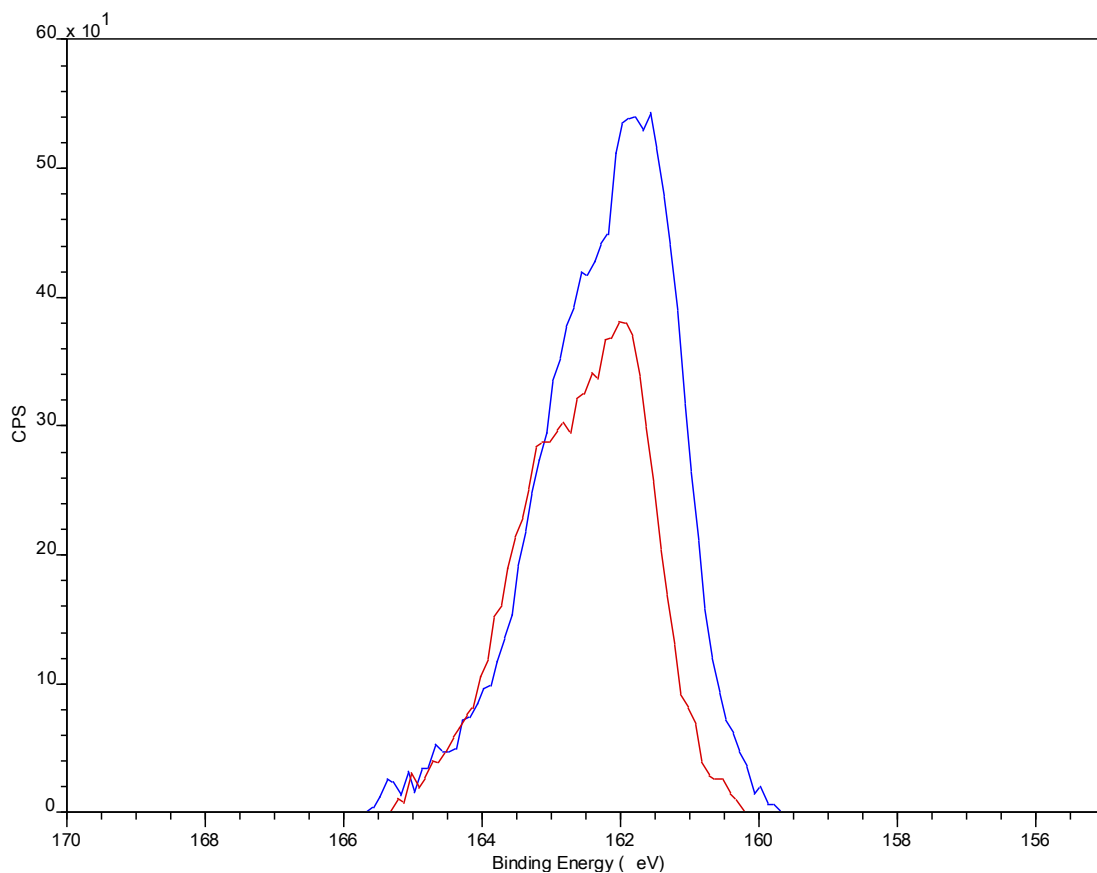


Figure 4.38. S 2p XPS spectra for doped ZnS-coated cellulose fibres (red) and doped ZnS quantum dots (blue).

The S 2p XPS spectra of doped ZnS-coated cellulose fibres and ZnS:Mn²⁺ quantum dots are shown in Figure 4.38. There is a shift in the XPS spectrum of

approximately 0.3 eV, further indication that bonding is taking place between the cellulose fibre surface and the doped ZnS quantum dots.

4.6. Synthesis of SiO₂-coated ZnS:Mn²⁺ Quantum Dots

In order to improve the photoluminescence emission from ZnS:Mn²⁺ quantum dots, an attempt was made to coat them with a layer of SiO₂.

The major limiting factor in the photoluminescence of ZnS:Mn²⁺, is radiationless recombination of an electron-hole pair at a surface defect site before a photon of light can be emitted (refer to Figure 1.18).

These surface defect sites result from so called 'dangling', meaning unsaturated surface bonds¹⁷⁸. Saturation of these unsaturated bonds with an inorganic capping layer such as SiO₂ has been reported to lead to a remarkable increase in the photoluminescence emission of ZnS:Mn²⁺ quantum dots^{142, 179}, as more electron-hole pairs are able to recombine at the site of luminescent centres rather than at the sites of defects.

The methods outlined in 2.2.14 were used to coat ZnS:Mn²⁺ quantum dots (synthesised in 2.2.11) with SiO₂. Unfortunately, both these methods were unsuccessful. This leads to the deduction that the SiO₂ coating on the surface of the ZnS:Mn²⁺ quantum dots is not uniform, and that defects are still present that lead to radiationless recombination of photogenerated electron-hole pairs.

A PL spectrum of SiO₂-coated ZnS:Mn²⁺ quantum dots is shown in Figure 4.39 and shows a drop in luminescence compared with uncoated ZnS:Mn²⁺ (Figure 4.10) Therefore, there has been no increase in photoluminescence on coating the ZnS:Mn²⁺ quantum dots with silica.

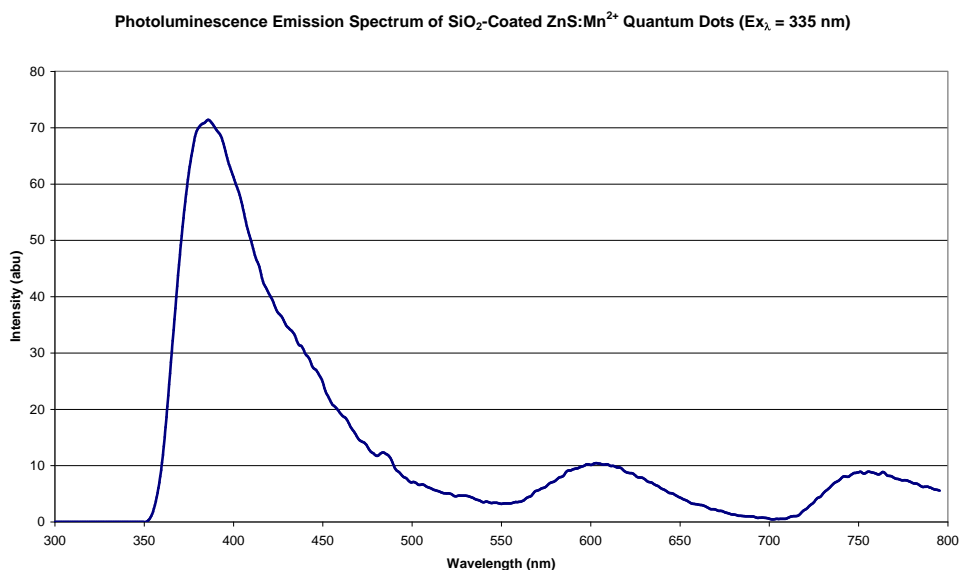


Figure 4.39. Photoluminescence emission spectrum of SiO₂-coated ZnS:Mn²⁺ quantum dots.

4.7. Synthesis of ZnS:Ag⁺ Quantum Dots

Attempts were made in order to dope ZnS with Ag⁺ in order to produce blue emitting ZnS quantum dots (2.2.13). Doping ZnS with Ag⁺ proved unsuccessful.

For a dopant to be included in the host lattice, its solubility must be equal or lower than that of the host. For Ag⁺, the solubility difference between Ag₂S ($K_{sp} = \sim 8 \times 10^{-51}$) and ZnS ($K_{sp} = \sim 2 \times 10^{-25}$) proved to be much too large.

A number of methods (summarised in Table 2.9) were used to attempt doping of ZnS with Ag⁺. The rationale behind these syntheses was to either complex Ag⁺ to keep it in solution and prevent the precipitation of Ag₂S^{130, 138, 141}, to use hydrothermal treatment in order to force Ag⁺ into the ZnS lattice due to high pressure¹⁴⁰, or to bring about the reaction using microwave energy¹³⁹.

All were unsuccessful and produced grey/black precipitates (Ag₂S) that did not exhibit any photoluminescence (Figures 4.40 and 4.41) due to the immediate precipitation of Ag₂S as a result of its extremely low K_{sp} . Therefore, co-precipitation with ZnS was not possible.

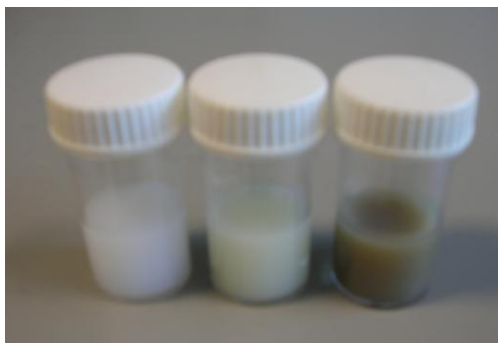


Figure 4.40. Photograph depicting the colours of doped ZnS quantum dots, (L-R), ZnS:Mn²⁺, ZnS:Cu²⁺ and the unsuccessful ZnS:Ag²⁺ (more likely a mixture of ZnS and Ag₂S).

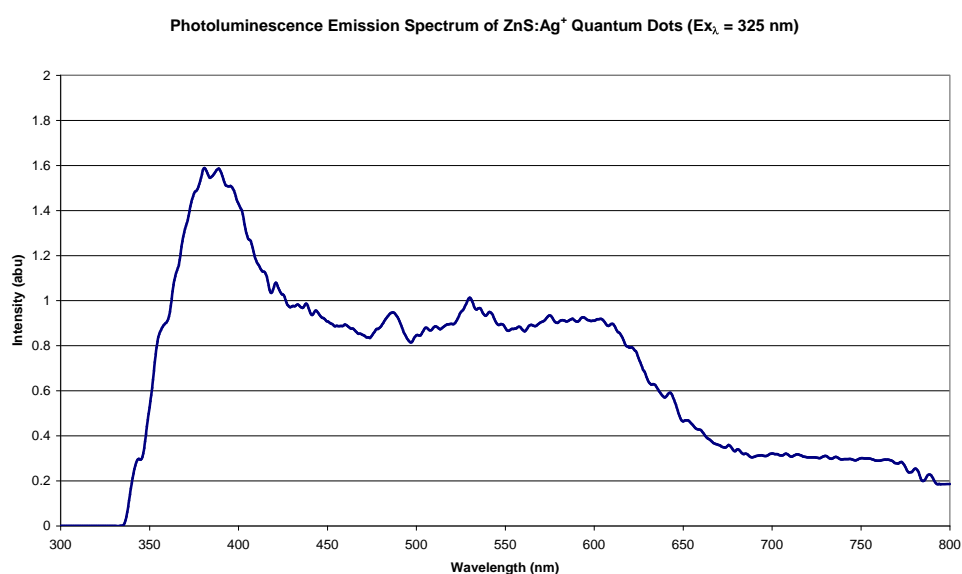


Figure 4.41. Photoluminescence emission spectrum of ZnS:Ag⁺ quantum dots.

The lack of success in repeating these methods here to produce ZnS:Ag⁺ quantum dots, must lead to the suggestion that the literature reports listed in Table 2.9 are not wholly correct. The respective authors show no photo evidence of a visible blue emission and offer very little in the way of photoluminescence spectroscopy data.

One can also postulate that perhaps the authors have been confused by the blue/UV emission arising from S²⁻ vacancies in the ZnS lattice, and that coprecipitates of ZnS and Ag₂S have been formed as opposed to ZnS:Ag⁺ quantum dots. The research conducted in this PhD programme has shown that

the difference in the solubilities of ZnS and Ag₂S is much too large to overcome when using an aqueous chemical precipitation method.

4.8. Chapter Summary

Doped-ZnS quantum dots were synthesised by a simple chemical precipitation method (2.2.11 and 2.2.12) and characterised by AA, PL spectroscopy, SEM, XPS and XRD. Mn²⁺ and Cu²⁺ doped varieties gave rise to pink/orange and green emissions respectively. The quantum dots were approximately 2 nm in diameter and were crystallised in the zinc blende structural type.

Kraft fibres (cellulose) were then successfully coated with these materials to produce photoluminescent cellulose fibres. Several approaches were used to coat the fibres with doped ZnS quantum dots – the ‘colloid’, ‘double dip’, ‘PDADMAC’ and ‘in situ’ methods. The most successful in providing a uniform coating was the ‘in situ’ approach (2.2.15 and 2.2.16), whereby the whole fibre surface was coated with doped ZnS quantum dots, including individual fibrils.

An attempt was made to coat ZnS:Mn²⁺ quantum dots with SiO₂ to improve the photoluminescence emission by reducing the surface defect states. This proved unsuccessful and the photoluminescence of the quantum dots decreased as a result.

Also investigated as a dopant was Ag⁺ (for blue emission), however, this proved unsuccessful. For Ag⁺, the large solubility difference between ZnS and Ag₂S proved to be too great to include Ag⁺ in the ZnS lattice, even when complexing agents, hydrothermal and microwave synthesis methods were used.

Chapter 5

ELECTROMAGNETIC INTERFERENCE (EMI) SHIELDING

As discussed in section 1.7, both electrically conducting and magnetic samples are candidates for EMI shielding materials. The lack of processability of conducting polymers and nanoparticles means they are not useful by themselves – instead they need to be attached to a workable substrate. Several samples were synthesised here, using newsprint, unbleached Kraft board and unbleached cotton fabric as the substrate, and their EMI shielding properties evaluated at the Defence Science and Technology Organisation (DSTO) in Melbourne, Australia. This work follows on from the work done on magnetic Kraft fibres.

Newsprint, unbleached Kraft board and unbleached cotton fabric were coated by magnetite nanoparticles synthesised in 2.2.2. The substrates were unable to be coated as easily as the individual Kraft fibres due to the presence of sizing agents in the paper sheet. Instead, a starch binder was used to adhere the nanoparticles to the surface of the particular substrate, painted on to provide a smooth and uniform coating (2.2.9).

For polypyrrole-coated samples a chemical polymerisation was used, as described in 2.2.8, with the dopant (*p*-TSA) amount varied to obtain optimum conductivities. Substrates coated with both magnetite and polypyrrole were synthesised simply by coating a polypyrrole-coated substrate with magnetite using the method described in 2.2.10

5.1. Scanning Electron Microscopy (SEM)

The SEM images presented in Figures 5.1 and 5.2 show the morphology of an uncoated sample of newsprint. The fibre structure can be seen, including the individual fibrils at higher magnification.

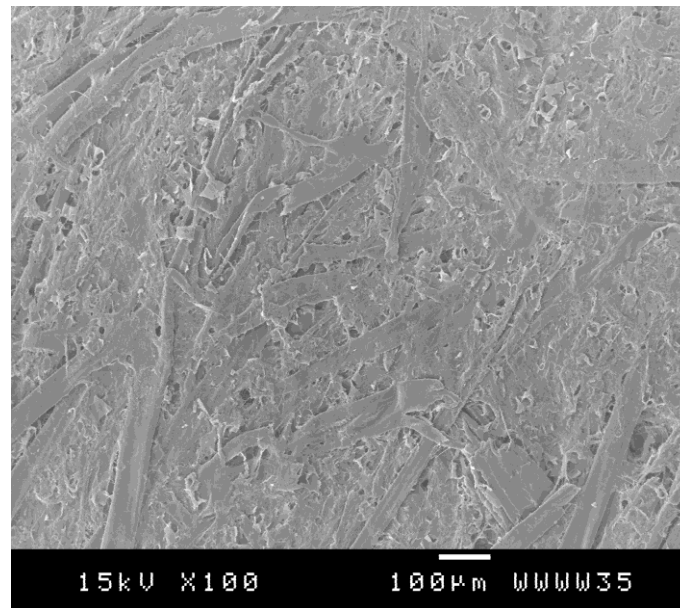


Figure 5.1. Low magnification SEM image of uncoated newsprint.

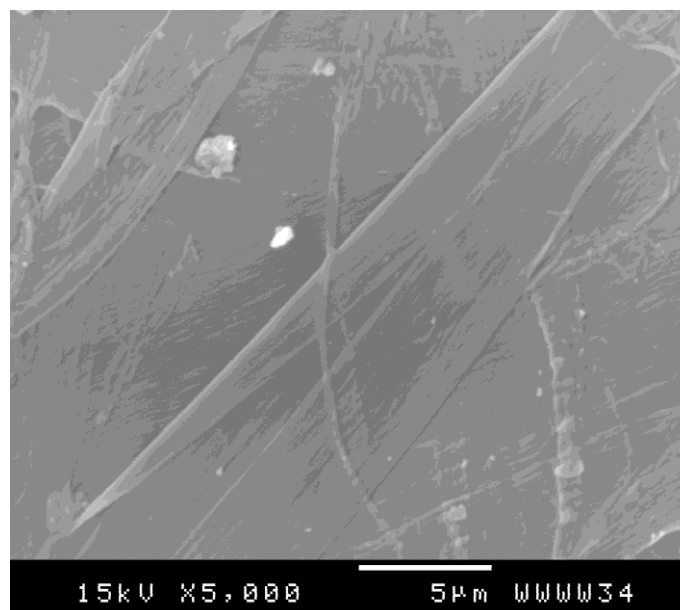


Figure 5.2. SEM image of fibre surface of uncoated newsprint showing starch binder particles.

On coating with magnetite by the use of a starch binder, a distinct morphology change is observed (Figures 5.3 and 5.4), largely due to the particles of the starch binder. The coating covers the entire sheet, and none of the fibres or fillers can be seen.

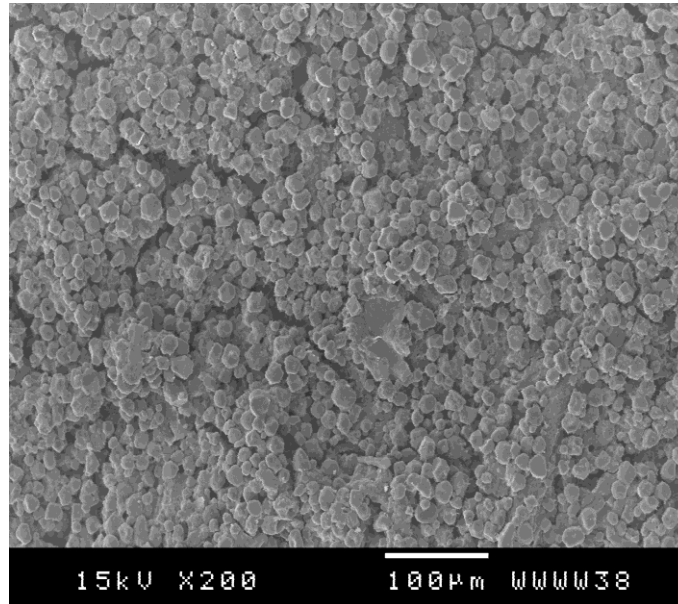


Figure 5.3. Low magnification SEM image of magnetite-coated newsprint.

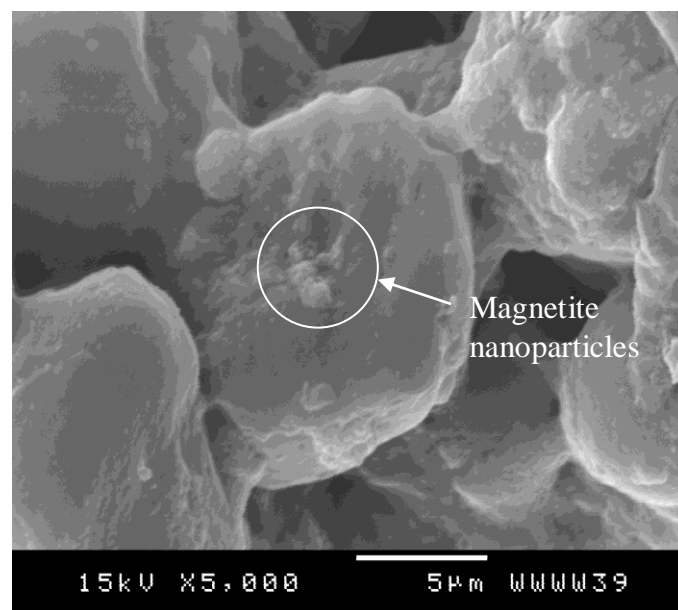


Figure 5.4. SEM image of magnetite-coated newsprint showing magnetite agglomerations present in the starch coating,

The starch binder gives a 'globular' morphology of spheres approximately 20 μm in diameter, in which agglomerations of magnetite nanoparticles are present both inside and out.

On coating with polypyrrole, a complete coating can be observed (Figures 5.5 and 5.6). Some areas exist with excess polypyrrole. This may reduce the overall conductivity of the samples and in turn reduce the shielding effectiveness (1.7).

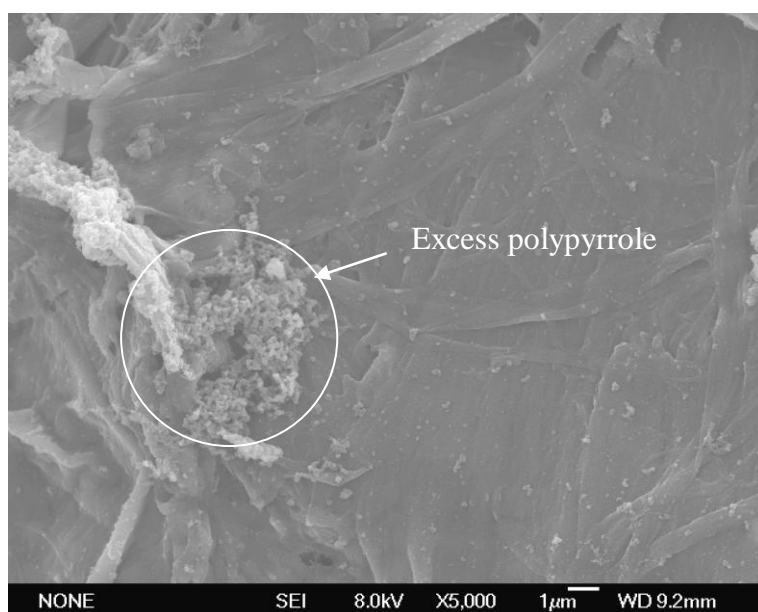


Figure 5.5. SEM image of polypyrrole-coated newsprint.

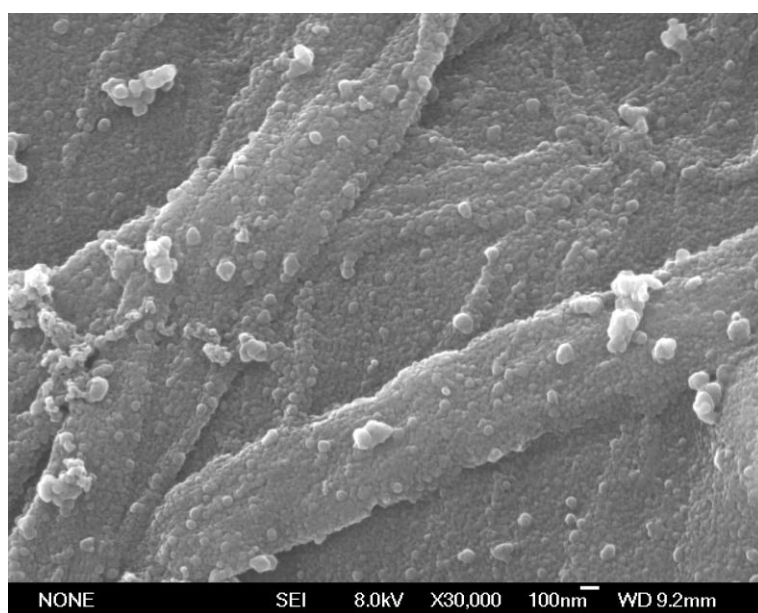


Figure 5.6. High magnification SEM image of polypyrrole-coated newsprint.

Polymer particles (of approximately 100-150 nm) are visible on the surface and on individual fibrils. This is concordant with results obtained in previous work by Johnston *et al.*¹⁰⁸ in which individual cellulose fibres and wool fibres were coated with polypyrrole and polyaniline.

Bonding is facilitated through hydrogen bonding (1.2) between the surface hydroxyl groups present on the cellulose fibre surface, and the nitrogen lone pairs of the polypyrrole backbone.

Newsprint samples coated first with polypyrrole and then with magnetite, shown in Figures 5.7 and 5.8, display a morphology similar to that of magnetite-coated newsprint. The coating (consisting of approximately 20 μm spheres of starch binder containing magnetite agglomerations) covers the whole surface of the paper and none of the fibres can be seen.

Cracks appear on the surface of the material and arise from the drying of the starch binder. It is not known how these cracks affect the shielding effectiveness of the materials, as no samples were synthesised without cracks.

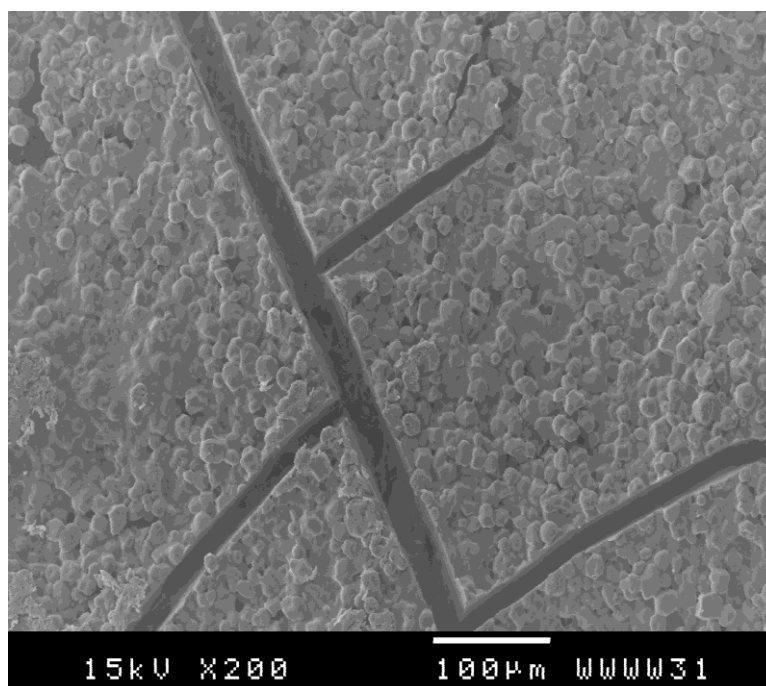


Figure 5.7. Low magnification SEM image of magnetite and polypyrrole-coated newsprint.

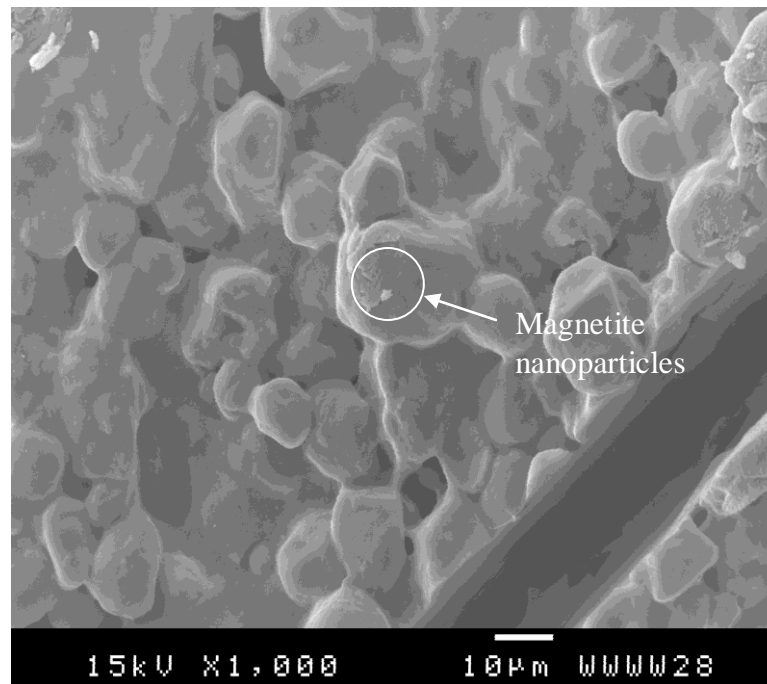


Figure 5.8. SEM image of magnetite and polypyrrole-coated newsprint.

The SEM image shown in Figure 5.9 shows the morphology of an uncoated sample of Kraft board. Like newsprint, the fibre structure can be seen, in particular, the long Kraft fibres – characteristic of the chemical pulping process (1.2.6.2). The individual fibrils are also visible.

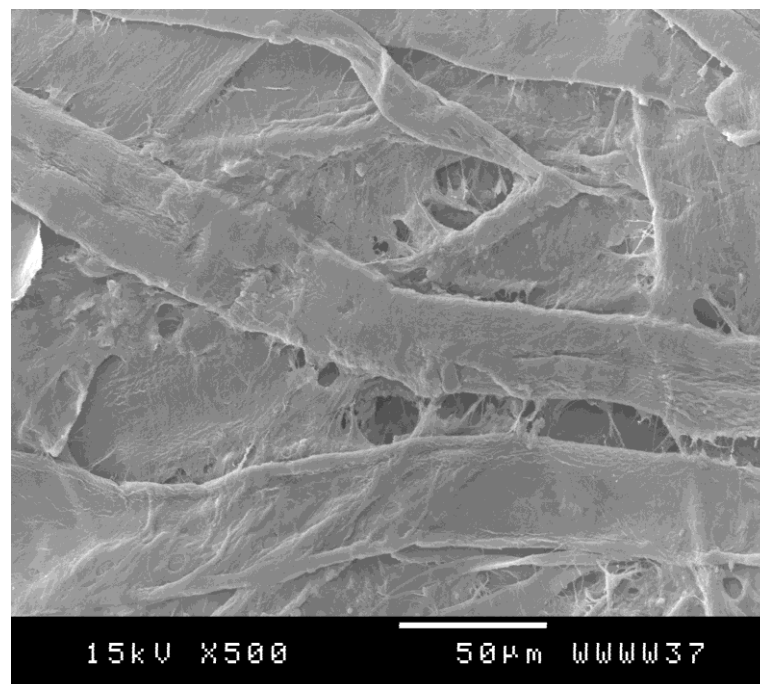


Figure 5.9. SEM image of uncoated Kraft board.

A comparison with SEM images of magnetite-coated samples (Figures 5.10 and 5.11) shows a morphology change due to the coating, largely associated with the 'globular' starch binder.

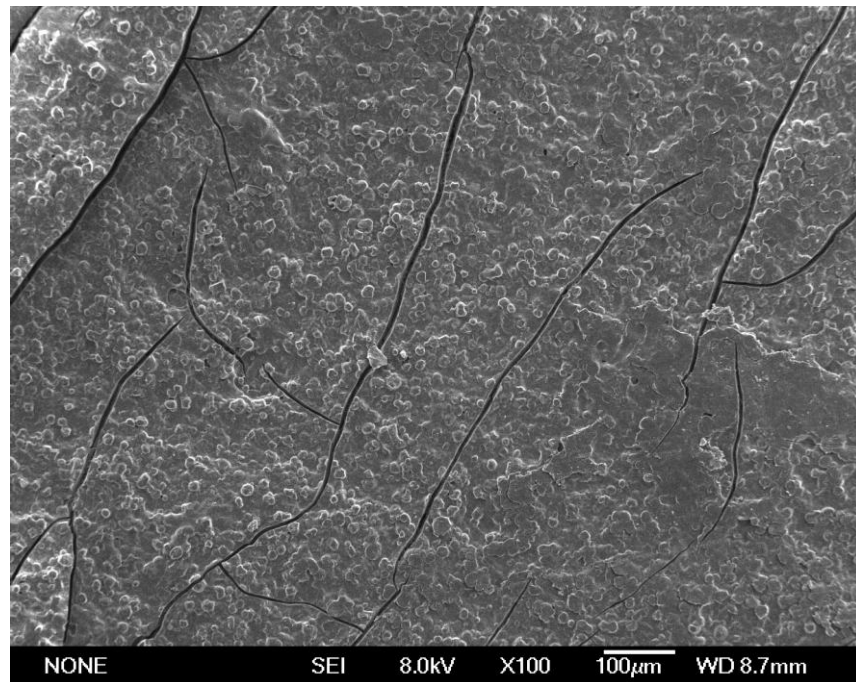


Figure 5.10. SEM image of magnetite-coated Kraft board.

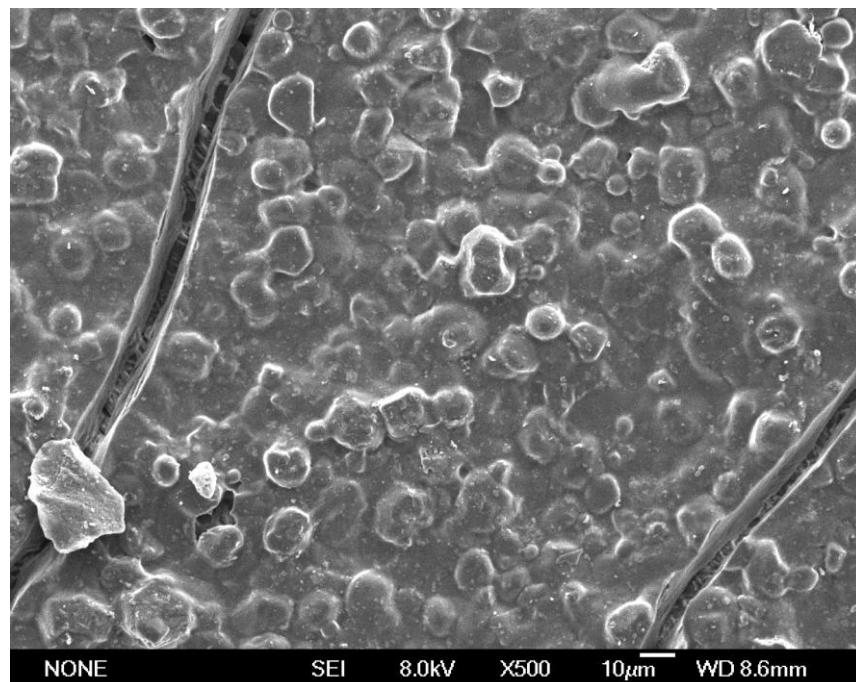


Figure 5.11. SEM image of magnetite-coated Kraft board.

This is comparable to magnetite-coated newsprint, where the coating (consisting of 20 μm spheres of starch containing magnetite agglomerations) covers the entire surface, and no fibres can be seen. Again cracks are present on the surface of the material and arise during the drying of the starch binder.

Polypyrrole-coated Kraft board (Figures 5.12-5.14) show a morphology similar to that obtained for newsprint coated samples (Figures 5.5 and 5.6) and in previous work involving polypyrrole coated cellulose, wool and possum fibres¹⁰⁸.

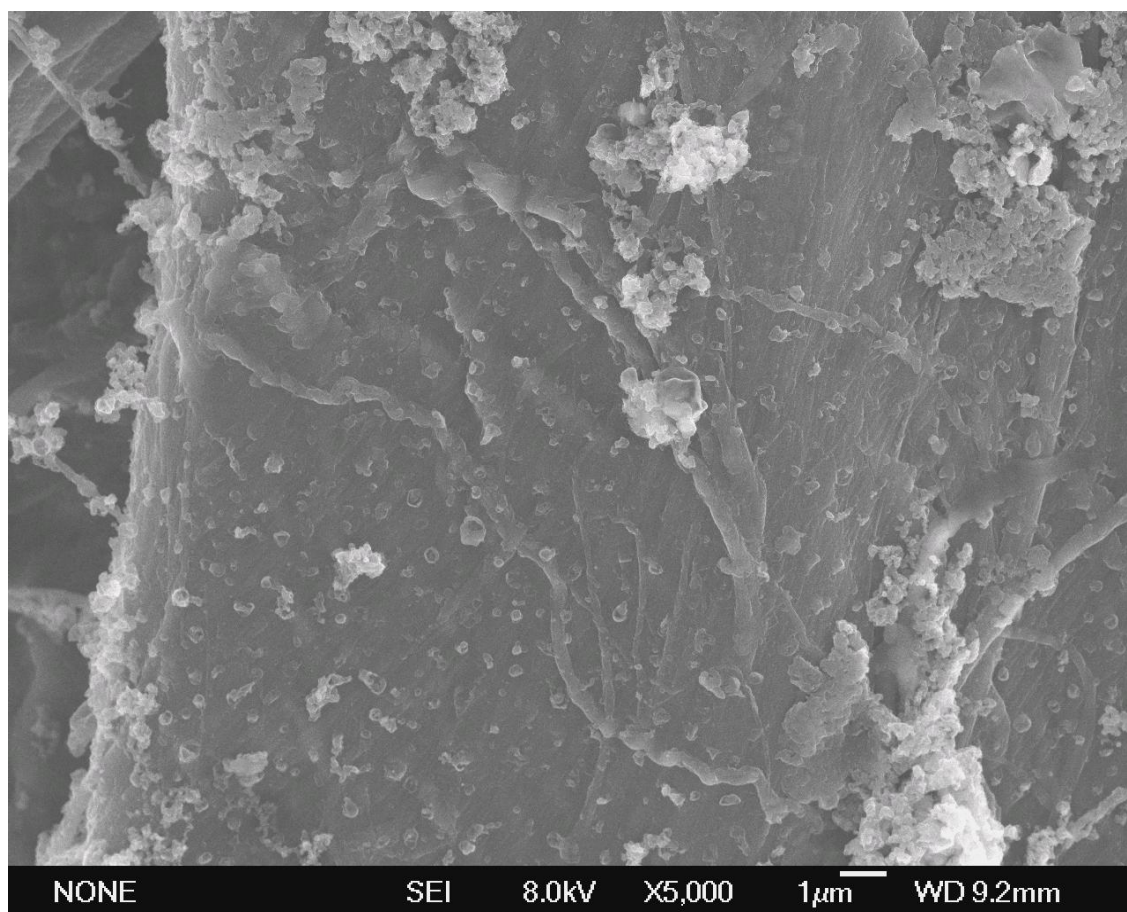


Figure 5.12. SEM image of polypyrrole-coated Kraft fibres.

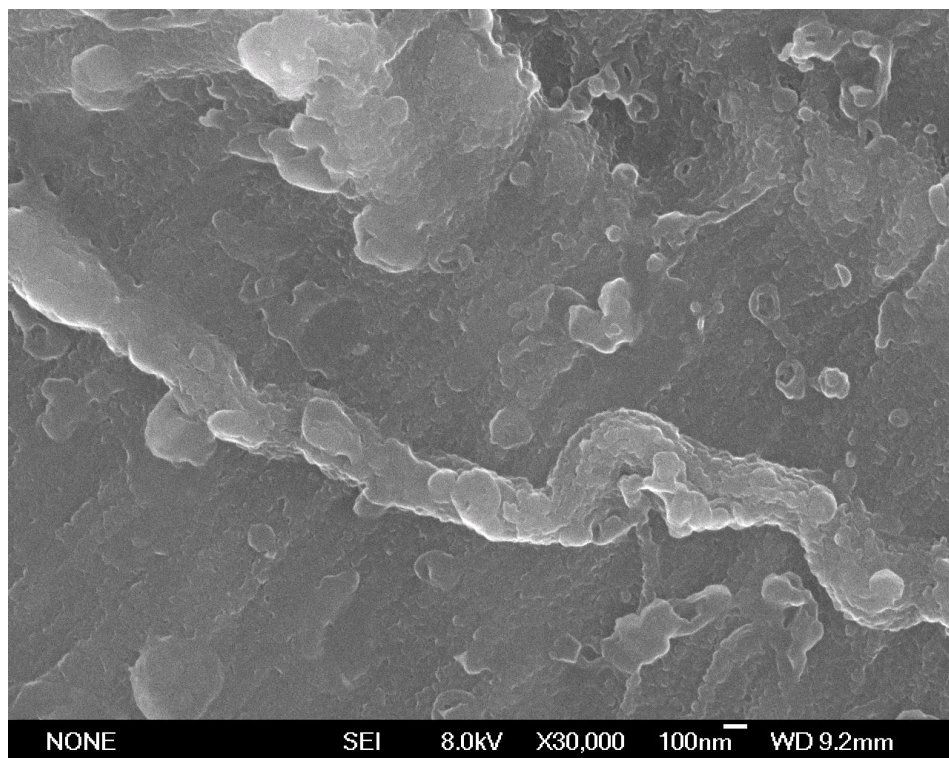


Figure 5.13. SEM image of polypyrrole-coated Kraft board, showing individually coated fibrils.

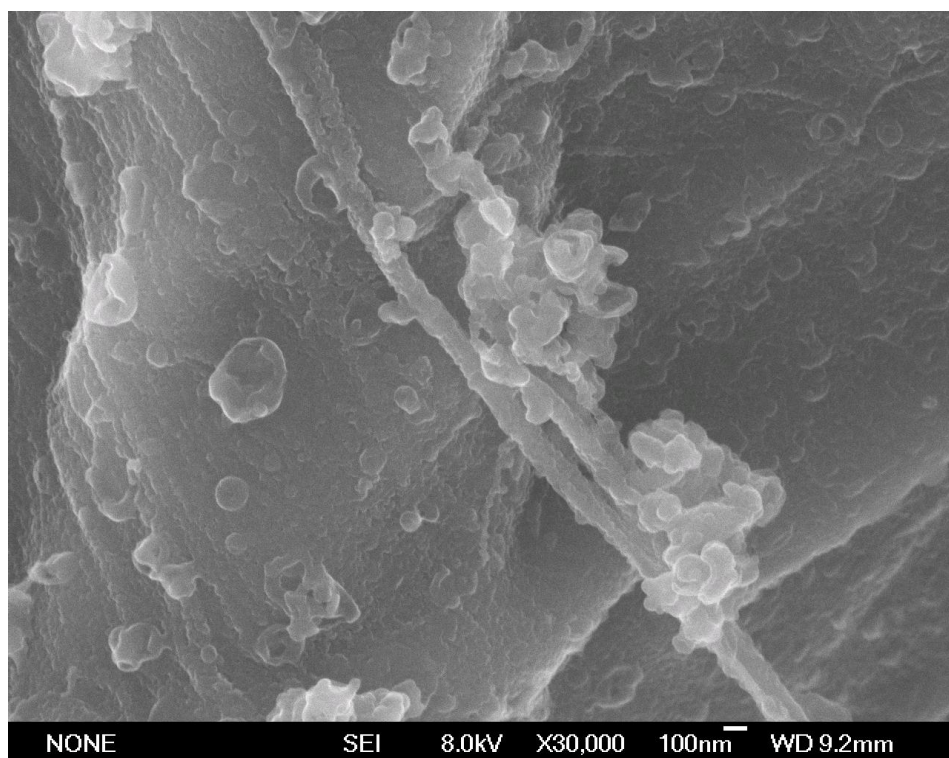


Figure 5.14. SEM image of polypyrrole-coated Kraft board, showing individually coated fibrils.

The fibre surface and individual fibrils are completely encapsulated with polypyrrole particles approximately 100-150 nm in size. The white areas visible on the surface of the fibre arise from the charging of excess polypyrrole.

EDS maps of polypyrrole-coated Kraft fibres are shown in Figure 5.15.

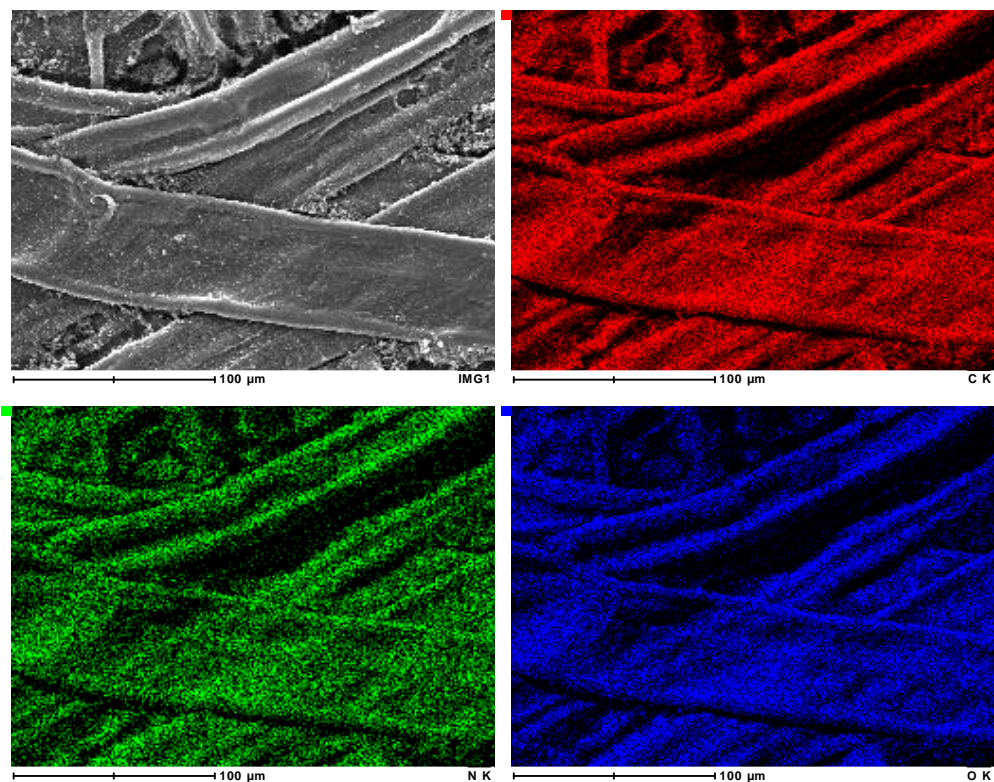


Figure 5.15. EDS maps of polypyrrole-coated Kraft fibres, showing the presence of C, N, and O on the fibre surface, confirming polypyrrole has completely encapsulated the fibre.

The maps of C, N, and O correlate extremely well, and confirm that the surface is coated evenly with polypyrrole.

As is the case with magnetite and polypyrrole-coated newsprint, the morphology of magnetite and polypyrrole-coated Kraft board (Figure 5.16 and 5.17) is essentially the same as magnetite-coated Kraft board.

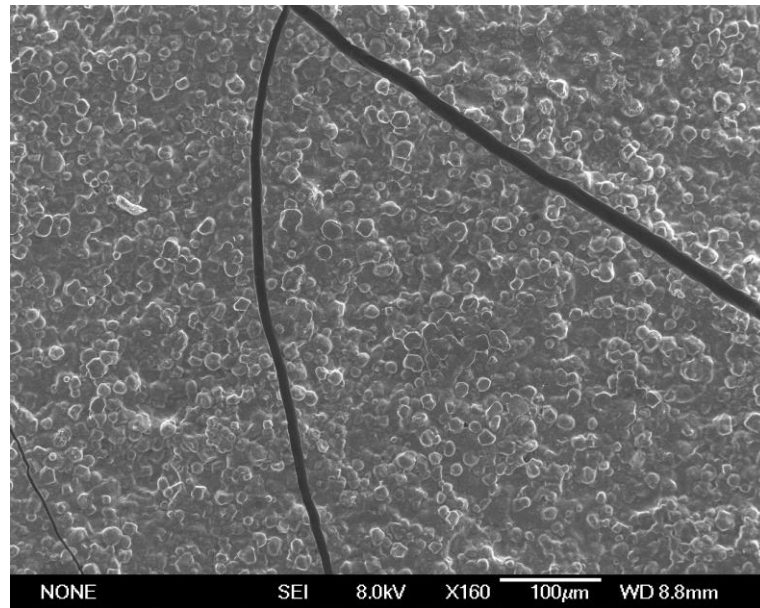


Figure 5.16. Low magnification SEM image of magnetite and polypyrrole-coated Kraft board.



Figure 5.17. SEM image of magnetite and polypyrrole-coated Kraft board.

The individual fibres and the additional polypyrrole coating cannot be seen underneath the starch particles containing magnetite agglomerations.

Again, the particle size of the starch binder containing magnetite is approximately 20 µm. Cracks again appear on the surface of the material and occur in the drying of the starch binder.

EDS maps of magnetite and polypyrrole-coated Kraft board are shown in Figures 5.18 and 5.19. The maps of C, N, O and Fe confirm the presence of polypyrrole and magnetite coatings on the surface of the Kraft board, while the high magnification EDS images shown in Figure 5.19 show the magnetite present as agglomerations in the starch binder, but overall the coating is uniform.

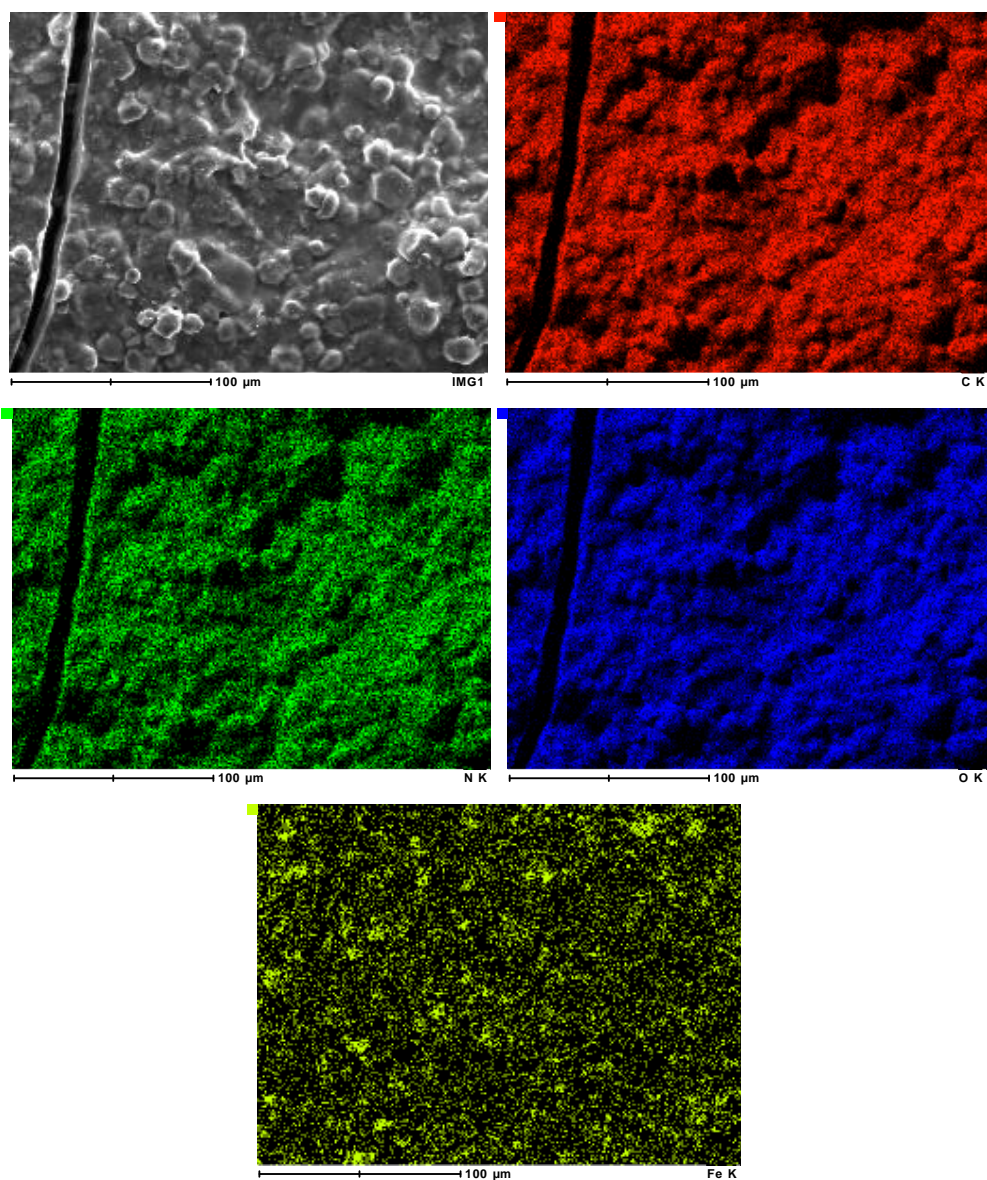


Figure 5.18. EDS maps of polypyrrole and magnetite-coated Kraft fibres, showing the presence of C, N, O and Fe on the fibre surface.

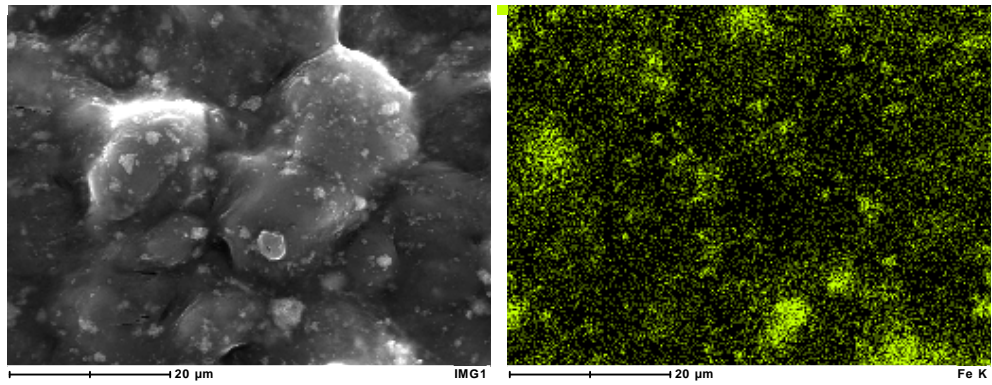


Figure 5.19. High magnification EDS map of Fe, showing the magnetite agglomerations present within the starch binder.

An SEM image of uncoated cotton fabric is shown in Figures 5.20 and 5.21. The individual yarns are visible.

Magnetite-coated cotton fibres (Figure 5.22) display the morphology of the starch binder as seen in magnetite-coated newsprint and Kraft board. However, in the case of cotton, the individual yarns can be seen through the starch and magnetite coating. Again, the particle size of the starch binder containing magnetite agglomerations is approximately 20 μm.

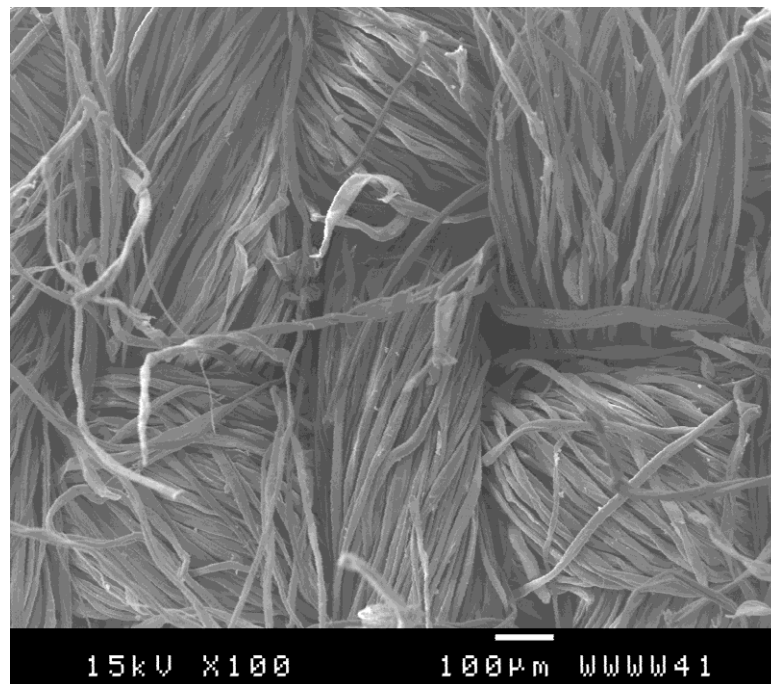


Figure 5.20. Low magnification SEM image of uncoated cotton fabric.

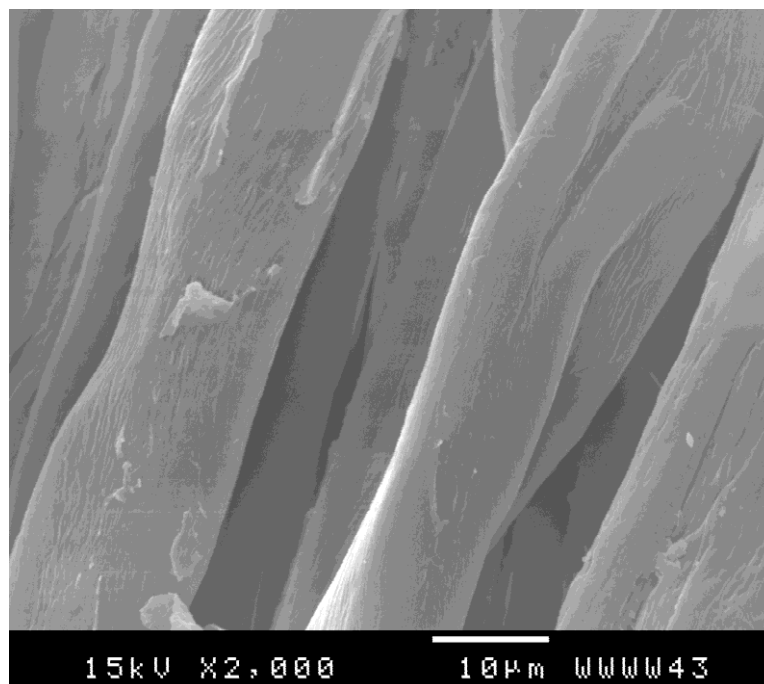


Figure 5.21. SEM image of uncoated cotton fabric.

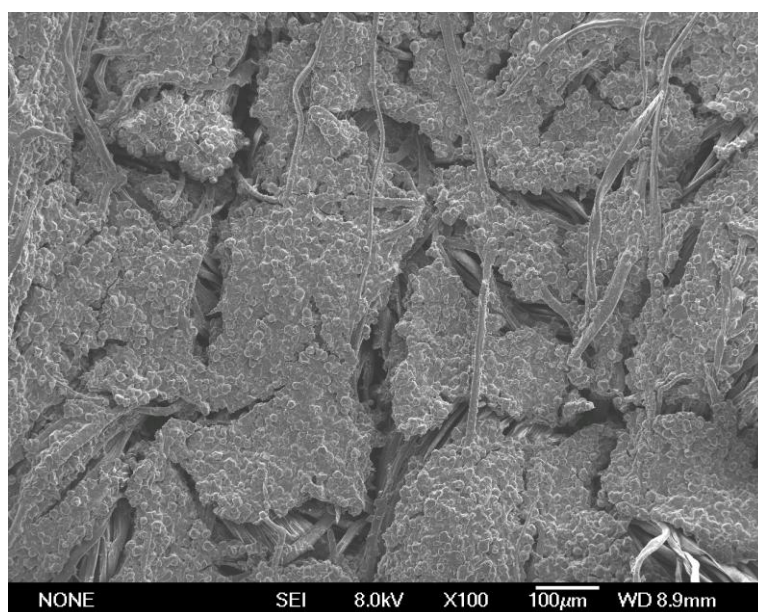


Figure 5.22. Low magnification SEM image of magnetite-coated cotton fabric.

On coating with polypyrrole (Figures 5.23 – 5.25), the cotton surface, including the individual fibrils, becomes completely encapsulated with the polymer.

The cellulose surface of cotton is very similar to that of paper fibres, and so bonding is also facilitated through hydrogen bonding (1.2) between the surface

hydroxyl groups of the cellulose fibre, and the lone pairs present on the nitrogen of the polypyrrole backbone.

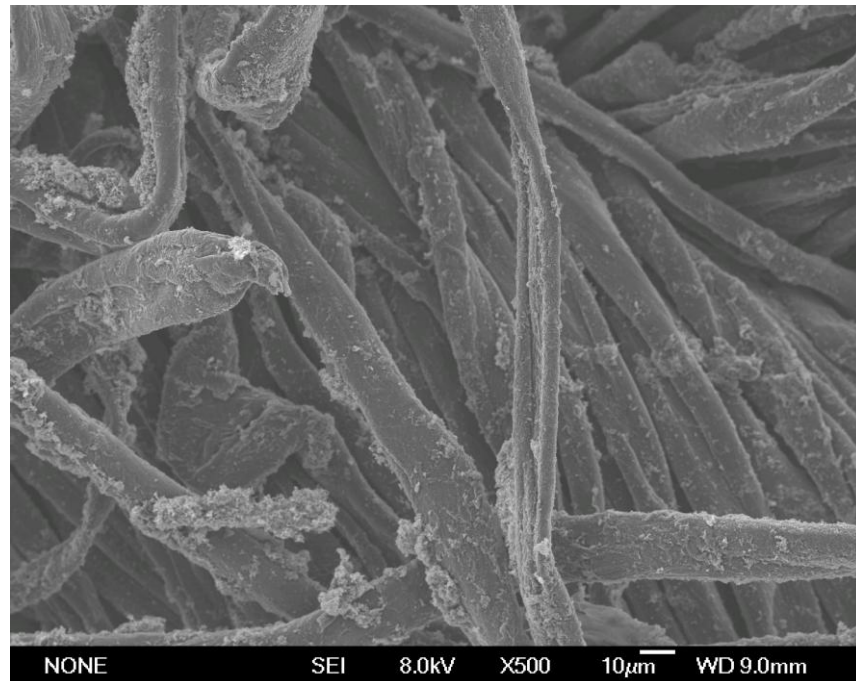


Figure 5.23. Low magnification SEM image of polypyrrole-coated cotton fabric.

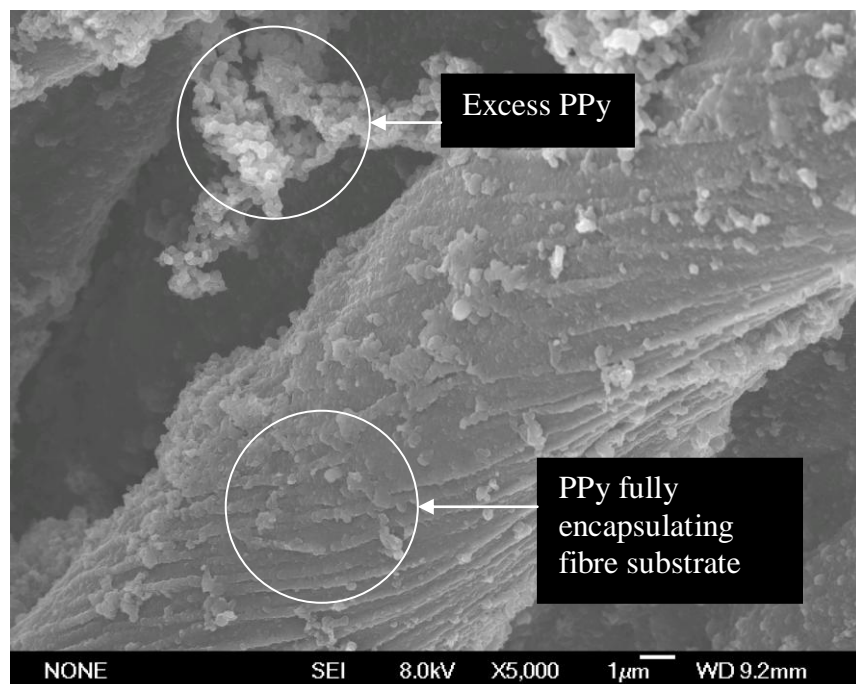


Figure 5.24. SEM image showing polypyrrole-coated cotton fibres.

The particles are present on the surface as small spheres, approximately 100-150 nm in diameter. Such results are similar to polypyrrole-coated newsprint and Kraft board in this research, and also to results obtained in previous research involving cellulose, wool and possum fibres, and paper sheets¹⁰⁸.

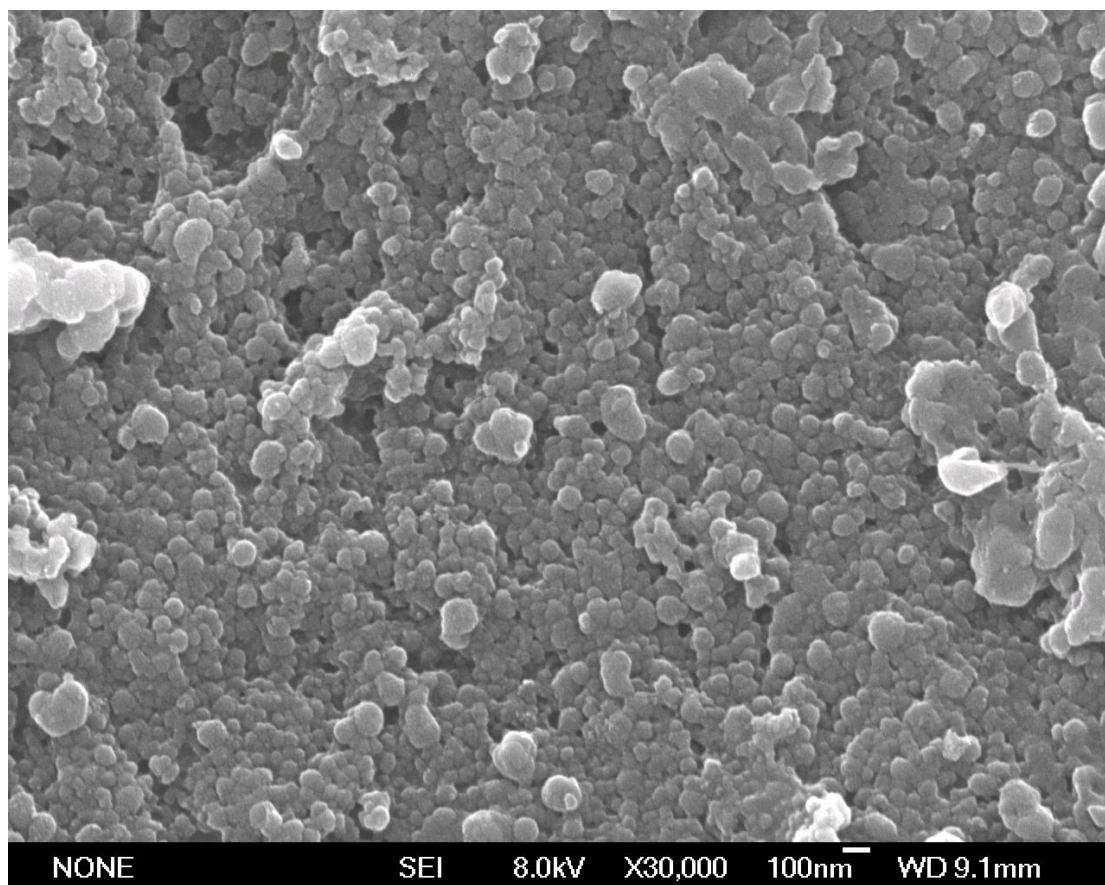


Figure 5.25. SEM image showing polypyrrole coating on cotton fibre surface.

EDS maps of polypyrrole-coated cotton fibres are shown in Figure 5.26. The maps of C, N, and O correlate well with the complimentary SEI image and hence confirm the presence of the polypyrrole coating on the surface of the cotton fibres.

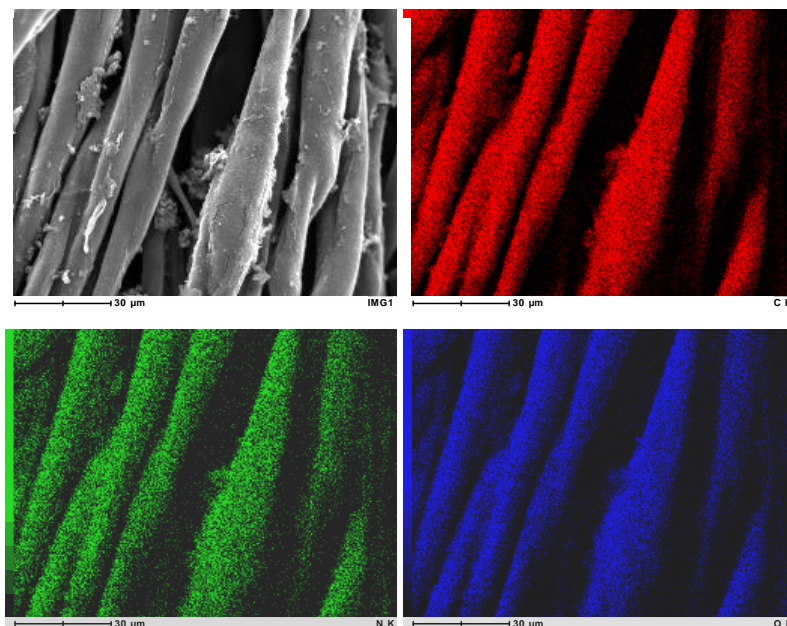


Figure 5.26. EDS maps of polypyrrole-coated cotton fabric, showing the presence of C, N, and O on the fibre surface, confirming polypyrrole has completely encapsulated the fibre

The morphology of polypyrrole and magnetite-coated cotton fabric (Figures 5.27 and 5.28) is similar to that obtained for magnetite-coated cotton fabric. In this case however, the polypyrrole coating present on the surface can be seen on the individual yarns visible beneath the starch and magnetite coating,

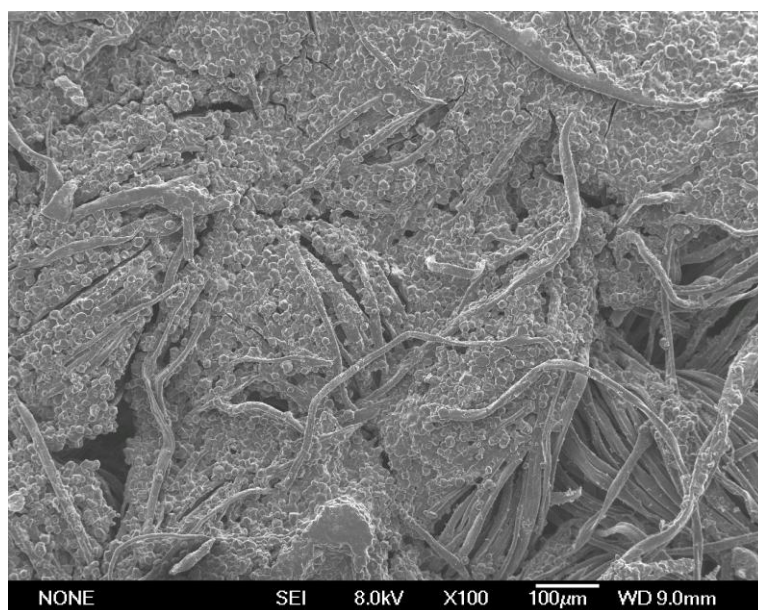


Figure 5.27. Low magnification SEM image of magnetite and polypyrrole-coated cotton fabric.

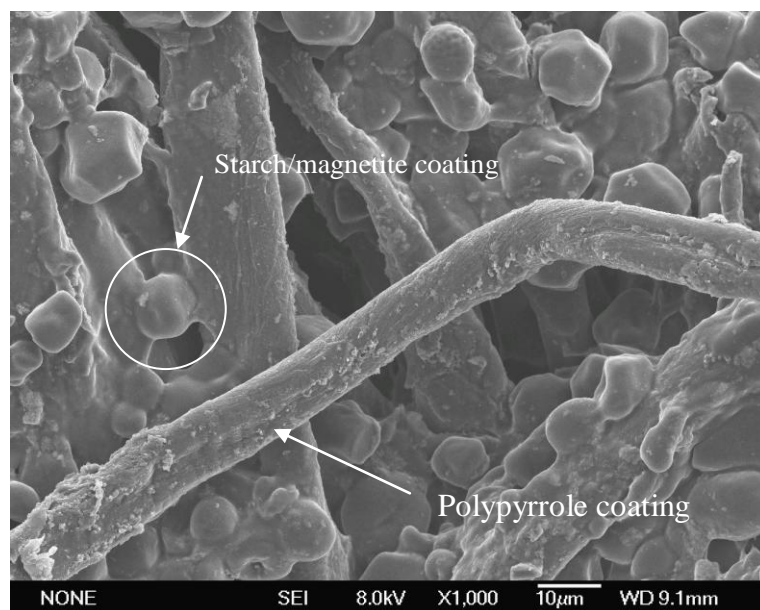


Figure 5.28. SEM image of magnetite and polypyrrole-coated cotton fabric.

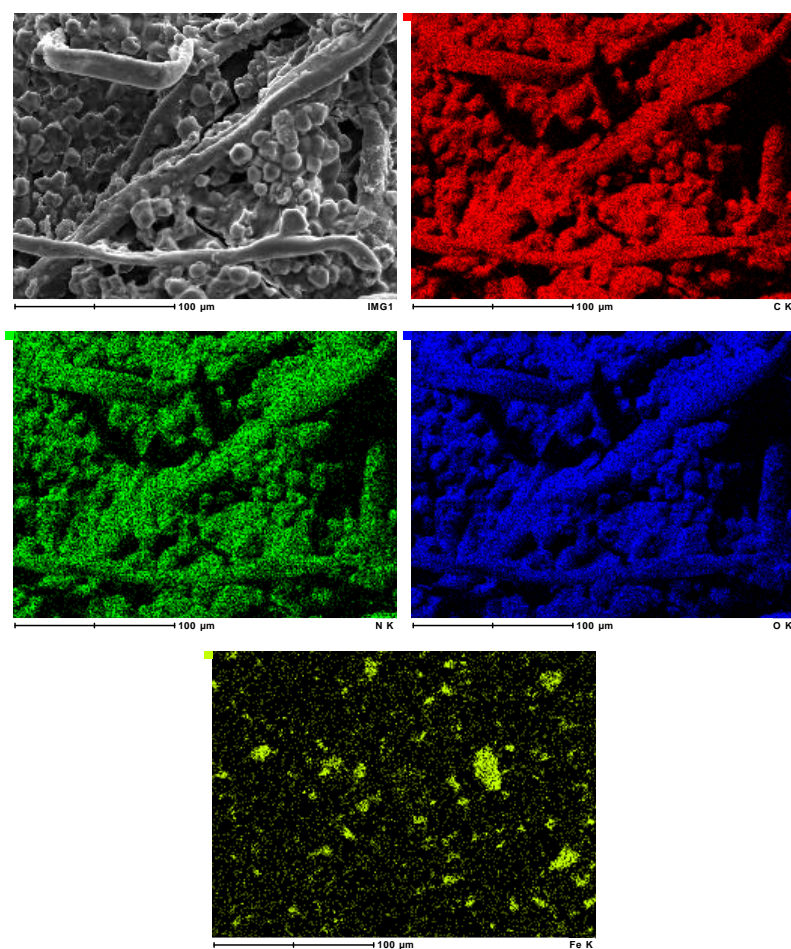


Figure 5.29. EDS maps of polypyrrole and magnetite-coated cotton fabric, showing the presence of C, N, O and Fe on the fibre surface.

The EDS maps of C, N, O and Fe for polypyrrole and magnetite-coated cotton fabric are shown in Figure 5.29. The maps correlate well and confirm that the surface of the cotton fabric is coated with polypyrrole and that magnetite is present across the surface also, particularly in agglomerations.

5.2. DC Conductivity Measurements

The polymerisation of pyrrole gives a homogenous coating of conducting polypyrrole on the surface of the particular substrate. The substrates, originally light in colour, appear black due to the high absorption across the visible spectrum by conjugated polymers⁹⁸.

A series of experiments was conducted in order to optimise the conductivity based on the concentration of pyrrole (Table 5.1).

Sample	Pyrrole concentration (mol dm ⁻³)	Conductivity (S cm ⁻¹)
ACS3-02C	0.05	0.03
ACS3-02D	0.1	0.3
ACS3-02E	0.2	1.2
ACS3-02F	0.5	0.4

Table 5.1. Table summarising the conductivities of a variety of polypyrrole-coated cotton fabrics, based on the concentration of pyrrole monomer used in the synthesis.

It was found that the optimum concentration of pyrrole monomer was 0.2 mol dm⁻³. This is also evident on examining photographs of the coated materials (Figure 5.30), as materials synthesised with lower concentrations of pyrrole monomer appear ‘patchy’ and uneven. At pyrrole concentrations of 0.5 mol dm⁻³ a large amount of excess polypyrrole is present on the surface of the substrate, which could account for the decrease in conductivity achieved using this monomer concentration.

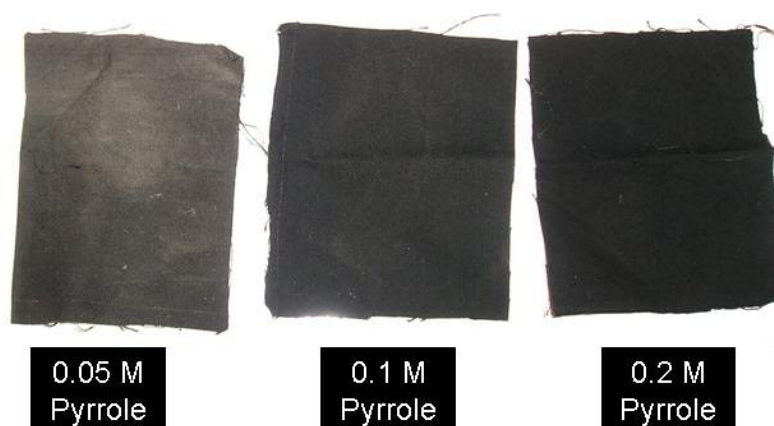


Figure 5.30. Photograph showing polypyrrole-coated cotton fabrics synthesised using different pyrrole monomer concentrations.

A pyrrole monomer concentration of 0.2 mol dm^{-3} was then used for all subsequent syntheses involving pyrrole.

A range of polypyrrole-coated cotton fabric samples doped with *p*-toluenesulfonic acid were synthesised with the aim of increasing the conductivity of the samples. These are summarised in Table 5.2.

Sample	PPy concentration (mol dm^{-3})	<i>p</i> -TSA concentration (mol dm^{-3})	Conductivity (S cm^{-1})
ACS3-08A	0.2	0.02	0.5
ACS3-09A	0.2	0.05	0.9
ACS3-09B	0.2	0.1	0.8
ACS3-10B	0.2	0.125	1.6
ACS3-10C	0.2	0.2	0.8

Table 5.2. Table summarising the conductivities of a variety of polypyrrole-coated cotton fabrics, based on the concentration of *p*-toluenesulfonic acid used in the synthesis.

Two polypyrrole-coated cotton fabrics doped with *p*-toluenesulfonic acid were prepared, one at room temperature (20°C) and one in a refrigerator set at 2°C . It was found that a lower temperature gave a higher conductivity. A possible explanation for this is that a lower thermal energy allows more time for the polymer chains to align and hence increases conductivity axially. It is not

possible to complete the polymerisation at an even lower temperature as the solvent (water) will freeze. These results are summarised in Table 5.3 below. All subsequent syntheses involving pyrrole were carried out at 2 °C.

Sample	PPy conc. (mol dm ⁻³)	p-TSA conc. (mol dm ⁻³)	Temperature (°C)	Conductivity (S cm ⁻¹)
ACS3-10B	0.2	0.125	20	1.6
ACS3-11A	0.2	0.125	2	3.6

Table 5.3. Effect of temperature on the conductivity of polypyrrole-coated cotton fabrics.

5.3. EMI Shielding Measurements

When a material is subjected to electromagnetic radiation, some of the radiation is reflected or absorbed and some is transmitted (1.7). An insulating material will generally transmit almost all the incident radiation, while a very highly conducting material (eg. a metal) will reflect almost all the incident radiation.

The shielding effectiveness of a metal plate is shown in Figure 5.31. It can be seen from the plot, that between 1-18 GHz almost none of the EMI radiation is transmitted through the sample.

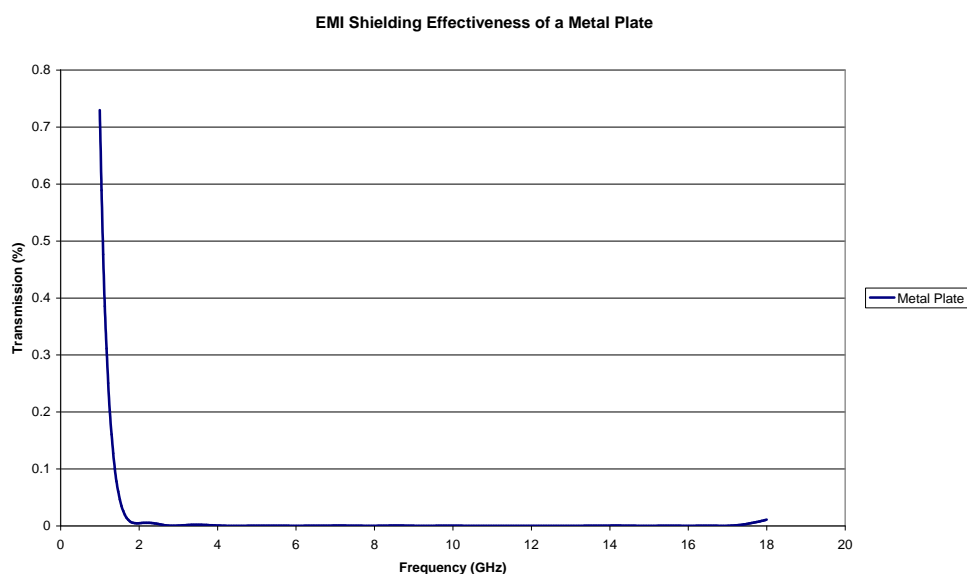


Figure 5.31. EMI shielding effectiveness of a metal plate.

The shielding effectiveness of coated newsprint samples can be seen in Figures 5.32 and 5.33.

In the 1-18 GHz range, a maximum shielding effectiveness of approximately 5 % occurs at 17 GHz for magnetite and polypyrrole-coated newsprint. Even though this is not a large value by shielding EMI shielding standards, it is larger than that of the individual components - polypyrrole-coated newsprint (~ 2 %) and magnetite-coated newsprint (~ 2 %). This indicates that the two coatings have a synergistic effect on the overall EMI shielding properties of the material.

The same applies in the 16-40 GHz range (Figure 5.33). Magnetite and polypyrrole-coated newsprint shows a shielding effectiveness of approximately 10 % while polypyrrole-coated newsprint and magnetite-coated newsprint show a maximum shielding effectiveness at 18 GHz, of approximately 5 % each.

A low shielding effectiveness can be attributed to a low conductivity and a small material thickness (1.7 and equation 2.5). This may well be the case here.

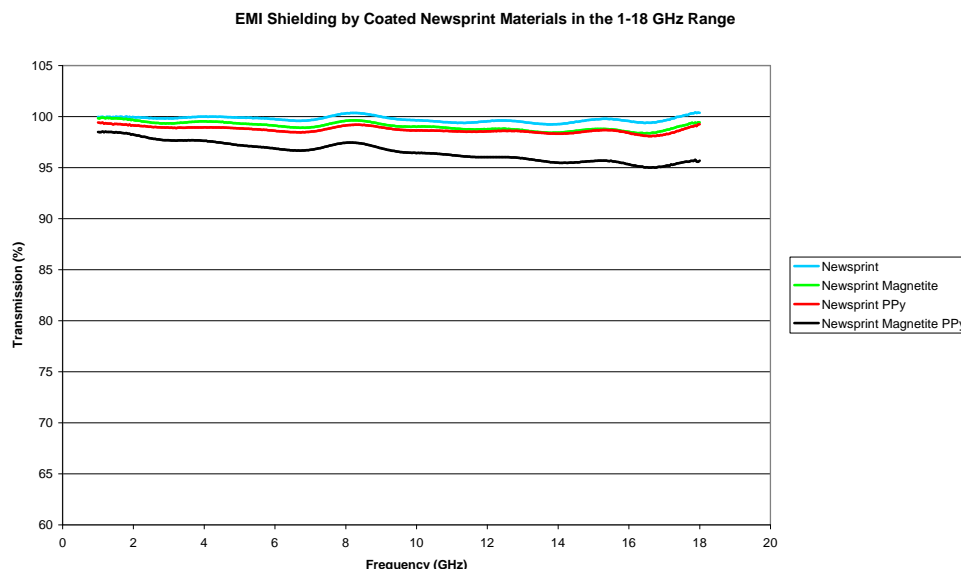


Figure 5.32. EMI shielding effectiveness of coated newsprint samples in the 1-18 GHz range.

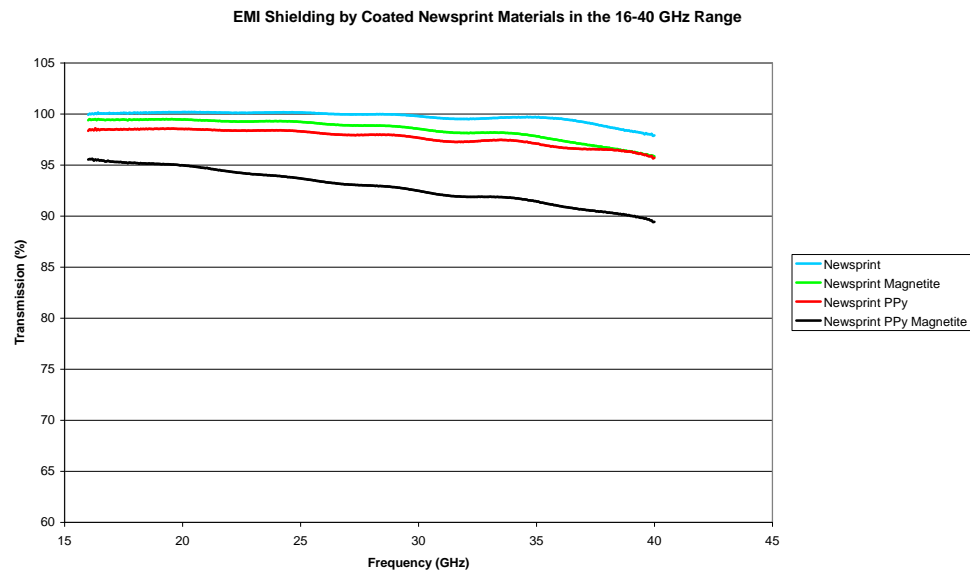


Figure 5.33. EMI shielding effectiveness of coated newsprint samples in the 16-40 GHz range.

Figure 5.34 shows the shielding effectiveness of coated Kraft board samples in the 1-18 GHz range.

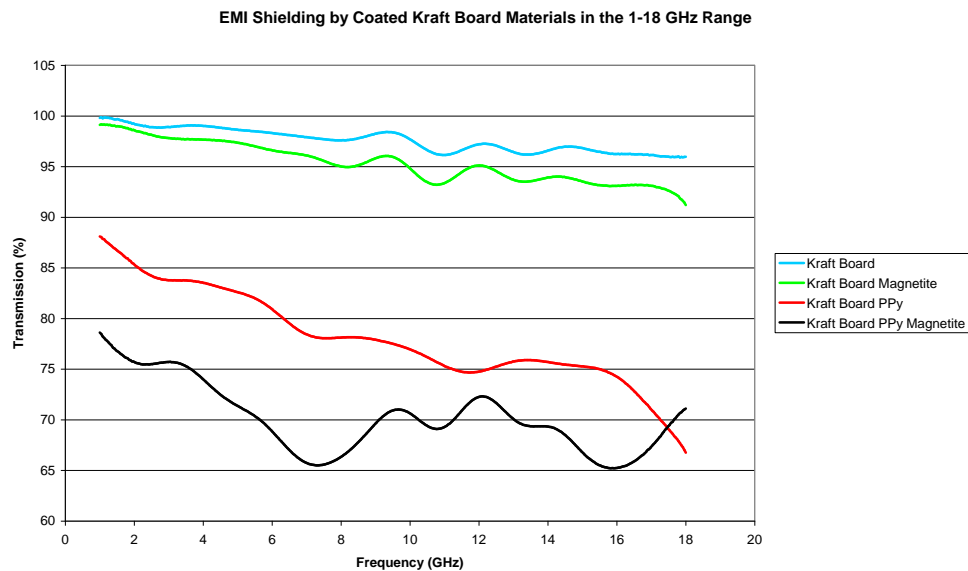


Figure 5.34. EMI shielding effectiveness of coated Kraft board samples in the 1-18 GHz range.

A maximum shielding effectiveness of 35 % is obtained at 16 GHz for polypyrrole and magnetite-coated Kraft board. This is far greater than that of

coated newsprint samples and is attributable to higher electrical conductivity and increased thickness (Table 5.4).

Again a synergistic effect can be seen on using both polypyrrole and magnetite as a coating, as the maximum shielding effectiveness for magnetite-coated Kraft board is approximately 8 %, and the maximum shielding effectiveness for polypyrrole-coated Kraft board is 32 % (although this value is lower than that of polypyrrole and magnetite-coated Kraft board for most of the frequency range).

The same synergistic effect is seen in the 16-40 GHz range (Figure 5.35). Magnetite and polypyrrole-coated Kraft board shows a shielding effectiveness at 40 GHz of approximately 33 % while polypyrrole-coated Kraft board and magnetite-coated Kraft board show a maximum shielding effectiveness at 40 GHz, of 31 and 12 % respectively.

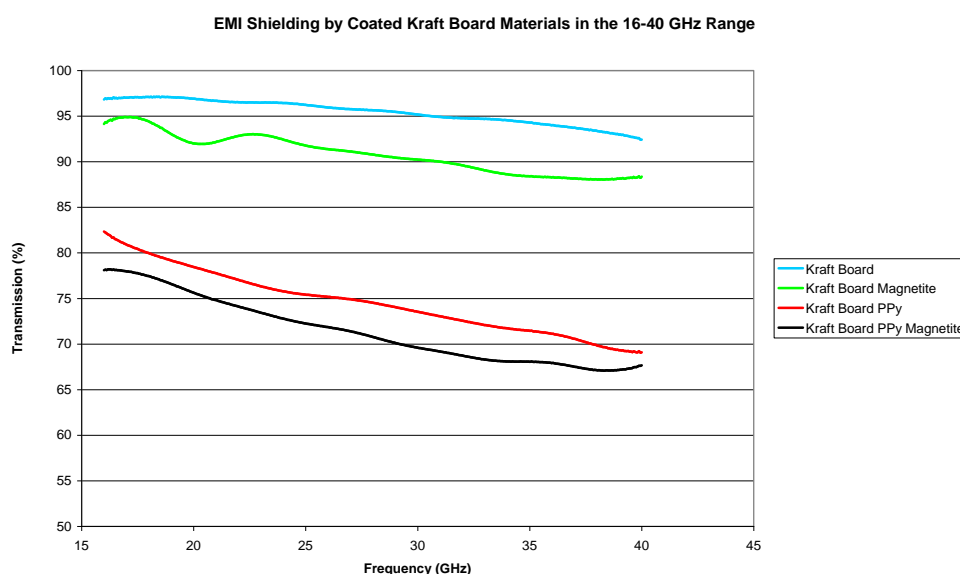


Figure 5.35. EMI shielding effectiveness of coated Kraft board samples in the 16-40 GHz range.

Coated cotton samples show the best performance in EMI shielding, which is possibly due to their greater thickness (Table 5.4) and their more absorbent qualities. A plot of their shielding effectiveness in the 1-18 GHz range can be seen in Figure 5.36.

A maximum shielding effectiveness at 17 GHz of 43 % is obtained by the polypyrrole and magnetite-coated cotton sample. This is in concurrence with the other samples measured and again shows the synergistic effect of the polypyrrole and magnetite coating, as the maximum shielding effectiveness for polypyrrole-coated and magnetite-coated cotton samples alone is 38 % and 11 % respectively.

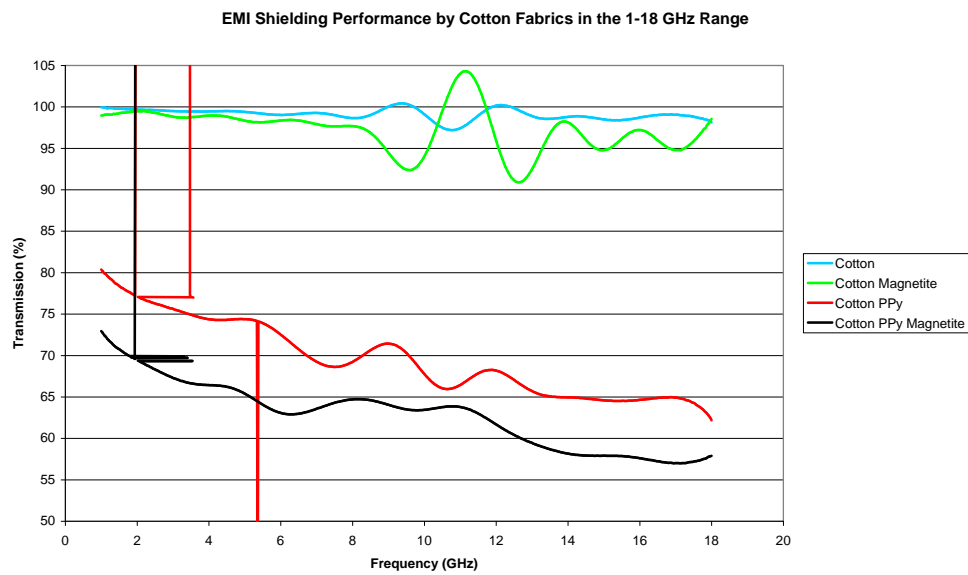


Figure 5.36. EMI shielding effectiveness of coated cotton fabrics in the 1-18 GHz range.

In the 16-40 GHz range, the same synergistic effect can be seen (Figure 5.37).

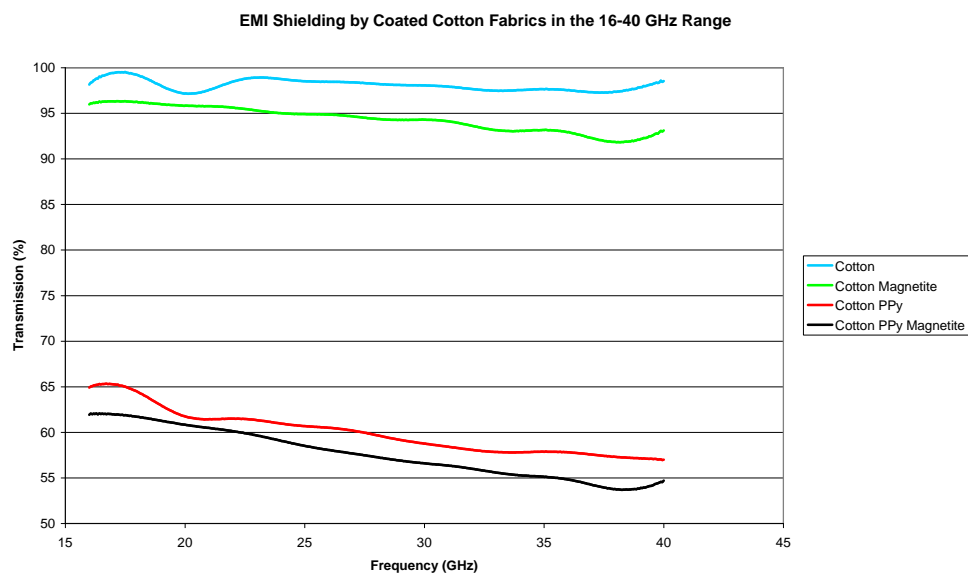


Figure 5.37. EMI shielding effectiveness of coated cotton fabrics in the 16-40 GHz range.

A maximum shielding effectiveness at 38 GHz of approximately 47 % can be seen for polypyrrole and magnetite-coated cotton fabric, whereas for polypyrrole-coated cotton fabric and magnetite-coated cotton fabric, the maximum shielding effectiveness at the same frequency is 43 % and 8 % respectively.

The cotton samples show the greatest shielding effectiveness. One explanation for this is their greater thickness (ranging from 0.3 to 0.38 mm) compared to newsprint and Kraft board (0.08 to 0.2 mm and 0.23 to 0.34 mm, respectively). These properties are summarised in Table 5.4, and a graphical comparison can be seen between polypyrrole and magnetite-coated substrates in Figures 5.38 and 5.39.

Sample	Thickness (mm)	Shielding Effectiveness (%)	
		1-18 GHz	16-40 GHz
Newsprint	0.08	1	2
Newsprint + Magnetite	0.19	2	4
Newsprint + PPy	0.12	3	4
Newsprint + Magnetite + PPy	0.2	5	11
Kraft board	0.23	4	8
Kraft board + Magnetite	0.31	9	12
Kraft board + PPy	0.28	33	30
Kraft board + Magnetite + PPy	0.34	35	33
Cotton	0.3	2	3
Cotton + Magnetite	0.37	9	8
Cotton + PPy	0.32	38	43
Cotton + Magnetite + PPy	0.38	43	47

Table 5.4. Table showing the thicknesses of a number of substrates and their shielding effectiveness.

As discussed in section 1.7, electrical conductivity also plays a major part in the shielding effectiveness of a material. The reflection loss is a function of the ratio of $\frac{\sigma_r}{\mu_r}$ whereas the absorption loss is a function of the product of $\sigma_r \times \mu_r$, where σ_r is the electrical conductivity of the shield with respect to copper metal, and μ_r is the magnetic permeability of the shield relative to free space¹⁰⁹. Hence the

electrical conductivity and magnetic properties of the shield are important in determining its overall shielding effectiveness.

A plot showing the shielding effectiveness of a range of polypyrrole-coated cotton samples with different conductivities is shown in Figure 5.40.

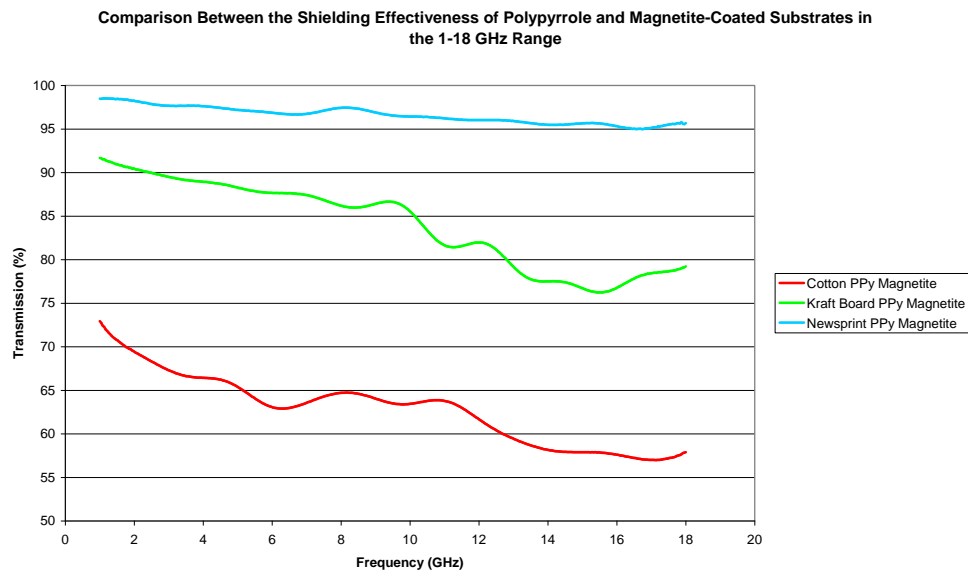


Figure 5.38. Plot showing the comparison between shielding effectiveness in the 1-18 GHz range of a number of substrates with different thicknesses.

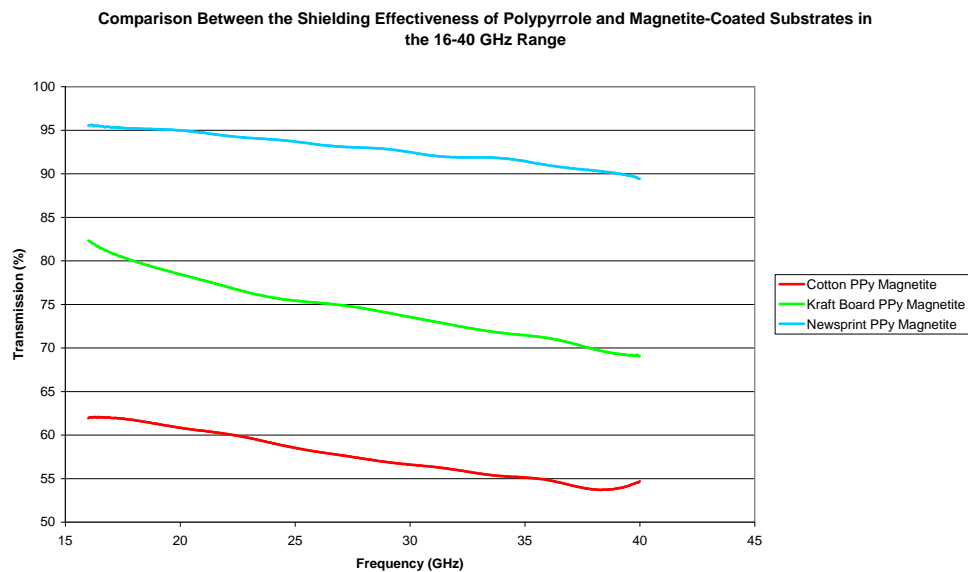


Figure 5.39. Plot showing the comparison between shielding effectiveness in the 16-40 GHz range of a number of substrates with different thicknesses.

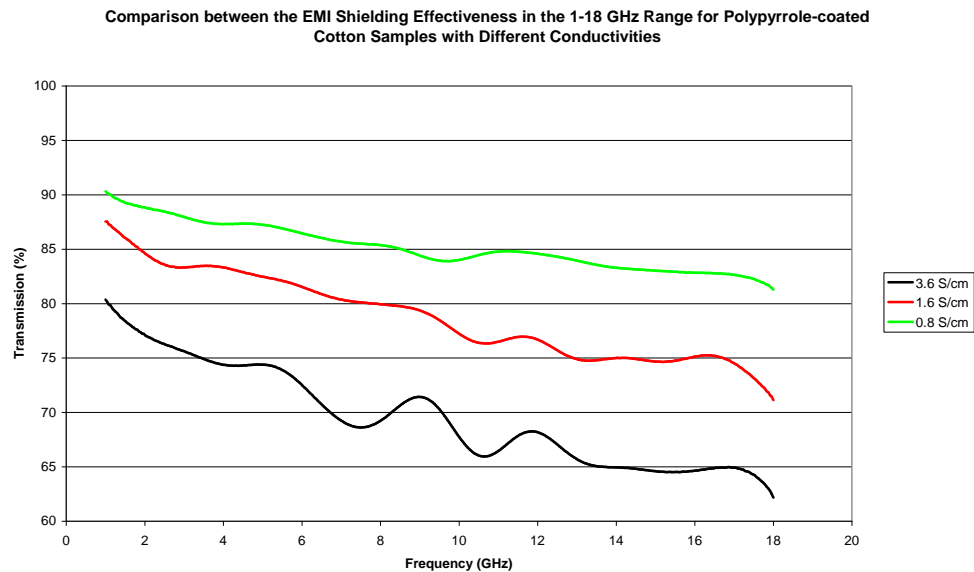


Figure 5.40. Effect of conductivity on EMI shielding effectiveness of polypyrrole-coated cotton samples in the 1-18 GHz range.

5.4. Chapter Summary

Hybrid materials of cellulose substrates, including newsprint, Kraft board and cotton fabric, were synthesised and characterised using DC conductivity measurements, free space measurements for EMI shielding, and SEM.

The greatest shielding effectiveness is obtained using samples coated with both polypyrrole and magnetite. The shielding effectiveness is highest using cotton fabric, presumably as it is thicker than Kraft board and newsprint. A maximum shielding effectiveness of approximately 43 % in the 1-18 GHz range and 47 % in the 16-40 % range is obtained with polypyrrole and magnetite-coated cotton fabrics. This falls far from the required values at 1 GHz for commercial and military applications such as wi-fi and radar shielding¹¹⁰.

Although a considerable amount of work needs to be done in order to increase the conductivity of such materials compared with others in the literature^{111, 112}, it can be seen that a synergistic effect can be gained from the use of polypyrrole and magnetite as a coating for EMI shielding. In some cases the gain in shielding effectiveness is approximately 10 %.

Chapter 6

INKJET PRINTING

Doped ZnS:Mn²⁺ quantum dots were formulated for inkjet printing at CSIRO Forest & Biosciences, Melbourne, Australia. The quantum dot ‘inks’ and substrates they were printed on were characterised using Cotec Profilometer Measurements, Photoluminescence Spectroscopy (PL), Scanning Electron Microscopy (SEM), Transmission Electron Microscopy (TEM) and Viscosity Measurements.

6.1. Printer Properties

The printer used for the inkjet printing was a 2811 Dimatix Materials Printer (FUJIFILM Dimatix, USA), which required an ink with specific fluid properties (summarised in Table 2.3). This printer was a drop-on-demand (DOD) inkjet printer driven by a piezoelectric crystal (Section 1.8).

A significant amount of time was spent in order to formulate a doped ZnS quantum dot ‘ink’ for inkjet printing (Table 2.16). ZnS:Mn²⁺ quantum dots, were again used as the base case, and if successful, the method would be transferred to other varieties of doped ZnS quantum dots, such as ZnS:Cu²⁺.

6.2. Surfactants

To develop doped ZnS quantum dots for inkjet printing, ‘soluble’* quantum dots must be obtained. If any solids are present that can agglomerate, the printhead will become blocked during the jetting process.

For the development of ‘soluble’ doped ZnS quantum dots, a screening of different surfactants was carried out in order to stabilise the colloid by electrostatic or steric stabilisation methods (described in 1.5.3 and 1.5.4). These surfactants are summarised in Table 2.16. Concentrations of surfactant were taken from the literature reports, and ranged from 0.01 – 1 wt. % of the total solution volume.

Many of the surfactants listed in Table 2.16 were unsuccessful in providing ‘soluble’ ZnS:Mn²⁺ quantum dots – many providing only short term stability, or a poor luminescence. The most successful surfactant in providing ‘soluble’ ZnS:Mn²⁺ quantum dots was mercaptosuccinic acid (MSA). This gave a clear solution with 0 % solids and an excellent photoluminescence emission that was stable for months.

Various amounts of MSA were used in order to find the optimal MSA:Zn²⁺ ratio. These are summarised in Table 2.14, which shows the optimal ratio to be 8:1. A photograph showing the different ratios of MSA:Zn²⁺ is shown in Figure 6.1

The method was then transferred to ZnS:Cu²⁺ quantum dots, in order to obtain a green quantum dot ‘ink’. The optimum MSA:Zn²⁺ ratio for ZnS:Cu²⁺ quantum dots is shown in Table 2.15, and is slightly less than that of ZnS:Mn²⁺, at 4:1.

* If a clear solution is formed, a stable colloid has been obtained. While the particles themselves are not soluble, the term ‘soluble quantum dots’ is the term used in the literature for a stable colloid of very small nanoparticles with minimal agglomeration.



Figure 6.1. Photograph of ZnS:Mn²⁺ quantum dots capped with MSA, showing different MSA:Zn²⁺ ratios. (L-R), 1:1, 1:2, 1:4, 1:8, 1:16 (Table 6.3).

Figure 6.2 shows the surface of the ZnS quantum dots capped with MSA. The stabilising agent is presumably bound through interaction between the sulfur groups on the surface of the quantum dot, and the thiol group of the MSA¹⁵⁵.

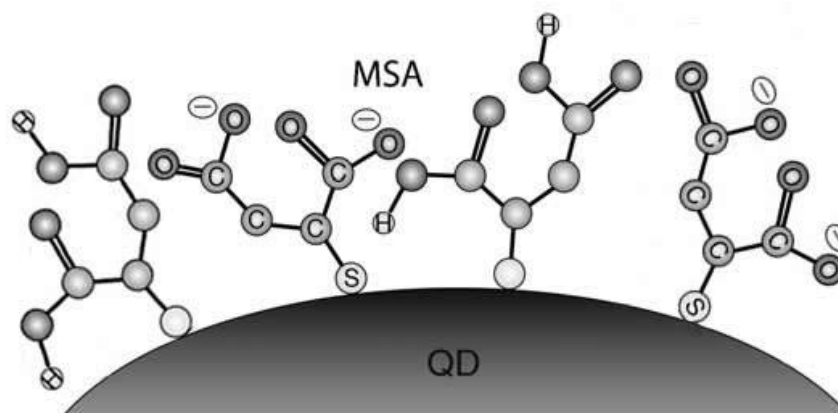


Figure 6.2. Schematic showing the binding of MSA to the ZnS quantum dot surface¹⁵⁵.

MSA is not a large molecule, and stabilisation must therefore occur electrostatically, rather than sterically, as discussed in section 1.5.3 and 1.5.4 of this thesis.

The IR spectra of both MSA and MSA-capped ZnS:Mn²⁺ are shown in Figures 6.3 and 6.4. On comparison between the two spectra, their difference is clear. Therefore, it can be deduced that a change in bonding is occurring. This is most

likely associated with the thiol group present in the MSA, as the thiol stretch at approximately $2550\text{--}2600\text{ cm}^{-1}$ has diminished on bonding to the ZnS:Mn^{2+} quantum dots. The spectra also differ in both the area of a disulfide stretch ($400\text{--}550\text{ cm}^{-1}$) and in the fingerprint region ($400\text{--}1000\text{ cm}^{-1}$), further indication that a change in bonding has occurred¹⁸⁰. In particular, the disulfide area is broadened, which suggests the vibrations of the MSA molecules have been changed considerably due to bonding of the MSA with the ZnS:Mn^{2+} quantum dots through the S.

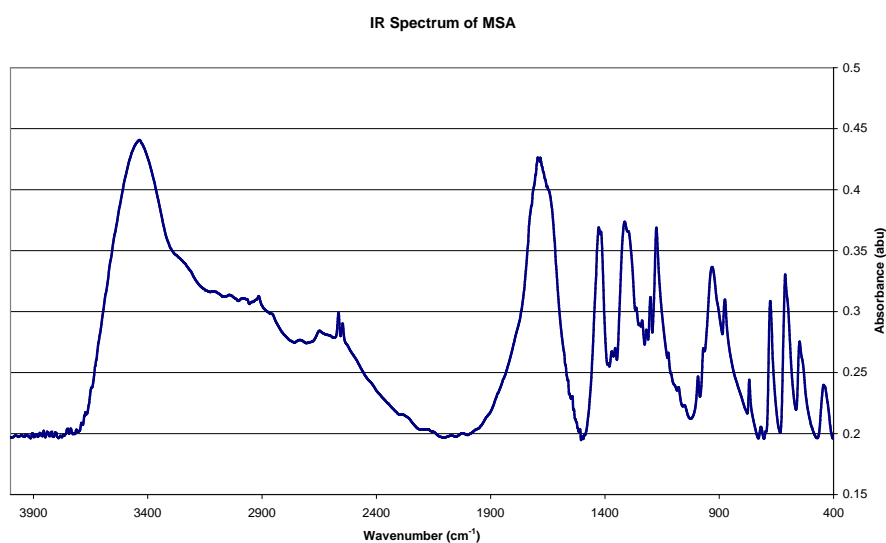


Figure 6.3. IR spectrum of MSA.

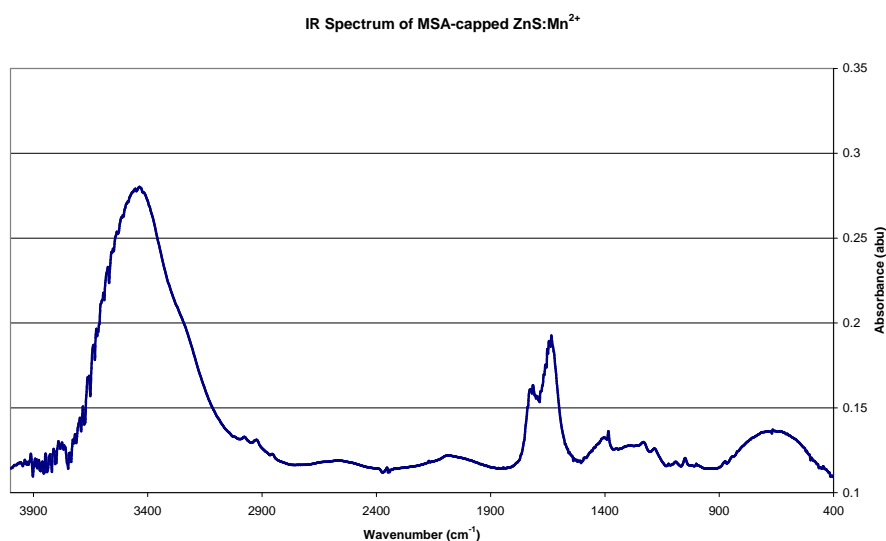


Figure 6.4. IR spectrum of MSA-capped ZnS:Mn^{2+} .

Over a time period of a couple of days however, the ZnS:Cu²⁺ quantum dot ‘ink’ becomes unstable in the MSA and a precipitate is formed. It appears that the S₂O₃²⁻ ligand used in the synthesis of ZnS:Cu²⁺ quantum dots to prevent the precipitation of CuS, is reduced to elemental sulfur.

6.3. Fluid Properties

The synthesised doped ZnS quantum dots ‘inks’ were then measured for their fluid properties in order to gauge how they might perform in inkjet printing.

Viscosity measurements were taken as outlined in 2.1.16. At 60 °C, a value of 4.1 centipoise was obtained, slightly below that of the specified printer requirements. The boiling point of the ‘ink’ was approximately 100 °C and the specific gravity was 1.09 g cm⁻³. Surface tension was not measured.

Although these values did not match the specifications of the printer exactly, the requirements were only guidelines, and it was decided to print the ‘ink’ as the values obtained were not unrealistic.

6.4. Inkjet Printing

The doped ZnS quantum dot ‘inks’ were then printed on a variety of substrates, including photo quality inkjet paper, photocopy paper, cotton fabric, PET film, ITO-coated PET film, silicon wafer and wool.

The images in Figure 6.5 show first printed photo paper printed with a strip of ZnS:Mn²⁺ quantum dots. On the left is the photo paper under normal light, while on the right, is the same piece of paper under UV light conditions.

The above success was followed by the successful printing of detailed images, as shown by the photographs in Figure 6.6 and 6.7 of a printed circuit board template and the Victoria University of Wellington logo.

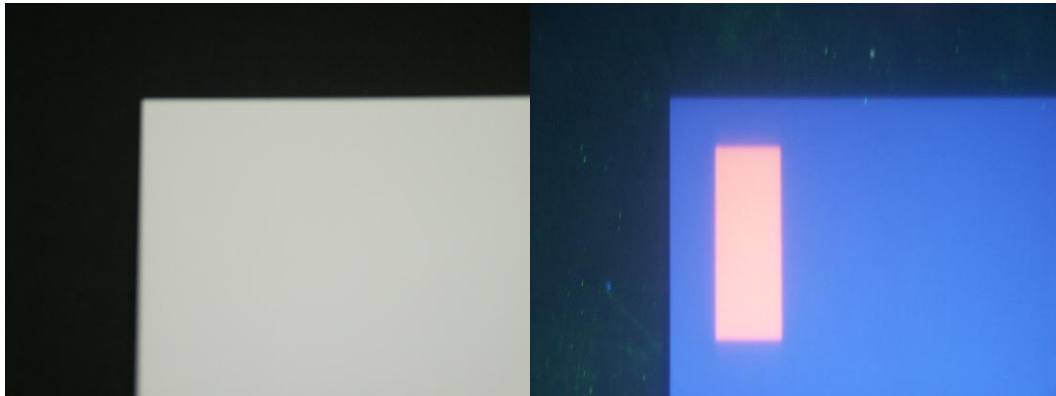


Figure 6.5. Photo quality inkjet paper with a strip of ZnS:Mn^{2+} quantum dots printed on the surface. Under normal light conditions (left), and under UV light conditions (right).

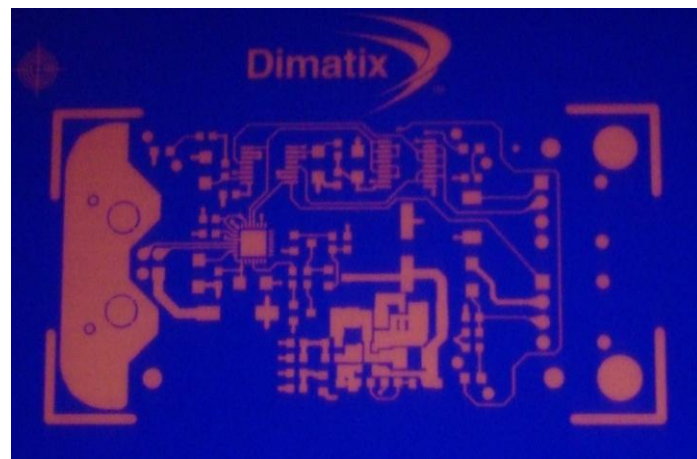


Figure 6.6. A detailed inkjet printed image of a printed circuit board template on photo quality inkjet paper using ZnS:Mn^{2+} quantum dots. Viewed under UV light.

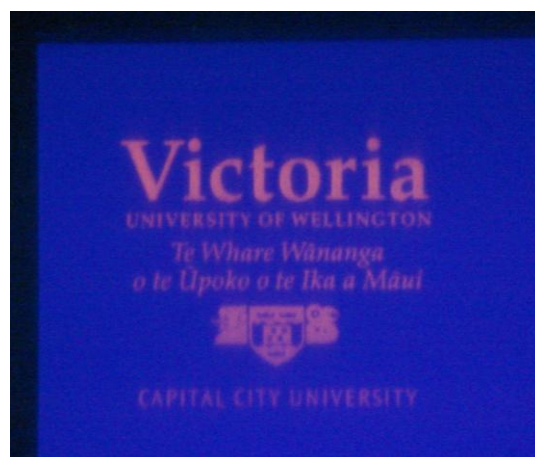


Figure 6.7. A detailed inkjet printed image of the Victoria University of Wellington logo on photo quality inkjet paper using ZnS:Mn^{2+} quantum dots. Viewed under UV light.

Several parameters in of the printer may be adjusted to improve the print quality and brightness, and include drop spacing and the number of layers printed. A lower drop spacing gives more ‘ink’ per unit area (or a higher ‘ink’ loading), and would result in an increase in print quality and brightness. At a drop spacing of 10 μm however, the substrate (photo quality inkjet paper) could not absorb all the ‘ink’, resulting in smearing of the print. Therefore a drop spacing of 15 μm was used throughout this study.

Another way to increase brightness is by changing the number of passes made (or layers printed) by the printhead over the substrate. In this study, the number of passes was set at either 1, 2 or 3, in order to obtain the best print. Figure 6.8 shows the difference between 1 and 2 layers. The image printed with 2 layers of ZnS:Mn^{2+} quantum dots is noticeably brighter.

On printing three layers however, the print began to smear, and the printing cycle was cancelled in order to maintain the cleanliness of the printhead.



Figure 6.8. Comparison between images printed using 1 layer (left) and 2 layers (right) of ZnS:Mn^{2+} quantum dots. Viewed under UV light.

ZnS:Cu^{2+} quantum dots were also inkjet printed onto photo quality inkjet paper. The copper-doped variety was unstable in the MSA surfactant, however, and as a result the ZnS:Cu^{2+} quantum dot ‘ink’ had to be prepared only a few hours before printing in order to obtain a stable and printable ‘ink’ containing no solids.

Once formulated however, the $\text{ZnS}:\text{Cu}^{2+}$ quantum dots posed no problems during the inkjet printing process. Figure 6.9 shows $\text{ZnS}:\text{Cu}^{2+}$ quantum dots inkjet printed on photo quality inkjet paper and illuminated with UV light, giving a green luminescence.

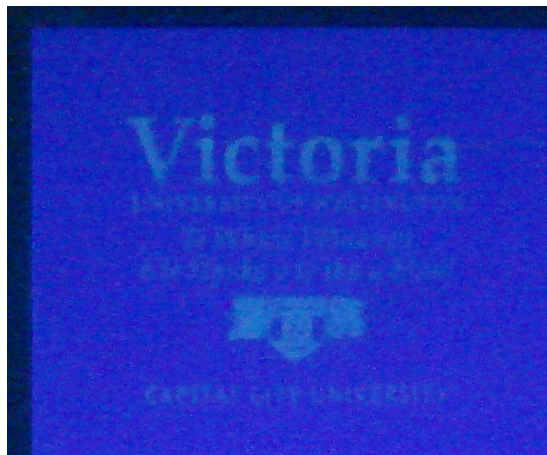


Figure 6.9. A detailed inkjet printed image of the Victoria University of Wellington logo on photo quality inkjet paper using $\text{ZnS}:\text{Cu}^{2+}$ quantum dots. Viewed under UV light.

Cotton fabric also performed well in print tests, although whiteners present in the cotton fabric produced a blue coloured background, making it difficult to photograph the emission under UV light. An image of $\text{ZnS}:\text{Mn}^{2+}$ quantum dots printed on cotton fabric is shown in Figure 6.10.

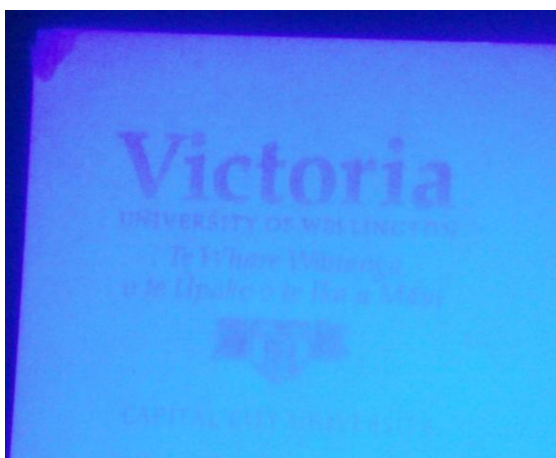


Figure 6.10. A detailed inkjet printed image of the Victoria University of Wellington logo on cotton fabric using $\text{ZnS}:\text{Mn}^{2+}$ quantum dots. Viewed under UV light.

Other substrates did not perform as well during the print tests as the photo quality inkjet paper. Patterns printed on PET film, PEDOT-coated PET film and silicon wafer were unable to be seen under UV illumination, even though the pattern was visible to the naked eye under normal light conditions, and is confirmed to be present by Cotec profilometer measurements taken in 2.1.4, and discussed in 6.8.

These substrates are all ‘flat’ surfaces, and perhaps an interesting phenomenon is occurring whereby light is reflected away from the surface, and in the process interfering with the visibility of the quantum dots luminescent properties. Another possibility is that the substrates are quenching the photoluminescence emission as illustrated in Figure 1.18. Exactly what is occurring is not understood yet, and further work is required.

Photocopy paper is only a filled paper with a rough absorbent surface, and its poor performance in printing tests can be attributed to the ‘spreading’ of the quantum dot ‘ink’ throughout the fibre matrix as it comes into contact with the paper structure.

6.5. Photoluminescence Spectroscopy (PL)

The photoluminescence properties of the doped ZnS quantum dot ‘inks’ and the printed substrates were measured as described in 2.1.10.

The photoluminescence emission spectrum of MSA-capped ZnS:Mn²⁺ quantum dots is shown in Figure 6.11. The large peak at approximately 600 nm is present, as in uncapped ZnS:Mn²⁺ (Figure 4.10). An interesting point to note is that the peak at 600 nm is larger than that of uncapped ZnS:Mn²⁺ quantum dots, indicating that the MSA cap has actually improved the luminescence of the quantum dots.

A possible reason for this is that the capping agent has reduced the number of surface defects present on the material, as discussed in 4.6. This would mean that there is a greater chance of a photogenerated electron hole pair recombining at a luminescent centre, rather than at the site of a defect, which leads to an increase in photoluminescence efficiency, as described by equation 1.5. The MSA capping agent has worked far better than silica (4.6 and Figure 4.39), a possible reason for this being that the MSA contains a thiol group that is more like the ZnS:Mn^{2+} quantum dot surface than is silica.

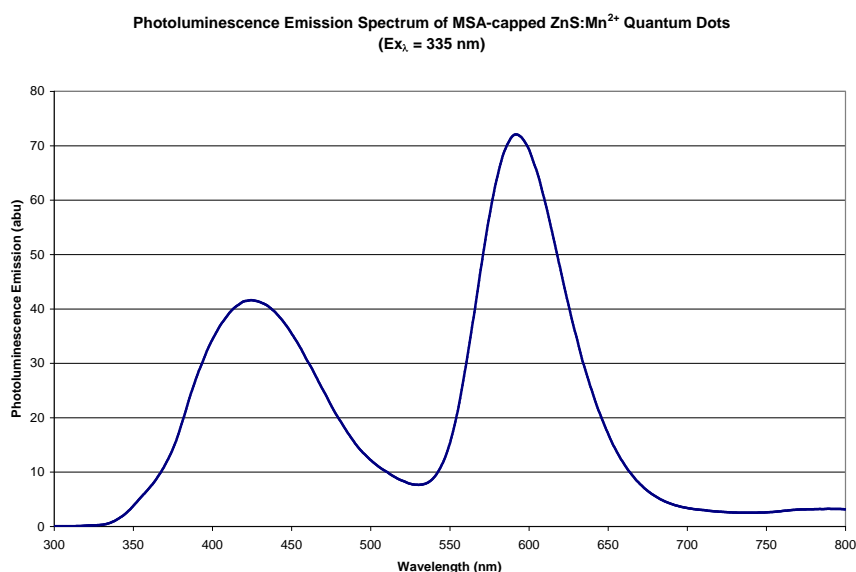


Figure 6.11. PL emission spectrum of MSA-capped ZnS:Mn^{2+} Quantum Dots.

On printing these quantum dot ‘inks’ onto the various substrates, the characteristic luminescence peaks ($\sim 600 \text{ nm}$ for ZnS:Mn^{2+} and $\sim 530 \text{ nm}$ for ZnS:Cu^{2+}) are observed, indicating the substrate has not altered the chemistry of the quantum dots.

The photoluminescence emission spectrum for ZnS:Mn^{2+} quantum dots inkjet printed onto photo quality inkjet paper are shown in Figures 6.12 and 6.13. Figure 6.12 shows the photoluminescence emission spectrum for one layer of ZnS:Mn^{2+} quantum dots, while Figure 6.13 shows the photoluminescence emission spectrum for two layers of ZnS:Mn^{2+} quantum dots.

The greater peak height at 600 nm in Figure 6.11 is indicative of the increased brightness arising from the printing of two layers (as observed visually in the photograph shown in Figure 6.6).

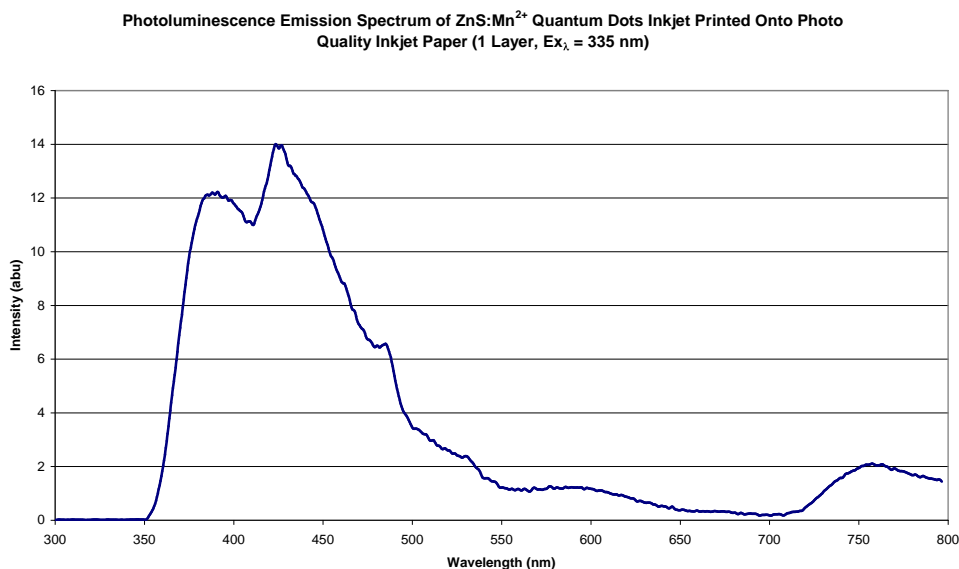


Figure 6.12. PL emission spectrum for one layer of ZnS:Mn²⁺ quantum dots printed onto photo quality inkjet paper.

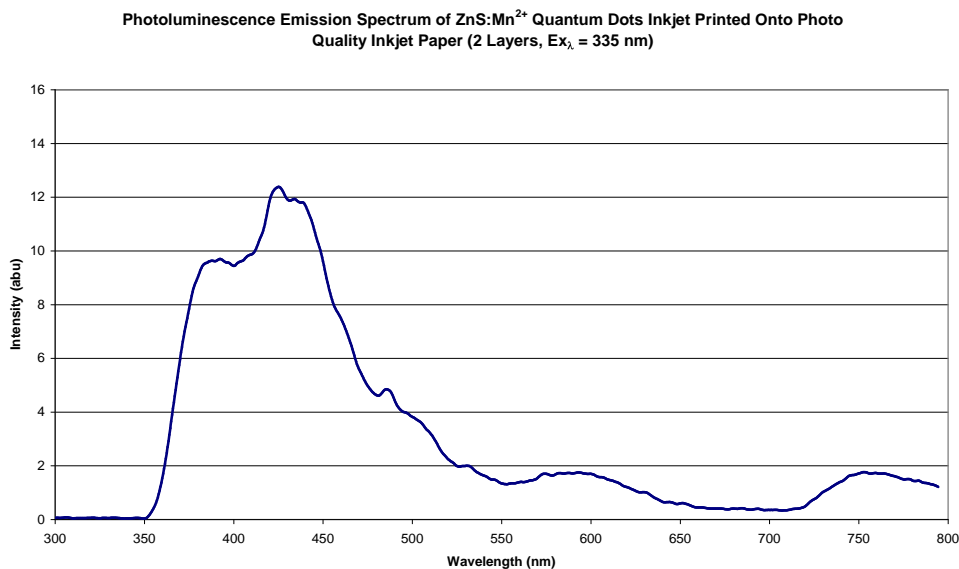


Figure 6.13. PL emission spectrum for two layers of ZnS:Mn²⁺ quantum dots printed onto photo quality inkjet paper.

The photoluminescence emission spectrum of two layers of ZnS:Mn^{2+} quantum dots inkjet printed onto cotton fabric is shown in Figure 6.14. Again, the characteristic emission at approximately 600 nm can be seen, indicating that the cotton has not changed the chemistry of the quantum dots.

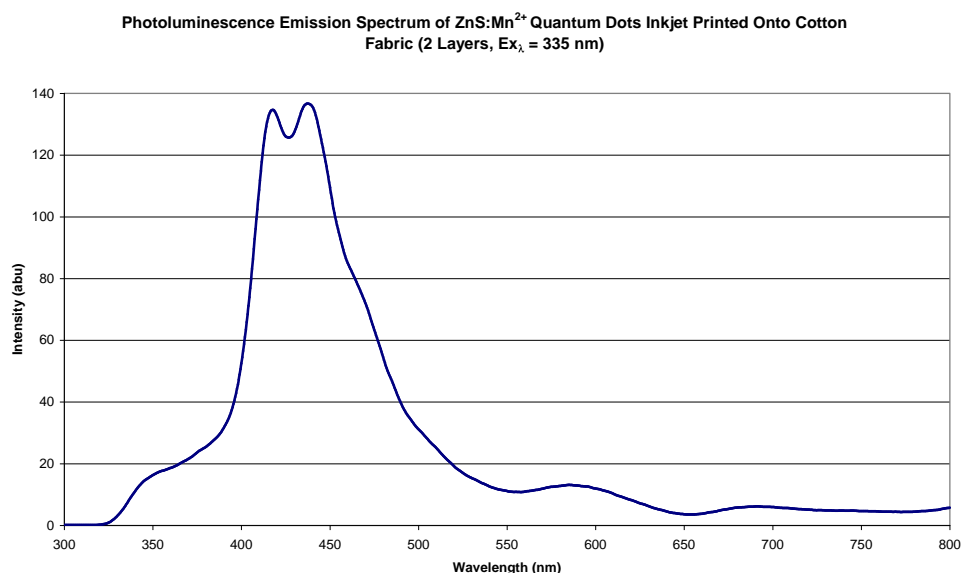


Figure 6.14. PL emission spectrum for two layers of ZnS:Mn^{2+} quantum dots printed onto cotton fabric.

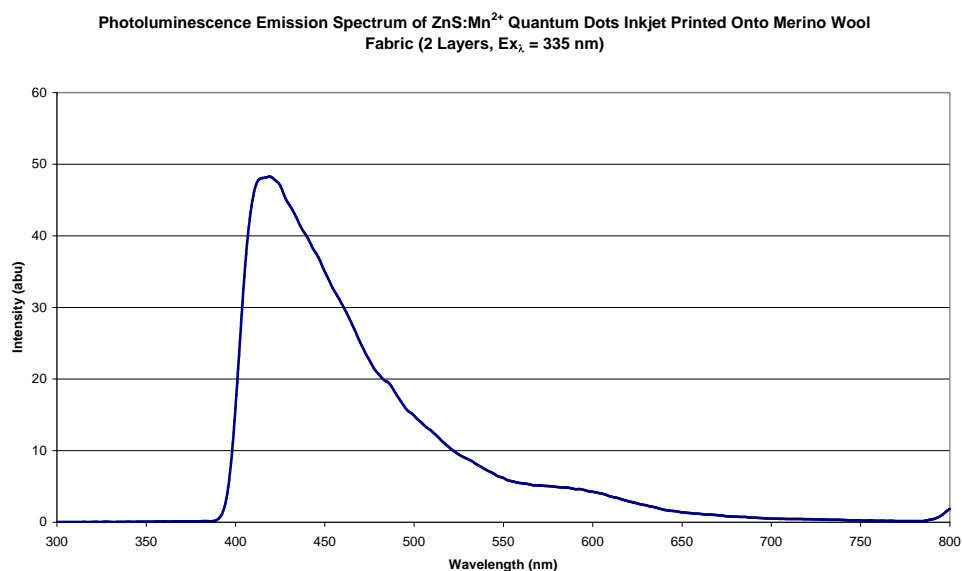


Figure 6.15. PL emission spectrum for two layers of ZnS:Mn^{2+} quantum dots printed onto merino wool fabric.

Merino wool was also used as a substrate for inkjet printing ZnS:Mn²⁺ quantum dots onto. Figure 6.15 shows the photoluminescence emission spectrum of two layers of ZnS:Mn²⁺ quantum dots inkjet printed onto merino wool fabric.

Again the characteristic emission at approximately 600 nm can be seen, along with the emission arising from the S²⁻ vacancy (4.3) and the luminescence characteristics of the wool substrate – different from those of cotton fabric, and photo quality inkjet paper shown already in Figures 6.12 – 6.14.

The photoluminescence spectrum of MSA-capped ZnS:Cu²⁺ quantum dots is shown in Figure 6.16.

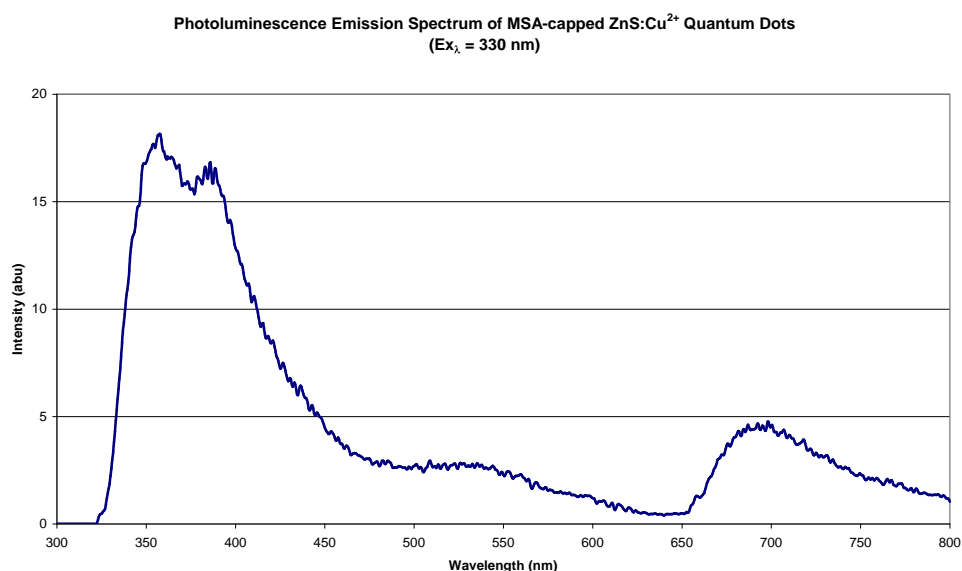


Figure 6.16. PL emission spectrum of MSA-capped ZnS:Cu²⁺ Quantum Dots.

The characteristic emission at approximately 530 nm is visible, although unlike the MSA-capped ZnS:Mn²⁺ variety, the capping agent does not seem to increase the luminescence of the material.

The photoluminescence emission spectrum for MSA-capped ZnS:Cu²⁺ quantum dots is also markedly different to that of the precursor ZnS:Cu²⁺ quantum dots synthesised in 2.2.12, whereas the photoluminescence emission spectra of MSA-

capped ZnS:Mn^{2+} quantum dots and the precursor ZnS:Mn^{2+} quantum dots synthesised in 2.2.11 are very similar – the only difference being the increase in relative peak heights of the ${}^4T_1\text{-}{}^6A_1$ emission ($\sim 600\text{ nm}$) and the S^{2-} vacancy emission ($\sim 430\text{ nm}$).

The photoluminescence emission spectrum of ZnS:Cu^{2+} quantum dots inkjet printed onto photo quality inkjet paper is shown in Figure 6.17.

Although the characteristic emission at approximately 530 nm can be seen visually in Figure 6.7, it seems to be masked in the photoluminescence spectrum by the luminescence of the photo quality inkjet paper substrate.

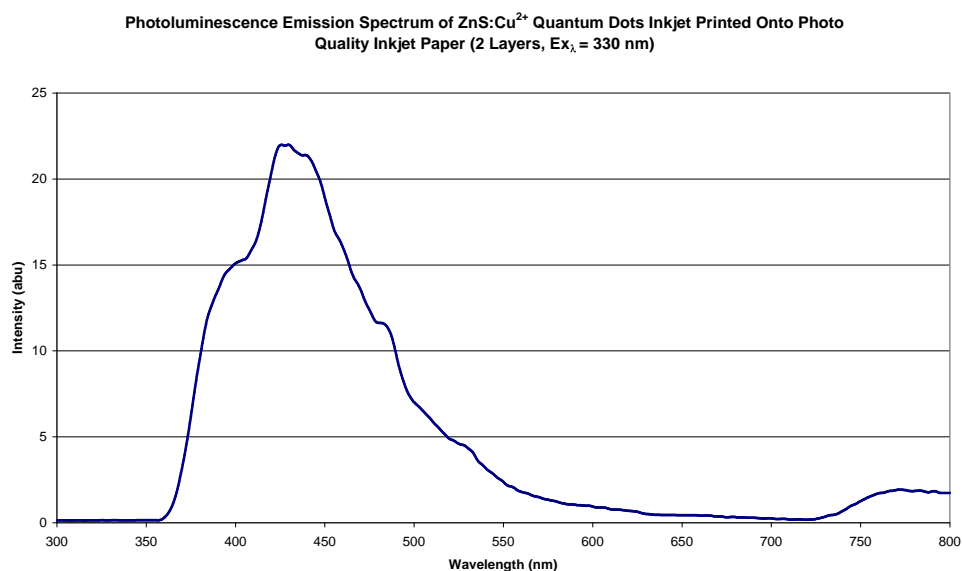


Figure 6.17. PL emission spectrum for two layers of ZnS:Cu^{2+} quantum dots printed on photo quality inkjet paper.

6.6. Scanning Electron Microscopy (SEM)

Cross sectional SEM images of two layers of ZnS:Mn^{2+} quantum dots inkjet printed onto photo quality inkjet paper are shown in Figures 6.18 – 6.21, at various magnifications.

The print pattern is visible as a series of lines on the surface of the photo quality inkjet paper that comprise part of the 'V' in the Victoria University of Wellington logo.

The cross section shows the structure of the paper, containing the pulp fibres sandwiched between two layers of a coating, most likely polyethylene. The silicon ink receptor layer sits on the surface of the paper, and is itself isolated from the paper.

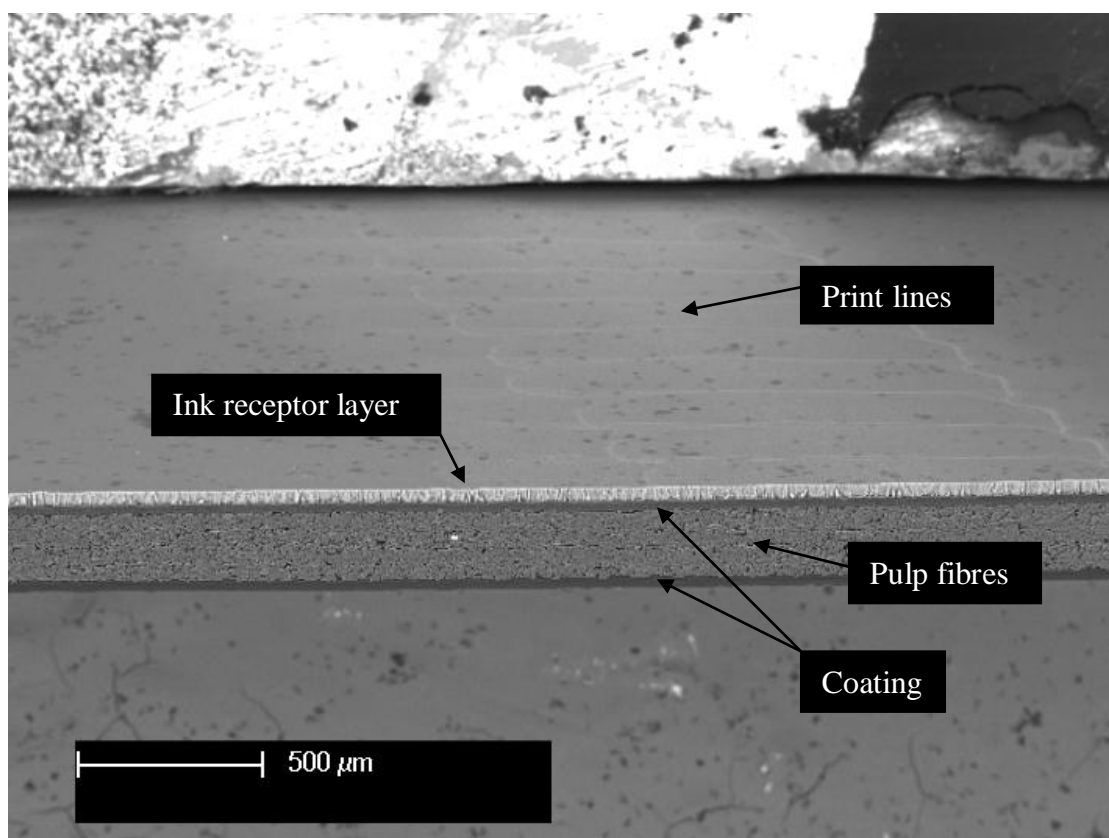


Figure 6.18. Cross sectional SEM image of photo quality inkjet paper printed with two layers of ZnS:Mn²⁺ quantum dots.

At higher magnifications (Figure 6.19 and 6.20), the uniform structure of the paper is even more apparent, and there is no evidence of any migration of the ZnS:Mn²⁺ quantum dots in the z-direction – important for print quality.

The only evidence of the ZnS:Mn^{2+} quantum dot ‘ink’ can be seen at the highest magnification (Figure 6.21), whereby the ‘ink’ can be seen as a thin bright line on the surface of the ink receptor layer. These results suggest that the quantum dots remained printed on the surface and have not penetrated the substrate in the z-direction, giving rise to the maximum luminescence.

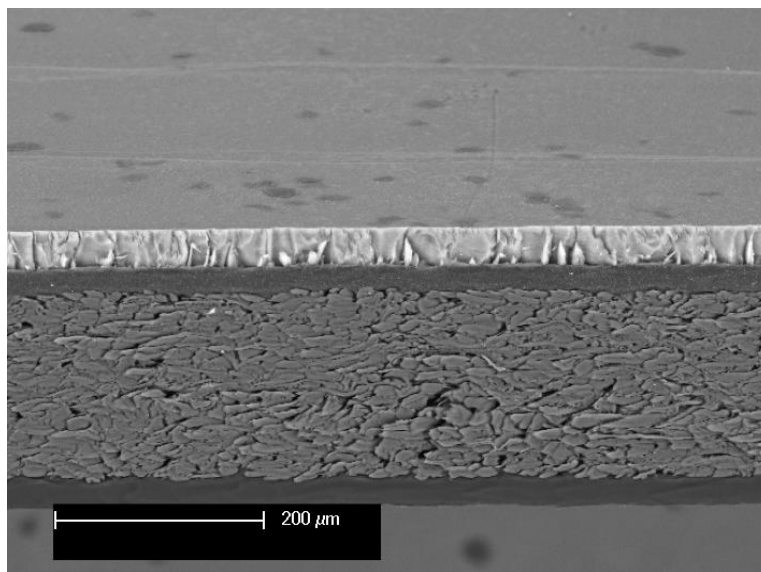


Figure 6.19. Cross sectional SEM image of photo quality inkjet paper printed with two layers of ZnS:Mn^{2+} quantum dots.

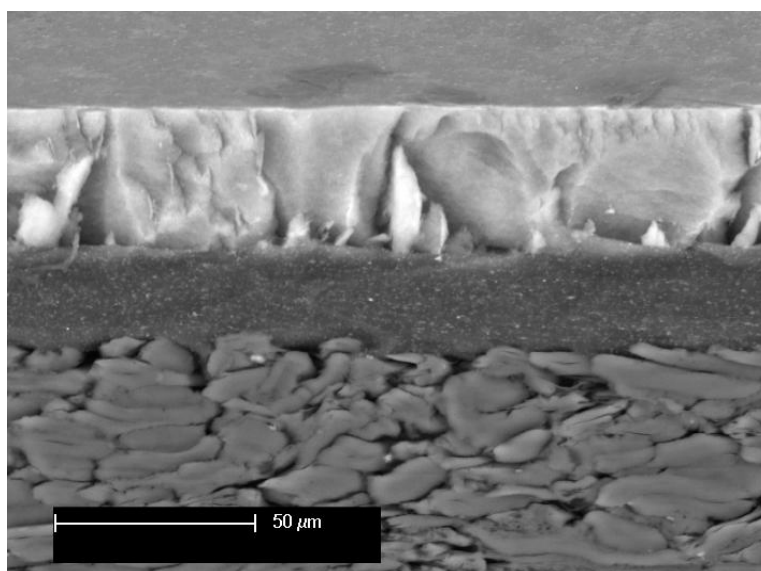


Figure 6.20. Cross sectional SEM image of photo quality inkjet paper printed with two layers of ZnS:Mn^{2+} quantum dots. Note: no evidence of z-migration.

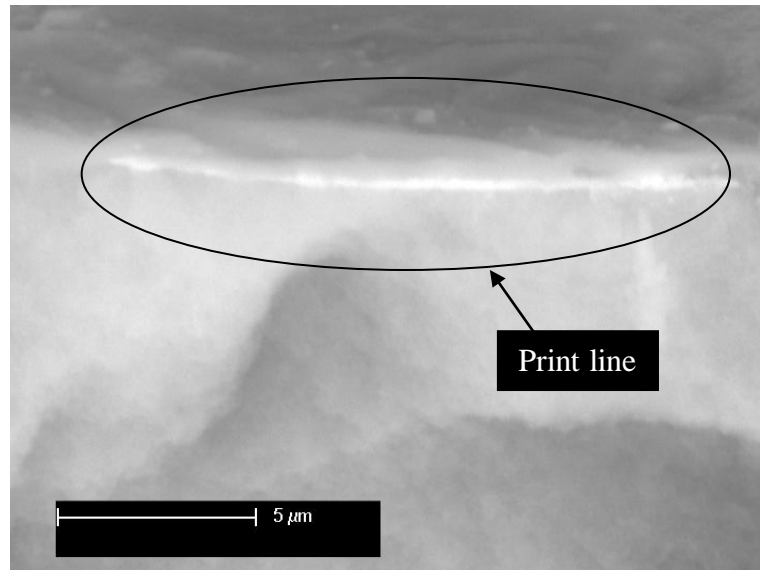


Figure 6.21. Cross sectional SEM image of photo quality inkjet paper printed with two layers of ZnS:Mn^{2+} quantum dots. At maximum magnification, the only evidence of the presence of quantum dots is a very thin bright line on the surface of the ink receptor layer.

6.7. Cotec Profilometer Measurements

Cotec Profilometer measurements of one layer of ZnS:Mn^{2+} quantum dots printed on a silicon wafer are shown in Figures 6.22 and 6.23 below.

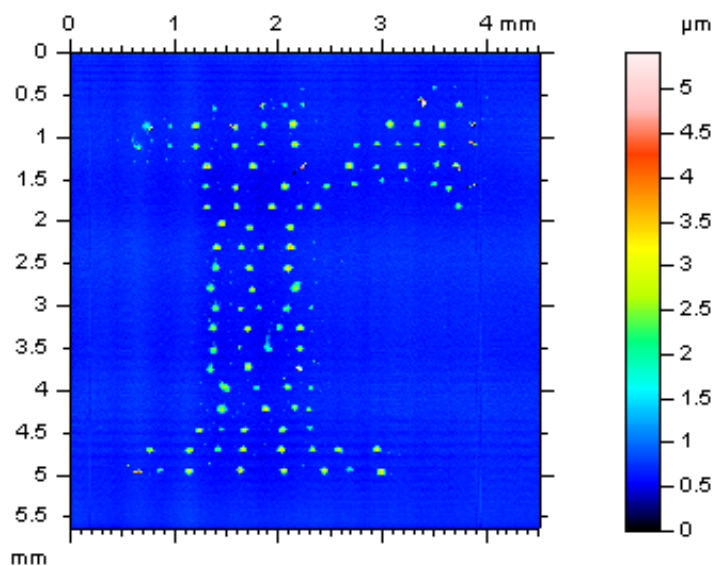


Figure 6.22. 2D Cotec Profilometer measurements of the letter 'r' in the Victoria University of Wellington logo, printed by with ZnS:Mn^{2+} quantum dots.

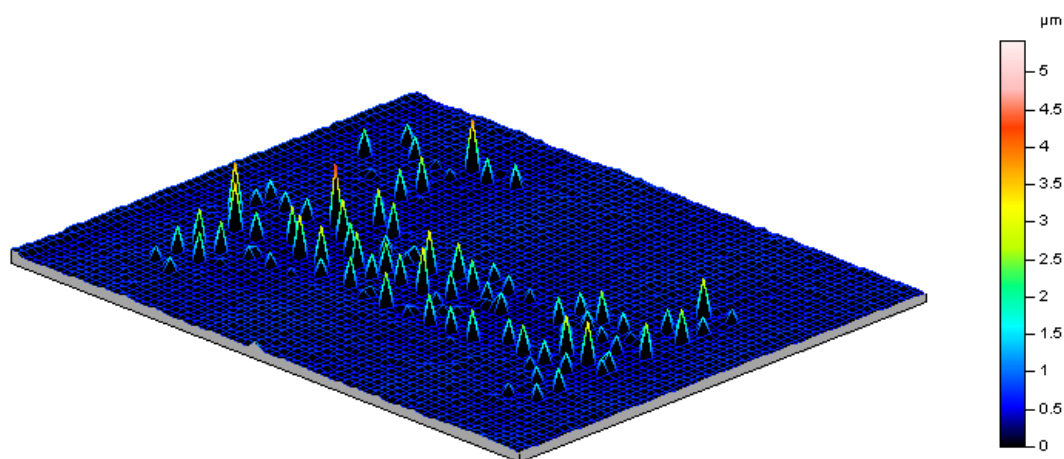


Figure 6.23. 3D Cotec Profilometer measurements of the letter 'r' in the Victoria University of Wellington logo, printed by with ZnS:Mn²⁺ quantum dots.

Due to the contact angle of the droplets on the hydrophobic surface, the droplets have remained as isolated droplets, rather than merging to form a continuous film. As a result, the droplets appear as a series of individual peaks, ranging in height from 0.5 – 4 μm. The drop spacing of 15 μm can also be seen from the images. Unfortunately though, doped ZnS quantum dots inkjet printed onto silicon wafer, did not show any visible photoluminescence.

This is probably due to the fact that silicon is a semiconductor. At 1.1 eV, the band energy of silicon is lower than that of ZnS. Hence, when an electron-hole pair is generated by the absorption of a photon of light, the charge carrier is conducted away from the luminescent centres in the doped ZnS lattice, and the electron-hole pair cannot recombine to produce luminescence. Instead it relaxes back to the ground state via a non-radiative transition.

6.8. Transmission Electron Microscopy (TEM)

Transmission electron microscopy was used to assess the particle size of the ZnS:Mn²⁺ quantum dots. From the TEM image shown in Figure 6.24, spherical particles approximately 40 – 80 nm in diameter can be seen.

Although there is a distinct lack of any visible crystal lattice fringes in these images (probably due to the presence of the MSA capping layer interfering with imaging), the quantum dots are still crystalline, as in order to produce a photoluminescence emission, the dopant must be included in a lattice.

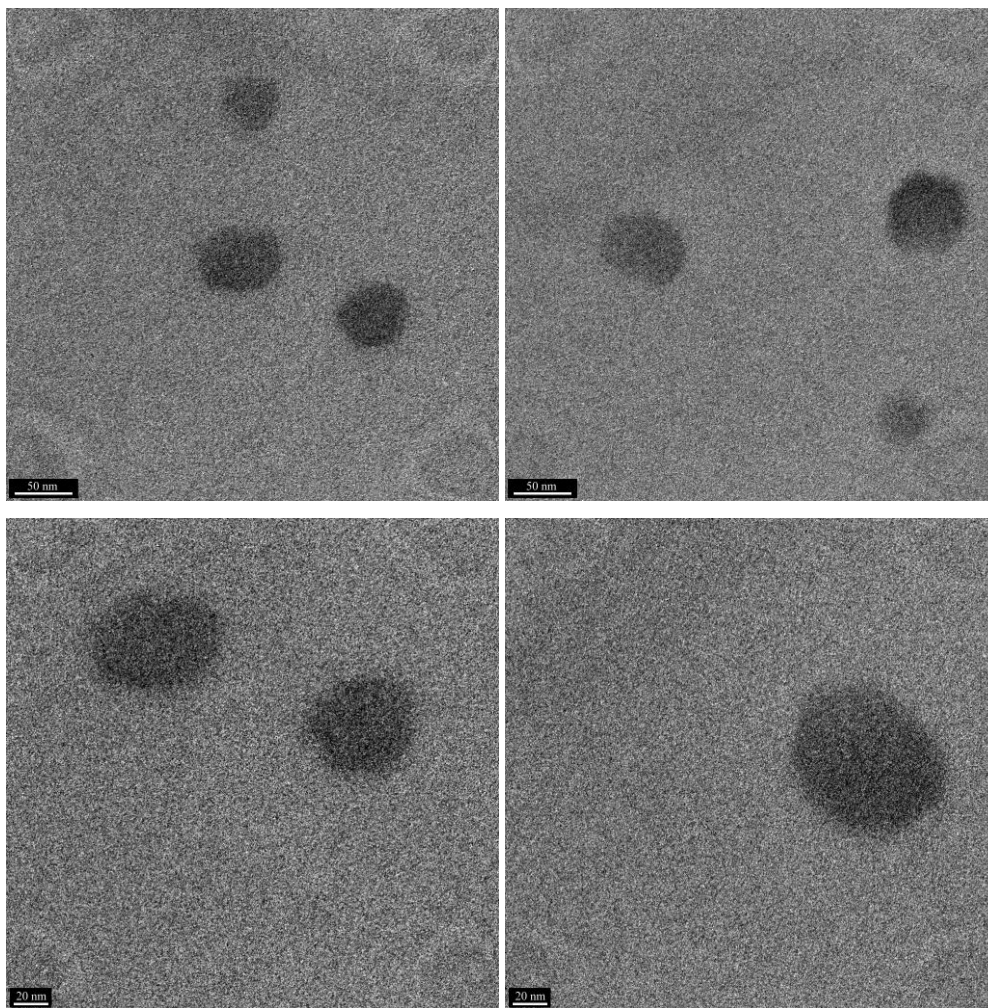


Figure 6.24. TEM images of MSA-capped ZnS:Mn²⁺ quantum dots.

6.9. Chapter Summary

Doped ZnS quantum dot inks were successfully formulated and inkjet printed onto various substrates, including photo quality inkjet paper, photocopy paper, cotton fabric, PET film, ITO-coated PET film, silicon wafer and wool.

A number of surfactants were tested initially in order to ‘solubilise’ doped ZnS quantum dots for inkjet printing. The most satisfactory of these was mercaptosuccinic acid (MSA), and stable MSA-capped ZnS:Mn²⁺ quantum dots were obtained. MSA-capped ZnS:Cu²⁺ quantum dots were unstable as the sodium thiosulfate used to complex Cu²⁺ ions during synthesis was reduced to elemental sulfur by the MSA, destroying any photoluminescence as a consequence.

The fluid properties of the quantum dot ‘ink’ were sufficiently close to those specified by the inkjet printer manufacturer, and the quantum dot ‘ink’ was successfully printed.

Best results were obtained using photo quality inkjet paper, and cotton fabric. One, two, or three passes were made over the substrate by the printhead (number of layers printed). For photo quality inkjet paper, the optimum number of passes was found to be two, before the capacity of the substrate was exceeded and the print was smudged. For cotton fabric, this was found to be three. Best results were also obtained for all substrates with a drop spacing of 15 µm and a reservoir temperature of 30 °C.

The doped ZnS quantum dot ‘inks’ and the printed substrates were characterised by a number of techniques including Cotec Profilometer measurements, PL Spectroscopy, SEM and TEM.

The photoluminescent qualities of the precursor doped ZnS quantum dots (synthesised in 2.2.11 and 2.2.12) were retained when ‘solubilised’ ZnS quantum dots were obtained. The substrates exhibited photoluminescence emission at approximately 600 nm and 530 nm, when printed with MSA-capped ZnS:Mn²⁺ and MSA-capped ZnS:Cu²⁺ quantum dots, respectively.

Such materials have potential application in the upcoming ‘smart’ packaging industry for advertising and as security papers. As doped ZnS is also an

electroluminescent material (1.4), this work represents the early stages of a printable electroluminescent display based on cellulose substrates.

Chapter 7

CONCLUSIONS

In this PhD research programme a suite of hybrid materials based on cellulose fibres and substrates and magnetic nanoparticles (magnetite, cobalt ferrite), conducting polymers (polypyrrole), and quantum dots (doped zinc sulfide), were successfully synthesised and characterised. These include:

- Cellulose fibres coated with magnetite and cobalt ferrite nanoparticles
- Cellulose substrates (newsprint, Kraft board, and cotton fabric) coated with magnetite nanoparticles, polypyrrole, or both
- Cellulose fibres coated with Mn^{2+} and Cu^{2+} -doped ZnS quantum dots
- Doped ZnS quantum dots inkjet printed

Initial applications tests were then carried out for:

- Electromagnetic interference (EMI) shielding (magnetite and polypyrrole coated cellulose substrates)
- Inkjet printing (doped ZnS quantum dots)

Magnetic nanoparticles of magnetite and cobalt ferrite were synthesised by the aqueous chemical methods listed in 2.2.2 and 2.2.3 and characterised using Alternating Gradient Magnetometry (AGM), Electron Dispersive Spectroscopy (EDS), Scanning Electron Microscopy (SEM), SQUID Magnetometry, Transmission Electron Microscopy (TEM), Vibrating Sample Magnetometry (VSM), X-ray Diffraction (XRD), X-ray Fluorescence (XRF) and X-ray Photoelectron Spectroscopy (XPS).

The nanoparticles were present in the spinel structure and had a particle size of approximately 12-26 nm for magnetite and approximately 80 nm for cobalt ferrite. The magnetic properties of the two materials were comparable to those in the literature for the respective nanoparticles. Magnetite nanoparticles were ferrimagnetic in character and had a saturation magnetisation of approximately 60 emu g^{-1} , a coercive field of 19-122 Oe, and a remnant magnetisation of 3-11 emu g^{-1} . Cobalt ferrite nanoparticles had a saturation magnetisation of approximately 61 emu g^{-1} , a coercive field of 80 Oe, and a remnant magnetisation of 7 emu g^{-1} .

Magnetite, with a particle size of 12 nm, was chosen to coat Kraft fibres due to its lower coercive field – ideal for EMI shielding applications. Kraft fibres coated with magnetite nanoparticles (2.2.4) are completely encapsulated by the magnetite nanoparticles, present on the surface in agglomerations approximately 100 nm in size.

The magnetite is bound to the surface of the cellulose fibre by hydrogen bonding to the surface hydroxyl groups present on the cellulose fibres. XPS analysis suggests bonding is taking place between the two components, indicated by shifts in the binding energy of Fe 2p electrons of up to 0.47 eV. The magnetic and structural properties of the magnetic nanoparticles remain unchanged on bonding to the fibre surface.

XRF analysis suggests the amount of magnetite nanoparticles present on the surface of the cellulose fibre is between 1.2 and 3.15 wt. %, depending on the amount of nanoparticles added during the synthesis.

The methods used here are extremely simple and cost-effective, and may give rise to new cellulose based materials for the development of magnetic papers for the EMI shielding area of the upcoming 'smart paper' industry.

Hybrid materials of cellulose (newsprint, Kraft board and cotton fabric) and polypyrrole were then combined with magnetic nanoparticles (2.2.7-2.2.9) synthesised in 2.2.2 and their properties characterised by a number of methods including DC conductivity measurements, EDS, and SEM. They were then tested for application in Electromagnetic Interference Shielding (EMI) at the Defence Science Technology Organisation in Melbourne, Australia.

The greatest shielding effectiveness is obtained using samples coated with both polypyrrole and magnetite. The shielding effectiveness is highest using cotton fabric, presumably as it is thicker than Kraft board and newsprint, and had a higher electrical conductivity. A maximum shielding effectiveness of approximately 43 % in the 1-18 GHz range and 47 % in the 16-40 % range is obtained with polypyrrole and magnetite-coated cotton fabrics. This falls far from the required value of 40 % at 1 GHz for commercial and military applications¹¹⁰.

Although a considerable amount of work needs to be done in order to increase the electrical conductivity of such materials compared with others in the literature^{111, 112}, it can be seen that a synergistic effect can be gained from the use of polypyrrole and magnetite as a coating for EMI shielding. In some cases the gain in shielding effectiveness is approximately 10 %.

Doped-ZnS quantum dots were synthesised by a simple chemical precipitation method (2.2.11 and 2.2.12) and characterised by Atomic Absorption Spectroscopy (AA), Photoluminescence (PL) Spectroscopy, SEM, XPS and XRD.

Mn²⁺ and Cu²⁺ doped varieties gave rise to pink/orange and green emissions at approximately 600 nm and 530 nm, respectively. The quantum dots were approximately 2 nm in diameter and were synthesised in the zinc blende phase.

Kraft fibres (cellulose) were then successfully coated with these materials to produce photoluminescent cellulose fibres. Several approaches were used to coat the fibres with doped ZnS quantum dots – the ‘colloid’, ‘double dip’, ‘PDADMAC’ and ‘in situ’ methods. The most successful in providing a uniform

coating was the ‘in situ’ approach (2.2.16 and 2.2.17), whereby the whole fibre surface was coated with doped ZnS quantum dots, including individual fibrils.

Other dopants were also investigated, such as Ag^+ (for blue emission), but proved unsuccessful as well. For Ag^+ , the large solubility difference between ZnS and Ag_2S proved to be too great to include Ag^+ in the ZnS lattice, even when complexing agents, hydrothermal and microwave synthesis methods were used.

Doped ZnS quantum dot inks were successfully formulated and inkjet printed onto various substrates, including photo quality inkjet paper, photocopy paper, cotton fabric, PET film, ITO-coated PET film, silicon wafer and wool.

A number of surfactants were tested initially in order to ‘solubilise’ doped ZnS quantum dots for inkjet printing. The most satisfactory of these was mercaptosuccinic acid (MSA), and stable MSA-capped ZnS:Mn^{2+} quantum dots were obtained. MSA-capped ZnS:Cu^{2+} quantum dots were unstable as the sodium thiosulfate used to complex Cu^{2+} ions during synthesis was reduced to elemental sulfur by the MSA, destroying any photoluminescence as a consequence.

The fluid properties of the quantum dot ‘ink’ were sufficiently close to those specified by the inkjet printer manufacturer, and the quantum dot ‘ink’ was successfully printed.

Best results were obtained using photo quality inkjet paper, and cotton fabric. One, two, or three passes were made over the substrate by the printhead (number of layers printed). For photo quality inkjet paper, the optimum number of passes was found to be two, before the capacity of the substrate was exceeded and the print was smudged. For cotton fabric, this was found to be three. Best results were also obtained for all substrates with a drop spacing of $15\text{ }\mu\text{m}$ and a reservoir temperature of $30\text{ }^\circ\text{C}$.

The doped ZnS quantum dot ‘inks’ and the printed substrates were characterised by a number of techniques including Cotec Profilometer measurement, PL Spectroscopy, SEM and TEM.

The photoluminescent qualities of the precursor doped ZnS quantum dots (synthesised in 2.2.11 and 2.2.12) were retained when ‘solubilised’ ZnS quantum dots were obtained. The substrates exhibited photoluminescence emission at approximately 600 nm and 530 nm, when printed with MSA-capped ZnS:Mn²⁺ and MSA-capped ZnS:Cu²⁺ quantum dots, respectively.

The suite of materials synthesised in this PhD research will provide the opportunity to develop papers and packaging materials based on cellulose fibres and substrates functionalized by nanoparticles, conducting polymers and quantum dots. This will add value, post paper manufacturing, to one of New Zealand’s largest export commodities by using low cost coating methods and inkjet printing.

It is envisaged that these new materials will see application in the upcoming ‘smart packaging’ and fashion industries for EMI shielding, security, and advertising applications.

Chapter 8

FUTURE WORK

The success of the work completed in this PhD thesis has opened up exciting possibilities for future work.

8.1. EMI Shielding

Initial EMI shielding results suggest that polypyrrole and magnetite-coated cotton fabric and Kraft board are promising materials for commercial EMI shielding applications. In this study the maximum EMI shielding effectiveness value obtained was approximately 50 % - significantly below the level required for commercial application. However, as the shielding effectiveness of material is dependant on its thickness, electrical conductivity, and magnetic properties, using a thicker substrate, a more conductive polymer, a higher loading of magnetite to the substrate, or a combination of all three, may help to increase the shielding effectiveness of the material.

The cotton substrate used in this study is 60 % of the thickness of other substrates used in the literature which give a shielding effectiveness of over 80 %^{111, 112}. When comparing the shielding effectiveness of polypyrrole and magnetite-coated newsprint with the equivalent cotton coated sample, the increase in thickness (almost double) results in a much improved performance. From this, it is easy to speculate that on moving from cotton fabric to a thicker substrate still, a further increase may be seen.

A possibility for increasing the conductivity of the material is the use of different dopants. In this study only *p*-toluenesulfonic acid was used, as it is commonly

used and well studied as a dopant for polypyrrole. However, the use of other dopants such as anthraquinonesulfonic acid, or iron tosylate, may also lead to an increase in conductivity of polypyrrole. Another possibility is to change the conducting polymer altogether, to one of a far higher conductivity such as PEDOT:PSS. One is limited to oxidative chemical polymerisation, however, as electrochemical methods are not suitable for the coating of large substrates.

Finally, the magnetic properties of the material may be improved simply by applying a greater amount of magnetite to the surface of the substrate. Another possibility is to use an electroplating method in which materials with a greater shielding effectiveness such as ferromagnetic iron metal, or a more conductive metal such as copper, are deposited over the polypyrrole coating on the surface of the substrate.

8.2. Inkjet Printing

The exciting work completed on the inkjet printing of quantum dots has opened up a plethora of possibilities for future work, as it is possible that any manner of quantum dots may be synthesised and formulated for inkjet printing. In particular, there exists huge potential for the development of cheap, flexible electronic materials based on cellulose substrates that can be easily printed on demand by a common inkjet printer.

ZnS:Mn²⁺ quantum dots are also electroluminescent. If sandwiched between two electrodes and an AC current applied, a visible emission results. A simple layer structure consisting of a back electrode, dielectric, ZnS:Mn²⁺ phosphor and transparent electrode, may be able to be inkjet printed onto cellulose substrates, resulting in a cheap electroluminescent display based on paper or cotton.

In this study only Mn²⁺, Cu²⁺, and Ag²⁺ were used to dope ZnS quantum dots. Throughout the literature there are many reports on the use of other transition

metal ions¹⁸¹⁻¹⁸³, rare earth ions¹⁸³⁻¹⁸⁵, or combinations of ions^{60, 74, 75, 186-191} (co-doping) to dope ZnS quantum dots. The possibility exists to explore these different dopants in order to gain several different emissions, or 'colours'.

ZnO is a promising material for use as a pressure sensor due to its piezoelectric character. Again, if ZnO quantum dots are able to be formulated for inkjet printing, together with current knowledge in the inkjet printing of electronic materials, a cheap, inkjet printable pressure sensor may be developed for the packaging industry to sense stresses on items during freight.

For the inkjet printing of quantum dot materials, the possibilities are almost endless.

Appendix A

PUBLICATIONS

NOVEL HYBRID MATERIALS OF CELLULOSE FIBRES AND DOPED ZNS NANOCRYSTALS

Aaron C. Small*, James H. Johnston.



Available online at www.sciencedirect.com



Current Applied Physics 8 (2008) 512–515

Current
Applied
Physics

An official journal of the KPS

www.elsevier.com/locate/cap
www.kps.or.kr

Novel hybrid materials of cellulose fibres and doped ZnS nanocrystals

Aaron C. Small*, James. H. Johnston

School of Chemical and Physical Sciences, Victoria University of Wellington, P. O. Box 600, Wellington, New Zealand

Available online 26 October 2007

Abstract

During the past decade semiconductor nanocrystals have been studied extensively, in particular ZnS nanocrystals doped with optically active luminescent centres. Such materials have created new opportunities in the areas of photo-voltaic solar cells and light-emitting diodes. In this study, photoluminescent cellulose fibres were prepared by coating bleached Kraft fibres (*Pinus radiata*) with ZnS nanocrystals doped with Mn^{2+} and Cu^{2+} ions. In doing so, the inherent properties of the fibre (such as tensile strength and flexibility) have been preserved, but imparted to it are the photoluminescent properties of the coating. A wet chemical synthesis method was used in which homogenous solutions of zinc salts and transition metal salts were precipitated with sodium sulfide. Dopant concentrations ranged from 0.1 to 2 wt%. After successive washings and sonication, the particles remained bonded to the surface of the fibre, and the fibres were able to be formed into a paper sheet. Samples were characterized by photoluminescence spectroscopy, scanning electron microscopy, X-ray diffraction, energy dispersive spectroscopy and X-ray photoelectron spectroscopy.

© 2007 Elsevier B.V. All rights reserved.

PACS: 61.46.Df; 68.37.Hk; 78.55.-m

Keywords: ZnS; Doping; Photoluminescence; Cellulose; Hybrid materials

NEW HYBRID MATERIALS OF MAGNETIC NANOPARTICLES AND CELLULOSE FIBRES

Aaron C. Small, James H. Johnston.*

*Submitted for publication in the Journal of Colloid and Interface Science, August, 2008.

NOVEL HYBRID MATERIALS OF CELLULOSE FIBRES AND NANOPARTICLES

A. C. Small, J. H. Johnston**

*Proceedings of the Nano Science and Technology Institute 2008 Conference, Boston, June, 2008.

*Submitted for publication in the Journal of Nanoparticle Research, May, 2008.

NOVEL HYBRID MATERIALS OF CELLULOSE FIBRES AND DOPED ZNS NANOCRYSTALS

Aaron C. Small*, James H. Johnston.

The MacDiarmid Institute for Advanced Materials and Nanotechnology, School of Chemical and Physical Sciences, Victoria University of Wellington, P. O. Box 600, Wellington, New Zealand.

aaron.small@vuw.ac.nz

Abstract: During the past decade semiconductor nanocrystals have been studied extensively, in particular ZnS nanocrystals doped with optically active luminescent centres. Such materials have created new opportunities in the areas of voltaic solar cells and light-emitting diodes. In this study, photoluminescent cellulose fibres were prepared by coating bleached Kraft fibres (*pinus radiata*) with ZnS nanocrystals doped with Mn²⁺ and Cu²⁺ ions. In doing so, the inherent properties of the fibre (such as tensile strength and flexibility) have been preserved, but imparted to it are the photoluminescent properties of the coating. A wet chemical synthesis method was used in which homogenous solutions of zinc salts and transition metal salts were precipitated with sodium sulfide. Dopant concentrations ranged from 0.1-2 wt%. After successive washings and sonication, the particles remained bonded to the surface of the fibre, and the fibres were able to be formed into a paper sheet. Samples were characterized by photoluminescence spectroscopy, scanning electron microscopy, X-ray diffraction, energy dispersive spectroscopy and X-ray photoelectron spectroscopy.

1. INTRODUCTION

The optical properties of doped semiconductor nanocrystals have been studied extensively in recent years [1]. Quantum confinement effects cause these materials to behave in remarkably different ways compared to

their respective bulk materials. ZnS is a II-IV semiconductor with a band gap of ~ 3.6 eV [1] and is an ideal host material.

Doped ZnS nanocrystals have attracted large amounts of interest since 1994 when Bhargava et al. reported for the first time that Mn²⁺ doped ZnS could yield high quantum luminescence efficiency [2]. The results suggested that doped semiconductor nanocrystals were a new class of luminescent material with potential application in displays, lighting and sensing.

As well as ZnS:Mn nanocrystals, a large amount of work has been dedicated to investigating the synthesis and properties of copper doped ZnS nanocrystals [3-6]. This is not only because ZnS:Cu is a widely used phosphor in its bulk form, but also on account of its stronger interaction with the ZnS host [3].

There are many other reports in the literature concerning the doping of ZnS with other species such as transition metal and rare-earth ions Pb²⁺, Ni²⁺, Eu³⁺, Sm³⁺, Tb³⁺ and Er³⁺ [7-11]. More recently attention has turned to co-doped ZnS nanocrystals such as Cu⁺-Cu²⁺, Co²⁺-Cu²⁺, Cu²⁺-Al³⁺, and Cu²⁺-RE (Ce³⁺, Er³⁺, Tb³⁺, Nd³⁺, Y³⁺) [12-15].

Cellulose, (C₆H₁₀O₅)_n, is a long-chain polymeric carbohydrate of β -glucose. It is the fundamental structural component of green plants [16]. Cellulose monomers (β -glucose) are linked together through 1,4 glycosidic bonds by condensation reaction. The cellulose chains are formed into micro fibrils that constitute the basic framework of the plant's cell. In micro fibrils, the multiple hydroxyl groups on the glucose units hydrogen bond with each other, holding the chains firmly together and contributing to their high tensile strength. Cellulose and its derivatives (paper, nitrocellulose, cellulose acetate, etc.) are principal materials generated by industry and enjoy a considerable economic investment [16].

2. EXPERIMENTAL

Doped ZnS nanocrystals were synthesized as free standing powders using a chemical precipitation method [3]. All reagents used were AR grade. Double distilled water was used for all experiments.

In a typical synthesis of Mn^{2+} doped ZnS particles, 10 cm³ of 1M ZnCl_2 , 10 cm³ of 0.01 M MnCl_2 and 10 cm³ of 0.5M sodium citrate solution were mixed and stirred at constant speed for 10 minutes. From a burette, 10 cm³ of 1M Na_2S was added drop wise. A white precipitate was formed immediately. The resulting suspension was centrifuged, washed with distilled water and freeze dried overnight.

In the case of Cu^{2+} doped ZnS, 10 cm³ of 1M ZnCl_2 , 10 cm³ of 0.01M CuCl_2 , 10 cm³ of 0.5M sodium citrate and 10 cm³ of sodium thiosulfate were mixed and stirred for 10 minutes. From a burette, 10 cm³ of 1M Na_2S was added drop wise. A white precipitate was formed immediately. The resulting suspension was centrifuged, washed with distilled water and freeze dried overnight. Dopant concentrations for both Mn^{2+} and Cu^{2+} ranged from 0.1-1 wt%.

A colloidal suspension of these nanocrystals was then added to an approx. 2 % suspension of bleached *pinus radiata* Kraft paper fibres and stirred vigorously for approx. 2 hours, after which they were filtered and washed with H_2O . The resultant coated fibres were then sonicated for 20 min in order to remove any loosely bound nanocrystals.

3. RESULTS AND DISCUSSION

Fig. 1 shows the photoluminescence emission spectrum of ZnS:Mn and ZnS:Cu powders synthesized by the aforementioned methods. An emission peak can be seen at approximately 600 nm, which can be attributed to the ${}^4T_1\text{-}{}^6A_1$ transition in Mn^{2+} [3]. The larger peak at 430 nm can be attributed to an emission due to S^{2-} vacancies in the ZnS lattice [3]. In the case of ZnS:Cu, a broad blue-green emission can be seen at approximately 530 nm. The source of this emission has been fiercely debated. A recent theory suggests the emission arises from the transition of an excited electron from the conduction band of ZnS to the t_2 level of excited Cu^{2+} [6]. On bonding to cellulose the emissions, as expected, do not change, as shown in Fig. 2 below.

The electron microscope images (Fig. 3) show spherical nanocrystals of doped ZnS have been formed. The particles are approximately 30 nm in diameter and appear to evenly coat the surface of the cellulose fibre.

From X-ray diffraction line broadening analysis, the average particle size is ~15 nm for both ZnS:Mn and ZnS:Cu nanocrystals. XRD patterns (Fig. 4.) indicate that ZnS nanocrystals are present in the zinc blende phase [6], and that doping does not change the crystal structure of the material.

Table 1 shows a comparison between literature values [18] and experimental values for 2θ peak positions.

Energy dispersive spectroscopy (EDS) indicates that the particles are indeed ZnS, as both Zn and S correlate exactly. In the case of the doped ZnS nanocrystals, the dopant correlates similarly with the Zn and S as well. From the EDS elemental maps of coated fibres, it appears that the coating is ZnS also, although the coating is presumably too thin and hence the dopant concentration too small for it to be detected.

X-ray photoelectron spectroscopy (XPS) shows shifts in the $2p$ electrons of Zn and S in both doped ZnS nanocrystals and in cellulose fibres coated with doped ZnS nanocrystals (Fig. 6). In some cases the shift is very large, up to 1.4 eV, indicating that strong bonding is occurring between the two compounds (Fig. 6). Interestingly this does not affect the photoluminescent properties of the doped ZnS nanocrystals. These shifts are summarized in Table 2.

4. CONCLUSIONS

In this work Cu^{2+} and Mn^{2+} doped ZnS nanocrystals were synthesized and hybrid materials of these nanocrystals and cellulose fibres were prepared and characterized using a number of techniques. It has been found that the nanocrystals are approximately 15nm in diameter. From SEM and EDS analysis, it has been shown that the doped ZnS nanocrystals coat the surface evenly and retain the photoluminescent properties

of their standalone powders. Emissions are ~ 600 nm for Mn^{2+} doped nanocrystals and ~ 530 nm for the Cu^{2+} doped variety.

REFERENCES

- [1] H. Hu, W. Zhang, *Optical Materials* 28 (2006) 536.
- [2] R. N. Bhargava, D. Gallagher, *Phys. Rev. Lett.* 72 (1994) 416.
- [3] L. Sun, C. Liu, C. Liao, C. Yan, *J. Mater. Chem.* 9 (1999) 1655.
- [4] W. Que, Y. Zhou, L. Lam, C. Chan, C. Kam, B. Liu, M. Gan, C. H. Chew, G. Q. Xu, S. J. Chua, S. J. Xu, F. V. C. Mendis, *App. Phys. Lett.* 73 (1998) 2727.
- [5] K. Manzoor, S. R. Vadera, N. Kumar, T. R. N. Kutty, *Mater. Chem. Phys.* 82 (2003) 718.
- [6] P. Yang, M. Lu, D. Xu, G. Zhou, *Appl. Phys. A* 73 (2001) 455.
- [7] A. A. Bol, A. Meijerink, *Phys. Stat. Sol. B* 224 (2001) 173.
- [8] P. Yang, M. Lu, D. Xu, D. Yuan, J. Chang, G. Zhou, M. Pan, *App. Phys. A* 74 (2002), 257.
- [9] L. Sun, C. Yan, C. Liu, C. Liao, D. Li, J. Yu, *J. Alloys and Compounds* 275-277 (1998) 234.
- [10] A. Huignard, T. Gacoin, J. Boilot, *J. Chem. Mater.* 12 (2000) 1090.
- [11] A. A. Bol, R. V. Beek, A. Meijerink, *Chem. Mater.* 14 (2002) 1121.
- [12] P. Yang, C. F. Song, M. K. Liu, G. J. Zhou, Z. X. Yang, D. Xu, D. R. Yuan, X. F. Cheng, *J. Phys. Chem. Solids* 63 (2002) 639.
- [13] P. Yang, M. K. Liu, G. J. Zhou, D. R. Yuan, D. Xu, *Inorg. Chem. Commun.* 4 (2001) 734.
- [14] A. Ishizumi, C. W. White, Y. Kanemitsu, *Appl. Phys. Lett.* 84 (2004) 2397.
- [15] P. Yang, M. K. Liu, D. Xu, D. L. Yuan, G. J. Zhou, *J. Lumin.* 93 (2001) 101.
- [16] J. C. Roberts, *Paper Chemistry*, Blackie Academic & Professional, Glasgow, 1991.
- [17] M. Jones, *Organic Chemistry*, W. W. Norton & Company, New York, 1997.
- [18] H. E. Swanson, R. K. Fuyat, *Natl. Bur. Stand. (U.S.) Circ.* 539, 16 (1953) 539.

FIGURES:

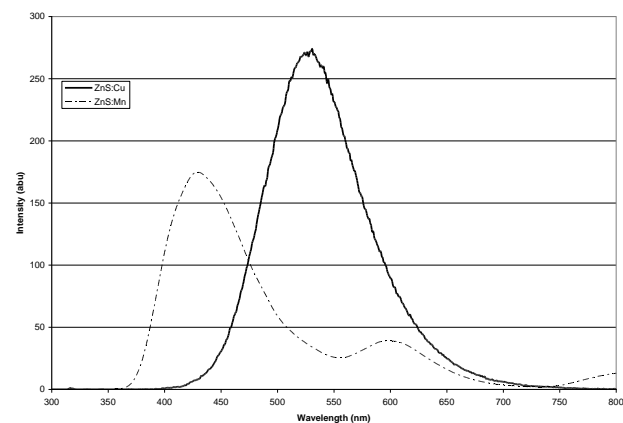


Fig. 1. Photoluminescence emission spectra of doped ZnS nanocrystals.

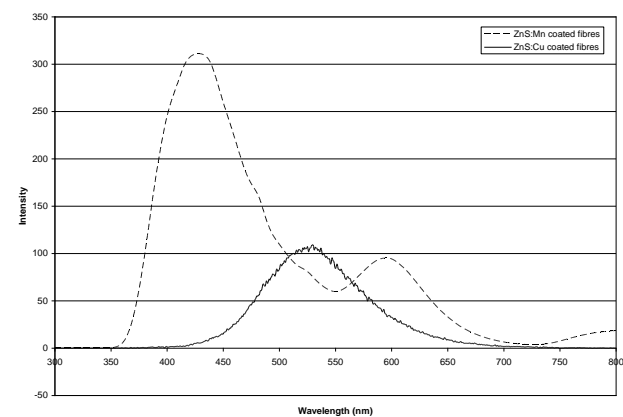


Fig. 2. Photoluminescence emission spectra of cellulose fibres coated with doped ZnS nanocrystals.

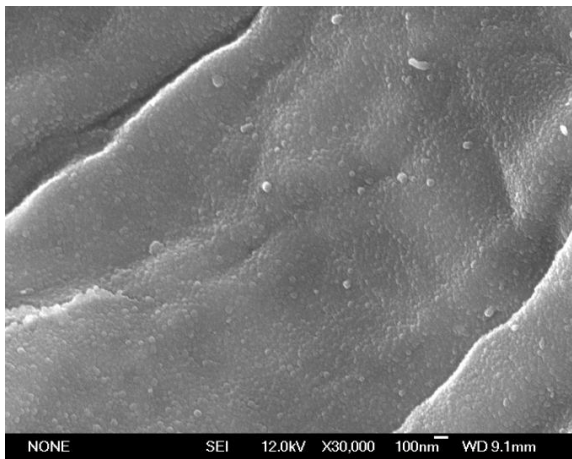


Fig. 3. SEM micrograph showing the surface of the cellulose fibre coated with Mn^{2+} doped ZnS nanocrystals.

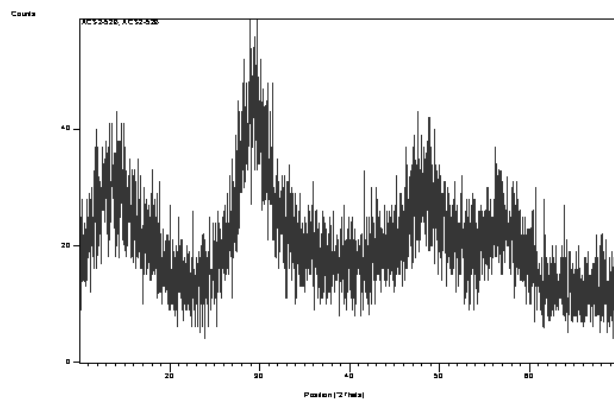


Fig. 4. XRD pattern for Cu^{2+} doped (0.6%) ZnS (Cu K α radiation).

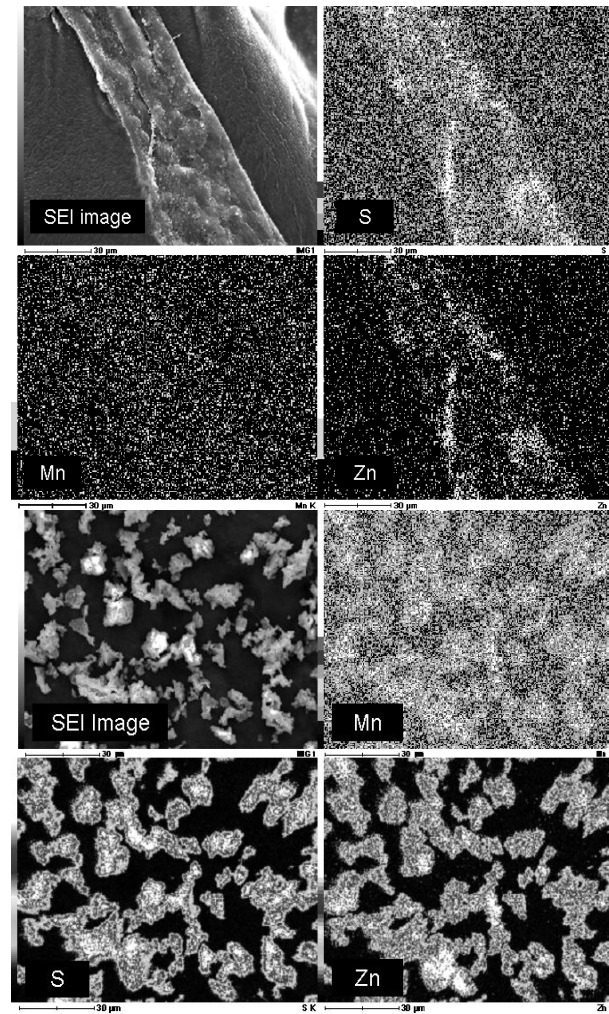


Fig. 5. EDS maps for Mn^{2+} doped ZnS nanocrystals (above) and cellulose fibres coated with Mn^{2+} doped ZnS nanocrystals (below).

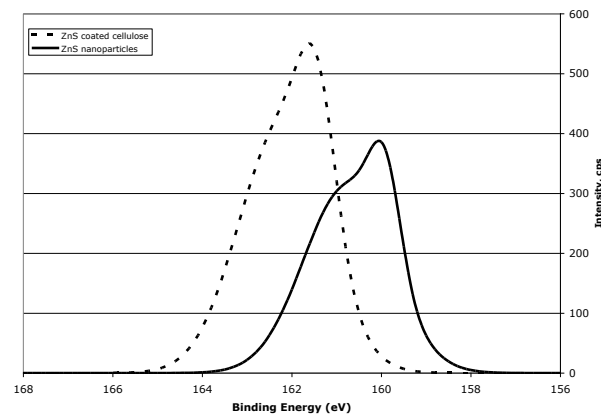
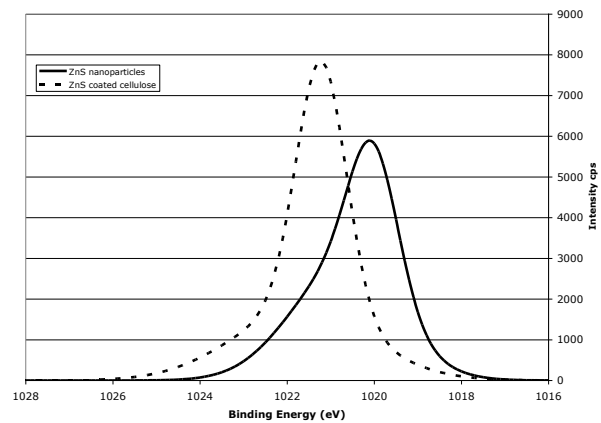


Fig. 6. XPS spectra for 2p electrons in ZnS:Mn nanocrystals and ZnS:Mn coated cellulose fibres. Zn 2p above and S 2p below.

Literature Value	Intensity	Experimental Value	Intensity
(°2θ)	(%)	(°2θ)	(%)
28.559	100	29.31	100
47.516	51	48.50	50
56.291	30	56.99	28

Table 1. Comparison between literature [18] and experimental values for 2θ peaks in ZnS.

	Mn ²⁺ doped ZnS	Coated Fibres
Zn 2p 1/2	1021.3 eV	1020.1 eV
Zn 2p 3/2	1044.3 eV	1043.3 eV
S 2p 1/2	161.5 eV	159.9 eV
S 2p 3/2	162.3 eV	160.8 eV

Table 2. XPS shifts for Mn²⁺ doped ZnS nanocrystals and cellulose fibres coated with Mn²⁺ doped ZnS nanocrystals.

NEW HYBRID MATERIALS OF MAGNETIC NANOPARTICLES AND CELLULOSE FIBRES

Aaron C. Small*, James H. Johnston.

The MacDiarmid Institute for Advanced Materials and Nanotechnology, School of Chemical and Physical Sciences, Victoria University of Wellington, P. O. Box 600, Wellington, New Zealand.

aaron.small@vuw.ac.nz

ABSTRACT: In this study, magnetic cellulose fibres have been prepared by coating bleached Kraft fibres (*pinus radiata*) with magnetite nanoparticles. In doing so, the inherent properties of the fibre (such as tensile strength and flexibility) have been preserved, but imparted to it are the magnetic properties of the coating. The surface coating approach used, differs from other methods in the literature in which the *lumen loading* or *in-situ* approach is taken. After successive washings and sonication, the particles remained bonded to the surface of the fibre, and the fibres could be formed into a paper sheet. The chemical and physical characterization of these materials were carried out using Scanning Electron Microscopy (SEM), Energy Dispersive X-ray Spectroscopy (EDS), X-ray Fluorescence Spectroscopy (XRF), X-ray Diffraction (XRD), X-ray Photoelectron Spectroscopy (XPS), and SQUID Magnetometry. SEM shows the surface of the fibres to be completely encapsulated by the ferrite nanoparticles. This is also confirmed by EDS. XRD line broadening analysis shows the average particle sizes of the nanoparticles range from 12-26 nm. The magnetic nanoparticles and coated Kraft fibres had magnetic saturation values of approximately 62-70 emu g⁻¹ and coercive fields of approximately 19-122 Oe.

1. INTRODUCTION

Hybrid materials are of interest due to the potential synergistic properties that may arise from the combination of two or more precursors. Two such precursors are paper fibres (cellulose) and magnetic nanoparticles. These hybrid materials exhibit the inherent properties of the fibre substrate, in particular flexibility and strength, and also the magnetic properties of the surface bonded nanoparticles.

Magnetically responsive cellulose fibres allow the investigation of new concepts in papermaking and packaging, security paper, and information storage. Potential applications are in electromagnetic shielding, magneto-graphic printing and magnetic filtering. Throughout the literature, there have been reports of superparamagnetic papers obtained through 'in-situ' synthesis of ferrites¹⁻³ and others concerning ferrimagnetic paper obtained by the 'lumen-loading' approach, whereby the lumen of the cellulose fibre is loaded with commercial pigments such as magnetite and maghemite. According to the literature, the 'lumen-loading' approach is necessary to diminish the loss of mechanical strength of the fibres, and the poor retention of the inorganic particles⁴⁻⁶, and that the 'in situ' approach offers greater control of both the magnetic properties and the variety of magnetic particles that can be incorporated into the final product.

We report a method different to both the 'in-situ' and 'lumen-loading' approach in which magnetic nanoparticles of magnetite are prepared separately⁷, mixed with Kraft pulp, and subsequently washed and filtered to give a magnetic paper with comparable magnetic properties and mechanical strength to those synthesised by the above-mentioned methods.

2. EXPERIMENTAL

Materials. Reagent grade chemicals (FeCl₂·4H₂O) purchased from BDH Chemicals Ltd. were used in all experiments. Aqueous NH₃ from Scharlan Ltd. (25% vol.) was also used. No special care was taken in order to isolate the system from atmospheric oxygen. Suspensions and solutions were prepared using double-

distilled water. Both bleached and unbleached Kraft pulp (*pinus radiata*) was obtained from Norske Skog Ltd. (Formerly Tasman Pulp & Paper Company Ltd.).

Synthesis. Magnetite (Fe_3O_4) nanoparticles were synthesized by adding aqueous ammonia (7 M, 50 cm³) drop wise from a burette to solutions containing dissolved $\text{FeCl}_2 \cdot 4\text{H}_2\text{O}$. Black precipitates were formed immediately⁷. As particle size is dependant on both the concentration of the precursor solution and the rate precipitation, various concentrations of precursor solution were used and the precipitation rate was kept constant. These are summarized in Table 1.

A colloidal suspension of these nanoparticles was then added to an approximately 2 wt. % suspension of bleached *pinus radiata* Kraft paper fibres and stirred vigorously for approximately 2 hours, after which they were filtered and washed with H_2O . The resultant coated fibres were then sonicated for 20 minutes in order to remove any loosely bound nanoparticles.

The magnetic particles and magnetic cellulose fibres produced were characterized by a number of methods. X-ray diffraction (XRD) measurements were taken on a Philips X-ray diffractometer using a $\text{Cu K}\alpha$ radiation source. Average particle size was calculated from the width of the XRD peaks under the Debye-Scherrer approximation (which assumes the small crystallite size to be the cause of line broadening) using CaCO_3 as a standard. Scanning Electron Microscopy (SEM) and Energy Dispersive X-Ray Spectroscopy (EDS) was performed on a JEOL-6500F instrument. SEM images were taken at a working distance of 10 mm and with an accelerating voltage of 15 kV and a probe current of 12 μA . EDS measurements were made with an accelerating voltage of 12 kV and a probe current of 16. Magnetic measurements were made at both 5 K and 300 K on a Quantum Design SQUID Magnetometer. Paper samples were cut into rectangular pieces 10 mm x 5 mm and measured parallel to the field. X-ray Photoelectron Spectroscopy (XPS) measurements were carried out using a Kratos Axis Ultra DL, equipped with a monochromatic Al $\text{K}\alpha$ X-ray source. Scans were run at 15 kV and 10 mA, with a pass energy of 160 eV for survey scans and 20 eV for narrow scans. The sample area was 300 x 700 mm. Curve fitting was done using the Fityk peak fitting program and all peaks fitted to a Gaussian peak shape. Binding energies were referenced to the C-C 1s photoelectron peak at 284.8 eV.

3. RESULTS AND DISCUSSION

Pinus radiata Kraft fibres coated with Fe_3O_4 nanoparticles retain the inherent properties of the fibre; tensile strength, flexibility, and the ability to be made into a sheet. The fibres also gain the magnetic properties of the surface bound nanoparticles.

A typical XRD pattern (Figure 1) shows that Fe_3O_4 is the major phase in all samples. Samples prepared with higher solution concentrations of $\text{FeCl}_2 \cdot 4\text{H}_2\text{O}$, have $\alpha\text{-FeOOH}$ is present as an impurity phase. Consistent with the literature⁸, the particle size decreases as the concentration of $\text{FeCl}_2 \cdot 4\text{H}_2\text{O}$ decreases. X-ray line broadening indicates that samples have an average particle size of between 12 and 26 nm, depending on solution concentration (Table 1).

By varying the concentration of Fe^{2+} in the precursor solution, different particle sizes were obtained. These are summarized in Table 1.

Magnetization versus applied field curves are presented in Figures 2 and 3. Saturation magnetization is independent of particle size but dependent on temperature. Fe_3O_4 -coated cellulose fibre samples show a saturation magnetization of $\sim 65 \text{ emu g}^{-1}$. This value is comparable to the saturation magnetization values for bulk Fe_3O_4 , indicating that the combination of cellulose fibres and magnetic nanoparticles does not affect the magnetic properties of the nanoparticles. The magnetic moment is also comparable to materials with similar Fe_3O_4 loadings^{2,3}. Lowering the concentration of Fe^{2+} in the precursor solution results in the formation of smaller particles, and changes the coercive field accordingly. Particle sizes calculated using the Debye-Scherrer approximation for XRD are only average particle sizes, hence a smaller average particle size means a larger number of particles will be in the superparamagnetic range, and as a consequence, the coercive field is lowered. Coercive fields at 300 K for these materials are very low; $H_c = \sim 20\text{-}120 \text{ Oe}$. A coercive field as low as this is ideal for application in electromagnetic shielding. The materials also possess small remnant fields of $\sim 3\text{-}11 \text{ emu g}^{-1}$ at 300 K, as shown in the magnetic hysteresis loops in Figures 2 and 3.

Optical microscope images (Figure 4) at 90x magnification show that the coated fibres (b) retain the same morphology as the precursor Kraft fibres (a). The brown colour of the fibres (a change from the original white) indicates they are coated with the Fe_3O_4 nanoparticles.

From the SEM images (Figure 5), the completeness of the coating can be seen. The Fe_3O_4 nanoparticles completely encapsulate the fibre and follow its morphology, similar to previous research involving cellulose fibres coated with conducting polymers⁹. This is also confirmed by examining the EDS map for Fe (Figure 6), which shows full coverage of the fibre surface. Nanoparticles are present on the surface of the cellulose fibres in agglomerations of ~ 100 nm, as no surfactant was used in the synthesis procedure. The fundamental particle size of the Fe_3O_4 nanoparticles in their agglomerates is determined from the XRD pattern using the Debye-Scherrer approximation as being between 12-26 nm.

XRF analysis shows the samples to be 0.5-2.8 wt. % Fe. The Fe 2p XPS spectrum of the Fe_3O_4 nanoparticles (Figure 7) shows the Fe_3O_4 and α -FeOOH phases to be present^{10,11}, consistent with XRD results. XPS analysis suggests that there is more α -FeOOH present than XRD analysis does. This is probably due to concentrated α -FeOOH at the surface, and as XPS penetrates to lesser depths than does XRD, more of it is shown in the XPS spectrum.

A comparison between the Fe 2p XPS spectrum of Fe_3O_4 coated cellulose fibres and Fe_3O_4 nanoparticles (Figure 9) shows a considerable shift to lower binding energy of up to 0.47 eV for both the 1/2 and 3/2 spin multiplicities of Fe in the coated samples. This shift confirms that there is chemical bonding between the Fe_3O_4 nanoparticles and the cellulose fibre surface, presumably through hydrogen bonding between the O in the Fe_3O_4 and α -FeOOH nanoparticles (Figure 9) and the H of the OH groups present in cellulose. The peak shape of the Fe 2p XPS spectrum of Fe_3O_4 -coated cellulose fibres does not change compared to that of the Fe_3O_4 nanoparticles by themselves. This indicates that the chemical bonding between the Fe_3O_4 nanoparticles and the cellulose fibre does not alter the chemistry of the nanoparticles. Table 2 summarizes the binding energies and shifts of these materials.

Even after repeated washing and sonication steps, the particles remain bound to the surface. This is contrary to other reports in the literature which state that particles on the fibre surface are removed in the washing step [1-3].

4. CONCLUSION

We have prepared Fe_3O_4 nanoparticles in aqueous solutions and at a range of concentrations and combined them with *pinus radiata* Kraft fibres to obtain magnetically responsive paper. The method is extremely simple and cost-effective which may lead to the development of magnetic papers in the shielding area of the upcoming 'smart paper' industry. The particle size of the nanoparticles ranges from 12-26 nm. The saturation magnetization of the nanoparticles ranges from 62-70 emu g⁻¹, with coercive fields in the range of 19-122 Oe. The combination of these nanoparticles with cellulose fibres sees no change in the magnetic properties. Nanoparticles are firmly bound to the fibre surface and fully encapsulate it.

ACKNOWLEDGMENTS

This work was supported by the MacDiarmid Institute for Advanced Materials and Nanotechnology. The authors wish to thank Prof. J. Tallon and Dr. G. Williams of Industrial Research Ltd. for help with magnetic experimental work.

REFERENCES

1. J. A., Carrazana-Garcia, M. A. Lopez-Quintela and J. Rivas-Rey, Colloids Surf., A, 121, 61 (1997)
2. J. A. Carrazana-Garcia, M. A. Lopez-Quintela and J. Rivas-Rey, IEEE Trans. Mag., 31, 3126 (1995)
3. R. H. Marchessault, P. Rioux, and L. Raymond, Polymer, 33, 4024 (1992).

4. S. Zakaria, B. H. Ong, and T. G. M. van de Ven, *Colloid Surf., A*, 251, 1 (2004)
5. S. Zakaria, B. H. Ong, T. G. M. van de Ven, *Colloids Surf., A*, 251, 31 (2004)
6. S. R. Middleton and A. M. Scallan, *J. Pulp Pap. Sci.*, 15, J229-J234 (1989)
7. P. Berger, N. B. Adelman, K. J. Beckman, D. J. Campbell, A. B. Ellis and G. C. Lisensky, *J. Chem. Ed.*, 76, 943 (1999)
8. D. Thapa, V. R. Palkar, M. B. Kurup and S. K. Malik, *Mater. Lett.*, 58, 2692 (2004)
9. M. J. Richardson, J. H. Johnston, T. Borrmann, *Current Applied Physics*, 6, 462 (2006)
10. J. Chastain, J. F. Moulder, W. F. Stickle, P. E. Sobol and K. D. Bomben, in *Handbook of X-ray Photoelectron Spectroscopy*, Perkin Elmer Corporation, Minn, USA, 1992.
11. J. F. Anderson, M. Kuhn, and U. Diebold, *Surf. Sci. Spectra*, 4, 266 (1998)

FIGURES:

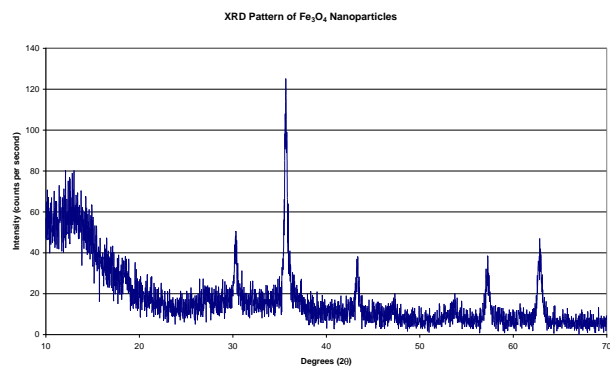


Figure 2. XRD pattern of synthesized Fe₃O₄ nanoparticles (sample 53D), * is the α-FeOOH phase.

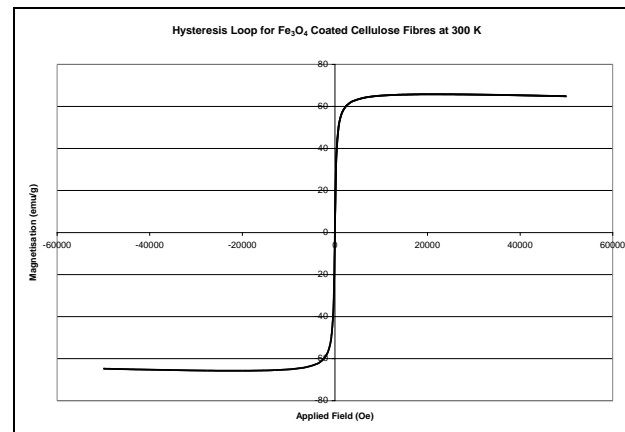


Figure 3. Magnetic hysteresis loop for Fe₃O₄-coated cellulose fibres at 300 K. Sample has an Fe loading of 2.88 wt. %.

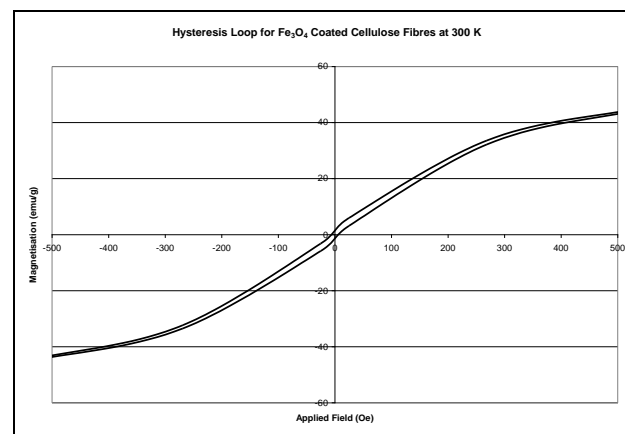


Figure 4. Magnified view of Fe₃O₄ hysteresis loop at 300 K. A small remnant magnetization is visible.

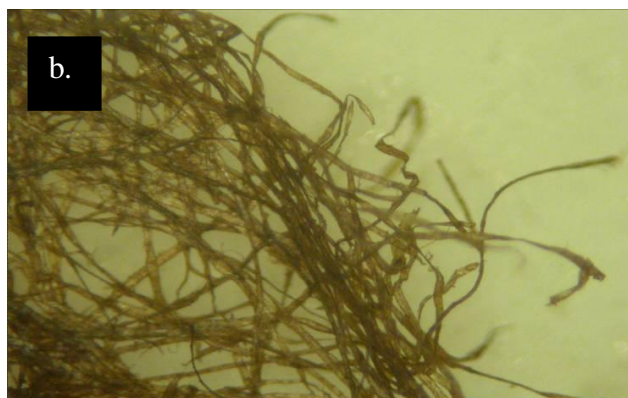
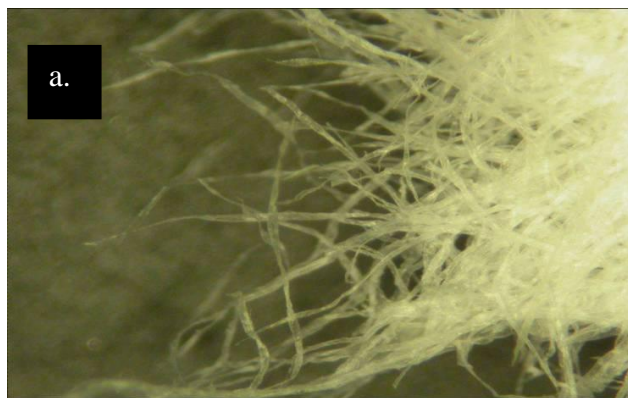


Figure 4. Optical microscope images (90x mag.) of uncoated cellulose fibres (a) and Fe₃O₄ coated Kraft fibres (b).

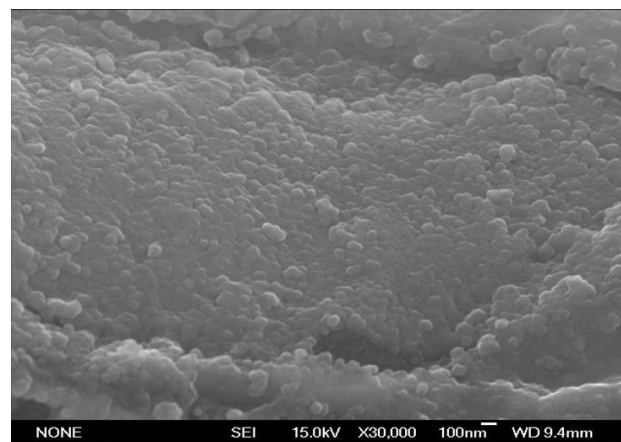
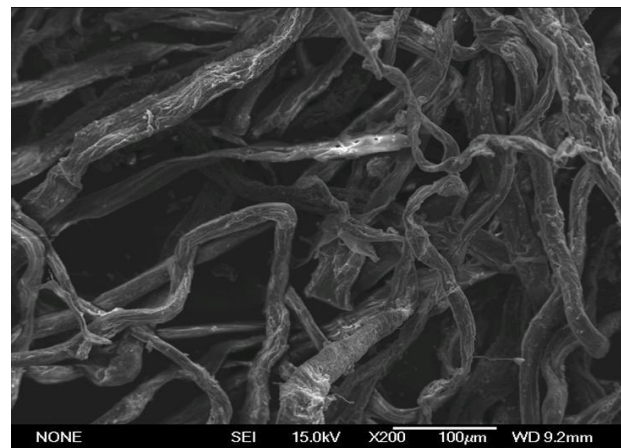


Figure 5. SEM images of Fe₃O₄ cellulose fibres.

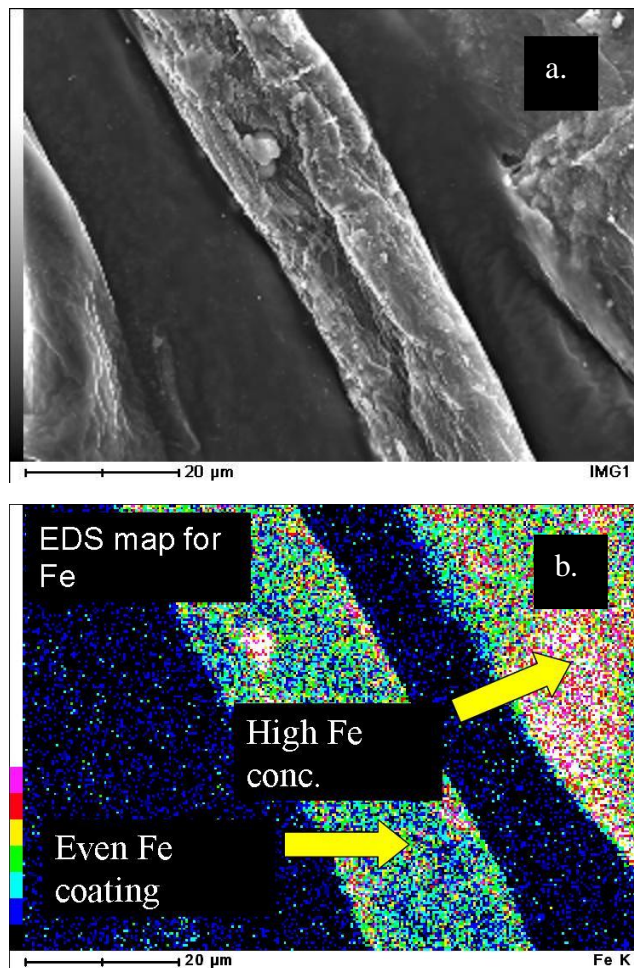


Figure 6. EDS images of Fe₃O₄ coated cellulose fibres, complementary SEI image (a) and elemental Fe map (b).

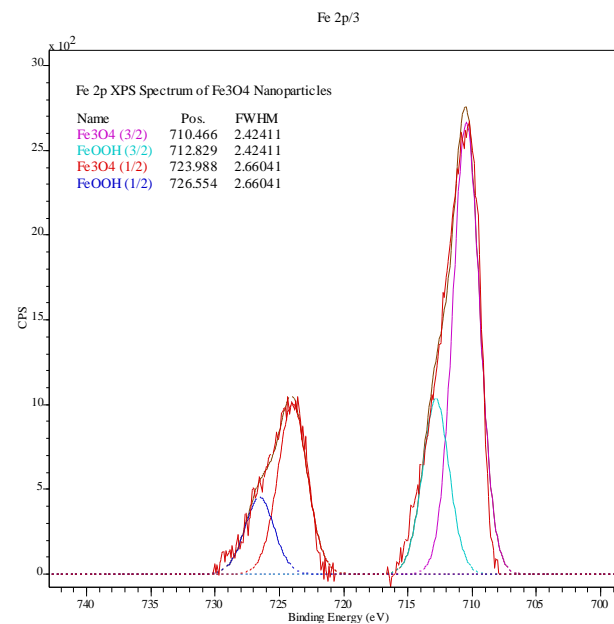


Figure 7. XPS spectrum of Fe₃O₄ nanoparticles.

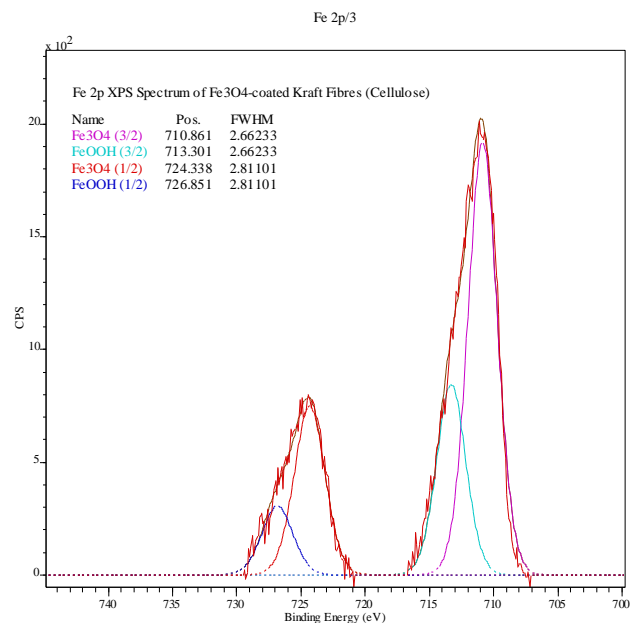


Figure 8. XPS spectrum of Fe₃O₄-coated cellulose fibres.

Sample	Solution conc. (mol dm ⁻³)	Average particle size (nm)	Saturation magnetization (emu g ⁻¹)	Coercive field (Oe)
53D	0.15	26	62	122
53E	0.03	24	62	112
53F	0.0025	15	70	42
53G	0.00125	12	63	19

Table 3. Effect of precursor solution concentration on particle size, saturation magnetization and coercive field of Fe₃O₄ nanoparticles.

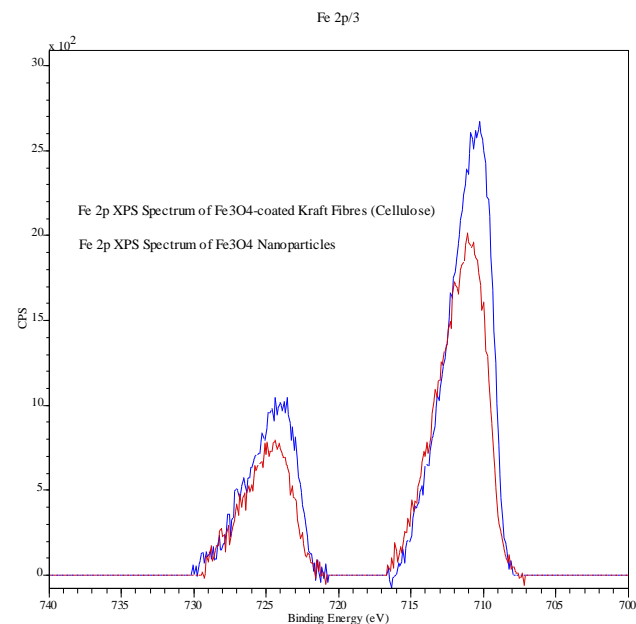


Figure 9. Comparison between Fe 2p XPS spectra of Fe₃O₄ coated Kraft fibres and Fe₃O₄ nanoparticles.

	Fe ₃ O ₄ nanoparticles	Fe ₃ O ₄ -coated cellulose fibres	
Species Present	Binding Energy (eV)	Binding Energy (eV)	Shift (eV)
Fe ₃ O ₄ (1/2)	723.988	724.338	0.35
Fe ₃ O ₄ (3/2)	710.466	710.861	0.395
α-FeOOH (1/2)	726.554	726.851	0.297
α-FeOOH (3/2)	712.829	713.301	0.472

Table 4. Summary of XPS binding energies and shifts for Fe₃O₄ nanoparticles and Fe₃O₄-coated cellulose fibres.

NOVEL HYBRID MATERIALS OF CELLULOSE FIBRES AND NANOPARTICLES

A. C. Small*, J. H. Johnston*

*Victoria University of Wellington and The MacDiarmid Institute for Advanced Materials and Nanotechnology, Wellington, New Zealand, jim.johnston@vuw.ac.nz

ABSTRACT: Hybrid materials are of interest due to the potential synergistic properties that may arise from the combination of two or more precursors. Such precursors are paper fibres (cellulose) and magnetic or photoluminescent nanoparticles. These materials exhibit the inherent properties of the substrate, in particular flexibility and strength, and also the properties of the surface bonded nanoparticles.

Keywords: cellulose, nanoparticles, magnetic, photoluminescent.

1. INTRODUCTION

Cellulose, $(C_6H_{10}O_5)_n$, is a long-chain polymeric carbohydrate of β -glucose. It is the fundamental structural component of green plants, in which the primary cell wall of the plant is predominantly cellulose, and the secondary wall contains cellulose with variable amounts of lignin. Lignin and cellulose, considered together, are termed lignocellulose, which (as wood) is the most common biopolymer on earth. Cellulose monomers (β -glucose) are linked together through 1,4 glycosidic bonds by condensation. Each monomer is oriented 180° to the next, as seen in Figure 1, and the chain is built up two units at a time.

The cellulose chains are formed into micro fibrils that constitute the basic framework of the plants cell. In micro fibrils, the multiple hydroxyl groups on the glucose units hydrogen bond with each other, holding the chains firmly together and contributing to their high tensile strength¹. Cellulose and its

derivatives (paper, nitrocellulose, cellulose acetate, etc.) are principal materials generated by industry and see a considerable economic investment.

Magnetically responsive cellulose fibres allow the investigation of new concepts in papermaking and packaging, security paper, and information storage. Potential applications are in electromagnetic shielding, magneto-graphic printing and magnetic filtering.

Doped ZnS nanoparticles have attracted large amounts of interest since 1994 when Bhargava *et al.*² reported for the first time that Mn^{2+} doped ZnS could yield high quantum luminescence efficiency. As well as ZnS:Mn nanoparticles, a large amount of work has been dedicated to investigating the synthesis and properties of copper doped ZnS nanoparticles.

The combination of doped ZnS nanoparticles and cellulose fibres could lead to the development of new security papers and cost effective display technology.

2. EXPERIMENTAL

Magnetite (Fe_3O_4) nanoparticles were synthesized by adding aqueous ammonia drop wise from a burette to solutions containing dissolved $FeCl_2 \cdot 4H_2O$. Black precipitates were formed immediately³. As particle size is dependant on both the concentration of the precursor solution and the rate precipitation, various concentrations of precursor solution were used and the precipitation rate was kept constant. These are summarized in Table 1.

In a typical synthesis of Mn^{2+} or Cu^{2+} doped ZnS particles, $ZnCl_2$, $MnCl_2$ or $CuCl_2$ and sodium citrate solution were mixed and stirred at constant speed for 10 minutes. From a burette, Na_2S was added drop wise. A white precipitate was formed immediately. The resulting suspension was centrifuged and then washed with distilled water.

A colloidal suspension of these nanoparticles was then added to an approx. 2 wt. % suspension of bleached pinus radiata Kraft paper fibres and stirred vigorously for approximately 2 hours, after which

they were filtered and washed with H₂O. The resultant coated fibres were then sonicated for 20 minutes in order to remove any loosely bound nanoparticles.

3. RESULTS AND DISCUSSION

3.1 Magnetic Nanoparticles

Pinus radiata Kraft fibres coated with Fe₃O₄ nanoparticles retain the inherent properties of the fibre; tensile strength, flexibility, and the ability to be made into a sheet. The fibres also gain the magnetic properties of the surface bound nanoparticles. Consistent with the literature³, particle size decreases as the concentration of FeCl₂·4H₂O decreases. X-ray line broadening indicates that samples have an average particle size of between 12 and 26 nm, depending on solution concentration. By varying the concentration of Fe²⁺ in the precursor solution, different particle sizes were obtained (Table 1). Magnetisation versus applied field curves are presented in Figures 2 and 3.

Saturation magnetisation is independent of particle size but dependent on temperature. Fe₃O₄-coated cellulose fibre samples show a saturation magnetisation of ~ 65 emu g⁻¹. This value is comparable to the values of saturation magnetisation of bulk Fe₃O₄, indicating that the combination of cellulose fibres and magnetic nanoparticles does not alter the magnetic properties of the nanoparticles. The magnetic moment is also comparable to materials with similar Fe₃O₄ loadings⁴. Lowering the concentration of Fe²⁺ in the precursor solution results in the formation of smaller particles, and changes the coercive field accordingly. Particle sizes calculated using the Debye-Scherrer approximation for XRD are only average particle sizes, hence a smaller average particle size means a larger number of particles will be in the superparamagnetic range, and as a consequence, the coercive field is lowered. Coercive fields at 300 K for these materials are very low; H_c = ~ 20-120 Oe. A coercive field as low as this is ideal for application in electromagnetic shielding. The materials also possess small remnant fields of ~ 3-11 emu g⁻¹ at 300 K, as shown in the magnetic hysteresis loops in Figures 2 and 3 above. Optical microscope images show that the coated fibres

retain the same morphology as the precursor Kraft fibres. The brown colour of the fibres (a change from the original white) indicates they are coated with the Fe₃O₄ nanoparticles. From the SEM image shown in Figure 4, the completeness of the coating can be seen. The Fe₃O₄ nanoparticles completely encapsulate the fibre and follow its morphology, similar to previous research involving cellulose fibres coated with conducting polymers⁵.

This is also confirmed by examining the EDS map for Fe (Figure 5), which shows full coverage of the fibre surface. Nanoparticles are present on the surface of the cellulose fibres in agglomerations of ~ 100 nm, as no surfactant was used in the synthesis procedure. This differs from the particle size calculated using the Debye-Scherrer approximation, where the individual crystallite size was calculated as being between 12-26 nm. XRF analysis shows the samples to be 0.5-2.8 % Fe. The Fe 2*p* XPS spectrum of the Fe₃O₄ nanoparticles (Figure 6) shows the Fe₃O₄ and α-FeOOH phases to be present⁶, consistent with XRD results. A comparison between the Fe 2*p* XPS spectrum of Fe₃O₄ coated cellulose fibres and Fe₃O₄ nanoparticles (Figure 7) shows a considerable shift to lower binding energy of up to 1.5 eV for both the 1/2 and 3/2 spin multiplicities of the coated samples. This shift confirms that there is chemical bonding between the Fe₃O₄ nanoparticles and the cellulose fibre surface, presumably through hydrogen bonding between the O in the Fe₃O₄ and α-FeOOH nanoparticles and the H of the OH groups present in cellulose. The shape of the Fe 2*p* XPS spectrum of Fe₃O₄-coated cellulose fibres does not change compared to that of the Fe₃O₄ nanoparticles by themselves. This indicates that the chemical bonding between the Fe₃O₄ nanoparticles and the cellulose fibre does not alter the chemistry of the nanoparticles. Even after repeated washing and sonication steps, the particles remain bound to the surface. This is contrary to other reports in the literature which state that particles on the fibre surface are removed in the washing step

3.2. Photoluminescent Nanoparticles

Figure 8 shows the photoluminescence emission spectrum of ZnS:Mn powders synthesized by the aforementioned methods.

An emission peak can be seen at approximately 590 nm, which can be attributed to the $^1A_g \rightarrow ^2T_g$ transition in Mn^{2+} . The larger peak at 480 nm can be attributed to an emission due to S^{2-} vacancies in the ZnS lattice⁷. In the case of ZnS:Cu, a broad blue-green emission can be seen at approximately 520 nm. The source of this emission has been fiercely debated. A recent theory suggests the emission arises from the transition of an excited electron from an S^{2-} vacancy in the ZnS lattice to the t_{2g} excited state of the Cu^{2+} dopant⁸.

Again, on bonding to cellulose fibres, the emissions are unaffected. X-ray photoelectron spectroscopy (XPS) shows that bonding is occurring between the doped ZnS nanoparticles and the cellulose surface, due to shifts in the 3/2 and 1/2 spin multiplicities of the 2p electrons of both Zn and S. In some cases the shift is large up to 1.4 eV (Figure 9).

On examining electron microscope images (Figure 10), it can be seen that spherical nanoparticles of doped ZnS have been formed. It is difficult to deduce particle size from these images as the particles have agglomerated due to the absence of a surfactant during the synthesis procedure. From x-ray line broadening analysis, the average particle size is ~15 nm for both ZnS:Mn and ZnS:Cu nanoparticles.

Electron dispersive spectroscopy (EDS) indicates that the particles are indeed ZnS, and in both cases, the dopant can be mapped as well.

4. CONCLUSIONS

Fe_3O_4 and Cu^{2+} and Mn^{2+} doped ZnS nanoparticles were synthesized and hybrid materials of these and cellulose fibres were prepared and characterized using a number of techniques. It has been shown that the nanoparticles coat the surface evenly and retain the magnetic and photoluminescent properties of their standalone powders.

REFERENCES

- [1] Wallenberrger and Weston, "Natural fibers, polymers and composites.", Kluwer Academic Publishers, 2004.
- [2] R. N. Bhargava, D. Gallagher, X. Hong, A. Nurmikko, Phys. Rev. Lett., 72, 416, 1994.
- [3] D. Thapa, V. R. Palkar, M. B. Kurup, S. K. Malik, *Mater. Lett.*, **58**, 2004, 2692-2694.
- [4] R. H. Marchessault, P. Rioux, L. Raymond, Polymer, 33, 4024, 1992.
- [5] M. J. Richardson, J. H. Johnston, T. Borrmann, Curr. Appl. Phys. 6, 462, 2006.
- [6] J. F. Anderson, M. Kuhn, U. Diebold, Surf. Sci. Spectra, 4, 266, 1998.
- [7] L. Sun, C. Liu, C. Liao, C. Yan, J. Mater. Chem. 9, 1655, 1999.
- [8] P. Yang, M. Lu, D. Xu, G. Zhou, Appl. Phys. A, 73, 455, 2001.

FIGURES:

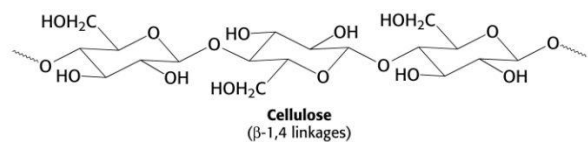


Figure 5. Structure of cellulose ($C_6H_{10}O_5$)_n.

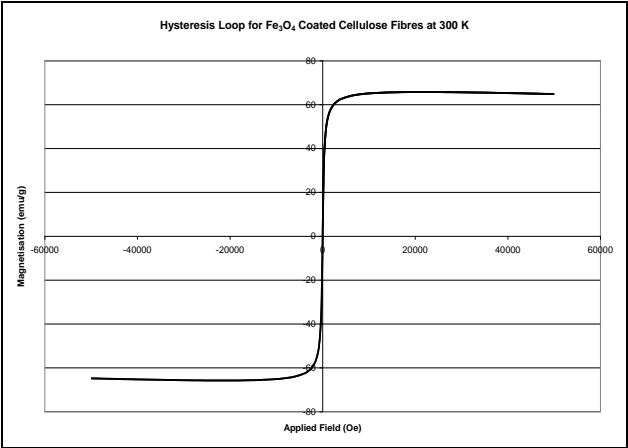


Figure 2. Magnetic hysteresis loop for Fe_3O_4 -coated cellulose fibres at 300 K. Sample has an Fe loading of 2.88 %.

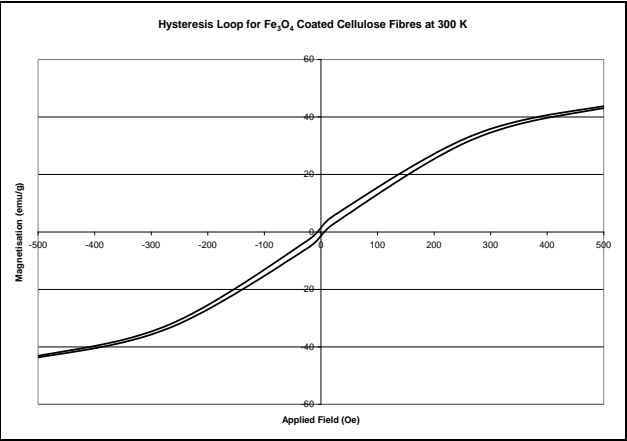


Figure 3. Magnified view of Fe_3O_4 hysteresis loop at 300 K. A small remnant magnetization is visible.

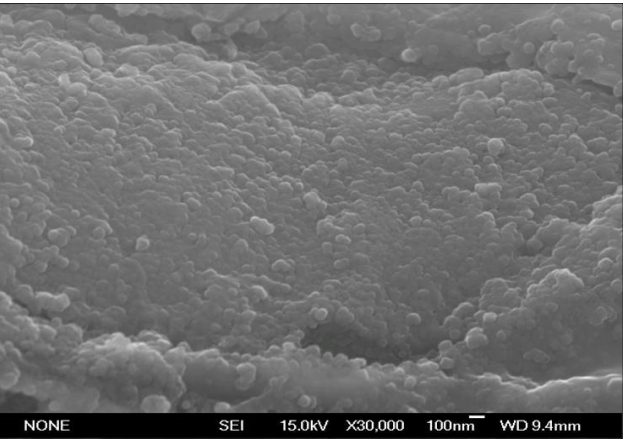


Figure 4. SEM images of Fe_3O_4 cellulose fibres.

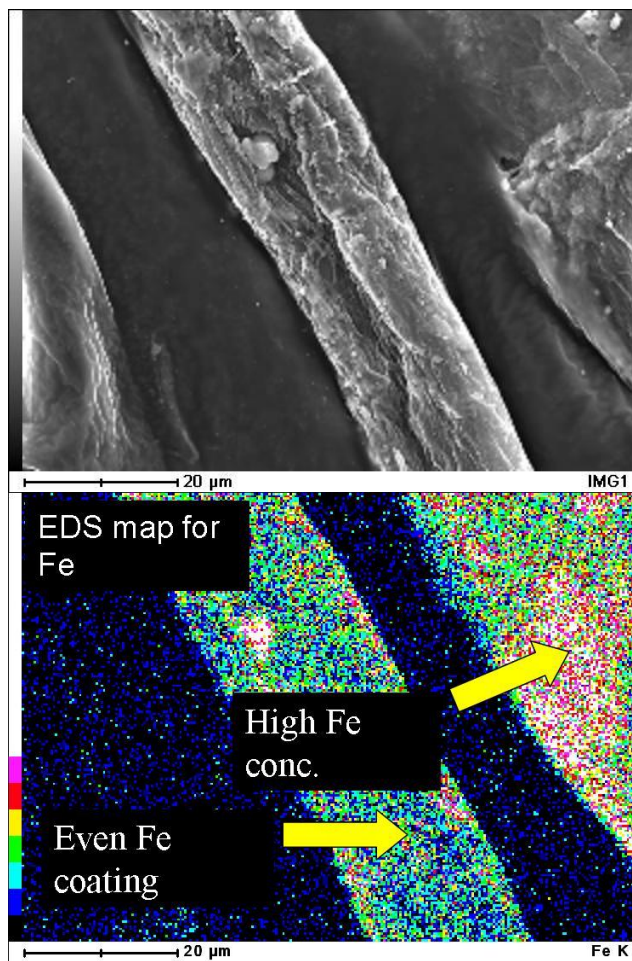


Figure 5. EDS images of Fe_3O_4 coated cellulose fibres, SEI image (above) and elemental Fe map (below).

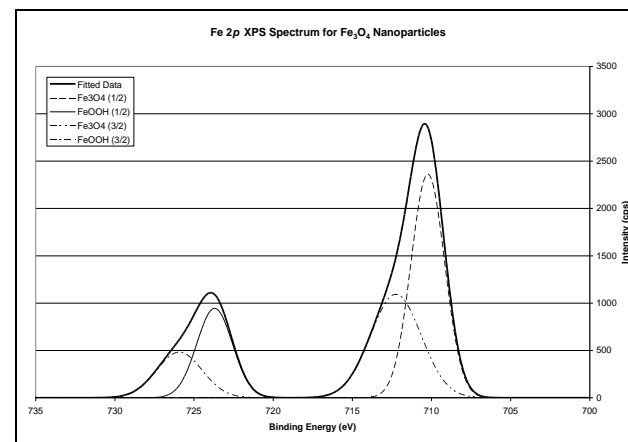


Figure 6. XPS spectrum of Fe_3O_4 nanoparticles.

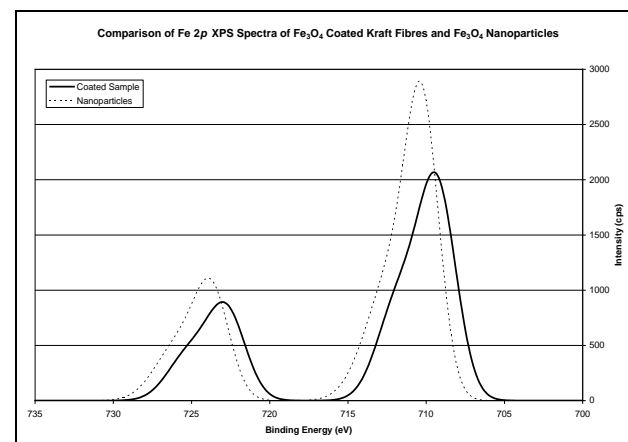


Figure 7. Comparison between Fe 2p XPS spectra of Fe_3O_4 -coated Kraft fibres and Fe_3O_4

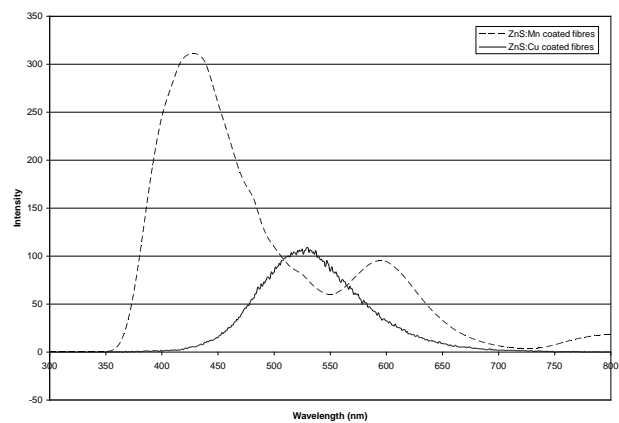


Figure 8. Photoluminescence emission spectra of doped ZnS nanoparticles.

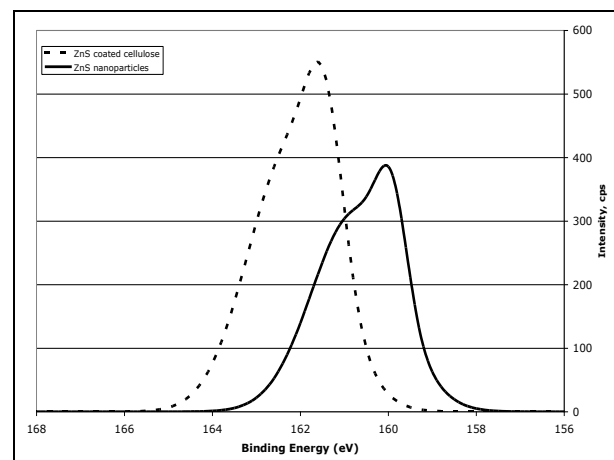
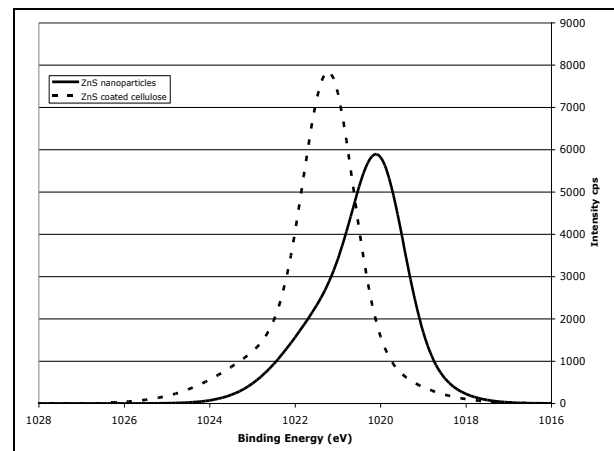


Figure 9. XPS spectra for 2p electrons in ZnS:Mn nanoparticles and ZnS:Mn coated cellulose fibres. Zn 2p above, and S 2p below.

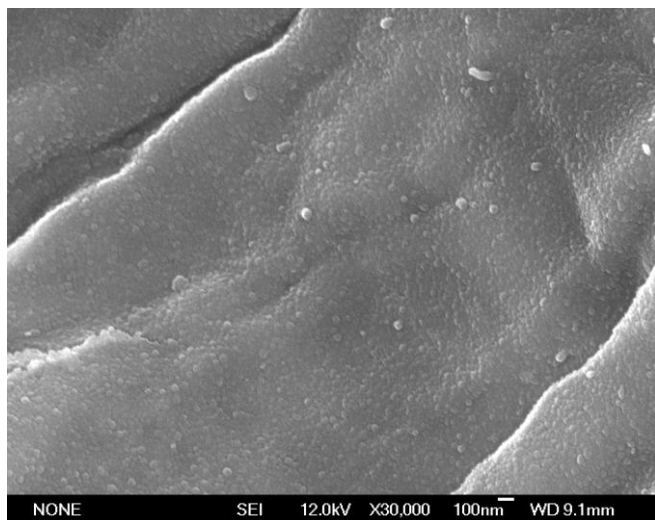


Figure 10. SEM micrograph showing the surface of the cellulose fibre coated with ZnS:Mn nanoparticles

Solution conc. (%)	Average particle size (nm)	Saturation magnetisation (emu g ⁻¹)	Coercive field (Oe)
3.00	26	62	112
0.60	24	62	122
0.05	15	70	42
0.025	12	63	19

Table 5. Effect of precursor solution concentration on particle size, saturation magnetisation and coercive field of Fe₃O₄ nanoparticles.

Appendix B

Conference Presentations

Aaron C. Small, James H. Johnston and Jeffery L. Tallon: Novel Hybrid Materials of Cellulose Fibres with Magnetic Nanoparticles, *International Conference on the Science and Technology of Synthetic Metals, Dublin, July, 2006.*

Aaron C. Small and James H. Johnston: Novel Hybrid Materials of Cellulose and Photoluminescent Nanoparticles, *AMN-3 Advanced Materials and Nanotechnology Conference, Wellington, February, 2007.*

Aaron C. Small and James H. Johnston: Novel Hybrid Materials of Cellulose Fibres and Photoluminescent Nanoparticles, *MC8: Advanced Materials by Chemical Design Conference, London, July, 2007.*

Aaron C. Small and James H. Johnston: Novel Hybrid Materials of Cellulose Fibres and Nanoparticles, *NSTI, Boston, 2008..*

Novel Hybrid Materials of Cellulose Fibres with Magnetic Nanoparticles



Aaron C. Small¹, James H. Johnston¹, Jeffery L. Tallon^{1,2}.

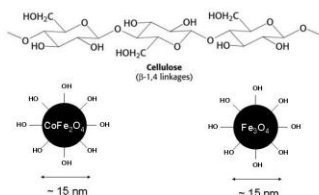
1. School of Chemical and Physical Sciences, Victoria University of Wellington, P. O. Box 600, Wellington, New Zealand. 2. Industrial Research Limited, P. O. Box 31-310 Lower Hutt, New Zealand.

1. Objective.

To develop novel magnetic fibres utilising flexible cellulose (paper) fibres and magnetic nanoparticles.

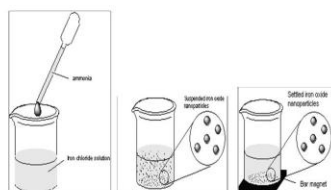
2. Introduction.

Hybrid materials are of interest due to the potential synergistic properties that may arise from the combination of two or more precursors. Two such precursors are paper fibres (cellulose) and magnetic nanoparticles. These hybrid materials exhibit the inherent properties of the substrate, in particular flexibility and tensile strength, and also the magnetic properties of the surface bonded nanoparticles. A hybrid material of this type has potential applications in the upcoming smart paper market of the packaging industry.



3. Experimental.

Magnetite and cobalt ferrite (Fe_3O_4 , CoFe_2O_4) nanoparticles were synthesized by adding aqueous ammonia (1 M, 50 cm³) dropwise from a burette to a solution containing dissolved CoCl_2 or FeCl_3 (2 M, 1.0 cm³) and FeCl_3 (1 M, 4.0 cm³). Black precipitates were formed immediately^{1,2}.



A colloidal suspension of these nanoparticles was then added to an approx. 2 % suspension of bleached *pinus radiata* Kraft paper fibres and stirred vigorously for approx. 2 hours, after which they were filtered and washed with H_2O . The resultant coated fibres were then sonicated for 20 min in order to remove any loosely bound nanoparticles.

• SEM images and EDS measurements were taken on a JEOL-6500F Scanning Electron Microscope.

• Magnetic measurements were taken on a Quantum Design SQUID Magnetometer housed at Industrial Research Ltd.

4. Results & Discussion.



Figure 1

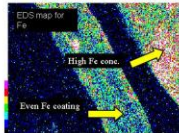
Pinus radiata Kraft fibres coated with Fe_3O_4 or CoFe_2O_4 nanoparticles retain the inherent properties of the fibre; tensile strength, flexibility, and the ability to be made into a sheet. The fibres also gain the magnetic properties of the surface bound nanoparticles, as is demonstrated in figure 1 above.

Optical microscope images (left) at 90x magnification show that the coated fibres (bottom photograph) retain the same morphology as the precursor Kraft fibres (top photograph).

From the SEM images shown below, the completeness of the coating can be seen. This is also confirmed by examining the EDS maps for Fe. X-ray line broadening and TEM indicate that the average particle diameter is approx. 14-16 nm.

It is thought that the nanoparticles are bound to the surface of the cellulose fibres by hydrogen bonding between the surface hydroxyl groups of both components.

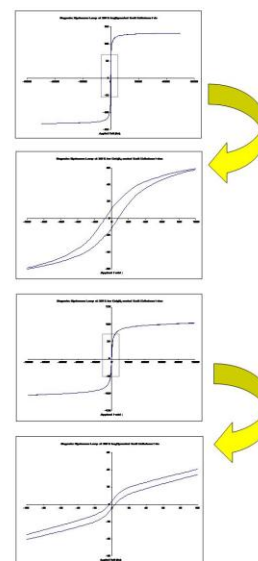
Even after repeated washing and sonication steps, the particles remain bound to the surface.



SQUID magnetometry shows the materials to be either weakly ferromagnetic or superparamagnetic in character. XRF analysis shows the samples to be 0.5-2.8 % Fe. The magnetic moment is comparable to materials with similar Fe_3O_4 and CoFe_2O_4 loadings^{2,3}.

Fe_3O_4 coated samples show a saturation magnetisation of ~ 120 emu g⁻¹, while CoFe_2O_4 coated samples show a saturation magnetisation of ~ 100 emu g⁻¹. These values are comparable to the values of saturation magnetisation of the respective bulk materials, indicating that the combination of cellulose fibres and magnetic nanoparticles has not seen a decrease in the magnetic properties of the nanoparticles.

Both samples show small remnant fields at 300 K; for Fe_3O_4 M_r = ~5 emu g⁻¹, while for CoFe_2O_4 M_r = ~12 emu g⁻¹. Coercive fields at 300 K for these materials are also very low; for Fe_3O_4 H_c = ~4 Oe, and for CoFe_2O_4 H_c = ~80 Oe. These data are summarized in the magnetic hysteresis curves for both samples, shown below.



5. Conclusions.

A hybrid material of paper fibres and magnetic nanoparticles has been successfully synthesized and characterized. Future work will involve optimising the magnetic properties and effectiveness of the coating, along with preliminary applications testing in collaboration with industry.

6. References.

- Berger, P., et al. *J. Chem. Ed.* 1999, **76**, 943-948.
- Camazon-Garcia, J. A., Lopez-Gutierrez, M. A., Rivas-Rey, J., *Colloids and Surface A*, 1997, **121**, 61-66.
- Zakaria, S., Ong, B. H., van de Ven, T. G. M., *Colloids and Surface A*, 2004, **251**, 1-4.

7. Acknowledgements.

- *This research is funded by The MacDiarmid Institute for Advanced Materials and Nanotechnology.
- *Industrial Research Limited for the use of their SQUID Magnetometer.
- *Dr. Grant Williams for assistance with magnetic measurements.

AMN-3, Wellington, 2007.

MC8, London, 2007.

Novel Hybrid Materials of Cellulose Fibres with Photoluminescent Nanoparticles

Aaron C. Small^{1,2}, James H. Johnston^{1,2}

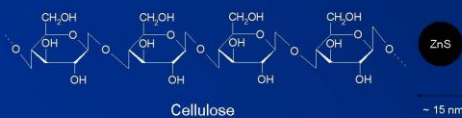
1. School of Chemical & Physical Sciences, Victoria University of Wellington. 2. MacDiarmid Institute of Advanced Materials and Nanotechnology

1. Objective.

To develop novel photoluminescent fibres utilising flexible cellulose (paper) fibres and photoluminescent nanoparticles.

2. Introduction.

Hybrid materials are of interest due to the potential synergistic properties that may arise from the combination of two or more precursors. Two such precursors are paper fibres (cellulose) and photoluminescent nanoparticles. These hybrid materials exhibit the inherent properties of the substrate, in particular flexibility and strength, and also the photoluminescent properties of the surface bonded nanoparticles. A hybrid material of this type has potential application in the upcoming smart paper market of the packaging industry.



3. Experimental.

Zinc sulfide (ZnS) nanoparticles doped with manganese or copper, were synthesized by adding a solution containing S^{2-} , dropwise from a burette, to a solution containing Zn^{2+} and either Cu^{2+} or Mn^{2+} . In the case of Cu^{2+} , thiosulfate solution was added in order to complex the Cu^{2+} ions, thus addressing solubility differences between ZnS and CuS.¹ A white precipitate was formed immediately. Dopant concentrations ranged from 0.1 to 1%.



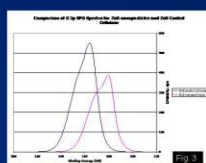
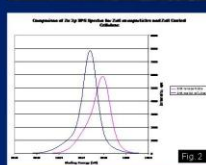
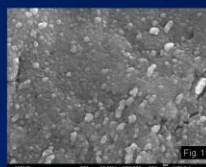
A colloidal suspension of these nanoparticles was then added to an approx. 2 % suspension of bleached *pinus radiata* Kraft paper fibres and stirred vigorously for approx. 2 hours, after which they were filtered and washed with H_2O . The resultant coated fibres were then sonicated for 20 min in order to remove any loosely bound nanoparticles.

• SEM images and EDS measurements were taken on a JEOL-6500F Scanning Electron Microscope.

• XPS was performed on a Kratos Axis Ultra DLD, equipped with a monochromatic Al K α x-ray source.

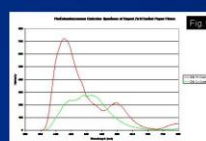
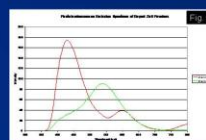
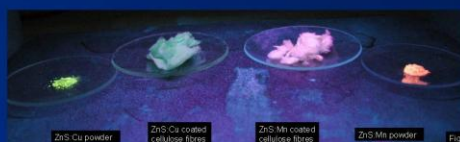
4. Results & Discussion.

From the SEM image (fig. 1), the completeness of the coating can be seen. Individual fibrils on the fibre surface are encapsulated. The fibre itself retains all the properties of an uncoated fibre, despite the surface coating of doped ZnS nanoparticles.



It is clear from XPS measurements of Zn 2p (fig. 2) and S 2p (fig. 3) that there is bonding between the doped ZnS nanoparticles and the fibre surface. This can be seen by comparing the XPS spectra of both doped ZnS nanoparticles and cellulose fibres coated with doped ZnS nanoparticles. There is a distinct shift in the binding energies of both the Zn and S 2p electrons, up to 1.4 eV.

XRD patterns indicate that ZnS nanoparticles have been formed and are present as the zinc blende phase² and are ~ 15 nm in diameter. It is also clear that the doping has no effect on the crystal structure of the material.



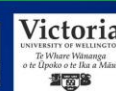
The photoluminescence of the nanoparticles can be seen above in figure 4. Excitation was at 320 nm. These emission colours correspond to the peaks in the photoluminescence emission spectra on the left (fig. 5 and 6). The emission at ~ 600 nm is attributed to the ${}^4T_1-{}^6A_1$ transition in Mn^{2+} , while the emission at ~ 550 nm is due to a transition from the conduction band of ZnS to the t_2 level of excited Cu^{2+} .²

5. Conclusions.

A hybrid material of paper fibres and photoluminescent nanoparticles was successfully synthesized and characterized. Future work will extend to other dopants and nanoparticles, their emission colours, the effectiveness of the coating, along with preliminary applications testing in collaboration with industry.

6. References.

1. Sun, L., et al. *J. Mater. Chem.* 1999, 9, 1655-1657.
2. Yang, P., et al. *Appl. Phys. A.* 2001, 73, 455-458.



NSTI, Boston, 2008.

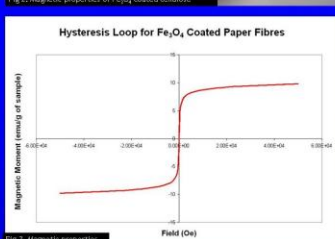
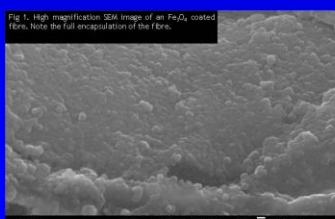
Novel Hybrid Materials of Cellulose Fibres and Nanoparticles

Aaron C. Small & James H. Johnston

Victoria University of Wellington & The MacDiarmid Institute, P. O. Box 600, Wellington, New Zealand.

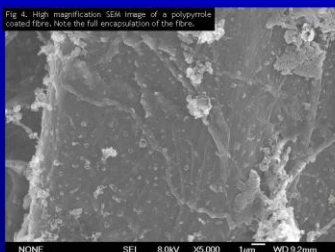
Magnetic cellulose fibres:

- Synthesised by coating bleached Kraft fibres with magnetic nanoparticles
- Nanoparticles synthesised by the method outlined by Thapa *et al.*¹
- SEM images (fig 1) show a completely encapsulated fibre
- Fibre retains inherent properties of the substrate, and gain magnetic properties of the coating (fig 2 and 3)
- A shift in the Fe 2p XPS spectrum of approx. 0.5 eV confirms bonding has occurred between the surface OH groups present on both components
- Such materials may see use in magnetic filtering, the security industry and in EMI shielding



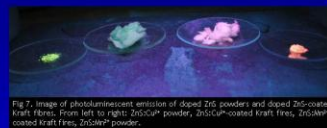
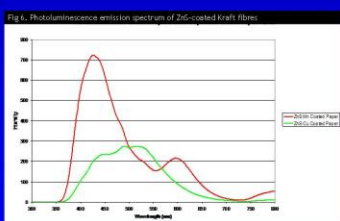
EMI Shielding:

- Synthesised by coating cellulose substrates with polypyrrole and magnetite
- SEM images (fig 4) show a complete coating

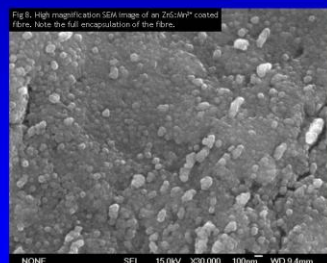


Photoluminescent cellulose fibres:

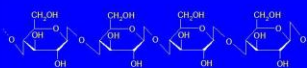
- Synthesised by coating Kraft fibres with doped ZnS nanoparticles
- Nanoparticles synthesised by the method outlined by Mu *et al.* and Sun *et al.*
- Doped with Mn²⁺ and Cu²⁺ to give emissions at approximately 600 nm (Mn²⁺) and 530 nm (Cu²⁺) (fig 6)
- Fibres retain their inherent properties and gain the photoluminescent properties of the doped ZnS (fig 7)



- SEM images show the completeness of the coating (fig 8)

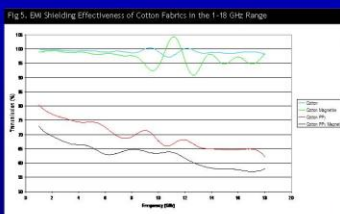


Cellulose:



- High tensile strength
- Suppleness (flexibility, conformability)
- Resistance to plastic deformation
- Water soluble
- Hydrophilic
- Wide range of dimensions
- Inherent bonding ability
- Ability to absorb modifying additives
- Chemically stable
- Relatively colorless

- Samples measured for their EMI shielding effectiveness in the 1-40 GHz range (fig 5)
- > 40 % shielding effectiveness in the 1-18 GHz range (fig 5)
- Synergistic effect of magnetite nanoparticles and polypyrrole (fig 5)



Inkjet Printing of ZnS Quantum Dots:

- Doped ZnS was made water 'soluble' by the use of capping agents
- Viscosity, surface tension and boiling point of the ink was
- Printed on a range of substrates (paper, plastic, ITO, glass, silicon)



- Such materials could see application in the fashion, packaging and security industries

Acknowledgements:

The authors would like to thank the following:

- Dr. Grant Williams and Prof. Jeffrey Tallon for help with magnetic measurements
- Dr. Andrew Amlet from DSTO Australia for help with EMI shielding measurements
- Dr. Noel Clark and Dr. Nafty Vanderhoeck from CSIRO Forest & Biosciences for help with inkjet printing

References:

- Thapa, D. L., *Materials Letters*, 2004, 58, 2692.
- Mu, J., Gu, D., Xu, Z. *Materials Research Bulletin*, 2005, 40, 2198.
- Sun, L., et al. *J. Mater. Chem.*, 1999, 9, 1655.

Appendix C

QUANTUM DOT FIBRES PATENT

PROVISIONAL SPECIFICATION

Synthesis and Binding of ZnS Nanocrystals to Natural or Synthetic Fibres

Filed in 2008 by:

INVENTORS

Michael J. Richardson, James H. Johnston, Thomas Borrmann, Aaron Small.

PROVISIONAL SPECIFICATION

Synthesis and Binding of ZnS Nanocrystals to Natural or Synthetic Fibres

INVENTORS

Michael J. Richardson, James H. Johnston, Thomas Borrmann, Aaron Small

TECHNICAL FIELD

The present invention is for the incorporation of inorganic quantum dots (semiconductor nanocrystals) within and on the fibre matrix of natural or synthetic fibres. As an example, zinc sulfide nanocrystals are presented

BACKGROUND ART

Metallic nanocrystals and inorganic “quantum dots” have been known for many hundreds of years – particularly as a wavelength-sensitive colouration for ceramics (for example the Lycurgus chalice of ancient Rome, fluorescing green under ultra-violet light) and stained glass (such as cathedral windows). However, it is largely within the last hundred years that the theoretical background has developed sufficiently to provide an understanding of these materials.

The defining feature of these particles and “dots” is their small radius (up to a few tens of nanometers) relative to the incident electromagnetic radiation. Within purely metallic particles conduction band electron waves become confined, leading to transverse and longitudinal resonance effects. By contrast, the band gap of an inorganic particle becomes distorted, a feature that may be used in a controlled manner by the intentional inclusion of heteroatoms (dopants) within the crystal lattice. A further consequence of the small particle diameter is the large

proportion of surface atoms or molecules to those in the core. The outer atomic monolayer is generally stabilised by binding to either a surfactant or excess reagent, leading to an imbalance between the core binding energies of the central and surface atoms of the particle.

Inventive effort and the resulting intellectual property to date has concentrated on the use of these quantum dots in optical electronic devices, particularly as light emitting diodes and display components (phosphors). For example, Chen disclosed in 2007 a method for fabricating Si, Al₂O₃ and GaAs-based quantum dots for light emitting diodes (USPTO 7,303,937) using chemical vapour deposition techniques. Andriessen disclosed in 2004 a method for preparing a thin layer inorganic light emitting device based on zinc sulfide (USPTO 6,724,141) for use in panel displays.

The use of quantum dots as a coating for flexible, fibrous substrates has been investigated on an elementary level. Cramer et. al (USPTO 6,645,569) disclosed in 2003 a method whereby nanocrystals may be printed with an ink-jet printer onto both hard and soft, including fibrous, materials. Soane et. al (USPTO 6,607,994) disclosed in 2003 a method for the application of nanocrystals to fibrous or web materials, wherein the nanocrystals were encapsulated in a polymeric coating.

However, due to physical abrasion many such treated fibres exhibit a loss of colour or functionality over time. It is apparent that there is a need for penetration of the nanocrystals to the core of the fibre. Thus, as the outer surface of the fibre becomes worn away, additional nanocrystals are exposed to the surface. The present application is thus concerned with the formation and application of quantum dots (for example zinc sulfide-based) within a natural or synthetic fibre.

SUMMARY OF THE INVENTION

The invention hereby disclosed is for the synthesis of quantum dots on the surface, and throughout the cross-section of natural and synthetic fibres.

BRIEF DESCRIPTION OF THE DRAWINGS

Figures 1a to 1d are energy dispersive spectra (EDS) of merino fibres cross-sections. a) Untreated, b) the same fibres after soaking in ZnCl_2 (1 M.) for 60 min., washing, and drying. The map has been artificially coloured white where high concentrations of zinc were found, black where no zinc was found. c) Cross-section of merino fibre, untreated, d) the same fibre after soaking in ZnSO_4 for 60 min., artificially coloured white where zinc was found, black where no zinc was found.

Figure 2. Excitation and emission (fluorescence) of non-bound ZnS particles.

Figure 3. Emission (photoluminescence) spectra of merino and merino:ZnS, prepared in Example 2, under excitation at 320 nm.

Figure 4. X-ray photoelectron spectra of the Zn 2p and S 2p lines of the free quantum dots prepared in Example 1, and the quantum dots bound to merino fibres, prepared in Example 2.

Figure 5. Emission (photoluminescence) spectra of nylon and nylon:ZnS, prepared in Example 3, under irradiation at 320 nm.

DETAILED DESCRIPTION OF THE INVENTION

The process and resulting material disclosed is applicable to inorganic quantum dots. By way of example, zinc sulfide-based quantum dot/fibre composites are presented.

The invention in the present application is a result of the discovery by the inventors of the absorption of specific ions by particular fibres. In the case of aqueous zinc chloride, for example, zinc has been found to be absorbed into the entire cross section of merino wool fibre. A minor amount is absorbed from a 1 M. aqueous solution within 10 minutes, while a substantial amount is visible under energy dispersive spectroscopy (EDS) after an hour. By contrast, zinc from a solution of zinc sulfate remains on the outer layer of merino wool.

The method of synthesis that follows is a modification of that originally proposed by Axmann [2004] for “free”, or non-bound ZnS quantum dots. The principle improvements added in the present disclosure are 1) use of the chloride, or other halide salts as a zinc base, 2) significant alteration of the ratios and pH of the solutions used, 3) subsequent formation of the quantum dots within the fibre matrix. The fibre is therefore used as a scaffold for the synthesis, preventing aggregation once formation is complete, and providing an easily handled material for post processing and fabrication into consumer goods.

The process hereby disclosed is as follows.

1. Soaking a sample of fibre (for example wool or nylon) in a solution of zinc chloride, to allow absorption of the metal ions. Optionally, the solution may be pH-adjusted. A dopant metal solution (usually manganese chloride, 0.01 M) may also be added to the zinc solution, and optionally a surfactant (usually L-cysteine, 0.25 M.).
2. After the desired soak time (generally between 10 and 60 minutes) the fibre may be removed from

the zinc/manganese solution, and (depending on the proposed end-use) then washed to remove excess reagent from the outer layer of the fibre. Alternatively, if a larger amount of ZnS is required on the surface of the fibre, the fibre may be left in the original zinc/manganese solution.

3. If removed from the initial zinc/manganese solution, the fibre is now placed into a beaker of water or dilute hydrochloric acid to keep it in an aqueous environment. Optionally, a further volume of aqueous surfactant (for example L-cysteine) may be added. The use of the surfactant is preferable for synthetic fibres, such as nylon.
4. Sodium sulfide (1 M, aqueous) is now added at an equimolar Zn:S ratio, preferably under an inert atmosphere, for example argon or nitrogen. For wool fibres, the amount of sulfide added must be decreased such that the pH of the solution remains approximately neutral.
5. The contents of the beaker are mixed gently, too ensure equal distribution of the sulfide solution, and left to stand at room temperature for 30 minutes. The beaker is then heated in a water bath for 60 minutes at 50°C, cooled, then ultra-sonicated for 10 minutes.
6. The fibre is washed at least three times in water and allowed to air dry.

EXAMPLES

Example 1: Preparation of non-bound ZnS:Mn particles

A solution of zinc (2 mL, 1.0 M, aqueous, prepared from zinc chloride) was placed in a vial (20 mL) to which was added aqueous manganese (2 mL, 0.01 M, prepared from manganese chloride), L-cysteine (2 mL, 0.25 M). The solution was preferably purged with argon before rapid addition of aqueous sodium sulfide (2 mL, 1.0 M) and left to stand for 30 minutes at room temperature, followed by 60 minutes at 50°C.

Example 2: Preparation of ZnS:Mn/Merino fibres

A solution of zinc (2 mL, 1.0 M, aqueous, prepared from zinc chloride) was placed in a vial (20 mL) to which was added aqueous manganese (2 mL, 0.01 M, prepared from manganese chloride), and a sample of untreated merino fibre (approximately 0.1 g). L-cysteine (2 mL, 0.25 M) was added to an equivalent reaction mixture, for comparison. The vials were then agitated to ensure complete wetting of the fibre, and allowed to stand for at least 10 minutes. A sample of fibre for XPS analysis was then removed from the vials containing the metal precursors and surfactant, and washed with distilled water before placing into vials containing an equivalent amount of water (due to the sensitivity of the analysis). The fibre for the remaining analyses were kept in the precursor solutions.

The vials were then purged with argon before rapid addition of aqueous sulfide (250 uL, approximately 1.0 M, prepared from sodium sulfide, also under argon). The resulting fibre quantum dot suspension was left to stand for 60 minutes at ambient temperature, followed by 60 minutes at 50°C, before washing with distilled water, sonicating and drying.

Measurement of the excitation spectra for the resulting fibre showed the presence of a peak at 320 nm. Subsequent fluorescence measurements recorded with an excitation wavelength of 320 nm displayed two principle peaks, the first (at approximately 390 nm) attributed to relaxation through defects in the zinc-sulfur lattice, the second (590 nm) attributed to relaxation through the manganese. Typical excitation and fluorescence spectra are shown in the Drawings (Figure 2 and Figure 3).

X-ray photoelectron spectra (XPS) of representative samples are shown in Figures 4a, 4e and 4f for sulfur, and 4b, 4d and 4f for zinc. While the bare merino fibre exhibits two peaks for sulfur, the first (at 164 eV binding energy) corresponding to cystine disulfide bonds in the keratin, the second (168 eV) due to the cysteine SH bonds (Figure 4a). The area, and hence atomic ratio of the two are approximately equal. The zinc sulfide quantum dots, alone, show a single peak at 162.2 eV, due to the surface Zn-S bonds (Figure 4c). The presence of

small “shoulder” on this peak suggest that some of the particle core, with subsequently modified binding energies is also visible to the photoelectron detector. After formation of the quantum dots within and on the fibre (Figure 4e) all three sulfur peaks are present, albeit with substantially different ratios. Significantly, the area of the cystine disulfide peak now dwarfs that of the cysteine sulfur. The only source of additional sulfur in the sample is from zinc sulfide, therefore the quantum dots are bound via disulfide linkages to the cystine of the fibre.

Examination of the Zn 2p X-ray photoelectron spectra for the same samples showed the expected 3/2 and 5/2 doublet of the quantum dots (Figure 4d). No zinc was observed for the untreated fibre (Figure 4b). After formation of the quantum dots within and on the fibre, an additional doublet becomes evident at higher binding energy (Figure 4f). This is attributed to binding of the particles to the cystine of the keratin in the fibre.

Example 3: Preparation of ZnS:Mn/Nylon fibres

A solution of zinc (2 mL, 1.0 M in hydrochloric acid (0.01 M), prepared from zinc chloride) was placed in a vial (20 mL), to which was added aqueous manganese (2 mL, 0.01 M, prepared from manganese chloride), and a sample of nylon (approximately 0.1 g). L-cysteine (2 mL, 0.25 M) was added to an equivalent reaction mixture, for comparison. The vials were agitated to ensure complete wetting of the fibre, then allowed to stand for at least 10 minutes. A sample of fibre for XPS analysis was then removed from the vials containing the metal precursors and surfactant, and washed with distilled water before placing into vials containing an equivalent amount of water (due to the sensitivity of the analysis). The fibre for the remaining analyses were kept in the precursor solutions.

The vial was then purged with argon before rapid addition of aqueous sulfide (2 mL, approximately 1.0 M, prepared from sodium sulfide, also under argon). The resulting quantum dot/fibre composites were left to stand for 30 minutes at ambient temperature, followed by 60 minutes at 50°C, before washing with distilled water, sonication and drying.

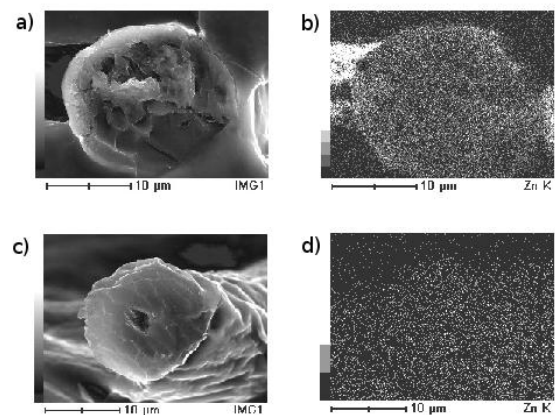
Irradiation at 320 nm provided confirmation of fluorescence. Detailed fluorescence measurements were conducted as per Example 2. Representative excitation and fluorescence spectra are provided in Figure 5.

REFERENCES

- H. Chen, et. al, “*Method of manufacturing a quantum-dot element*”(2007), USPTO 7,303,937.
- H. Andriessen, “*Particular type of a thin layer inorganic light emitting device*” (2004), USPTO 6,724,141.
- R. Cramer, et al, “*Method of applying nanoparticles*” (2003), USPTO 6,645,569.
- D. Soane, et al, “*Nanoparticle-based permanent treatments for textiles*” (2003), USPTO 6,607,994.
- Y. Axmann, “*Manganese doped ZnS nanoparticles : synthesis, particle sizing and optical properties*” (2004), Ecole Polytechnique Federale de Lausanne, Lausanne.
- B. Steitz, Y. Axmann, H. Hofmann, A. Petri-Fink, “*Optical properties of annealed Mn²⁺-doped ZnS nanoparticles*”, Journal of Luminescence, 128, (2008) 92–98.

FIGURES

Figure 1. EDS maps of merino fibres.



Cross-section of merino fibre, a) untreated, b) the same fibres after soaking in ZnCl_2 (1 M.) for 60 min., washing, and drying. The map has been artificially coloured white where high concentrations of zinc were found, black where no zinc was found c) Cross-section of merino fibre, untreated, d) the same fibre after soaking in ZnSO_4 for 60 min.

Figure 2. Excitation (monitoring at 590 nm) and emission (fluorescence) under excitation at 320 nm, of non-bound ZnS:Mn particles from Example 1.

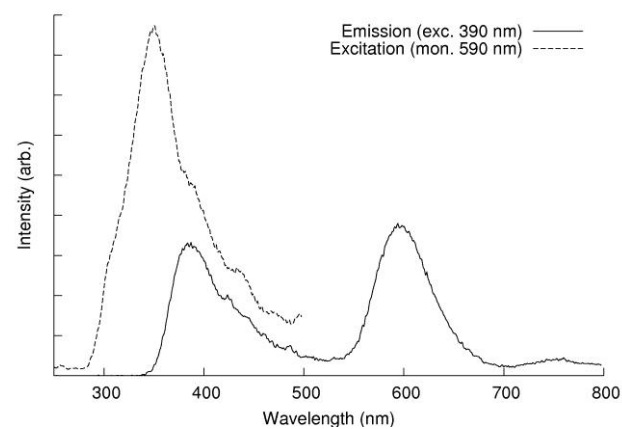


Figure 3. Emission (photoluminescence) spectra of Merino, ZnS:Mn/Merino, and ZnS:Mn/Merino/Cystiene, as prepared in Example 2, under excitation at 320 nm.

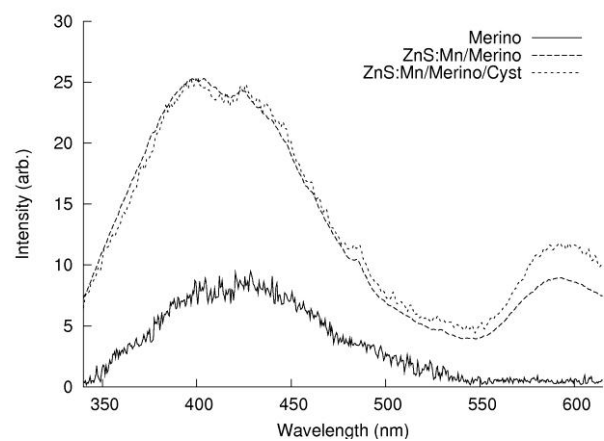


Figure 4. X-ray photoelectron spectra of sulfur (a, c, e) and zinc (b, d, e) of the merino fibres, quantum dots and quantum dot/fibre composite.

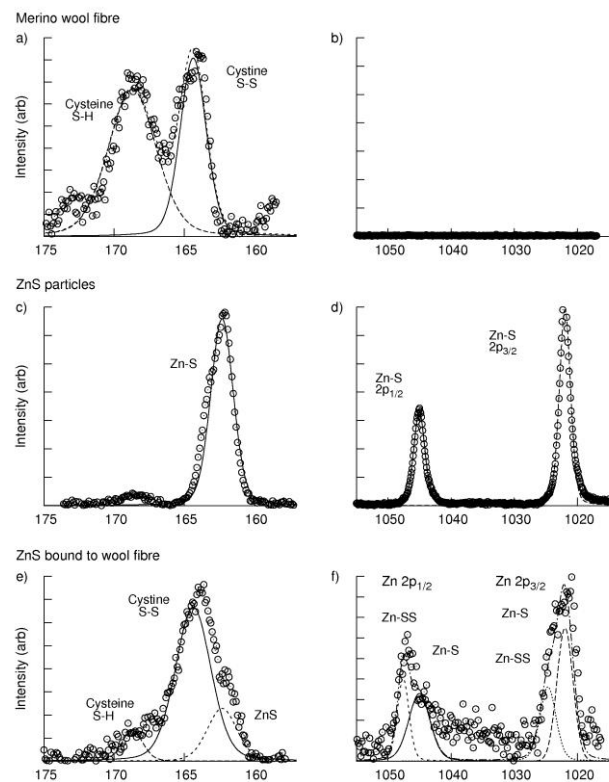
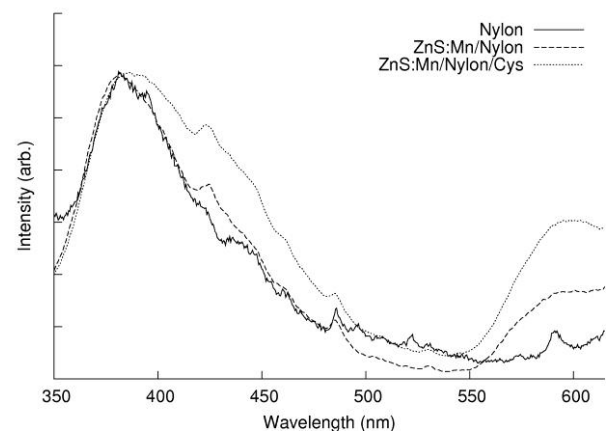


Figure 5. Emission (photoluminescence) spectra of nylon and ZnS:Mn/Nylon, prepared in Example 3, under irradiation at 320 nm.



BIBLIOGRAPHY

1. Wallenberger, F. T., Weston, N. E., *Natural Fibers, Polymers and Composites*, Kluwer Academic Publishers, Boston, 2004.
2. Roberts, J. C., *Paper Chemistry*, Blackie Academic & Professional, Glasgow, 1991.
3. Jones, M., *Organic Chemistry*, W. W. Norton & Company, New York, 1997.
4. Brown, R. M., *Cellulose and other Natural Polymer Systems: Biogenesis, Structure and Degradation*, Plenum Press, New York, 1982.
5. Smook, G. A., *Handbook For Pulp & Paper Technologists*, Angus Wilde Publications, Vancouver, 1992.
6. Kocurek, M. J., Stevens, F., *Pulp and Paper Manufacture*, Joint Textbook Committee of the Paper Industry, 1983.
7. Moraes, J., MSc Thesis, Victoria University of Wellington, 2004.
8. *Fundamentals of Magnetism and Magnetic Measurements*,
<http://www.qdusa.com/resources/techdocs.html>
9. Dunlop, D., J., Ozdemir, O., *Rock Magnetism: Fundamentals and Frontiers*, Cambridge University Press, Cambridge, 1997.
10. Neel, L., *Annals of Physics*, 1948, **3**, 137.
11. Neel, L., *Advances in Physics*, 1955, **4**, 191.
12. Bragg, W. H., *Philosophical Magazine*, 1915, **30**, 305.
13. Enkin, R. J., Williams, W., *Journal of Geophysics Research: Solid Earth*, 1994, **99**, 611.
14. Kim, Y. I., Kim, D., Lee, C. S., *Physica B*, 2003, **337**, 42.
15. *USA Pat.*, 3215572, 1965.
16. Berger, P., Adelman, N. B., Beckman, K. J., Campbell, D. J., Ellis, A. B., Lisensky, G. C., *Journal of Chemical Education*, 1999, **76**, 943.
17. van Ewijk, G. A., Vroege, G. J., Philipse, A. P. , *Journal of Magnetism and Magnetic Materials*, 1999, **201**, 31.

18. Rocchiccioli-Deltcheff, C., Franck, R., Cabuil, V., Massart, R., *Journal of Chemical Research*, 1987, 126.
19. Massart, R., *IEEE Transactions on Magnetics*, 1981, **MAG-17**, 1247.
20. Albornoz, C., Sileo, E. E., Jacobo, S. E., *Physica B*, 2004, **354**, 149.
21. Sun, Y., Ma, M., Zhang, Y., Gu, N., *Colloids and Surfaces A: Physiochemical Engineering Aspects*, 2004, **245**, 15.
22. Sidhu, P. S., Gilkes, R. J., Posner, A. M., *Inorganic Nuclear Chemistry*, 1978, **40**, 429.
23. Welo, L. A., Baudisch, O., *Philosophical Magazine*, 1925, **50**, 399.
24. David, I., Welch, A. J. E., *Transactions of the Faraday Society*, 1956, **52**, 1642.
25. Li, Y., Liao, H., Qian, Y., *Materials Research Bulletin*, 1998, **33**, 841.
26. Lin, Y. S., Hung, Y., Su, J. K., Lee, R., Chang, C., Lin, M. L., Mou, C. Y., *Journal of Physical Chemistry B*, 2004, **108**, 15608.
27. Matura, V., Guari, Y., Larionova, J., Guerin, C., Caneschi, A., Sangregorio, C., Lancelle-Beltran, E., Medhi, A., Corriu, R. J. P., *Journal of Materials Chemistry*, 2004, **14**, 3026.
28. Hirano, S., Yogo, T., Sakamoto, W., Yamada, S., Nakamura, T., Yamamoto, T., Ukai, H., *Journal of the European Ceramic Society*, 2001, **21**, 1479.
29. Chabra, V., Ayyub, P., Chattopadhyay, S., Maitra, A. N., *Materials Letters*, 1996, **26**, 21.
30. Kosak, A., Makovec, D., Drofenik, M., *Physica Status Solidi C*, 2004, **1**, 3521.
31. Anilkumar, M., Ravi, V., *Materials Research Bulletin*, 2005, **40**, 605.
32. Congiu, F., Concas, G., Ennas, G., Falqui, A., Fiorani, D., Marongiu, G., Marras, S., Spano, G., Testa, A. M., *Journal of Magnetism and Magnetic Materials*, 2004, **281**, 1561.
33. Folch, B., Larionova, J., Guari, Y., Guerin, C., Mehdi, A., Reye, C., *Journal of Materials Chemistry*, 2004, **14**, 2703.
34. Garcia-Cerda, L. A., Torres-Garcia, V. A., Matutes-Aquino, J. A., Ayala-Valenzuela, O. E., *Journal of Alloys and Compounds*, 2004, **369**, 148.
35. Huang, X. H., Chen, Z. H., *Journal of Crystal Growth*, 2004, **271**, 287.
36. Huang, X. H., Chen, Z. H., *Solid State Communications*, 2004, **132**, 845.

37. Huang, X. H., Chen, Z. H., *Journal of Magnetism and Magnetic Materials*, 2004, **280**, 37.
38. Huang, X. H., Chen, Z. H., *Materials Research Bulletin*, 2005, **40**, 105.
39. Liu, X. M., Fu, S. Y., Huang, C. J., *Journal of Magnetism and Magnetic Materials*, 2004, **281**, 234.
40. Long, J. W., Logan, M. S., Carpenter, E. E., Rolison, D. R., *Journal of Non-Crystalline Solids*, 2004, **350**, 182.
41. Seo, W. S., Jo, H. H., Lee, K., Kim, B., Oh, S. J., Park, J. T., *Angewandte Chemie: International Edition*, 2004, **43**, 1115.
42. Wu, K. H., Huang, W. C., *Journal of Solid State Chemistry*, 2004, **177**, 3052.
43. Zhang, W., Yang, Z., Liu, Y., Tang, S., Han, X., *Journal of Crystal Growth*, 2004, **263**, 394.
44. Zhang, Y. C., Qiao, T., Hu, X. Y., *Journal of Solid State Chemistry*, 2004, **177**, 4093.
45. Marchessault, R. A., Ricard, S., Rioux, P., *Carbohydrate Research*, 1992, **224**, 133.
46. Marchessault, R. A., Rioux, P., Raymond, L., *Polymer* 1992, **33**, 4024.
47. Ricard, S., Marchessault, R. A., *Materials Research Symposium Proceedings*, 1990, **197**, 319.
48. Rioux, P., Ricard, S., Marchessault, R. A., *Journal of Pulp and Paper Science*, 1992, **13**, J39.
49. Atkins, P., de Paula, J. , *Atkins' Physical Chemistry*, Oxford University Press, New York, 2002.
50. Vij, D. R., *Luminescence of Solids*, Plenum Press, New York, 1998.
51. <http://www.olympusmicro.com/primer/java/jablonski/jabintro/>
52. Hercules, D. M., *Fluorescence and Phosphorescence Analysis: Principles and Applications*, Interscience Publications, New York, 1966.
53. Shriver, D. F., Atkins, P. W., *Inorganic Chemistry*, Oxford University Press, New York, 1999.
54. Alivisatos, A. P., *Science*, 1996, **271**, 933.
55. Peng, X., Mingos, D. M. P., *Semiconductor nanocrystals and silicate nanoparticles*, Springer, New York, 2005.

56. Tang, H., Xu, G., Weng, L., Pan, L., Wang, L., *Acta Materialia*, 2004, **52**, 1489.
57. *CdS Materials Data Safety Sheet*, http://www.sciencelab.com/xMSDS-Cadmium_sulfide-9923232
58. Derfus, A. M., Chan, W. C. W., Bhatia, S. N., *Nano Letters*, 2004, **4**, 11.
59. Lewinski, N., Colvin, V., Drezek, R., *Small*, 2008, **4**, 26.
60. Yang, P., Lu, M., Xu, D., Yuan, D., Song, C., Liu, S., Cheng, X., *Optical Materials*, 2003, **24**, 497.
61. Wang, J., Gao, L., *Solid State Communications*, 2004, **132**, 269.
62. Li, Y., Chen, J., Zhu, C., Wang, L., Zhao, D., Zhuo, S., Wu, Y., *Spectrochimica Acta Part A*, 2004, **60**, 1719.
63. Bhattacharjee, B., Ganguli, D., Chaudhuri, S., Pal, A. K., *Thin Solid Films*, 2002, **422**, 98.
64. Toyoda, M., Watanabe, J., Matsumiya, T., *Journal of Sol-Gel Science and Technology*, 1999, **16**, 93.
65. Chen, W., Sammynaiken, R., Huang, Y., *Journal of Applied Physics*, 2001, **89**, 1120.
66. Lin, C. H., Bi-Shiou, C., Chang, C. H., Lin, J. D., *Materials Chemistry and Physics*, 2002, **77**, 647.
67. Sanchez-Lopez, J. C., Fernandez, A., *Thin Solid Films*, 1998, **317**, 497.
68. Sang, W., Qian, Y., Min, J., Li, D., Wang, L., Shi, W., Yinfeng, L., *Solid State Communications*, 2002, **121**, 475.
69. Bhargava, R. N., Gallagher, D., *Physical Review Letters*, 1994, **72**, 416.
70. Mirhabibi, A. R., Rabiee, M., Aghababazadeh, R., Moztazadeh, F., Hesarak, S., *Pigment and Resin Technology*, 2003, **32**, 358.
71. Mu, J., Gu, D., Xu, Z., *Materials Research Bulletin*, 2005, **40**, 2198.
72. Ishizumi, A., White, C. W., Kanemitsu, Y., *Applied Physics Letters*, 2004, **84**, 2397.
73. Yang, P., Lu, M., Xu, D., Yuan, D., Zhou, G., *Journal of Luminescence*, 2001, **93**, 101.
74. Yang, P., Lu, M., Xu, D., Yuan, D., Song, C., Zhou, G., *Journal of Physics and Chemistry of Solids*, 2001, **62**, 1181.

75. Yang, P., Lu, M., Song, C. F., Xu, D., Yuan, D. R., Cheng, X. F., Zhou, G. J., *Optical Materials*, 2002, **20**, 141.
76. Gavilian, E., Doussineau, T., El Mansouri, A., Smaïhi, M., Balme, S., Janot, M., *Comptes Rendus Chimie*, 2005, 1946.
77. Sahoo, Y., Goodarzi, A., Swihart, M. T., Ohulchanskyy, T. Y., Kaur, N., Furlani, E. P., Prasad, P. N., *Journal of Physical Chemistry B*, 2005, 3879-3885.
78. Wang, R., Xin, J. H., Tao, X. M., Daoud, W. A., *Chemical Physics Letters*, 2004, **398**, 250.
79. Napper, D. H., *Polymeric Stabilization of Colloidal Dispersions*, Academic Press Inc., London, 1983.
80. Russel, W. B., Saville, D. A., Schowalter, W. R., *Colloidal Dispersions*, Cambridge University Press, Cambridge, 1989.
81. Shirakawa, H., Louis, E. J., MacDiarmid, A. G., Chiang, C. K., Heeger, A. J., *Journal of the Chemical Society Chemical Communications*, 1977, **16**, 578.
82. Chiang, C. K., Fincher, C. R., Park, Y. W., Heeger, A. J., Shirakawa, H., Louis, E. J., Gau, S. C., MacDiarmid, A. G., *Physical Review Letters*, 1977, **39**, 1098.
83. Skotheim, T. A., Reynolds, J. R., *The Handbook of Conducting Polymers*, CRC Press, Boca Raton, 2007.
84. de Souza, J. E. G., *Synthetic Metals*, 2001, **119**, 383.
85. Sonosa, Y., *Synthetic Metals*, 2001, **119**, 267.
86. Wright, P. V., Wong, T. C. P., Chambers, P., Anderson, A. P., *Advanced Materials for Optics and Electronics*, 1994, **4**, 253.
87. Bhat, N. V., Seshadri, D. T., Nate, M. M., Gore, A. V., *Journal of Applied Polymer Science*, 2006, **102**, 4690.
88. Hakansson, E., Kaynak, A., Lin, T., Nahavandi, S., Jones, T., Hu, E., *Synthetic Metals*, 2004, **144**, 21.
89. Ding, J., Misoska, V., Price, W. E., Ralph, S. F., Tsekouras, G., Wallace, G. G., *Synthetic Metals*, 2003, **135-136**, 35.
90. Kaneko, M., *Synthetic Metals*, 2001, **121**, 53.
91. Too, C. O., *Synthetic Metals*, 2001, **123**, 53.
92. Korri-Youssoufi, H., *Synthetic Metals*, 2001, **119**, 265.

93. Lee, S. J., *Synthetic Metals*, **121**, 1691.
94. Ruseckas, A., *Synthetic Metals*, 2001, **119**, 603.
95. Xie, H., *Synthetic Metals*, 2001, **122**, 287.
96. Hohnholtz, D., MacDiarmid, A. G., *Synthetic Metals*, 2001, **121**, 1327.
97. Stenger-Smith, J., *Progressive Polymer Science*, 1998, **23**.
98. MacDiarmid, A. G., *Current Applied Physics*, 2000, **1**, 269.
99. Malinauskas, A., *Polymer*, 2001, **42**, 3957.
100. Harraz, F. A., *Journal of the Electrochemical Society*, 1994, **153**, C349.
101. Rane, S., Beaucage, G., *Polymer Data Handbook*, Oxford University Press, New York, 1999.
102. Wang, P., MacDiarmid, A. G., *Synthetic Metals*, 2001, **119**, 367.
103. Ranu, B. C., Hajra, A., *Tetrahedron*, 2001, **57**, 4767.
104. Jang, K. S., Han, S. S., Suh, J. S., Oh, E. J., *Synthetic Metals*, 2001, **119**, 107.
105. Oh, E. J., Jang, K. S., MacDiarmid, A. G., *Synthetic Metals*, 2001, **125**, 267.
106. Jang, K. S., Lee, H., Moon, B., *Synthetic Metals*, 2004, **143**, 289.
107. Johnston, J. H., Richardson, M. J., Moraes, J., Kelly, F., Borrmann, T. B., Appita, 2005.
108. Richardson, M. J., Johnston, J. H., Borrmann, T., *Current Applied Physics*, 2006, **6**, 462.
109. Wang, Y., Jing, X., *Polymers for Advanced Technologies*, 2005, **16**, 344.
110. Joo, J., Epstein, A. J., *Applied Physics Letters*, 1994, **65**, 2278.
111. Hakansson, E., Amiet, A., Kaynak, A., *Synthetic Metals*, 2006, **156**, 917.
112. Hakansson, E., Amiet, A., Nahavandi, S., Kaynak, A., *European Polymer Journal*, 2007, **43**, 205.
113. Kim, M. S., Kim, H. K., Byun, S. W., Jeong, S. H., Hong, Y. K., Joo, J. S., Song, K. T., Kim, J. K., Lee, C. J., Lee, J. Y., *Synthetic Metals*, 2002, **126**, 233.
114. Oittinen, P., Saarelma, H., *Printing*, Fatpey Oy, Helsinki, 1998.
115. de Gans, B. J., Hoeppener, S., Schubert, U. S., , *Advanced Materials*, 2006, **18**, 910.
116. Althues, A., Palkovits, R., Rumplecker, A., Simon, P., Sigle, W., Bredol, M., Kynast, U., Kaskel, S., *Chemistry of Materials*, 2006, **18**, 1068.
117. Althues, A., Henle, J., Kaskel, S., *Chemical Society Reviews*, 2007, **36**, 1454.

118. New Zealand Exports and Imports, <http://www.stats.govt.nz/economy/exports-and-imports/default.htm>
119. Flanders, P. J., *Journal of Applied Physics*, 1988, **63**, 3940.
120. Hakansson, E., Amiet, A., Kaynak, A., *Synthetic Metals*, 2006, **156**, 917-925.
121. Nicolson, A. M., Ross, G. F., *IEEE Transactions on Instrumentation and Measurement*, 1970, **19**, 377.
122. Anton, H., *Calculus*, New York, 1999.
123. Berger, P., Adelman, N. B., Beckman, K. J., Campbell, D. J., Ellis, A. B., Lisensky, G. C., *Journal of Chemical Education*, 1999, **76**, 943.
124. Thapa, D., Palkar, V. R., Kurup, M. B., Malik, S. K., *Materials Letters*, 2004, **58**, 2692.
125. Kim, Y. I., Kim, D., Lee, C. S., *Physica B*, 2003, **337**, 42.
126. Jolly, R., Petrescu, C., Thieblemont, J. C., Marechal, J. C., Menneteau, F. D., *Journal of Coated Fabrics*, 1994, **23**, 228.
127. Sun, L., Liu, C., Liao, C., Yan, C., *Solid State Communications*, 1999, **111**, 483.
128. Aylward, G., Findlay, T., *SI Chemical Data*, John Wiley & Sons, Australia, Brisbane, 2002.
129. Bol, A. A., Ferwerda, J., Bergwerff, J. A., Meijerink, A., *Journal of Luminescence*, 2002, **99**, 325.
130. Feldmann, C., *Advanced Functional Materials*, 2003, **13**, 101.
131. Khosravi, A. A., Kundu, M., Jatwa, L., Deshpande, S. K., *Applied Physics Letters*, 1995, **67**, 2702.
132. Lee, S., Song, D., Kim, D., Lee, J., Kim, S., Park, I. N., Choi, Y. D., *Materials Letters*, 2004, **58**, 342.
133. Lynch, W. E., Nivens, D., Helmly, B. C., Richardson, M., Williams, R. R., *Chemical Educator*, 2004, **9**, 1.
134. Peng, W. Q., Cong, G. W., Qu, S. C., Wang, Z. G., *Optical Materials*, 2006, **29**, 313.
135. Que, W., Zhou, Y., Lam, Y. L., Chan, Y. C., Kam, C. H., *Applied Physics Letters*, 1998, **73**, 2727.

- 136. Wang, M., Sun, L., Fu, X., Liao, C., Yan, C., *Solid State Communications*, 2000, **115**, 493.
- 137. Yang, P., Song, C., Lu, M., Zhou, G., Yang, Z., Xu, D., Yuan, D., *Journal of Physics and Chemistry of Solids*, 2002, **63**, 639.
- 138. Huang, F., Peng, Y., Lin, C., *Chemical Research in Chinese Universities*, 2006, **22**, 675.
- 139. Jian, W., Zhuang, J., Zhang, D., Dai, J., Yang, W., Bai, Y., *Materials Chemistry and Physics*, 2006, **99**, 494.
- 140. Luo, X., Cao, W., Zhou, L., *Journal of Luminescence*, 2007, **122-123**, 812.
- 141. Sun, J., Hao, E., Sun, Y., Zhang, X., Yang, B., Zou, S., Shen, J., Wang, S., *Thin Solid Films*, 1998, **327-329**, 528.
- 142. Steitz, B., Axmann, Y., Hofmann, H., Petri-Fink, A., *Journal of Luminescence*, 2008, **128**, 92.
- 143. Quan, Z., Wang, Z., Yang, P., Lin, J., Fang, J., *Inorganic Chemistry*, 2007, **46**, 1354.
- 144. Warad, H., Sugunan, A., Thanachayanont, C., Dutta, J., *Microscopy and Microanalysis*, 2005, **11**, 1912.
- 145. Yu, X., Yang, L., Yang, S., Zhou P., *Journal of Materials Research*, 2007, **22**, 1207.
- 146. Li, Y., Chen, J., Zhu, C., Wang, L., Zhao, D., Zhuo, S., Wu, Y., *Spectrochimica Acta Part A*, 2004, **60**, 1719.
- 147. Chatterjee, A., Priyam, A., Bhattacharya, S. C., Saha, A., *Colloids and Surfaces A: Physiochemical Engineering Aspects*, 2007, **297**, 258.
- 148. Lee, J. H., Kim, Y. A., Kim, K., Huh, Y. D., Hyun, J. W., Kim, H. S., Noh, S. J., Hwang, C., *Bulletin of the Korean Chemical Society*, 2007, **28**, 1091.
- 149. Kho, R., Torres-Martinez, C. L., Mehra, R. K., *Journal of Colloid and Interface Science*, 2000, **227**, 561.
- 150. Feldmann, C., *Advanced Functional Materials*, 2003, **13**, 101-107.
- 151. Feldmann, C., *Solid State Sciences*, 2005, **7**, 868.
- 152. Warad, H. C., Ghosh, S. C., Hemtanon, B., Thanachayanont, C., Dutta, J., *Science and Technology of Advanced Materials*, 2005, **6**, 296.

153. Sohling, U., Jung, G., Saenger, D. U., Lu, S., Kutsch, B., Mennig, M., *Journal of Sol-Gel Science and Technology*, 1998, **13**, 685.
154. Zhuang, J., Zhang, X., Wang, G., Li, D., Yang, W., Li, T., *Journal of Materials Chemistry*, 2003, **13**, 1853.
155. Algar, W. R., Krull, U. J., *ChemPhysChem*, 2007, **8**, 561.
156. Althues, A., Palkovits, R., Rumplecker, A., Simon, P., Sigle, W., Bredol, M., Kynast, U., Kaskel, S., *Chemistry of Materials*, 2006, **18**, 1068.
157. Manzoor, K., Vadera, S. R., Kumar, N., Kutty, T. R. N., *Solid State Communications*, 2004, **129**, 469.
158. Ghosh, G., Naskar, M., K., Patra, A., Chatterjee, M., *Optical Materials*, 2006, **28**, 1047.
159. Panda, S. K., Datta, A., Chaudhuri, S., *Chemical Physics Letters*, 2007, **440**, 235.
160. Pei, W., Kumada, H., Natusme, T., Saito, H., Ishio, S., *Journal of Magnetism and Magnetic Materials*, 2007, **310**, 2375.
161. Sun, J., Zhou, S., Hou, P., Yang, Y., Weng, J., Li, X., Li, M., *Journal of Biomedical Materials Research*, 2006, **80A**, 333.
162. Carrazana-Garcia, J. A., Lopez-Quintela, M. A., Rivas-Rey, J., *IEEE Transactions on Magnetics*, 1995, **31**, 3126.
163. Zakaria, S., Ong, B. H., van de Ven, T. G. M., *Colloids and Surfaces A: Physiochemical Engineering Aspects*, 2004, **251**, 1-4.
164. Zakaria, S., Ong, B. H., van de Ven, T. G. M., *Colloids and Surfaces A: Physiochemical Engineering Aspects*, 2004, **251**, 31-36.
165. Shchukarev, A., Sundberg, B., Mellerowicz, E., Persson, P., *Surface and Interface Analysis*, 2002, **34**, 284.
166. Johansson, L., Campbell, J. M., *Surface and Interface Analysis*, 2004, **36**, 1018.
167. McIntyre, N. S., Zetaruk, D. G., *Analytical Chemistry*, 1977, **49**, 1521-1529.
168. Anderson, J. F., Kuhn, M., Diebold, U., *Surface Science Spectra*, 1998, **4**, 266.

169. Moulder, J. F., *Handbook of x-ray photoelectron spectroscopy: a reference book of standard spectra for identification and interpretation of XPS data*, Physical Electronics Division, Perkin-Elmer Corporation, Minneapolis, 1992.
170. Abe, M., Ishihara, T., Kitamoto, Y., *Journal of Applied Physics*, 1999, **85**, 5705.
171. Sugimoto, T., Matijevic, E., *Journal of Colloid and Interface Science*, 1980, **74**, 227.
172. Damasceno Da Silva, L. R., Gushikem, Y., Do Carmo Goncalves, M., Rodrigues Filho, U. P., De Castro, S. C., *Journal of Applied Polymer Science*, 1995, **58**, 1669.
173. Briggs, D., Beaman, G., *Analytical Chemistry*, 1993, **65**, 1517.
174. Carrazana-Garcia, J. A., Lopez-Quintela, M. A., Rivas-Rey, J., *Colloids and Surfaces A: Physiochemical Engineering Aspects*, 1997, 61.
175. Gallagher, D., Heady, W. E., Racz, J. M., Bhargava, R. N., *Journal of Materials Research*, 1995, **10**, 870.
176. Sooklal, K., Cullum, B. S., Angel, S. M., Murphy, C. J., *Journal of Physical Chemistry*, 1996, **100**, 4551.
177. Deroubaix, G., Marcus, P., *Surface and Interface Analysis*, 1992, **18**, 39.
178. Eychmuller, A., *Journal of Physical Chemistry B*, 2000, **104**, 6514.
179. Li, H., Shih, W. Y., Shih, W. H., *Nanotechnology*, 2007, **18**, 1.
180. Silverstein, R. M., *Spectrometric identification of organic compounds* John Wiley & Sons, Hoboken, NJ, 2005.
181. Bol, A. A., Meijerink, A., *Physica Status Solidi B*, 2001, **224**, 173.
182. Yang, P., Lu, M., Xu, D., Yuan, D., Chang, J., Zhou, G., Pan, M., *Applied Physics A*, 2002, **74**, 257.
183. Hu, H., Zhang, W., *Optical Materials*, 2006, **28**, 536.
184. Sun, L., Yan, C., Liu, C., Liao, C., Li, D., Yu, J., *Journal of Alloys and Compounds*, 1998, **275-277**, 234.
185. Qu, S. C., Zhou, W. H., Liu, F. Q., Chen, N. F., Wang, Z. G., *Applied Physics Letters*, 2002, **80**, 3605.

186. Manzoor, K., Vadera, S. R., Kumar, N., Kutty, T. R. N., *Materials Chemistry and Physics*, 2003, **82**, 718.
187. Liu, J. Z., Yan, P. X., Yue, G. H., Chang, J. B., Qu, D. M., Zhuo, R. F., *Journal of Physics D: Applied Physics*, 2006, **39**, 2352.
188. Ehlert, O., Osvet, A., Batentschuk, M., Winnacker, A., Nann, T., *Journal of Physical Chemistry B*, 2006, **110**, 23175.
189. Yang, P., Lu, M., Xu, D., Yuan, D., Song, C., Zhou, G., *Applied Physics A*, 2002, **74**, 525.
190. Nakanishi, Y., Yamashita, H., Shimaoka, G., *Japanese Journal of Applied Physics*, 1981, **20**, 2261.
191. Chen, W., Joly, A. G., Malm, J., Bovin, J., *Journal of Applied Physics*, 2004, **95**, 667.